



UNIVERSITA' DELLA CALABRIA

Dipartimento di Ingegneria per l'Ambiente e il Territorio e Ingegneria Chimica – DIATIC

Dottorato di Ricerca in

Scienze e Ingegneria dell'Ambiente, delle Costruzioni e dell'Energia – SIACE

CICLO

XXXII (32)

TITOLO TESI

Innovative Low-fouling Membranes - an Advanced Coating Approach
using UV-LED Polymerisation

Settore Scientifico Disciplinare CHIM/06 – Chimica Organica

Coordinatore: Ch.mo Prof. Salvatore Critelli

Firma

Firma oscurata in base alle linee guida del Garante della privacy

Supervisore/Tutor: Ch.mo Prof. Bartolo Gabriele

Dott. Alberto Figoli

Firma

Firma oscurata in base alle linee guida del Garante della privacy

na

Firma oscurata in base alle linee guida del Garante della privacy

Prof. Dr. -Ing. Jan Hoinkis

Firma

Firma oscurata in base alle linee guida del Garante della privacy

Dottorando: Dott. Ephraim Gukelberger

Firma

Firma oscurata in base alle linee guida del Garante della privacy

Acknowledgements

Foremost I would like to express my sincere gratitude to my supervisors of my thesis, Prof. Bartolo Gabriele, Dr. Alberto Figoli and Prof. Dr.-Ing. Jan Hoinkis for giving me the chance to do my PhD in such an enriching topic. I cannot express enough gratitude for the continued support, encouragement and the professional guidance throughout my PhD period. I am truly grateful for being involved in the EU funded *VicInAqua* project, initiated by my direct superior Prof. Dr.-Ing. Jan Hoinkis, and work within a unique sustainable aquaculture project which deals with today's global problems. He also gave me liberty to make my own decisions in the technical coordination and grow further in my physical and mental abilities. It has been truly fulfilling being part of his team.

Furthermore, special thanks go to Dr. Francesco Galiano who was really supportive within my stay in Rende (CS), Italy, during my PhD period. With his vast experience he was a huge help in clarifying fundamental questions about my research. Beyond he was a true help in clearing up administrative questions and requirements. Dr. Raffaella Mancuso was certainly one of the most important persons since she kept synthesising the AUTEAB surfactant in a professional way and provided a high-quality product— without her help I could not have coated even one membrane.

It has been my real pleasure to have Talha Sami Atiye as my project colleague. No one but him made the stay in Kisumu, Kenya, the most pleasant, bringing me unforgettable memories. He was a major part in establishing the *VicInAqua* project and with it the installation of the pilot MBR. *Asante sana rafiki*. I am also truly grateful for having such enjoyable colleagues Edgardo Cañas-Kurz and Ulrich Hellriegel who have a great sense of humour paired with a professional work attitude. Our stimulating discussions really helped me to achieve even better work results. Sometimes a rattlesnake tracks down a bird even if it hides in deepest, rearmost corners of a gasifier— stay humble and grateful.

I would like to express my special thanks to all the staff members of the Faculty of Electrical Engineering & Information Technology and with particular focus, my deepest gratitude to Jan Wernthal and Gerd Westermann for the encouragement, insightful comments and immense knowledge about the construction of the automated coating setups.

Margarita Aleksandrova supported me in all the fundamental questions about analytics which was a basic element of my work. I will never forget her competence, her unconditional patience and very pleasant manner. I want to thank Dr. Denis Neher and Dr. Fino Scholl for being a true inspiration as they embody the German virtues of hard-working and determined research engineers like hardly no other. Janna Bockelmann, you are a creative virtuoso, thank you for all the support and inspiring discussions, your share in this work will never be forgotten.

Last but not least, I am overwhelmed and, in all humbleness, and gratefulness for receiving unconditional support from my family throughout my entire PhD period. It was a great comfort and relief to know about their support. I want to thank my brother and my future sister in law for their endless patience and encouragement, spending hours of their valuable holiday at my expense.

Spring 2020

Ephraim Gukelberger

Acknowledgements

Abstract

Overcoming hurdles connected with increasing water scarcity exacerbated by climate change is one of the major challenges of this century. Membrane bioreactors (MBR) have been applied for more than two decades improving the water recovery of industrial and domestic wastewater treatment processes and ease this situation. Occurring membrane fouling phenomena pose a massive drawback for achieving a highly efficient filtration in the long run.

One fouling mitigation approach is the novel low-fouling membrane coating using a polymerisable bicontinuous microemulsion (PBM). In this thesis, the membrane coating process and the layer polymerisation mainly initiated by UV-LED light was systematically studied. A casting process was evaluated on small scale samples (0.0085 m²) and further developed. For the first time UV-LED light induced PBM coating has been applied on a pilot scale of 3.125 m² membrane surface area. Studies included the validation of a modified, low cost surfactant to reduce overall synthesis costs. Membrane pore intrusion of the low viscous PBM during the casting coating presented an obstacle to meet competitive filtration capacities compared to commercial ultrafiltration (UF) polyethersulfone (PES) membranes. Viscosity modification towards higher values was studied based on controlled radical polymerisation inhibition. Additionally, a high discrepancy to the pristine PBM coating solution was determined. The development and construction of an automated coating machine enabled high production quantities. Ultimately, the novel coating was tested in a customised pilot MBR for the treatment of domestic wastewater. The pilot tests allowed the direct and simultaneous comparison between a PBM coated and commercial PES module. Short stress tests through a flux step profile and a long-term operation were carried out under constant flux conditions. The PBM coated membrane showed lower permeability with a higher increase in the specific transmembrane pressure (TMP) within a 137-day trial period. Subsequently, post studies validated the chemical stability of the coating material qualitatively.

Various experiments revealed limitations for low-strength domestic wastewater application in terms of lower critical flux. Based on these findings, a feasibility study of spray coating technology using two different atomisation approaches on a lab scale was conducted. Spray coating prevents shearing between the casting knife, the liquid PBM and the membrane surface which reduces the pore intrusion effect potentially.

Abstract

Various preliminary spray tests were examined to study the surface coverage along the membrane width in correlation with the given spray parameters. It was shown that there were structural differences of the polymerised coating layers compared to the casting coating techniques. In conclusion, spray coating using dual-fuel nozzles improved the membrane performance. Furthermore, high operation flexibility helped to produce defined spray coverages and layer thickness for any type of coating material as well as membrane substrate. However, some effects remain unclear. This requires a more fundamental study of material properties and atomisation technologies related to polymerisable bicontinuous microemulsions due to complex interactions.

Key Words: MBR, low fouling, membrane modification, microemulsion, spray coating

Contents

1	Introduction	1
1.1	<i>Background and motivation</i>	1
1.2	<i>Previous work</i>	2
1.3	<i>Objective</i>	4
1.4	<i>Scope and organisation of thesis</i>	4
2	Fundamentals of Membrane Technology	8
2.1	<i>Membrane application and their requirements</i>	8
2.1.1	UF membrane type, suitable materials and application	12
2.1.1.1	Polymeric membranes	12
2.1.1.2	Ceramic membranes	12
2.1.1.3	Metallic membranes	12
2.1.2	Membrane module configuration for MF/ UF application	13
2.1.3	Key parameters for membrane application	14
2.2	<i>Membrane separation processes</i>	15
2.2.1	Resistance model	15
2.2.2	Concentration polarisation	16
2.3	<i>Membrane bioreactor</i>	19
2.3.1	MBR design	20
2.3.2	Anaerobic MBR	22
2.3.3	Decentralised MBR application	22
2.3.4	Energy efficiency improvement strategies	24
2.4	<i>Membrane fouling</i>	25
2.4.1	Cake layer formation	26
2.4.2	Biofouling	27

2.4.3	Fouling propagation	28
2.4.4	MBR fouling prevention and removal	30
2.5	<i>Membrane modification</i>	31
2.5.1	Membrane key parameters and characterisation	31
2.5.1.1	Pore size and pore distribution	32
2.5.1.2	Surface properties	32
2.5.1.3	Rheology	36
2.5.1.4	Durability	38
2.5.2	Modification technologies	39
2.5.3	Membrane coating technologies	40
2.5.3.1	Spin coating	40
2.5.3.2	Dip coating	41
2.5.3.3	Casting coating	41
2.5.3.4	Spray coating	42
2.5.3.5	Basics of atomisation	43
2.5.3.6	Theoretical considerations about ultrasonic spray coating	45
3	Polymerizable Bicontinuous Microemulsion – Fundamentals and Literature Review	51
3.1	<i>Definition of microemulsion systems</i>	51
3.2	<i>Thermodynamic background</i>	52
3.2.1	Comparing macro- and microemulsions	53
3.2.2	Critical micelle concentration and varying microstructures	54
3.3	<i>Literature review</i>	55
3.3.1	Microemulsion – scope of use	55
3.3.2	Polymerisable microemulsion systems in research and industry	57
3.4	<i>PBM modification based on UV-LED polymerisation</i>	58
3.4.1	Radical polymerisation	59
3.4.2	UV-LED light induced polymerisation	60
3.4.3	Basic elements for the work carried out	61
4	Materials and Methods	66
4.1	<i>Materials used</i>	68
4.1.1	PBM composition	68
4.1.2	Pipetting errors and membrane properties	70
4.1.3	Casting coating tool and UV-LED lamp	71
4.1.3.1	Casting coating tool	71
4.1.3.2	UV-LED lamp	72

4.2	<i>Characterisation methods</i>	74
4.2.1	Rheology	74
4.2.2	Modifying PBM viscosity	74
4.2.3	Surface tension measurements	75
4.2.4	Molecular structure identified by nuclear magnetic resonance	76
4.2.5	FTIR measurements	77
4.2.5.1	Validating irradiation homogeneity	78
4.2.5.2	FTIR verifying chemical stability	79
4.2.6	Contact angle measurements	80
4.2.7	Atomic force microscopy	80
4.2.8	Scanning electron microscopy	81
4.2.9	Confocal light microscopy	82
4.3	<i>Experimental setup</i>	83
4.3.1	Membrane cross-flow test unit	84
4.3.2	Modifying PBM viscosity by controlled radical polymerisation	87
4.3.3	Automated membrane coating system	91
4.3.3.1	Process parameters	91
4.3.3.2	Control system for automatic membrane upscaling	96
4.3.3.3	Final assembly and coating sequences	98
4.3.4	Pilot scale setup	99
4.3.4.1	MBR setup and PBM module integration	99
4.3.4.2	Methodology	102
4.3.5	Spray coating setup	105
4.3.5.1	Pressure nozzle	105
4.3.5.2	Duel-fuel nozzle	106
4.3.5.3	System description	107
4.3.5.4	Challenges for PBM atomisation using piezo ceramics	110
5	Preliminary Experimental	112
5.1	<i>Polymerisation homogeneity measured with FTIR</i>	113
5.2	<i>Uneven coating layer</i>	113
5.3	<i>Casting coating tool</i>	114
5.4	<i>Casting coating parameter adjustment</i>	116
5.5	<i>Membrane pore intrusion phenomenon</i>	117
5.6	<i>Observations by confocal microscopy</i>	118
5.7	<i>Surface tension</i>	120

6	Results and Discussion	124
6.1	<i>Casting coating application</i>	126
6.1.1	Classic and modified AUTEAB	126
6.1.1.1	Contact angle measurements	127
6.1.1.2	Atomic force microscopy	128
6.1.1.3	Model foulant tests comparing classic and modified AUTEAB	129
6.1.2	Constant flux operation on lab scale	130
6.1.3	Chemical resistance tests	131
6.2	<i>Feasibility of PBM viscosity modification for UF application</i>	133
6.2.1	Protocol development	133
6.2.2	Rheological examination	138
6.2.3	Verifying the feasibility for pilot scale trials	140
6.3	<i>PBM upscaling for pilot scale domestic wastewater treatment</i>	142
6.3.1	PBM performance tests treating real domestic wastewater	142
6.3.2	Comprehensive water analysis	146
6.3.3	PBM stability validated by FTIR measurements	148
6.3.4	Comparing lab scale with pilot scale	150
6.4	<i>Spray coating application</i>	154
6.4.1	Comparing spray nozzle principles	154
6.4.2	Spray coverage of the dual-fuel nozzle	158
6.4.3	Membrane performance tests	161
6.5	<i>Casting versus spray coating</i>	163
6.5.1	Contact angle measurements	163
6.5.2	Scanning electron microscopy	164
6.5.3	Chemical characterisation by solid state NMR	166
6.5.4	Membrane performance test	167
7	Conclusion and Future Work	172
7.1	<i>Conclusion</i>	172
7.2	<i>Future Work</i>	174
	References	177
	Annex	195

Abbreviations and Symbols

Abbreviations

Acronym	Description	Function
AFM	Atomic force microscopy	
anMBR	Anaerobic MBR	
APS	Ammonium persulfate	REDOX initiator
AUTEAB	acryloyloxyundecyltriethylammonium bromide	Main surfactant
BaTiO ₃	Barrium titanate	
BHT	2,6-Di-tert-butyl-4-methylphenol	
BSA	Bovine serum albumin	
CA	Cellulose acetate	
CAM	Contact angle measurements	
CAS	Conventional activated sludge system	
CH ₄	Methane	
Co	Cobalt	
CO ₂	Carbon dioxide	
CP	Concentration polarisation	
DI water	Deionised water	
ED	Electro dialyses	
eEPS	EPS outside of the cell layer	
eEPS _c	High contented carbohydrate EPS	
eEPS _p	High contented protein EPS	
EGDMA	Ethylene glycol dimethylacrylate	Cross-linker
EOR	Enhanced oil recovery	
EPS	Extracellular polymeric substances	
eSMP _c	High contented carbohydrate SMP	
eSMP _p	High contented protein SMP	
Fe	Iron	
FO	Forward osmosis	
FO	Forward osmosis	
FS	Flat-sheet	
FTIR	Fourier transform infrared spectrometer	
FTS	Field treatment system	
FU	Frequency converter	
Ga	Gallium	
H ₂	Gaseous hydrogen	
H ₂ O ₂	hydrogen peroxide	
H ₂ S	Hydroxide sulphate	

H ₃ PO ₄	phosphoric acid	
HA	Humic acid	
HEMA	1,2-Ethandiol mono(2-methylpropenoate)	Co-surfactant
HF	Hollow fibre	
Hg	Mercury	
HNO ₃	nitric acid	
ICIC	5-isocyanato-isophthaloyl chloride	
iMBR	Immersed/submerged MBR	
IMS	Integrated membrane systems	
In	Indium	
IP	Ingress Protection	
Irgacure 184	1-Hydroxy-cyclohexyl-phenyl-ketone	Photo initiator
KOH	potassium hydroxide	
LED	Light emitting diode	
MBR	Membrane bioreactor	
MD	Membrane distillation	
MEA	Membrane electrode assemblies	
MF	Mircofiltration	
MMA	Methyl methacrylate	Oil phase (nonpolar)
MPD	m-phenylenediamine	
N ₂	Gaseous nitrogen	
NaClO	Sodium hypochlorite	
NaOH	Sodium peroxide	
NF	Nanofiltration	
NMR	Nuclear magnetic resonance	
NO _x	Nitrogen oxide emissions	
O ₂	Gaseous oxygen	
-OH	hydroxyl group	
PA	Polyamide	
PAN	Polyacrylonitrile	
Pb[Zr _x Ti _{1-x}] ₂ O ₇	Zirconated lead	
PBM	Polymerisable Bicontinuous Microemulsion	
PE	Polyether	
PEC	Polyether composites	
PEG	Polyethylene glycol	
PEGDA	Poly(ethylene glycol) diacrylate	
PES	Polyethersulfone	
PFC	Phase-fire control	
PID	Proportional–integral–derivative	
PMMA	Polymethylmethacrylate	
PP	Polypropylene	
PS/PSU	Polysulfone	
PVDF	Polyvinylidene difluoride	
PWM	Pulse width modulation	
PZT	Lead zirconate titanate	
RAS	Recirculation aquaculture system	
RO	Reverse Osmosis	
SA	Sodium alginate	
SEM	Scanning electron microscopy	
sMBR	Side-stream MBR	
SMP	Soluble microbial products (excreted and detached EPS)	
SW	Spiral wound	
TEMPO	2,2,6,6-Tetramethyl-1-piperidinyloxy	Radical inhibitor
TiO ₂	Titanium oxide	
TiO ₂	Titanium oxide	
TMEDA	N,N,N',N'-Tetramethylethylene-diamine	APS activator

WSP Wastewater stabilisation pond

Greek Symbols

Symbol	Description	Unit
$\dot{\gamma}$	Shear rate	s ⁻¹
ϵ_S	Membrane porosity	%
λ_{PMMA}	Heat convection coefficient of PMMA	W·m ⁻¹ ·K ⁻¹
μ_L	Kinematic viscosity of liquid	m ² ·s ⁻¹
ρ_a	Density of surrounding	g·cm ⁻³
ρ_L	Density of liquid	g·cm ⁻³
τ_M	Membrane tortuosity	-
$\Delta\dot{\gamma}$	Shear rate gradient	sec ⁻¹
γ	Shear rare	
γ_{LL}	Interfacial surface tension (liquid-liquid)	m·Nm ⁻¹
δ	Concentration polarisation boundary layer	μm
ζ	Coating degree	%
η	Dynamic viscosity	mPa·s
θ	Contact angle	°
λ	Wavelength	nm
ν	Kinematic viscosity	m ² ·s ⁻¹
ν	Withdrawal viscosity	mm·s ⁻¹
ν_E	Frequency of emitted light	sec ⁻¹
σ	Surface tension	m·Nm ⁻¹
σ_L	Surface tension of liquid	m·Nm ⁻¹
σ_{LS}	Interfacial surface tension (liquid/solid)	m·Nm ⁻¹
σ_S	Surface tension of solid	m·Nm ⁻¹
φ	Meniscus	°
Φ	Angle between drop apex and maximum drop diameter	°
φ_{rel}	Relative humidity	%
ω	Rotational speed	Rad·s ⁻¹
Ω	Electric resistance	V·A ⁻¹
β	Capillary constant	mm
ρ	Density	g·cm ⁻³
τ	Shear stress	Pa

Latin Symbols

Symbol	Description	Unit
A	Surface area	m ²
a ₀	Effective head group area	-
A _p	Atomisation pressure	bar
CA	Contact angle	°
Ca ₂₊ ⁺	Calcium	mg·L ⁻¹
c _b	Liquid bulk concentration	mg·L ⁻¹
CFV	Cross-flow velocity	m·sec ⁻¹
c _g	Gel concentration	mg·L ⁻¹
c _p	Specific heat capacity	J·kg ⁻¹ ·K ⁻¹
c _p	Permeate concentration	mg·L ⁻¹
Cl ⁻	Chloride	mg·L ⁻¹
COD	Chemical oxygen demand	mg·L ⁻¹
d ₀	Atomisation droplet diameter	μm

D_B	Brownian diffusion coefficient	$m^2 \cdot sec^{-1}$
D_{eff}	Effective diffusion coefficient	$m^2 \cdot sec^{-1}$
d_m	Membrane pore diameter	nm
d_M	Molecule diameter	nm
$d_{m,max}$	Maximum pore diameter	nm
DO	Dissolved oxygen	$mg \cdot L^{-1}$
d_s	Outer needle diameter	mm
d_s	Capillary diameter	mm
$dTMP \cdot dt^{-1}$	Specific transmembrane pressure increase	$mbar \cdot min^{-1}$
$dTMP_n$	Transmembrane pressure difference	mbar
$\frac{du}{dx}$	Concentration gradient	$mg \cdot L^{-1} \cdot \mu m^{-1}$
$\frac{dx}{du}$	Velocity gradient	sec^{-1}
$\frac{dy}{dx}$		
ΔG	Gibbs free energy	J
ΔG_k^0	Gibbs free energy, kinetically driven	J
ΔG_{th}^0	Gibbs free energy, thermodynamically driven	J
Δp_{hyd}	Hydraulic pressure difference	bar
ΔH	Enthalpy difference	J
Δp	Pressure difference (feed-pemeeate)	bar
Δs	Entropy (disorder)	$J \cdot K^{-1}$
ΔT	Temperature difference	K
Δt_i	Time of inhibition	min
ΔU	Internal energy difference	J
Δx	Displacement	mm
E	Energy of emitted light	W
E_a	Activation energy	J
F	Force	N
F	Fan pressure	bar
f_a	Excitation frequency	Hz
f_{crit}	Critical frequency for droplet separation	Hz
FI	Flow meter	$L \cdot h^{-1}$
g	Gravitational force	$kg \cdot m \cdot s^{-2}$
h	Planck constant	$J \cdot s$
h_m	Capillary rise inside the membrane pores	m
HRT	Hydraulic retention time	h
J	Flux	$L \cdot h^{-1} \cdot m^{-2}$
J_{CP}	Concentration polarisation flux	$L \cdot h^{-1} \cdot m^{-2}$
J_{crit}	Critical flux	$L \cdot h^{-1} \cdot m^{-2}$
J_{DI}	Deionised water flux	$L \cdot h^{-1} \cdot m^{-2}$
J_F	Flux caused by fouling phenomena	$L \cdot h^{-1} \cdot m^{-2}$
k	Transfer coefficient	$m \cdot s^{-1}$
K^+	Potassium	$mg \cdot L^{-1}$
k_B	Brownian transfer coefficient	$m \cdot s^{-1}$
k_{η}	Effective comply factor	-
k_{tot}	Total heat transfer coefficient	$W \cdot m^{-2} \cdot K^{-1}$
Latin symbol	Description	Unit
l_c	Surfactant length	nm
LEP	Liquid entry pressure	bar
M	Nozzle liquid supply	$mL \cdot min^{-1}$
\dot{m}	Mass flow rate	$kg \cdot s^{-1}$
Mg_2^+	Manganese	$mg \cdot L^{-1}$
MLSS	Mixed liquor suspended solids	$g \cdot L^{-1}$
MWCO	Molecular weight cut off	kDalton or Dalton

Na^+	Sodium	$\text{mg}\cdot\text{L}^{-1}$
NH_4^+	Ammonium	$\text{mg}\cdot\text{L}^{-1}$
NO_2^-	Nitrite	$\text{mg}\cdot\text{L}^{-1}$
NO_3^-	Nitrate	$\text{mg}\cdot\text{L}^{-1}$
Oh	Ohnesorge number	-
OLR	organic loading rate	$\text{Kg}\cdot\text{m}^{-3}\cdot\text{day}^{-1}$
p_1	Reference pressure	bar
p_2	Adjusted pressure	bar
P	Pressure safety opening	bar
PI	Presssure	bar
PO_4^{3-}	Phosphate	$\text{mg}\cdot\text{L}^{-1}$
\dot{q}	Irradiation intensity	$\text{W}\cdot\text{cm}^{-2}$
\dot{Q}_{amb}	Heat input ambient into glovebox	W_{th}
\dot{Q}_{el}	Heat output	W_{el}
\dot{Q}_{HX}	Heat capacity radiator	W_{th}
\dot{Q}_{LED}	Heat input LED	$W_{\text{el}}, W_{\text{th}}$
\dot{Q}_{PBM}	Heat input PBM	W_{th}
\dot{Q}_{th}	Electrical power	W_{th}
\dot{Q}_{tot}	Total heat input into glovebox	W_{th}
r	Membrane pore radius	m, mm, nm
R	Drop diameter	mm
RAM	Random-Access Memory	kByte
R_C	Reversible cake layer resistance	m^{-1}
R_{CP}	Concentration polarisation resistance	m^{-1}
R_F	Irreversible cake layer resistance	m^{-1}
R_m	Resistance of virgin membrane	m^{-1}
RMS	Root mean square of surface roughness	nm
R_q	Quadratic mean value of surface roughness	nm
s	Wet layer coating thickness	μm
s_m	Membrane thickness	μm
s(t)	Wet layer thickness, time dependent	μm
s_0	Wet layer thickness, t=0	μm
SO_4^{2-}	Sulphate	$\text{mg}\cdot\text{L}^{-1}$
SRT	Sludge retention time	h
t	Time	s, min, h
T	Temperature	$^{\circ}\text{C}$
$T_{\text{air, in}}$	Coolant inlet temperature radiator	$^{\circ}\text{C}$
$T_{\text{air, out}}$	Coolant outlet temperature radiator	$^{\circ}\text{C}$
T_{amb}	Ambient temperature	$^{\circ}\text{C}$
t_{crit}	Time critical flux is achieved	min
T_{gb}	Glove box inner temperature	$^{\circ}\text{C}$
$T_{\text{liquid, out}}$	Air outlet temperature radiator	$^{\circ}\text{C}$
$T_{\text{liquid, in}}$	Air inlet temperature radiator	$^{\circ}\text{C}$
TIC	Total inorganic carbon	$\text{mg}\cdot\text{L}^{-1}$
TMP	Transmembrane pressure	mbar
TN	Total nitrogen	$\text{g}\cdot\text{L}^{-1}$
TOC	Total organic carbon	$\text{mg}\cdot\text{L}^{-1}$
TS	Total solids	$\text{g}\cdot\text{L}^{-1}$
TSS	Total dissolved solids	$\text{g}\cdot\text{L}^{-1}$
Tt	Tortuosity	-
U_0	Rel. velocity between liquid and surrounding	$\text{m}\cdot\text{s}^{-1}$
\dot{V}_1	Reference spray volume flow	$\text{mL}\cdot\text{min}^{-1}$
\dot{V}_2	Desired spray volume flow	$\text{mL}\cdot\text{min}^{-1}$

\dot{V}_B	Volume flow bulk phase	$L \cdot h^{-1}$
\dot{V}_{unit}	Atomisation volume flow	$L \cdot min^{-1}$
v	Volume of aliphatic tail	nm
V AC	Volt alternating current	V
V DC	Volt direct current	V
We	Weber number	-
WP	Permeability	$L \cdot h^{-1} \cdot m^{-2} \cdot bar^{-1}$
x_i	Number of coated squares	-
z	Drop height	mm

1 Introduction

Humans only extract around 9% of the available global fresh water resources. Therefore, there is no global water shortage. However, the quality of available fresh water sources deteriorates and local supply greatly varies in time and location, being unevenly distributed among the regions. For instance, humid areas of the Himalaya, India, have precipitations of around $12,000 \text{ L}\cdot\text{m}^{-2}\cdot\text{year}^{-1}$ whereas records in highly arid regions in the Middle East and northern parts of Africa only show rainfalls $<100 \text{ L}\cdot\text{m}^{-2}\cdot\text{year}^{-1}$ (Blanchon, 2017). The prevailing water stress is ever increasing due to: (1) an increasing pollution through direct discharge of industrial and domestic wastewater into water bodies, (2) a limited access to fresh water resources resulting in geostrategic conflicts between riparian states and (3), the rapid population growth in arid areas leading to scenarios where demand exceeds the supply of natural resources. Tapping ancient ground water assets and the expansion of deep well drilling destroys vegetation and the basis of life of many local farmers (Gerten, 2018). These situations tend to aggravate in course of the anthropogenic climate change as climate zones shift and weather extremes escalate. Aiming to ease the situation, mankind evokes for innovative approaches to enable a higher level of potable reclamation and water reuse. Especially water reuse of domestic and industrial discharge streams is under focus. Lower specific energy consumption relative to e.g brackish and seawater desalination reduce operation costs and thus amortisation. In addition, industrial water recovery does not compete with existing potable reclamation strategies since lower effluent standards qualities prevail (Li et al., 2008). Hence, water reuse is a key element for securing global water supply also in the course of the climate change.

1.1 Background and motivation

Centralised conventional activated sludge (CAS) systems reach their limit and infrastructure for regional and national water supply are dilapidated in many regions. Old and faulty water pumps for water distribution and collection have high-energy consumptions requiring replacement (Gu et al., 2016). For instance, the United States Environmental Protection Agency (EPA) stated that only the United States would have to invest around 45 billion dollars within 20 years to maintain their water supply infrastructure (Gude, 2015). Economic as well as ecological reasons scream for a paradigm shift in water policies.

Maintenance of existing systems must go hand in hand with establishing innovative technologies that focus more on decentralised water reuse.

A membrane bioreactor (MBR) is a combination of conventional biological degradation coupled with a physical separation process using a membrane as barrier. This makes large installation of sedimentation and flotation tanks obsolete. There are different MBR with varying membrane and system configuration. Decentralised MBR plants offer the advantage of low infrastructure for water supply if wastewater streams are tapped and reused on-site (Massoud et al., 2009). Thereby, it also prevents disputes relating to land rights which substantially reduces the setup time. MBRs have been applied industrially for more than 25 years. The benefits over conventional wastewater treatment systems are the higher effluent quality achieved, a lower foot-print, their modularity and simple scalability which helps to meet site-specific requirements. Altogether, MBR represents a promising technology to alleviate the situation of ever-increasing global water stress (Jefferson et al., 2000; Judd, 2010; Hoinkis et al., 2012; Andrade et al., 2013; Arribas et al., 2015; Gude, 2015). Despite their great advantages, a bottleneck of MBR is the prevailing so-called fouling phenomena. Fouling refers to inorganic/organic dissolved and suspended solids attaching to the membrane surface and inside the pores. The increasing pressure drops increase pump energy and can even lead to membrane replacement. Higher capital investment and specific energy consumption, compared to conventional CAS, limits the use of application. However, the currently biggest MBR plant in Stockholm, Sweden, is an example of rigorous policies helping to further establish this technology. The stringent environmental standards for the effluent quality in combination with a high population density make MBR highly attractive (Katz and Grundestam, 2016). Globally, scientists focus on different approaches pursuing a lower membrane fouling propensity for a reduction of specific energy consumption. Besides intelligent remote control of operation parameter such as air scouring, hydraulic load and cleaning protocol adaption, experience based chemical dosage and back-flushing help to keep fouling on a minimum level. Constructive changes include specific system designs improving hydrodynamic conditions and inflow to the membranes and improved pre-filtration for any MBR type (Krzeminski et al., 2017).

Within this thesis, discussions about membrane fouling mitigation are the core element covering the possibility of membrane coating technology. A polymerisable bicontinuous microemulsion (PBM) was coated onto commercially available ultrafiltration (UF) polyethersulfone (PES) membranes. Linked by strong electrostatic forces to the substrate, the low-fouling coating also including an antimicrobial surfactant should help to improve membrane performance in long-term.

1.2 Previous work

Microemulsions have gained serious attention throughout the last decades and have been part of numerous studies, first investigated by Schulman and Hoar in 1943 (Eastoe, 2003). Microemulsions are multiphase systems commonly comprised of at least three different components. In this work, surfactant molecules reduced the interfacial surface tension between the two immiscible liquids water and methyl methacrylate (MMA).

The formed microemulsion solutions hold advantages for diverse applications. The co-surfactant 2-hydroxyethyl methacrylate (HEMA) contains a hydrophilic hydroxyl group (-OH) and should help to mitigate fouling effects in combination with the quaternary ammonium salt as head of the acryloyloxyundecyldiethyl ammonium bromide (AUTEAB) main surfactant.

Figoli (2001) duplicated the idea from Gan et al. (1994; 1997) of forming PBM nanostructured liquid membranes for facilitated oxygen transfer. He further discussed transport phenomena and fundamentals of microemulsion formation and clarified influences on the micellar formation with varying shape and size. Polymerisation was done by UV-light and REDOX initiation determining the efficacy via weight loss measurements of previously polymerised samples. He finally assessed the obtained PBM membrane through different methods, e.g. field emission scanning electron microscopy (FESM) or thermoporometry.

Based on these results, Galiano (2013) focused on the application of PBM coated membranes. They compared a commercial non-polymerisable surfactant (DTAB) with the self-developed and synthesised AUTEAB surfactant and used chemical REDOX initiation. He improved thereby the polymerisation degree validated with weight loss determinations analogous to Figoli (2001). He identified 20°C as the optimum polymerisation temperature to initiate the polymerisation reaction. Surface roughness analysis with atomic force microscopy (AFM) was used to examine the smoothing effect of PBM coating layer by a 70% reduction in surface roughness. He also examined the pore size distribution showing that PBM coated membranes have around 62% and 30% smaller membrane pores prepared with DTAB and AUTEAB, respectively. At the same time, a narrower distribution could be achieved resulting in a 63% lower molecular weight cut-off (MWCO) relative to the commercial PES membrane. Advantages of PBM coating were also indicated by a contact angle reduction (31%) and improved antimicrobial behaviour for PBM layers against gram-negative E.coli bacteria. Filtration tests at constant transmembrane pressure (TMP) were carried out with model wastewater using red and blue dye as well as humic acid (HA) for 11 cm² coated membrane cuts (Galiano, 2013). Deowan (2013) copied Galiano's findings and tested REDOX based PBM on 0.33 m² membrane module inside a small lab scaled MBR. They examined the performance treating model wastewater consisting of blue and red dye simulating wastewater treatment of a textile wastewater (Deowan, 2013). Later, when applied in a pilot MBR in Tunisia, PBM showed higher critical flux values in long-term operation in comparison to commercial PES membranes (Deowan et al., 2015). However, REDOX initiated polymerisation has one major hindrance for industrial applications. The curing process takes long with >20 min independent of the coated layer thickness. Photo-induced polymerisation is known to have very short curing times; however, it depends on the exposure source and photo-initiator used.

Schmidt (2016) researched state-of-the-art UV-LED lamps showing a better ecological footprint than mercury and doted mercury lamps.

Longer service life and faster clocking due to no warm-up and cool-down phases bring several benefits for the coating process. Schmidt determined the photo-initiator Irgacure 184 as most suitable for the application, matching the exposure wavelength of the UV-LED without overlapping absorption spectra of other PBM components.

A considerable reduction of the curing time has been realised with UV-LED initiation to meet the high production quantity demand for upscaling processes. Various coating parameters were defined to create optimum coating layers between 4 and 20 μm wet layer thickness. Humic acid was used as model foulant for various lab scaled performance tests (membrane area: 84 cm^2). Schmidt first observed the pore intrusion phenomenon and utilized the biodegradable polyethylene glycol (PEG) as viscosity enhancer to address the problem. However, this modification resulted in a complete loss of filtration performance (Schmidt, 2016). Therefore, pore intrusion remains a big obstacle for UV-LED polymerised PBM coatings.

Comparing REDOX based with UV-LED initiated polymerisation, UV-LED coating shows lower permeability when using humic acid as model foulant. Hence, further efforts must be taken to better understand the differences in polymerisation achieved with the two different initiation attempts. So far, no field trials with real wastewater have been carried out for UV-LED initiated PBM coatings which is important to get a better insight into prevailing mechanisms.

1.3 Objective

The main objective of this work is to study fundamental process conditions for UV-LED based PBM polymerisation. The target is to achieve best possible coating layer properties to ultimately test the novel low-fouling coating under real conditions treating raw domestic wastewater. Based on the results, further coating improvement strategies should be developed and validated. To meet these objectives, the following tasks were defined:

- (1) Study of a modified AUTEAB surfactant of lower purity as a decisive component of PBM solution in comparison with the classic AUTEAB in order to reduce synthesis and thus coating layer costs substantially
- (2) Investigation of membrane pore intrusion to derive a possible strategy for modifying the liquid PBM viscosity. A coherent strategy should be developed and validated
- (3) Identification of critical parameters in the membrane coating process by a casting knife in order to improve reproducibility for higher production quantities and enable coating surface area up to 0.11 m^2
- (4) Upscaling of PBM membrane coating within the pilot project “VicInAqua” and comparison of the novel PBM membrane module with a commercially available UF PES module. Analysis of the filtration performance and examining the long-term stability
- (5) Developing and testing of an advanced coating strategy based on previous findings to improve the PBM coating process to further enhance membrane fouling mitigation and improve overall membrane performance.

1.4 Scope and organisation of thesis

This thesis is divided into six parts.

Chapter 2 covers fundamentals of membrane technology and describes essential material properties, which influence the water filtration process.

An insight about existing membrane types is given with special emphasis on micro- and ultrafiltration (MF/UF) membranes commonly applied in MBRs. It lists membrane key parameter and examines them more closely. Moreover, fouling phenomena including their formation and propagation is explained. The last section covers the background of atomising technologies and identifies advantages and disadvantages for each method related to membrane layer coating. Correlations of operating parameters are highlighted and two possible membrane coating technologies are studied. The findings of the literature research constitute the base for the conclusions drawn on this thesis.

Chapter 3 outlines the fundamental principles of microemulsion system formation and the influence of surfactant type on the micellar structure. It gives examples of the extensive use of microemulsion and PBM systems within the industry and research. Reference to membrane coating application were justified and the propagation for radical polymerisation further highlighted. Background information of previous works are given and relevant aspects for this thesis explained in detail.

Chapter 4 gives an outline of the materials and methods used. Potential measuring errors are discussed. Given information about governed parameters for PBM as well as membrane characterisation will facilitate a better understanding of the conducted work. The chapter comprises details about the developed experimental setups which design depended on previous derived contexts. Test protocols are specified for laboratory experiments using a membrane cross-flow test unit. Relevant parameters for this study are clarified. The chapter, moreover, contains the test-setup for modifying the PBM's viscosity in order to reduce the membrane pore intrusion. Temperature measurements of the polymerisation process were conducted to improve the understanding of the chemistry. A self-developed and constructed automated membrane coating machine enabled the production of large PBM coated membrane quantities. Background information about the pilot MBR treating domestic wastewater are outlined. For a direct comparison between a PBM coated and a commercial PES membrane module, the submerged MBR (sMBR) was equipped with two permeate lines including similar periphery. To improve the coating procedure, an automated spray coating setup was developed and two different spray nozzle types investigated on their spray mist pattern. The approximate spray coverage for different fluid was determined to adjust spray parameters for the PBM coating.

Chapter 5 emphasises preliminary experiments which outcome laid the foundation for the developed experimental setups and showed the urgency for further investigations. The need for an automated coating procedure is discussed more thoroughly. Two types of casting tools based on different casting principles were validated on their performance and the possibility of their integration into the automated process. The optimum casting speed and contact pressure were determined. Furthermore, pore intrusion for pristine PBM of very low viscosity was quantified through confocal light microscopy using fluorescent nanoparticles incorporated in the liquid PBM prior to the coating. Pendant drop investigations of the pristine PBM set the reference value for spray coating experiments also using different fluids.

Chapter 6 includes the main results achieved and discussions made. A synthesis modification of the AUTEAB surfactant considerably reduced the batch production costs but at the cost of slightly lower product purity.

Therefore, focus was given on reproducing laboratory results achieved by the classic AUTEAB before synthesis modification and the modified AUTEAB. Investigations focused on membrane characterisations such as contact angle measurements (CAM), atomic force microscopy (AFM) and filtration performance tests using a membrane cross-flow setup. The second part depicts the feasibility study of PBM viscosity modification through controlled radical polymerisation using a strong radical inhibitor. The exothermal polymerisation propagations were evaluated via temperature measurements and a modification strategy carved out. Different viscosities were produced and the relation to the permeability of coated membranes established. Finally, the results were compared with the pristine PBM and the optimum viscosity set for the membrane coating upscaling process. Subsequently, the results gained within the pilot scale tests treating raw domestic wastewater within the VicInAqua pilot project are shown. Yielded data includes conducted flux step tests simulating harsh filtration conditions and a long-term operation at constant flux conditions. Thereby, two different PBM modules batches were tested. Conclusively, the last section illustrates the innovative spray coating approach using a pressure based and assisted twin-fuel nozzle for PBM atomisation. Relation between operative parameters and the spray coverage are explained and finally, membrane performance tests using a humic acid solution show the potential of this technology. PBM coating characterisation via SEM and NMR analysis was done to compare casting and spray coating. Accordingly, the benefits and advantages of spray coating technology applied for PBM membranes coatings are highlighted.

At last, **chapter 7** summarises the conducted work, gives a conclusion of the most significant findings and suggests further activities for achieving a better filtration performance.

2 Fundamentals of Membrane Technology

Membranes are very thin – dense or porous – separating layers allowing for a mass transport through them. Natural membranes are omnipresent and are essential for our survival as they are responsible for the kidney function, transport of vitamins, etc. Synthetic or technical membranes are nowadays extensively used within domestic and industrial application. Already in 1748, Jean-Antoine Nollet first described the naturally occurring osmosis phenomenon by using swine bladder as membrane separation layer (Mulder, 1996). In the mid till late 19th century researcher not just investigated membrane processes but also established first relations between solute concentration, partial pressure and electrical properties. Theoretical considerations were then intensified by i.a. Langmuir (1917) who developed an experiment in which he proved the polar and hydrophobic properties of membrane cells. Whereas Dannielli and Davson (1935) developed a first molecular model considering proteins (Heimburg, 2007). Hence forward, the working principle behind membrane cells gained more and more interest in science and finally the fundamentals of material separation were adapted to technical membrane separation processes (So et al., 1973). Although numerous efforts have been made to fully understand the fundamentals of membrane and associated difficulties in the respective application, the exact mechanisms are not fully ascertained. Therefore, this chapter highlights the basics about membranes and the prevailing separation processes. Furthermore, focus is specifically given on micro- and ultrafiltration (MF/UF), pressure driven, membranes which are commonly used for domestic and industrial wastewater reuse inside membrane bioreactors (MBRs).

2.1 Membrane application and their requirements

There are numerous synthetic/technical membranes varying in structure, morphology and material properties. The interaction of all characterising parameters determines the separation mechanism and finally the field of application. Present day processes comprise organic (polymer and liquid) as well as inorganic (metal, ceramic, glass) membranes each perfectly designed for its specific final use. Individually, categorising membranes can be done in many ways. Membranes with passive transport do not require additional energy to facilitate material transport but are driven by a growing entropy. Active transport against a gradient only occurs when energy is added. More precisely, non-porous or dense membranes are subjected to a passive transport which gives the selective property.

Porous layers having defined pores enable higher flux rates and their selectivity is primarily determined by the particle molecular weight and shape relative to the pore size and distribution. The material structure, visualised by a cross-section view, can be of symmetric/isotropic and asymmetric/anisotropic nature. The latter combine the advantages of dense, very thin membranes of very high selectivity and the porous membranes with high permeability. The porous, much thicker support gives the mechanical strength and does not contribute to the flow resistance compared to the filtration-active dense layer. Figure 2-1 highlights the asymmetric structure in cross-section view of a polyethersulfone (PES) UF membrane. For the filtration, only the top dense film actively contributes to the separation process. From the compact top to the bottom, the material gets more porous. In this case, a non-woven support additionally increases the resistance and simplifies handling, transport and storage.

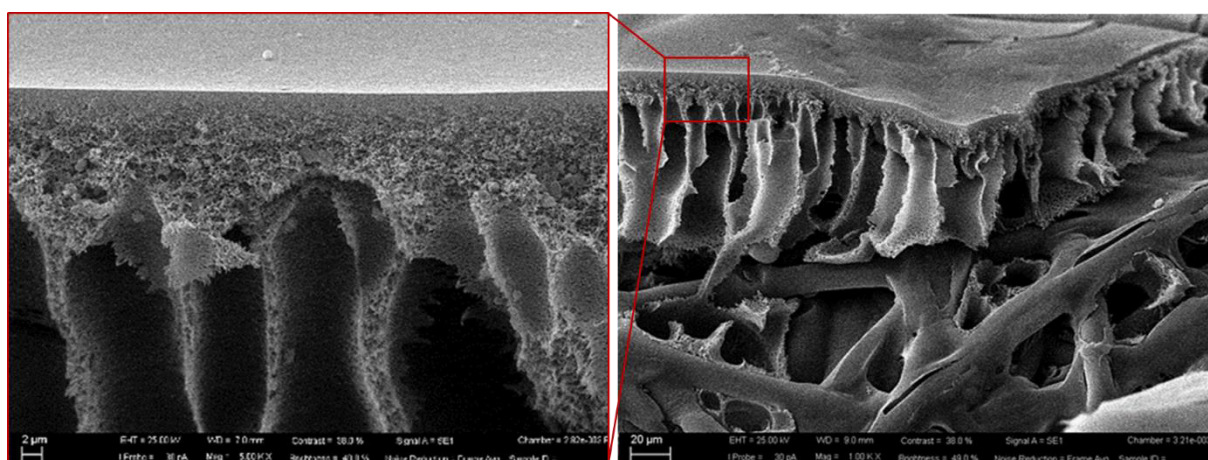


Figure 2-1 Cross-section of an asymmetric ultrafiltration polyethersulfone membrane

Membrane technology includes all process-related gaseous and liquid separations by means of a permeable or semi-permeable membrane. The separation driving force thereby depends on the final application and can be divided into:

- Thermally driven
- Electrically driven
- Concentration driven
- Pressure driven

Membrane distillation (MD) refers to thermally driven processes where a liquid evaporates due to a heat input which causes a pressure gradient enabling permeation through the membrane pores (Li et al., 2008). A preferably porous and hydrophobic membrane is used to separate vapour molecules from a hot feed stream which is then cooled down and condensed on the permeate side. The driving force is a high temperature above the boiling point of the respective liquid to be separated by evaporation. In this way, by MD, either the condensed permeate is the achieved product or the feed stream is highly concentrated to get a valuable brine solution for subsequent crystallisation. The entire process runs at atmospheric pressure and by using waste heat or solar thermal energy, MD is a very energy-efficient separation. Research has been dealing with this technology for over 50 years, starting in 1963, but is not yet mature.

Potential application can be found in the galvanic industry for water or material recovery, desalination activities or the fertiliser industry for extracting/purifying ammonium. Moreover, this technique can easily separate valuable products as gold (Au), palladium (Pd) or chrome (Cr) from a given intake stream (Li et al., 2008).

Electrically driven membrane separation processes such as electrodialysis (ED) can be found e.g. in batteries for temporary energy storage. With the reverse transport water can be converted into hydrogen (H₂) which can be further converted into the easy storable methane (CH₄) if combined with CO₂ capture. Moreover, fuel cells again convert the chemically bound energy in the fuel (CH₄ or H₂) with an oxidising agent into electric energy. Pervaporation, as an example of a concentration driven separation process is used to purify liquid material flows or to separate traces from the bulk phase.

Among others, the transport in dialysers is concentration driven. A dialyser is a tool to remove solutes from a given solution, specifically recirculated blood. Thereby, dissolved substances diffuse through a semi-permeable membrane along a concentration gradient. This method of purifying the blood takes over the actual kidney function in case of kidney failure and collapse. The natural process has been adapted by i.a. Bagastyo et al.. He investigated a three-compartment electrodialyser for fluoride and phosphate removal of highly contaminated feed streams (4,540 and 9,720 mg·L⁻¹, respectively) within the fertiliser industry (Bagastyo et al., 2017).

Pressure driven membrane separation is commonly used either for water purification application, potable reclamation or for domestic and industrial water reuse. Basically, the given relation is: the denser the membrane the smaller the contaminants retained and the higher the pressure (see also Table 2-1).

The beginning of reverse osmosis (RO) membranes dates back to 1953 which was made of an asymmetric cellulose acetate (CA) layer. Spiral wound modules were first developed in 1964 for industrial ultrapure water generation used within the semi-conductor industry. Other material nowadays used are polyamide (PA) or cross-linked polyether composites (PEC) offering high rejection rates >99% due to their dense architecture. The high rejection rate leads to high accumulation of multi and monovalent salt ions close to the membrane which substantial increases the osmotic pressure. Accordingly, very required high pressures elevate the pump energy consumption making RO an energy-intense technology. Nevertheless, considering vaporisation with subsequent controlled condensation as water purification, RO is highly competitive and unrivalled for seawater desalination¹ Besides customary facilities at 80 bar operation pressure, high pressure RO reaching up to 160 bar further reduce brine management costs but also show high scaling potential (Li et al., 2008).

Nanofiltration (NF) has evolved from the RO technology in 1970 to increase the permeate flux at reasonable feed pressure and multivalent rather than monovalent ions rejection rates, therefore known as “low-pressure RO”. Whereas RO produces permeate qualities above required levels for many applications, NF is used for surface and groundwater softening by carbonate/multivalent ion removal.

¹ Multi-stage flash distillation becomes more relevant at higher operation temperatures and waste heat utilisation

Made of cellulose acetate (CA), polyethersulfone (PES), polyamide (PA) or polysulfone (PS). They can be found in pharmacy for persistent organic, pesticides and antibiotic removal.

Ordinarily, NF are designed as flat-sheet (FS), multi-tubular (MT) and hollow fibre (HF) membrane modules. Field of application are the textile, pulp/paper, food, leather industry and treating of highly contaminated leachates from landfills. NF forms a bridge between RO and UF membranes overlapping strongly in pore size and application (Li et al., 2008).

Microfiltration and ultrafiltration (MF/UF) are low pressure membranes due to their highly porous structure enabling high flux rates. 1960 first UF membranes were used to recover electrodeposition paint in the automotive sector and is nowadays extensively used in pharmaceutical application such as purification/concentration of enzymes, antibiotics or proteins. In the course of the ever-increasing water scarcity, new water resources are being exploited. Not to compete with the purified, extremely clean water from brackish, ground and seawater streams by NF/RO, MF/UF reduces fresh water consumption of industries and communities by effluent reclamation. The rather porous membranes are able to retain suspended and colloidal solids as well as microorganism and are sometimes coupled with either NF/RO as pre-treatment or ozonisers to achieve superior water qualities. Current research also focuses on the targeted concentration of activated sludge for aerobic digestive processes. Biogas (methane) as well as algae oil for alternative fuel, syngas and chemical basic products can be produced. MF/UF membranes are available as flat sheet, tubular, hollow fibre and spiral wound modules. Polymers make the greatest share of the MF/UF production whereas inorganic (ceramic, glass and metal) materials are used more and more due to steady cost reduction and especially due to their superior performance relative to polymer materials (Li et al., 2008).

Table 2-1 Pressure driven membrane separation processes and main characteristics (Yoon, 2016)

Process		Pore size	Required pressure level	Separation potential of substances*	Application
Microfiltration	MF	>0.1 μm	0.1 – 2 bar	Bacteria, suspended solids	Wastewater treatment, cold sterilisation
Ultrafiltration	UF	> 10 nm	0.1 – 5 bar	Viruses, Bacteria	Domestic and industrial water reuse
Nanofiltration	NF	> 1 nm	3 – 20 bar	Multivalent ions, viruses	Drinking water purification
Reverse Osmosis	RO	< 1 nm	10 – 100 bar	Dissolves salts, monovalent ions, atoms	Seawater desalination, arsenic remediation

*strong transition in separation potential between the technologies

As it can be seen, fields of application are numerous and it is common to combine two or more technologies (IMS = integrated membrane systems) to achieve best results in terms of pre-treatment as well as effluent quality. Due to the far-reaching membrane technology, majority of respective procedures are not further considered and the work that is described within this thesis only focuses on MF and UF membranes, which are world-wide in operation for industrial as well as domestic water reuse.

2.1.1 UF membrane type, suitable materials and application

2.1.1.1 Polymeric membranes

Polymers are high molecular weight components with changing polymer chain length which in fact influences the final structure. Polymeric membranes are the most widely spread membrane type due to the lowest production costs amongst all membrane materials (Mulder, 1996). In contrast, there is less temperature and chemical stability and therefore also a shorter service life. Polymers predominantly used for MF/ UF filtration are:

- Polyethersulphone/polysulfone (PES/PSU)
- Polyvinylidene difluoride (PVDF)
- Polysulphone (PS)
- Polyethylene (PE)
- Polypropylene (PP)
- Polyacrylonitrile (PAN)

Whereby PES and PVDF membranes are most frequently found. Polymer membranes are mainly used in water treatment technologies since they are easy and cheap to produce.

2.1.1.2 Ceramic membranes

Ceramic membranes are more costly and are of a high specific weight. Its excellent properties nevertheless, make them a popular membrane for particularly heavy polluted, high strength wastewater. Ceramic membranes have a high chemical, mechanical and thermal stability with the ability of steam sterilisation and back flushing at high pressures. The high bacterial and abrasive resistance and high durability result in a desirable long service life. Together with comparable high flux rates, ceramic membranes are used in the (1) chemical industry for catalyst separation, cleaning and recycling of organic solvents (2) metal industries for heavy metal recovery from harsh wastewaters also containing glass fibre and grinding residues or (3) in the textile and pulping industry for biomass and algae dewatering or fractionation and sterilization.

2.1.1.3 Metallic membranes

Metallic membranes have their origin in gas separation within the beverage industry. They are made of aluminium (Al), stainless steel (VA2, VA4), titanium (Ti) or palladium (Pd) yielding in the highest temperature and chemical resistance for extremely harsh operating conditions. Other benefits over polymer and ceramic membranes are inter alia robust, bear low-fouling propensity and have an unparalleled high flux. Manufactured by plasma oxidation, a precise control of the membrane thickness and the pore size/distribution is possible. In addition, metallic membranes have straight channels instead of interconnected and highly tortuous membrane pores which reduces the pressure drop. Despite their comparatively thin layer, they offer a high mechanical strength. Higher flux rates in long-term are realised by a low-fouling potential through the possibility of surface charging being able to repel desired solutes, colloids and particles.

Concisely, metallic membranes, despite the high production costs, are cost-effective considering their advantages for specific application. With pore sizes down to 1 nm (NF membranes) and a very narrow pore size distribution, metallic membranes offer excellent qualities for even virus removal. Palladium can be found in prevailing high temperature conditions such as hydrogen (H₂) separation, water-gas-shift (WGS) and methane steam reforming. It is quite common to have ceramics as supportive layer for palladium membranes to save expensive material. Their highly inert and sterilisable feature make them attractive for bacterial analysis, detection and diagnostic systems. The outstanding wear and corrosion resistant layer is perfect for treating hot oil, gas, wastewater streams or strong acids and leaches (Li et al., 2008).

2.1.2 Membrane module configuration for MF/ UF application

MF/UF membrane module configuration are plate-and-frame, hollow fibre, tubular or spiral wound. Starting with plate-and-frame modules, the module construction has been continuously evolved to satisfy various treatment requirements.

Plate-and-frame modules consist of many individual flat-sheet (FS) membrane sheets and are assembled with a defined distance to one another. Flat sheets are in general laminated to a metal or more frequently a plastic spacer giving the mechanical stability. The permeate pump is connected to the module sucking the clean product through the membranes which reject the contaminants present in the feed stream. Depending on feed composition, contamination and operating parameters, the distance of the individual sheets differs to obtain beneficial hydrodynamic conditions. For wastewater treatment in membrane bioreactors (MBR), submerged FS modules are installed in vertical position. For fouling mitigation, membrane air scouring is achieved with a blower beneath the module. A good bubble formation with an even distribution over the membrane surface improves system stability and filtration efficiency. Plate-and-frame modules are more expensive to produce but have different advantages in operation control. Hydrodynamic conditions are much better understood than for HF modules and can thus be better controlled to improve the fouling reduction potential.

HF modules have low specific costs but flow conditions inside has not yet been fully elucidated. Fibre bundles are either packed inside a pressure vessel or loosely moving inside the feed stream. In both cases the module is pressurised from the inside, permeate is pumped off at the end of the collecting plate where all fibres are connected (Baker, 2004). Membrane systems can have very high packing densities if equipped with HF modules. The limiting factor are the poor hydrodynamic conditions prevailing. The fibre diameter commonly is 100-200 µm and the fibre length is limited by the ever increasing pressure loss. HF are most common in MBR for industrial and domestic wastewater treatment. A very big advantage over alternative configurations is the ability to back-flush the hollow fibres with high pressures to remove deposits from the surface and internal pores. Together with the low production costs, this is an essential reason for the broad use in MBR system for wastewater reuse.

Multi-tubular (MT) membranes like hollow fibres are hollow bodies but of bigger size since the filtration takes place from the inside to the outside. Respectively, the tube diameter is in the centimetre range to reduce particulate deposition which results in clogging of the porous membrane from the inside. A stack of tubular membranes make a module which are manifold in series with sequential permeate outlets (Baker, 2004).

Spiral wound (SW) modules contain an endless membrane wrapped around a perforated permeate collection pipe with a feed spacer in between. The feed flows across the membrane and is steadily concentrated as the clean water flows off as permeate. Spiral wound have lower cross flow velocities which favours concentration polarisation (CP) and thus scaling and fouling on the membrane surface (see section 2.2.2). Therefore, the feed spacer also acts as turbulence promoter reducing the CP boundary layer. Usual high pressures maintain a high transport through the membrane (Baker, 2004).

Ultimately, each application requires a specific membrane module configuration. Besides investment costs, operation costs should also be taken into account before deciding over a certain system design. While HF and SW modules are simply and cheaper to produce, FS are more costly but hydrodynamic conditions and fouling phenomena are much better understood. With this knowledge, fouling effects can be significantly reduced and thus specific energy consumption as well as chemical cleaning intervals (Le-Clech, 2006; Judd, 2006). Focusing on industrial and domestic wastewater reuse, HF membranes dominate the global market before the FS execution but the latter is still in focus. For instance, Deowan et al. successfully integrated a large-scale aerobic MBR with FS submerged membrane modules into a laundry factory to reduce fresh water consumption by 80% when coupled to RO membranes. Due to legal regulations prices for wastewater feed-in sharply increased and the textile service Klingelmeyer GmbH & Co. KG in Darmstadt, Germany, had to take measures in order to remain competitive (Deowan et al., 2013). In times of stringent discharge legislation, prices per m³ polluted effluent tripled and a three year pay-off time was achieved.

2.1.3 Key parameters for membrane application

Membrane technologies can be distinguished according to the measures taken to achieve desired effluent qualities from a given wastewater matrix. Thereby, the demand often changes with varying feed water contaminants. Membrane properties, plant modularity, operating mode and membrane module design have to match requirements for treating diverse feed water compositions to required effluent qualities. (Li et al., 2008). Above all, capital investment decides on the final system configuration. Focusing on the membrane itself, it ideally fulfils the following requirements (Drioli and Giorno, 2016):

- High selectivity and constituent removal efficiency
- High permeability/ low flow resistance
- Ideal pore size and narrow pore size distribution
- Thermal, chemical and mechanical stability
- Optimum surface features (charge and roughness)

How the listed membrane parameters contribute to the filtration performance and fouling behaviour will be discussed in more detailed hereafter. Again it is pointed out that the following assumptions and views within this thesis are based on considerations pertaining to MF/UF membranes applied for domestic and industrial wastewater reuse application. In this regard, MBR is a most promising tool to combating water scarcity in general and moreover also in remote areas lacking entire infrastructure and clean water supply.

2.2 Membrane separation processes

Depending on its application and the operation parameters, membranes vary greatly in geometry (e.g. pore size, surface roughness) and material properties (e.g. hydrophobicity, electrical potential). Independent of its use, all membranes aim at a correspondingly high selectivity and permeability (Judd, 2006). Transport through membranes is either of convective or diffusive nature depending on the membrane pore size. Described by the so-called solution diffusion model, molecules dissolve in dense membrane architecture driven by the concentration gradient between the feed and permeate with following diffusion to the permeate side. Permeable membranes largely repulse solutes determined by the given membrane selectivity.

In contrast, the hydrodynamic model describes the rejection of macromolecules mainly occurring in micro- and ultrafiltration. This chapter only discusses phenomena applying for pressure-driven membrane operation only. The relation given in equation 2-1 is valid only for clean water filtration but exemplifies some fundamental correlations (Hoinkis & Lindner, 2007). According to 2-1, the flux J (volume flow per unit membrane area) is proportional to the square of the membrane pore diameter d_m . Considering pure water flux – membranes of bigger pore diameter offer much higher volume flows (Baker, 2004). Further influencing parameters are the membrane porosity ϵ_s and the fluid viscosity η which depends on the temperature T . The membrane thickness s_m is inversely proportional to the flux. Particular attention must be given on s_m and d_m when membrane modifications through additional coating layers are being sought (see section 2.5.2). Porosity ϵ_s and tortuosity τ_t are important characteristics also determining selectivity and rejection rate. However, they are rather difficult to obtain and barely controllable during membrane production. The tortuosity T_t is a factor describing the pore geometry and is usually specified by the manufacturer. Δp is the pressure difference between the feed and permeate flow.

$$J = \frac{\epsilon_s \cdot d_m^2}{32 \cdot \eta(T) \cdot \tau_t} \cdot \frac{\Delta p}{s_m} \quad 2-1$$

2.2.1 Resistance model

Simplified, water passes through the porous media forced by an existing pressure gradient. Thereby, different appearing resistances reduce the permeate flux through the membrane. The filtration process, as forced volume flow through a porous layer, can be derived from Darcy's law, see equation 2-2 below, also known as "resistance-in-series-model" (Figure 2-2, right).

$$J = \frac{\Delta p}{\eta (R_m + R_{CP} + R_c + R_f)} \quad 2-2$$

With Δp and the specific resistance of the membrane itself (R_m), the resistance resulting from the concentration polarisation (R_{CP}), the mainly reversible cake layer (R_c) and the irreversible fouling R_f ($R_{\text{poreblocking}} + R_{\text{adsorption}}$). It becomes apparent that for constant flux conditions ($J = \text{const}$), the transmembrane pressure must rise since the cake and fouling resistance increase in time due to particle deposition on the membrane surface in course of the selective filtration process. The dynamic viscosity η of the water depends on temperature, constituents and their concentration. The resistance-in-series-model is generally accepted in literature and can be slightly modified based on the expected resistant. The specific membrane resistance (R_m) varies with the membrane used changing with membrane pore shape, size and distribution, tortuosity and membrane thickness (equation 2-1). Tng et al. stated that the membrane resistance changes in time by compaction due to the hydrodynamic forces and altering caused by frequent chemical cleaning and the aggressive chemicals applied (2015). Nonetheless, in view of the following considerations, this factor is not taken into account. For clean water operation, fouling in time does not take place and the membrane resistant can be derived from membrane flux tests. When membranes are exposed to fouling (see section 2.4), the specific resistances increase according to the restrained constituents and fouling mechanisms. Considering R_m validated through the clean water tests, the sum of R_c and R_f can be calculated with collected data e.g. from model fouling experiments. The resistance-in-series-model can help to identify the different fouling effects to better understand the fouling propensity of a membrane. The elimination or reduction of specific fouling species can be achieved by appropriate measures such as intense membrane scouring, adaption of chemical cleaning protocol or membrane modification (Yoon, 2016).

2.2.2 Concentration polarisation

Membranes reject solutes in the feed water bulk phase depending on their electrochemical potential, shape and molecular weight (selectivity). As a consequence, the rejected constituents accumulated on the membrane surface forming a boundary layer. This formation of a concentrated layer on the membrane during the filtration process is called the “concentration polarisation” (CP) which leads to a reversible flux decline during the operation. At an increasing rate, the concentration of solutes within the boundary layer exceeds the concentration in the bulk phase resulting in a back diffusion of solutes driven by the now existing concentration gradient. Depending on the hydrodynamic flow conditions, the boundary layer builds up until the back diffusion reaches steady state with the convective transport of the bulk water phase and the water flow through the membrane (membrane flux J , see Figure 2-2, left; Yoon, 2016).

The effect of CP occurs in nearly any membrane separation process, however, depending on membrane configuration, bulk water composition and also operative parameters, in stronger or weaker form. For MF/UF filtration especially high flux declines can be observed, caused by: (1) a high wastewater load containing high COD level and various contaminants, (2) high achieved rejection rates which support the accumulation of substances near the membrane surface, (3) the majority of sludge flocs and other substances present in the wastewater have a low diffusion coefficient reducing the back diffusion transport into the bulk phase leading to a thicker boundary layer, and (4) the much higher flux rates relative to other membrane applications such as NF/RO membranes (Mulder, 1996). As just mentioned, CP depends on not just hydrodynamic regulations but moreover is a phenomenon based on thermodynamic and chemical principles. For a better understanding, Figure 2-2 also highlights the concept of the concentration polarisation model (left), firstly examined by Porter (1972). The convective flow \dot{V} of the bulk water phase transports solutes and constituents to the membrane surface where they are rejected determined by the membrane selectivity. In the further course, as more and more molecules get restrained, the CP layer thickness builds up until a steady state with the diffusion back into the bulk phase is reached. The driving force results from the concentration gradient between bulk concentration and higher concentrations within the boundary layer δ . It is assumed that the concentration on top of the membrane surface reaches the maximum value of c_g which is the gel or solubility concentration. Once this concentration is reached, solutes will start to precipitate forming a resistive gel or cake layer resistance R_c . Further increasing solute accumulation leads to a thicker gel layer or compaction of this very same.

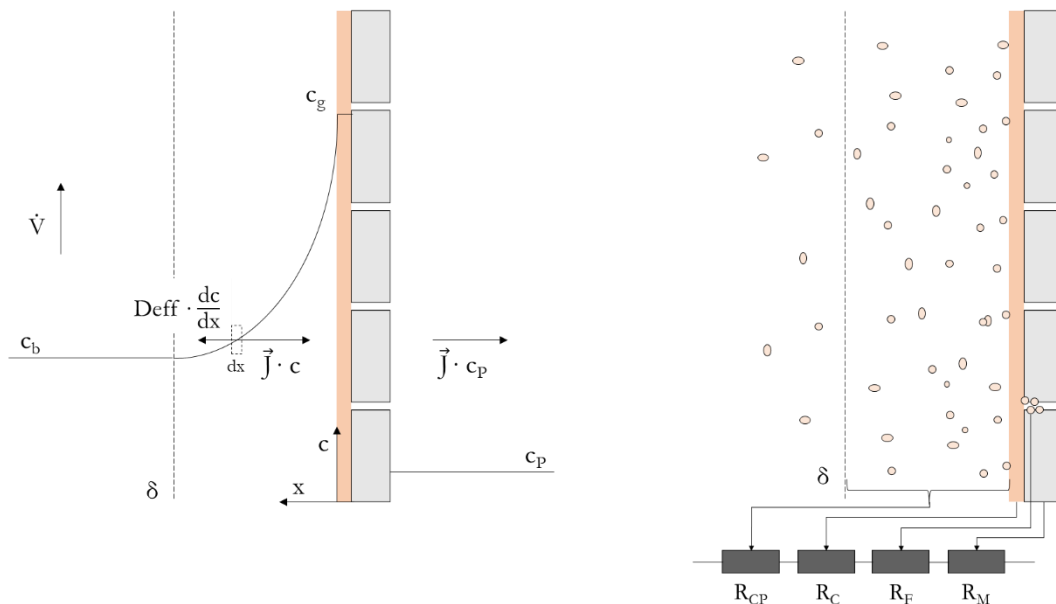


Figure 2-2 Concentration polarisation model (left) and in-series-resistance-model (right)

Equation 2-3 depicts the mathematical relation at steady-state conditions which can be simply obtained by a mass balance including the back-diffusion described by Fick's first law. Further on, the rejection rate is considered to be 100% and no solute permeate flux ($\vec{J} \cdot c_p = 0$) occurs. By integration over the boundary conditions $x_0 = 0 / c_0 = c_g$ and $x_1 = \delta / c_1 = c_b$, defining the transfer coefficient k as a function of $\frac{D_{eff}}{\delta}$ and assuming completely constituent removal ($c_p = 0$), the following conclusions can be drawn.

The CP depends on the permeate flux and the transfer coefficient as an indicator of the hydrodynamic conditions. To reduce the CP layer either the applied flux should be reduced (lower constituent accumulation) or the hydrodynamic forces, e.g. through turbulence effects enhanced. Solute characteristics (molecular weight, size) and setup factors (e.g. membrane module configuration, pump speed) determine the final action to be conducted (Porter, 1972).

$$J \cdot c = D_{\text{eff}} \frac{dc}{dx} + J \cdot c_p \quad \xrightarrow{\text{integration over } \delta} \quad J = \frac{D_{\text{eff}}}{\delta} \cdot \ln \left(\frac{C_b}{C_G} \right) \quad \xrightarrow{k = \frac{D_{\text{eff}}}{\delta}} \quad J = k \cdot \ln \left(\frac{C_b}{C_G} \right) \quad 2-3$$

As mentioned, the concentration within the boundary layer reaches its maximum at the gel concentration c_g . c_g is independent of the bulk water concentration c_b and thus, for higher c_b values, the back diffusion is reduced leading to a higher CP. On the contrary, higher membrane flux is achieved by turbulent flow conditions supporting the mass-transfer back into the bulk phase. As it becomes apparent, this simplified assumption (equation 2-3) cannot completely justify the effect of the occurring boundary layer and limitations of membrane separation processes. Different phenomena influence the final boundary layer thickness, induced by concentration polarisation, as follows:

The shear-induced diffusion back to the bulk phase is caused by the collisions between the molecules (the bigger the higher the shear-induced back transport) as they are much more frequent in the concentrated boundary layer than in the bulk phase. Moreover, the “inertial lift” caused by different kinetic energy levels of the solutes can reduce CP. As water flows through the membrane module, a velocity profile develops inside the body with peak values in the centre bulk phase. Close to the membrane surface (as it is assumed to be the wall in the flow body) the solute convective velocity becomes zero. According to the velocity profile, the solute undergoes a certain drag, induced by the velocity gradient resulting from the particle velocity on the side facing the membrane surface and the side facing the bulk phase. In course of this “tubular pinch effect”, the kinetic energy of particles close to the membrane surface becomes high and move to regions of lower kinetic energy back into the bulk between membrane surface and bulk centre (Yoon, 2016). The tubular pinch effect is stronger for laminar flow since it shows a more distinct velocity profiles relative to turbulent flow. Brownian diffusion considers the random movement (jittering) of solutes, particles and colloids due to their thermal energy. According to the Stokes-Einstein-relation (equation 2-4),

$$D_B = \frac{k_B \cdot T}{3 \cdot \pi \cdot \eta \cdot d_M} \quad 2-4$$

the Brownian diffusion coefficient D_B increases with increasing absolute temperature T and decreasing diameter d_M of the corresponding molecule. Also, the lower dynamic viscosity η , the higher D_B . By time molecules tend to move towards the bulk phase also enhanced by the shear-induced diffusion/ collision with adjacent molecules. Thereby, k_B is the Brownian transfer coefficient.

Concentration polarisation is commonly a reversible effect and the initial flux can be regained totally if no further fouling occurred (gel layer formation or pore blocking). Nevertheless, if the volume flow through the membrane exceeds the steady-state flux according to equation 2-3 and becomes higher than the total diffusive back transport, particles and molecules deposit on the membrane surface leading to cake layer formation and incipient gel precipitation. With time, the latter forms a second “dynamic” membrane causing a major resistance to the water flow. In spite of, studies showed that this dynamic membrane also has a protective nature to prevent further intermediate pore blocking of the membrane (Porter, 1972). According to equation 2-3 it is obvious that the formation of concentration polarisation boundary layer depends on the diffusivity of constituents forming the water matrix. In terms of MF/UF application, it has been shown that particles, colloids and macromolecules show rather low diffusivities which increases CP and thus the resistance R_{CP} . In NF/ RO application, a high osmotic pressure can occur which supports the back-diffusion into the bulk phase. Smaller restrained particles and dissolved substances show higher diffusion coefficients D_{eff} further reducing the CP. The high operation pressure increases the turbulence within the membrane modules causing lower gel concentrations (and thus CP). MF/UF membranes are particularly susceptible to fouling phenomena due to characteristic wastewater containing various contaminants, solids, extracellular polymeric substances (EPS) and other diverse macromolecules (Le-Clech, 2006).

As compelling consequence, CP near the membrane surface exacerbates fouling processes. It is therefore important to consider a reduction of concentration polarisation to reduce membrane fouling propensity. Turbulences in spiral wound modules are promoted by integrated spacers. Higher scouring rates in MF/UF membrane modules in submerged MBR systems reduce CP at the expense of higher energy consumptions due to bubble formation with inefficient air compressors. Feed or back pulsing has been applied and the efficacy validated in various studies valid for all kind of module constructs (Gao et al., 2019). In general, the technologies for process optimisation reach towards lowering the TMP at a given flux to reduce the specific energy consumption (Baker 2004). A more detailed progression overview of the fouling processes and prevailing correlations is given in section 2.4.

2.3 Membrane bioreactor

A membrane bioreactor (MBR) basically is a conventional activated sludge (CAS) water treatment system combined with a membrane acting as physical barrier for contaminant separation. This configuration facilitates a very high quality of effluent at comparatively small foot-prints (Monclús et al., 2015). CAS traditionally use flotation and sedimentation tanks, a clarifier for post treatment and – in some cases – a further disinfecting post-treatment. MBR technology with MF/UF membranes can retain particulates, solutes, bacteria and some viruses according to Table 2-1. Marrot et al. for instance studied the use of MBR technology for water reuse within the manufacturing sector and concluded better removal efficiencies compared to CAS systems (Marrot et al., 2004). MBR demonstrably and unquestionably provides higher quality over conventional technology for wastewater reuse. Large spaces for settling and flotation basins become obsolete. As a consequence of the membrane filtration, much higher total solids (TS) and sludge age can be achieved.

Higher sludge age corresponds to higher bacterial activity and thus to higher biodegradation of organic components (Bernal et al., 2012). On the contrary, larger bacterial colonies consume more oxygen resulting in higher energy consumption for aeration. For improved cross-flow over the submerged membranes, air scouring is usually increased. Moreover, a high TS increases the slurry viscosity and affects membrane fouling propagation as described in section 2.4.

2.3.1 MBR design

MBR can be divided into two categories, respectively the membrane module installation situation. Initial systems were designed as side-stream MBR (sMBR) where the membrane module is placed externally to the reactor tank. This configuration necessitates an additional recirculation pump providing enough (positive) pressure to drive the effluent through the membrane. Thereby, a high turbulent flow enables a distinct fouling reduction (Figure 2-3, left). The high viscous sludge is thereby inevitably entrained which leads to the usually higher energy consumption relative to submerged or immersed MBR (iMBR; Tiang et al., 2007). Despite several approaches to reduce specific energy consumption of sMBR (air injection into the module to reduce fouling; Shimizu et al, 1996) first iMBR were operated in 1989 with a simplified construction reducing capital investment (Chiemchaisri and Yamamoto, 1994). Consequently, with times of new scientific evidence, MBR setup has changed and additionally to the aeration of activated sludge tank, a second blower has been installed below the membrane module, scouring the particles and constituents from the membrane surface. Fouling propensity is reduced sustainably and by decoupling of oxygen supply for the bacteria and membrane scouring, electricity can be saved. The system design and dimensions (Figure 2-3, left), mainly depends on the wastewater matrix and required effluent quality for further domestic or industrial reclamation but also on location and local conditions. Nonetheless, both – sMBR and iMBR – are always composed of one reactor tank which is the aerated zone for nitrifying, thus converting ammonium (NH_4^+) into nitrate (NO_3^-). Aerobic bacteria break down macromolecules and produce further biomass. The nitrate is converted into gaseous nitrate (N_2) inside an anoxic denitrification tank and subsequently released into the environment. The anoxic compartment (volume) is designed based on total nitrogen levels (TN) but is similar for both systems and thus excluded of the illustration. While sMBR are operated with positive pressure, iMBR membrane are exposed to negative suction pressures. iMBR give higher operative flexibility, overall lower specific energy consumption and higher membrane packing densities (higher specific capacity; Tian et al., 2007). However, aeration still accounts for the majority of the overall electricity consumption (Figure 2-3, right). Cross-flow enhancement with the filtration blower is energy intense and vary greatly with air bubble configuration. Either small or coarse bubble scouring, uniform or rather selective inflow result from the system requirements and the waste water composition. In each case whatsoever, aeration positively affects membrane fouling propensity. Nearly any MBR type contains energy consumers as listed, only varying in auxiliaries and dosing pumps for chemical additives. It is fairly common to combine membrane technologies to achieve multiple filtration stages of different selectivity (Alvarino et al., 2015). In this way, higher effluent qualities for potable reclamation or an improve wastewater pre-treatment prior to the MBR inlet can be obtained (Luo et al, 2015).

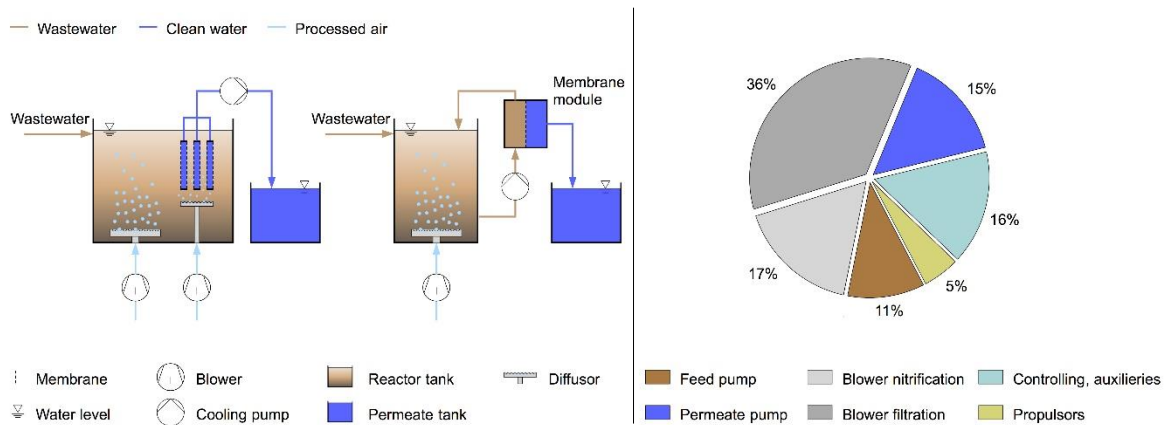


Figure 2-3 General MBR design (left) and energy consumer for common MBR applications (right; Gu et al., 2017; Krzeminski et al., 2017)

Despite their industrial use for over two decades and against three decades of development, there is ample room for further reducing the specific energy consumptions. First documented values ranged between 5-8 kWh·m⁻³_{effluent} (van Dijk and Roncken, 1997), however, through decisive improvements, specific energy consumptions dropped to around 0.4 kWh·m⁻³_{effluent} (Gu et al., 2016). This in turn is still substantially higher compared to conventional CAS systems as their energy consumption is satisfied with <0.1 kWh·m⁻³ and in some cases dropping to <0.05 kWh·m⁻³ (Gu et al., 2017). For both systems, the specific energy consumption changes considerably with installed capacity since blowers and pumps have highest efficiencies at high volumetric flow rates. In addition, investment costs are reduced inversely proportional to their installation size (Krzeminski et al., 2012). High effluent quality, the low foot-print and its modularity are decision making criteria for membrane bioreactor throughout various applications. Nevertheless, the comparatively high specific energy consumption prevents a broader use. Due to the inevitable fouling process, membranes are blogged and operation pressure has to be increased to maintain the desired flux. Besides, systems can also lack well balanced hydrodynamic conditions and highly efficient operation scenarios. Although sMBR generally have a higher specific energy consumption (Judd, 2006) they are still in demand for treating difficult and high-strength wastewater discharges such as found in leachate and laundry wastewater. Nowadays, very high cross-flow velocities are obtained to significantly reduce concentration polarisation and thus fouling phenomena (*Waterlean HQ*, 2019).

In the course of the energy transition and development of smart grid systems (industry 4.0) controlling strategies gain more attention. Developments towards sophisticated smart sensors for fully autonomous, independent operation. The low-foot print and the ability to be easily executed and fully autonomous make MBR especially attractive for decentralised application. In fact, MBR's full potentials have not been fully exploited and their specific energy consumption is likely to decrease to more competitive numbers. If more efforts will be taken for process advancement developments, MBR will be a key to overcoming major water challenges in the future.

2.3.2 Anaerobic MBR

Anaerobic MBR (anMBR) systems nowadays gain more attention due to their ability of continuous methane (CH_4) production. AnMBR are filtration systems without aeration for bacterial oxygen supply. Cross-flow in iMBR is commonly obtained with collected and pressurised methane whereas in sMBR circulation pumps with high recirculation rates assume this task (Le-Clech et al., 2005). Anaerobic bacteria can produce high amounts of biogas due to their high microbial activity. Higher organic loads result in higher sludge viscosities having much higher fouling character (Smith et al., 2014). Anaerobic bacteria are more prone to toxic compounds in the feed water. High salt concentration cause dehydration leading to a drop in methane production. Moreover, methanogenic bacteria are especially susceptible to sulphide components (H_2S). Specifically high H_2S amounts are known to reduce biogas production through repression of anaerobic bacteria activity (Chen et al., 2016). Besides wastewater composition, pH value, sludge retention time (SRT) and organic loading rate (OLR) determine the rate of the biogas produced. Biogas quality is rated up to 90% methane content under very controlled, ideal conditions achieved in small-scale units (Liao et al., 2010). In this way specific methane production of around $0.4 \text{ L CH}_4 \cdot \text{g}^{-1} \text{COD}_{\text{removal}}$ are reported (Chen et al., 2016).

Ordinarily, anMBR technology is coupled with MBR to reduce the impact of high feed inlet fluctuations and to keep fouling in a controllable range. AnMBR also do not contain nitrifying bacteria converting ammonium into nitrite/nitrate, which would then pass the membrane causing intoxications if ammonia is formed. Considering that the produced methane is processed and consumed on-site (e.g. co-generation unit) anMBR can be a promising technology due to their potential for independence in energy supply. Waste heat recovery further raises the reactor tank temperatures and thus the specific biogas production rate. Self-sufficiency of anaerobic MBR is increased and for some cases is more sustainable than biogas production from e.g. forestry and agriculture biomass. Their economic efficiency depends on local conditions and infrastructure for biomass transport (Schmidt et al., 2012). The potential for a high degree of energy autarky makes anMBR highly interesting for decentralised application.

2.3.3 Decentralised MBR application

Water reclamation in remote areas becomes increasingly important. In terms of the climate change and the intertwined energy-water nexus, decentralised wastewater treatment at its place of origin is desired to avoid high expenditure on infrastructure. Higher effluent quality achieved by MBR and the comparatively compact system further support this paradigm shift from centralised to decentralised water treatment. Fulfilling this strategy multiple remote facilities using MBR for wastewater reuse exist:

- **Marine application:** the most decisive factor for MBR on board is the low footprint and high recovery rate since the transport of large clean tanks can be significantly reduced. For instance, on a large cruise ship an aerobic MBR is operated with a $650 \text{ m}^3 \cdot \text{day}^{-1}$ capacity without the necessity of further post-treatment for domestic reuse (Wärtsilä, 2013).

- **Domestic use:** different independent studies have shown that MBR are very well suited for greywater treatment in office complexes and hotel facilities (Atanasova et al., 2017; Meuler et al., 2008). Santasmasas et al. combined an aerobic MBR with a biological oxidation and chlorination post treatment to provide 1,500 L cleaned water daily (Santasmasas et al., 2013). Moreover Lamine et al. introduced MBR technology in public buildings with a disinfecting UV-lamp stage reducing the fresh water consumption by 48%. Yet, pay off time was calculated to 23 years for this case (2017).
- **Irrigation systems:** Battilani et al. developed a prototype comprising of an aerobic MBR, a modular field treatment system (FTS), a commercial gravel filter and a specific heavy-metal adsorption unit. With this setting, high E.coli and coliform bacteria removal was achieved. Heavy metals, in specific arsenic, cadmium, copper, lead, chromium and zinc could be effectively reduced for irrigation and fertigation in gardening and agriculture (Battilani et al., 2010).
- **Aquaculture use:** a completely new approach for using MBR was investigated within the VicInAqua project at the Lake Victoria basin in Kisumu, Kenya. A submerged, aerobic MBR treated domestic wastewater for topping up the water inside a recirculation aquaculture system (RAS). It thereby compensates 3-4 m³ daily water losses through evaporation and filter back flushing. (VicInAqua, 2016). The schematic of the system setup including the pilot MBR is shown in Figure 2-4. This project has been realised to also test the innovative low-fouling coating which was further developed within this thesis. The customised pilot MBR was designed to compare the low-fouling coated membrane module with a commercial UF PES module.

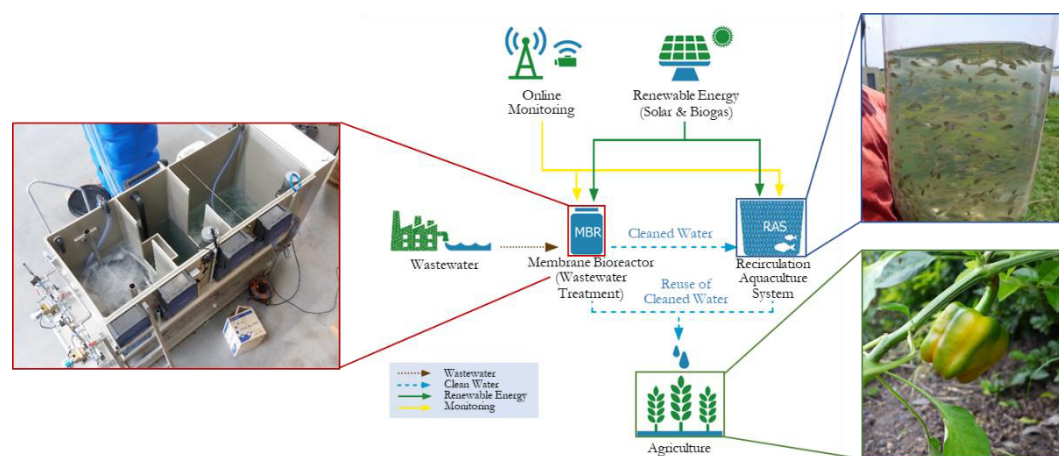


Figure 2-4 Schematic drawing of the VicInAqua project with integrated pilot MBR

In the near term, MBRs will account for a significantly larger share of decentralised water treatment systems and green building concepts for smart cities. This development focuses on environmental benign and pollution reducing concepts by reducing and saving energy, land and material input (Rashidi et al., 2015). Integrated membrane systems (IMS) are a key factor to comply with ever-stringent legislation and to comply with steadily changing requirements. IMS couples two or more membrane technologies in which the first stage usually acts as pre-filtration for the second stage. In this way, vary diverse wastewater streams can be treated and differently desired effluent qualities achieved.

This flexibility will be crucial in prospective developments (Rashidi et al., 2015). Nevertheless, the acceptability of membrane bioreactors suffers from its comparatively high specific energy costs compared with conventional CAS systems. The reason is the use of membranes retaining organic matter causing reversible and irreversible pressure drops due to fouling. This requires specific process control to maintain the filtration process, its efficacy and efficiency.

2.3.4 Energy efficiency improvement strategies

The membrane is undoubtable the core element of MBR technology and thus has served as basis for numerous scientific and industrial projects. Research activates have focused on reducing the overall energy consumption by limiting the fouling extend of the membrane. The following paragraph exemplifies different low-fouling approaches which has been applied for membrane bioreactor application using MF/UF membranes and also give a short insight of common efficiency improvement strategies. Valid for all, the effluent quality is not or only little affected (Verrecht et al., 2010, Monclús et al., 2015).

Non-constructive solutions are desired for existing systems and include remote monitoring technologies and parameter control. Such an approach was realised by Ferrero et al. who used data recording in combination with a mathematical model to calculate the time-dependent transmembrane pressure increase and anticipate the further fouling progression. With this “performance-based” control system, he was able to reduce the energy consumption of membrane aeration about 21% simply by continuously adapting the aeration (On/Off) control (Ferrero et al., 2011). Based on these findings, Monclús et al. developed a dynamic and self-regulating control strategy for the frequency and scour cycle length by slope calculation. Actual values for the flux and TMP were compared with the operation history. With this robust control system he could adjust the blower frequency based on the specific situation (Monclús et al., 2015). Considering the local conditions, aeration adaption resulted in 14-20% of overall energy consumption. Air scouring control helped to reduce the power input or to reduce the installed blower capacity. Another dynamic online measuring tool (MBR-VFM) was developed by Huyskens et al. which was based on TMP and flux monitoring. Through continuous process surveillance, it was even possible to distinguish between reversible and irreversible fouling by comparing the specific pressure increase ($dTMP/dt$ [mbar/min]) with the previous operation values. The tool decided about back flushing frequency and duration or the amount of chemicals added to the process to achieve initial membrane performance (Huyskens et al, 2011). Independent studies examined the percentage energy consumption by aeration related activities to 54% (Gude, 2015), 60% (Gu et al., 2017) and 53% respectively 68% (Krzeminski, 2012). Therefore, aeration contributes largely to the total energy consumption but small changes of investments can make a big difference. In a different study of Gabarrón et al., focus was given on changing the permeate flow rate (hydraulic load) to reduce the specific power consumed by the permeate pump. Membrane flux was raised above the manufacturer's recommendation which on the one hand supported cake layer formation resulting in higher TMP. On the other hand, additional resistance of the cake layer enhances membrane selectivity which was beneficial for the effluent quality.

In conclusion, the higher energy amount consumed was negligibly small related to the resulting lower specific energy consumption in kWh·m⁻³ of the permeate pump (Gabarrón et al., 2014).

Constructive operation enhancements for MBR application can be a change in reactor design such as tangential feed inlet to support the hydraulic conditions leading to higher cross-flow rates and optimized bacteria growth. Low-pressure valves instead of conservative valves reduced high line pressure drops. The advantage accounted for 2-3 times lower TMP values which was significant considering the low material and time expenditure (Gabarrón et al., 2014). Whenever local conditions allow the use of gravitational pressure head, gravity-assisted system designs should be considered. This not only reduces the energy consumption but moreover improves the robustness thus reducing the maintenance costs as shown by Codianne (Codianne, 2015). A novel way of improving the membrane scour effect was attempted by Eliseus et al. A slightly tilted membrane module increases the drag force of the incoming air bubbles onto the fouling particles attached to the surface. The result showed the process efficacy: a 260 % higher flux at constant TMP with comparable air and pump flow rates. In contrast, only the membrane facing the air bubble flow could contribute to the effective permeate flow which reduced the active membrane area participating in the filtration. (Eliseus et al., 2017).

Theoretic modelling is a great tool to understand the complexity of wastewater filtration processes. By reality approximation based on lab scaled data preliminary estimates about major projects can be made. Model based analysis give the opportunity to evaluate any system configuration independent of its installation capacity or investment costs (Boyle-Gotla et al., 2014). Verrecht et al. carried out a dynamic model which reproduced a small-scaled MBR for domestic wastewater treatment. In extend of this study, he evaluated different inflow conditions such as wastewater composition. Optimum operation conditions were found to have 23% lower energy consumption based on air supply optimisation and reduced sludge retention time (SRT). In the model, the total-N and total P- removal was reduced by higher air flow rate (Verrecht et al., 2010). To gain higher knowledge of hydrodynamics and fouling phenomena correlation, Böhm et al. conducted research on air bubble modelling with the implementation of drag and lift forces. The model validated the influence of air bubble diameter, inflow character and mounting position of the membrane module. After final parameter adjustment, the energy saving of the air scoring totalled to a 70% reduction for best-case scenarios (Böhm et al., 2012).

Contrary to conventional technologies for improving the overall MBR efficiency, membrane modification has become more and more relevant within the last 15 years driven by fouling mitigation targets, enhanced selectivity or improved water permeability. Fouling effects are complex since different phenomena occur simultaneously. Depending on the wastewater matrix, membrane fouling is more or less severe.

2.4 Membrane fouling

Membranes are more or less exposed to harsh environments where suspended and dissolved organic and inorganic matter limit the membrane performance. Pore- and intermediate blocking are caused by adsorption and deposition as well as biofouling growth over time.

These processes increase the membrane resistance hampering the water molecule flow through the physical barrier. For a constant pressure TMP driven process, fouling results in flux decline whereas at constant flux conditions, the applied pressure (TMP) increases to maintain the set volume flow. As salts, metal oxide and clay mainly cause inorganic fouling in NF/RO filtration. This chapter, however, only focuses on the propagation of fouling layers caused by particulates, colloids and extracellular polymeric substances (EPS) covering proteins, humic substances and carbohydrates which are predominant in MF/UF filtration (Le-Clech, 2006).

Fouling is complex due to various parameter interaction. For instance, component interactions in the unique feed water matrix depend on operating parameters such as temperature, pressure, dissolved oxygen level and hydrodynamics (Liu et al., 2006; Hohlman and Ohlinger, 2007). Finally, the membrane structure and its properties determine the selectivity and retention of specific constituents which also affects the fouling extend. Therefore, identification of the feed water matrix as well as membrane characteristics should get high attention within a system design phase. Activated sludge in characteristic MF/UF systems contain suspended particles (inert material, bacteria flocs), colloids and solutes; their chemical and physical properties mainly determine the adsorption level on and inside the membrane pores (Rosenberger et al., 2005). In this sense, it seems that the mixed liquor suspended solids (MLSS) is likely to show different fouling contributions. MLSS $<6 \text{ g}\cdot\text{L}^{-1}$ showed less fouling potential, MLSS between $8\text{-}12 \text{ g}\cdot\text{L}^{-1}$ did not affect the fouling progression at all whereas MLSS above $15 \text{ g}\cdot\text{L}^{-1}$ did have a significant impact on fouling phenomena. However, the dependency on the feed water matrix is highly complex and results in diverse effects causing reversible and irreversible fouling (Rosenberger et al., 2005).

2.4.1 Cake layer formation

Cake layer formation refers to the deposition of accumulated particles and solutes on the membrane surface. Once particle depositions become more extensive, a cake layer forms creating the additional resistance R_c (see equation 2-2). Thereby, larger particles result in a lower pressure drop due to the lower packing density. Over time, the cake layer becomes more compacted and thicker as more and more particulates reach from the bulk phase to the membrane surface. As the cake layer formation becomes more distinct, the membrane resistance R_c further increases. Smaller particles reach the void spaces of the porous cake layer and reduce the porosity which further impairs the permeability in time. Contrary to common wisdom, TMP does not directly affect cake layer compaction. However, if cake layer compaction occurs – according to the existing cumulative pressure within the cake layers – it starts from the bottom. At corresponding pressure, the deposition configuration starts to change and depending on structure, size and shape, result in cake layer collapse. The increasing pressure drop over the membrane results in lower permeability which is compensated by higher TMP values. The compaction force gets higher and higher ending up in a sudden and steep TMP rise known as the “sudden TMP jump” (Le-Clech, 2006). Existing, very diverse wastewater compositions make it difficult to make accurate statements about the exact cake structure and collapse time. Poorasgari et al. (2015) however, determined a 49-78 mbar TMP threshold for an MBR unit treating municipal wastewater below which cake layer compression did not occur.

Cake layer formation gives an additional membrane resistance serving as a filter layer and as a result of this, the permeate quality can be improved (Mannina and Cosenza, 2013). When larger particles deposit on the membrane surface, they accumulate finally forming a dynamic membrane on top. As the dynamic membrane grows, it prevents smaller particles to adsorb on the membrane surface and directly inside the membrane pores. By this mean, severe and irreversible fouling is alleviated reducing the pressure drop at constant permeate flux rates. Lee et al. supported this assumption through scanning electron and atomic force microscopy. He confirmed a direct relation between microorganism accumulations on the membrane surface with a significantly lower pressure increase (Lee et al., 2001). Ordinarily, cake layer can be largely removed by chemical cleaning.

Particles and colloids which are smaller than the membrane's molecular weight cut off are likely to penetrate inside the pores where final adsorption and deposition takes place. As the cake layer builds up in time, it serves as additional filter layer. Internal pore deposition and pore blocking basically occurs within the first stage of filtration resulting in rapid flux declines for constant pressure (TMP) operation. Progressive, internal fouling is known to be irreversible and in long-term leads to irrecoverable permeate flux and in the end to costly membrane replacement.

2.4.2 Biofouling

Biofouling refers to the attachment and further growth of microorganism on the membrane surface. Bacteria, proteins and polysaccharides adhere to the membrane surface ultimately forming a biofilm with extracellular polymeric substances (EPS). It has been shown that especially EPS play a significant role in membrane fouling. EPS are long molecular, natural polymers which are excreted by microorganisms enabling microbial agglomerates. EPS serves as nutrient storage and protective layer for the microorganism. A distinction is made between EPS at the outside of the cell layer (eEPS) and the excreted EPS detached from the microorganism through hydrolysis and diffusion (SMP = soluble microbial products). A further breakdown can be found in literature between EPS of high contented carbohydrates (eEPS_c and eSMP_c) and high contented protein EPS (eEPS_p and eSMP_p). A clear discrimination within membrane fouling effects, however, is difficult to make since sampling and analysis methods vary greatly and the existing results of different studies must be considered with caution. Nevertheless, through various studies, biofouling has been considered as most severe fouling phenomena that can result in significant permeate flux drops (Lee et al., 2001). As shown by Saeki et al. biofouling is also affected by operation parameters such as cross-flow rate, permeate flux and molecular weight cut-off (MWCO). Effect of changing TMP has shown slight differences in biofouling propensity specifically during the initial test phase but requires further detailed studies (Saeki et al., 2017). EPS are organics such as humic/fulvic acid-like substances and proteins and contribute to the major biofouling, as shown by Wang et al. During a long-term study of submerged MBR using UF membranes with a mean pore size of 0.2 μm , He differentiated between the biofouling caused by mixed liquor and EPS. He also stated that lower wastewater temperatures reduced the fouling rate caused by EPS (Wang, 2009). Polysaccharides are also known to be critical for potential accumulation in the CP layer and creating gel layers on top of the membrane surface.

By analysing and comparing 6 different case studies, a strong impact on the fouling rate, defined with the specific TMP increase in time could be concluded. Thereby, different fractions of the EPS resulted in different performance loss but quantitatively, the results could not be directly compared due to big differences in sampling and analysing methods. Moreover, direct correlation between fouling rate and operation parameters such as MLSS, loading and flux rate have been reported (Rosenberger et al., 2005). Generally, irreversible fouling processes were derived from high EPS and SMP concentrations.

2.4.3 Fouling propagation

Membrane fouling propagation can be divided into different stages, characterized by a lighter or stronger pressure increase caused by different fouling phenomena. A constant pressure (TMP) and a constant flux operation should be viewed separately. The latter is much more pertinent to practical application. Nowadays, constant TMP operation are more likely found in lab scale experiments. They are used for examination of specific membrane and fouling resistances according to the resistance model (see section 2.2.1). The main challenge for constant TMP operation is the flux decline in time due to increasing fouling (Figure 2-5, left). The clean water flux J_{DI} is constant and linear proportional to the TMP (Figure 2-5, right). A flux reduction due to the concentration polarisation (J_{CP}) is reversible and the real flux characterised by fouling effects (J_F) is correspondingly lower. The initial, rapid flux decline is presumably caused by SMP intensified by the electrostatic attraction between membrane surfaces (Le-Clech, 2006). Moreover, within the initial stage, pore size and molecular weight of the contaminants determine the rate of internal fouling (Yuan and Zydney, 2000). Within the next stage, small particles and colloids start to deposit and attach on and inside the pores as they are carried by the feed flow towards the membrane surface. The CP builds up and as more and more particles accumulate, back-diffusion equates the streaming forces (equilibrium), characterized by the plateau reached.

Fouling in constant flux operation are more severe since the particulate accumulation does not diminish in time as it does for constant TMP and corresponding declining flux. The self-accelerating effect of particulate deposition, cake layer formation and biofouling growth ultimately lead to a filtration collapse resulting in exponential TMP rise. More specific, this process propagation can be split into the following propagation stages according to current knowledge.

- **1st propagation stage**

When the virgin membrane touches the wastewater-activated sludge mixture, passive adsorption of particularly proteins and microorganisms happens instantaneously even at stationary conditions. The interaction between the membrane surface and the wastewater determines the adsorption rate. Random collisions of particulates and SMP and temporary deposition on the surface occur. This leads to subsequent nucleation which then makes further attachment more likely as the membrane surface properties become less relevant (Le-Clech, 2006). Within this stage, pore size and distribution as well as surface chemistry still have significant influence on the fouling propagation.

- **2nd propagation stage**

As nucleation begins, deposition of particulates, microorganisms and SMP becomes more frequent and by time covers the entire membrane surface. At this point, cake layer starts to grow, supported by the growing gel layer resulting from the increasing pressure. Within this stage, literature has shown that pore size does not necessarily affect the permeability anymore since the cake layer has formed a dominant porous dynamic membrane (Yoon, 2016).

- **3rd propagation stage**

The third stage is characterised by a self-acceleration process finally leading to exponential – or sudden TMP increase. As the cake layer grows, the porous structure leaves void spaces in which the smaller particles move. Thus, the cake layer porosity diminishes and the pressure increases to maintain the constant flux conditions. With growing thickness, a cumulative gravitational force of the top sublayers acting on the bottom sublayers causes a shift of rigid particles. Both effects lead to a more compact cake formation, starting from the bottom to the top until a cake layer collapse follows. Simultaneously, self-acceleration takes also place due to locally inhomogeneous fouling on micro- and macroscale. As some pores are inevitably blocked completely, the lost flux must be instantly compensated by other pores to maintain the constant permeate flux. Fouling is accelerated in these pores since more contaminants reach further inside the pores attach on the surface. By time, more pores continue to get blocked until few open pores are not able to cover the permeate flux value anymore. At this point the TMP jump becomes irreversible. Inhomogeneous fouling is a result of uneven membrane scouring causing location of poor convection and particulate detachment. Considering the pressure head acting on the membrane (vertically submerged module), the cumulative pressure increases in depth which also changes the force acting on the membrane. An even suction pressure over the membrane surface is assumed here.

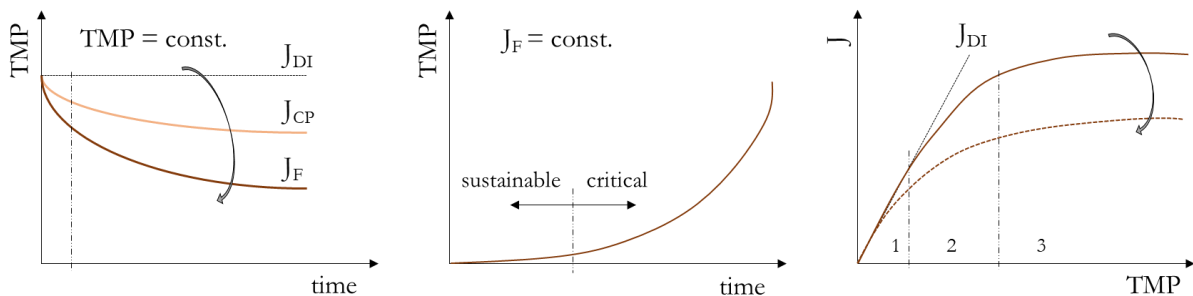


Figure 2-5 Flux and TMP propagation using wastewater

Critical flux

The critical flux is defined as the volume flow per m^2 membrane area above which the flux does not increase linearly with increasing transmembrane pressure. Once the critical flux is exceeded, irreversible fouling occurs due to the self-accelerating nature. The critical flux for one specific membrane treating a unique wastewater matrix changes with sludge viscosity (temperature), cross-flow velocity, air scouring conditions, specific solute-membrane interactions and membrane properties as explained before (Le-Clech, 2006).

For stable long-term operation at minimised periodical chemical cleaning, MBR systems should be run below the critical flux, further characterised as “sustainable” or “sub-critical” flux. This in mind, Pollice et al. reviewed studies which differentiated between the two operation mode (Figure 2-5, mid). Therefore, the specific pressure increases in time, given as $dTMP \cdot dt^{-1}$, and critical time t_{crit} until the critical flux mode is reached were defined (Pollice et al., 2005). Above this critical point, accumulation near the membrane exceeds the back-diffusion of rejected constituents. Now, there is no linear relation between flux and pressure. Occasionally, a strong and weak form of the critical flux is characterised. The strong form – at lower TMP – can be derived from the pure water flux J_{DI} (Figure 2-5, right, region 1) with higher flux rates obtained at higher pressures. Whereas the weak form critical flux deviates from the water flux J_{DI} right from beginning. In the further filtration course, lower flux rates are obtained in the mass-transfer region (Figure 2-5, right, region 3). Ultimately, progression reaches the critical flux region with permanent fouling and decoupling of flux and pressure correlation. Differences arise from a reversible and irreversible (internal) fouling characterising the strong and weak form (Yoon, 2016). To identify current operations on their sustainability, the specific pressure increase per time step should be examined. The flux step test method gives a rough indication for sustainable membrane operation in a short time enabled by harsh filtration conditions with flux rates far above known critical flux values (Le-Clech, 2003; Monclús, 2011).

More than over two decades, researchers have been devoted their time to further access the principles that lay behind fouling phenomena. This contributed to a much better understanding of existing fouling processes and their effects on membrane separation processes. However, many questions about the actual mechanism behind the fouling growth could not be completely resolved. Many studies are contradictory in their obtained results. Therefore, some work focused on establishing standardised procedure for fouling expand evaluation and its specific proportions contributing to the resistance increase (Rosenberger et al., 2005).

2.4.4 MBR fouling prevention and removal

Membrane fouling surely is the most severe issue when it comes to filtration processes and has been subject of several research activities (Yu *et al.*, 2008; Mannina and Cosenza, 2013). In the course of fouling – assuming constant flux operation – TMP is slightly rising in the beginning and based on the acerbating fouling in time, reaches a threshold above which chemical cleaning must be conducted to not risk a total membrane collapse. Thereby, fouling extend and membrane type define the chemical cleaning activities carried out to regain the initial TMP (Wang et al., 2014). However, it is worth striving for taking appropriate measures in advance to chemical use against irreversible fouling. Aggressive chemicals such as sodium hypochlorite (NaOCl) alter the membrane structure over time (Basile et al., 2015). To obtain a first-rate cross-flow at minimised fouling potentials, air scouring exerts drag forces from the formed bubbles on the sludge flocs and particulates present on the membrane surface. In addition, higher cross-flow rates increase the turbulence between the membrane sheets and reduce the CP accordingly. Back washing is generally applied in periodic intervals, timer-based on experience values, or conducted after reaching a pre-defined TMP value.

Mannina and Cosenza examined the impact of individual back washing frequencies ranging between 1 to 9 min. Operating costs as well as cleaning cycle deviations from the manufacturer's specifications (Mannina and Cosenza, 2013). Likewise, other authors extended the time between the back-flush periods which had little to no positive effect on the operation efficiency (Gabarrón, 2014). When physical cleaning such as back-washing, relaxation, and enhanced scouring does not result in a total TMP recovery, chemical cleaning becomes evident. Common cleaning protocols for MF/UF membranes within MBR systems are as follows: prior to chemical dosing, rough cleaning by e.g. water jets to remove loose and coarse particles as well as attached sludge flocs. An oxidative cleaning with sodium hypochlorite (NaOCl) followed by an alkaline cleaning using sodium hydroxide (NaOH) removes present biofilm and gel layers from the membrane surface. Subsequent citric acid cleaning removes lime and salt hydrates. The cleaning protocol may vary with manufacturer, wastewater composition and fouling stage. Harsh mechanical cleaning is rarely carried out and is more relevant in long-term as last resort before membrane replacement (Monclús et al., 2015).

Described cleaning methods all directly affect the water treatment process. By adding chemicals or by interventions for changing the machinery in terms of membrane module removal for ex-situ cleaning or the reversed flow for back-flushing. It has been shown that consistent cleaning improves overall system performance but at the same time higher energy consumptions and operational expenditures are expected (Gabarrón et al., 2014). Membrane cleaning is an integral part during filtration system operation. If used regularly following the universal guidelines and moreover the procedure adapted to the specific application, it is an essential element for a safe long-term operation. It also reduces the specific energy costs as frequent cleaning maintains the membrane filtrate performance. Nevertheless, preventing fouling phenomena are should be prioritised over cleaning procedures to further reduce consumables and chemical addition. For this reason, many researchers have been devoted to other low-fouling approaches, for instance the modification of membrane by surface or structural modification. Coating layers or incorporation of different nanoparticles could also enhance the rejection rate (see Table 2-2).

2.5 Membrane modification

Minimising fouling effects will help to overcome for further spread MBR technology. Besides (reversible) high TMP increase, fouling also inevitably affects the membrane's life span due to applied, frequent back-flushing (high mechanical strain) and extensive chemical cleaning. Polymer membranes showed a clear change in polymer structure over time (Basile et al., 2015). Membrane modification has therefore been a serious strategy to improve the performance in the long-term (Table 2-2 give some excerpts).

2.5.1 Membrane key parameters and characterisation

There are various membrane parameters which influence the membrane performance such as selectivity and filtration capacity. The following paragraphs list these material parameters and give an explanation about the fundamental relations with the filtration process. Characterisation principles are highlighted and the parameter assessment clarified. The aim of membrane modification is to alter the membrane architecture or surface properties and positively change one or more of these key parameters.

2.5.1.1 *Pore size and pore distribution*

Current studies show that – assuming constant hydrodynamic system conditions – the permeability quality for ultrafiltration membrane is not perceptibly affected by pore sizes ranging from 0.03 – 0.45 μm . Chemical oxygen demand (COD), total organic carbon (TOC) and turbidity removal did not differ noticeably and even comparable virus removal efficiencies were achieved if the membrane integrity was intact (Yoon, 2016). Independent of the (nominal) membrane pore size, particles in the bulk phase deposit on the membrane surface. As more particles accumulate, deposits form a second porous layer on top of the membrane itself, considered as “dynamic membrane”. The packing density and structure depends on the constituents inside the feed water causing a certain pressure drop (see cake layer formation). This pressure drop is only dominated by the membrane pore size in the beginning of the filtration but weakens in time when the dynamic membrane builds up. After certain operation time, the dynamic layer forms a closed, porous structure finally acting as membrane (Yuan et al., 2000). Yoon demonstrated that 0.45 μm membrane pores are able to reject much smaller silica particles with a 0.05 μm nominal size. He also validated that the permeate turbidity decreased substantially within the first 6 hours reaching a plateau after a dynamic membrane layer was formed. In certain studies, additive dosing to the water matrix resulted in higher flux rates since the additives formed a dynamic layer and prevented further internal pore blocking of the feed components. The dynamic layer was also easier to be removed (reversible fouling) (Yoon, 2016). Either way, pore size only effects the filtration to a certain degree being also influenced by other membrane parameters such as the hydrophilicity and surface charge.

2.5.1.2 *Surface properties*

Surface tension

Considering a liquid bulk phase, each molecule is surrounded by adjacent molecules between which attractive and repulsive binding forces prevail. Added up, these forces neutralize each other. At the liquid-gaseous surface however, due to missing binding forces from the gas phase, a force arises in direction towards the bulk phase. This surface force compensates the force imbalance and restores the force equilibrium. The surface tension is a liquid material property which significantly affects the material properties such as atomisation capability for spray coating application (see section 2.5.3.4).

Surface tension measurements can be assessed by several techniques including pressure and force-based methods. Within this work, measurements were carried out using the optical pendant drop method. A liquid is slowly suspended through a small capillary syringe until it forms a more or less spherical droplet at the end of the capillary. Data evaluation is done for the droplet shape which depends on the surface tension-gravity balance. Despite common wisdom of a highly accurate measurement, the sensitivity of pendant drop method is strongly reduced for border regions of small and big bond numbers (Saad et al., 2011). The bond number is a dimensionless index and can be interpreted as the ratio of volume force acting on the liquid drop and the force resulting from the surface tension. High accuracy is obtained by elongated droplets rather than spherical droplets.

The best data can thus be gained for bigger drop volumes as the gravitational force becomes more dominant. In general, bigger needle diameters should be preferred over small ones (Saad et al., 2011).

Figure 2-6 below gives a schematic illustration of the measurement principle. A free droplet would form a spherical drop in result of the existing surface tension and the prevailing pressure difference between droplet and surrounding. For small volumes, the surface tension is dominant preventing the detachment of the drop from the capillary opening (KRÜSS, 2010). The pendant drop method is an optical technique based on grey level analysis requiring a good contrast between liquid and gaseous phase. Surface tension calculations follow the Young-Laplace relation, listed as equation 2-5. The surface tension related force tries to form spherical drop shape. The pressure difference Δp between the liquid and surrounding (either liquid or gaseous) should be therefore known. Both curvature radii, the horizontal radius R_1 as well vertical radius R_2 are determined optically, depicted by Figure 2-6. The gravitational influence tends to forms elongated drop shapes, described in equation 2-6 with the hydrostatic pressure Δp_{hyd} . Depending on drop volume, the elongation is more or less pronounced changing the total drop height z from the capillary tip to the drop apex. The drop shape ultimately gives the surface tension but is not freely scalable. The software algorithms use specific parameters for geometrical drop shape adjustment until the calculated shape coincides with the actual drop in the video analysis.

$$\Delta p = \sigma \cdot \left(\frac{1}{R_1} + \frac{1}{R_2} \right) \quad 2-5$$

$$\Delta p_{\text{hyd}} = \Delta \rho \cdot g \cdot z \quad 2-6$$

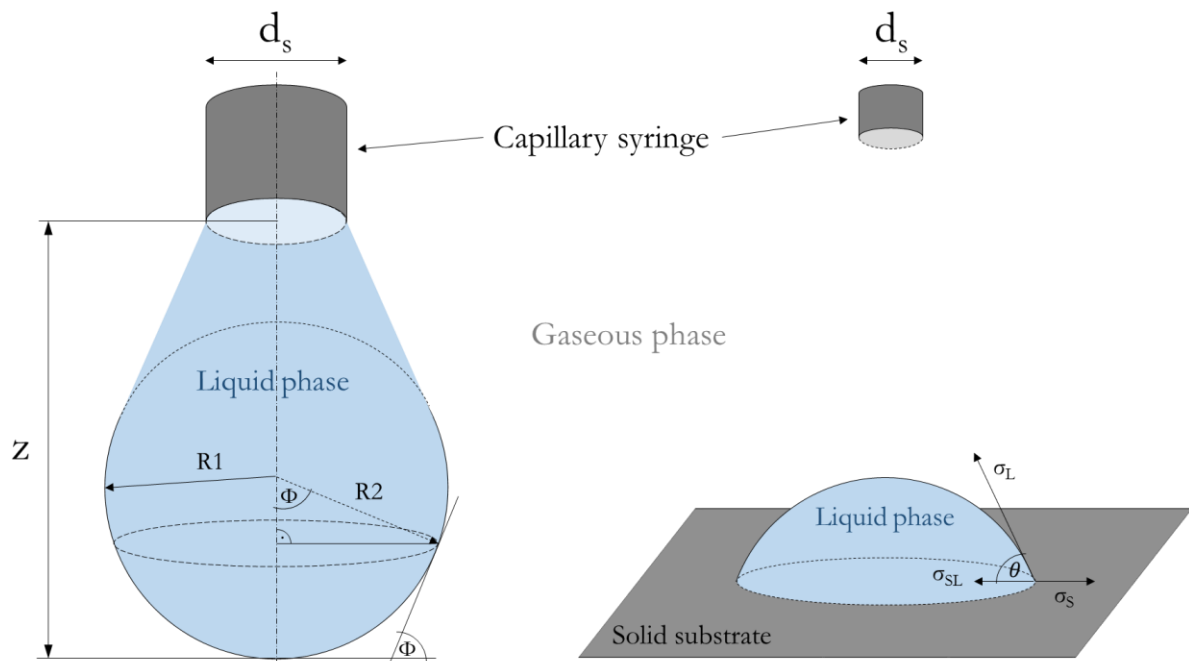


Figure 2-6 Pendant drop method (left) for surface tension determination and sessile drop method (right) for contact angle measurements using optical gray level analysis

Differences in the yielded data can arise and should be treated with caution if one compares differently achieved results (Matínez-Babuena, 2017). For instance, impurities measured over conductivity may cause interfacial contamination disturbing the surface force equilibrium.

Hydrophilic properties

“Same loves same” applies for the attraction and repulsion of hydrophobic and hydrophilic contaminants present in the wastewater matrix. Hydrophilic membranes contain polar groups and the (polar) water molecules tend to domicile at the surface. On the other hand, hydrophobicity is the affinity of binding nonpolar substances such as proteins and humic substances. In the course of filtration, hydrophobic substances are better repelled before reaching the surface and initiate fouling phenomena. The membrane surface’s behaviour can be indicated by measuring the contact angle between an applied fluid (mostly DI-water) and the solid membrane interface. This relationship between both parameters has been proven repeatedly in various studies. Rahimpour and Madaeni for instance increased the amount of hydrophilic hydroxyl groups (-OH) in PES membranes by adding the surfactant 2-hydroxyethylmethacrylate (HEMA). Contact angle measurements (CAM) conducted via sessile drop technique were reduced with increasing HEMA amount in the polymer substrate. Likewise, the flux for milk water increased at constant pressure operation (Rahimpour and Madaeni, 2010). The sessile drop method works with grey level analysis requiring a clear contrast from the specimen itself and the liquid droplet. The schematic layout of the setup is depicted in Figure 2-6, right.

The liquid entry pressure (LEP) is the minimum pressure for the passage of water through the membrane and gives the indication of wettability potential. Derived from the Young-Place equation (equation 2-5), LEP becomes negative for $\theta < 90^\circ$ meaning that the water passage is spontaneously. For $\theta > 90^\circ$, however, the pressure becomes positive and this additional (relative) pressure must be applied for water passage through the porous substrate. Contact angles $\theta < 90^\circ$ indicate a hydrophilic membrane, whereas contact angles $\theta > 90^\circ$ speak for a hydrophobic membrane surface. Therefore, a lower wetting/ contact angle indicates a higher hydrophilicity, which is known to repel various hydrophobic matter.

$$\text{LEP} = - \frac{2 \cdot \beta \cdot \sigma \cdot \cos(\theta)}{d_{m,\max}} \quad 2-7$$

The LEP depends on the material properties: d_{\max} as the maximum pore diameter, the pore geometry or capillary constant β and the surface tension σ at the air-liquid interface. In practice application, CAM is usually examined with the widely used sessile drop technique. As it can be seen, the pore diameter has a big influence onto LEP and considering the wide pore size distribution of commercial membranes LEP may vary significantly. In that sense, different membrane spots are measured for the contact angle and the mean value is calculated to reduce peak values influence. As discussed previously, membrane altering through standard filtration in long-term and more specific chemical cleaning with strong oxidants, e.g. sodium hypochlorite NaOCl, causes chain scission (degradation in polymer chain length) and leaching effects (material loss into liquid).

It is sound to say that CAM is not just a tool to describe the performance of virgin membranes but also a way to validate membrane altering based on CA variations in time (DataPhysics instrument, 2019).

Wastewater application favour from hydrophilic membranes by repulsing nonpolar molecules along the membrane surface. Attachment of nonpolar organic matter, known to cause serious fouling, is reduced.

Membrane surface roughness RMS

Smooth surfaces reduce potential deposits of microorganisms and bacteria on the membrane surface due to missing “hooks” where they could attach to (Louie J.S., 2006). A rougher surface structure provides spots of low flow velocities where particulates and microorganism tend to settle down. Resulting low shear rates within this area also minimise chance of removal during normal filtration and membrane surface scouring. Moreover, a rougher surface simply provides higher areas for colloids and charged ions to be adsorbed thus increasing fouling affinity. In these regards, minimising the roughness depth from lowest to highest peak and reducing the mean roughness given in the root mean square (RMS) is of high interest. The surface roughness is measured by atomic force microscopy (AFM) where a sharp tip mounted to a cantilever moves across the membrane surface in x and y-axis. To avoid plastic deformation of the specimen, the tip is operated in tapping mode to stay within the elastic module of the sample material. The detector measures the tip deflection by an electrical response which changes in distance from tip to detector. The gained data is characteristic for each specimen surface texture. Finally, the gathered data is evaluated and highlighted as a 3D map (Johnson and Hilal, 2017).

The relation between surface roughness and flux performance was shown by Woo et al. who evaluated two MF PVDF membranes of different surface roughness with RMS 47 and 166 nm, respectively. Other properties were similar such as mean pore diameter, contact angle and manufacturer conditions. After 120 min lab tests using humic acid as model foulant ($100 \text{ mg}\cdot\text{L}^{-1}$), the flux decline of the smoother surface was around 12% lower with a corresponding normalized flux of -21%. In addition, SEM pictures of the rougher fouled membrane surface subsequent to the fouling experiments showed higher HA contamination which was a clear indication that low surface roughness leads to lower fouling propensity (Woo et al., 2015).

Surface charge/ ZETA potential

Electrically charged surfaces interact with counterions in electrolyte solutions. Fluids containing freely movable ions are overall electrical neutral. Once an electrical field is applied, negatively charged ions (anion) move towards the anode while negatively charged ions (cation) move to the opposite site, the cathode, due to the strong electrostatic interactions. At the solid-liquid interface, the electric solution is not natural anymore and an electrical double layer forms within differently charged ions are attracted and similarly charged ions repulsed back into the solution bulk phase. This process was first described by the Helmholtz model which was then further developed by Stern (1924), Grahame (1947) and Bockris-Müller-Devanathan-Model (1963). The new model also considered back-diffusion and influence of solvent/solvations onto the electrical double layer. More specifically, depending on surface charge and chemical composition, counter ions dissolved in the bulk water phase are adsorbed at the surface. This developed immobile electrical charged double layer is the Stern plane with a superimposed share plane and diffusion layer.

It is assumed that there was a counter play between electrostatic forces, shear-induced and Brownian diffusion (Ehrhard, 2016). General information about the electric charge of particles and surfaces is given with the Zeta-potential. Therefore, experimental measurements are conducted in a specific membrane cell where an electrolyte solution overflows the membrane. Due to the solid-liquid interaction, there is a developing voltage profile along the measuring distance. Besides the surface charge of the specimen, Zeta potential measurements are influenced by convective transports, diffusion, temperature, solvent and solute concentration and composition, etc. (Yoon, 2016). Thus, caution must be given if discussions are held solely based on this parameter. It is therefore not surprising that results of numerous studies diverge.

However, despite some studies showing that the Zeta potential has a sustainably impact on membrane filtration processes using UF membranes, majority of executed work draws a different conclusion. The initial moment the membrane (assuming a charged surface) gets in contact with the wastewater, molecules immediately start to be adsorbed on the surface. From now on, the membrane surface charge is no longer a decisive factor determining the fouling propensity. For instance, Yoon describes that membranes of different Zeta potential show a similar surface charge after introducing into the same wastewater matrix (Yoon 1998). Hobbs et al. derived similar relations proofing that the initial Zeta potential does not correlate with the fouling progress (Hobbs et al. 2000). It is worth mentioning that wastewater consists of very diverse species of macromolecules/colloids/EPS and other organic matter. It is therefore extremely difficult to anticipate the exact influence of the Zeta potential on the final application. In addition, surface properties can change over time due to membrane altering and chemical cleaning using strong oxidants (Levitsky et al., 2011). In any way, the Zeta potential, as well as the surface tension, can be used to measure the wear and tear of membranes. This could help to make more accurate statements about the membrane's lifespan.

2.5.1.3 *Rheology*

Rheology describes the flow and deformation characteristics of a sample body due to external forces in the two aggregate states, solid and liquid. Rheology refers to the plastic deformation rather than elastic flow behaviour. Ideal fluids deform plastically if subjected to an external force. During the deformation, the energy is dissipated through sliding friction between the lattice molecules. Newtonian fluids show linear correlation between the shear rate and shear strain, and are characterised by a constant viscosity coefficient which changes in temperature. Non-Newtonian fluids show viscosities independent of the applied shear strain and show also elastic besides the plastic deformation, therefore also characterised as viscoelastic body. To distinguish between both principles, the term viscosity has been defined as their resistance to deformation (measured as a force) at defined shear rates. Describing the rheology of a specific fluids is important as it inevitably effects numerous processes. Relevant applications can be found in pharmaceutical use such as injection of therapeutic protein solutions. High protein concentrations lead to high change in flow behaviour which negatively affects the injection (Inoue et al., 2014). Paint and coating materials must meet requirements for levelling behaviour, pigment dispensability or film thickness. In most cases, complex multiphase formulations are developed for various application.

It is of great importance to test these materials under conditions relevant for end user application (quality control) and to maintain the properties during transportation. Rheological investigations make an important part in coating applications such as brushing, spraying and rolling (Malvern Instruments, 2015). Other relevant applications are the beverage industry covering vegetables in a thin protective layer by dip coating (Cisneros-Zevallos and Krochta, 2003).

Specifically, for membrane coating application the viscosity has direct impact on the way the liquid can be spread over the membrane surface. For instance, if applying casting coating techniques, occurring shear stress on the material could cause variations in viscosity if non-Newtonian fluids are used. On the other hand, selectively changing the coating material flow behaviour could be beneficial to reduce penetration into the porous structure. As the membrane is highly porous with wide pore distributions, pore intrusion levels vary and with it the quality and reproducibility.

Principle relations for viscosity measurement are given below. To determine a liquid's viscosity, the liquid is put between a moving cone and a resting, heatable measuring plate (Figure 2-7). As the cone starts rotating at a given speed, the shear rate $\dot{\gamma}$, the rotational movement exerts a friction force to the liquid due to the rough cone surface. A linear velocity profile develops starting from the resting measuring plate ($u_{\text{plate}}=0$). The flow gradient "du" results from the viscous behaviour and the lattice friction between the molecules, called shear flow or Taylor-Couette-flow for incompressible fluids. With the developing velocity gradient, the shear rate $\dot{\gamma}$ can be assessed according to equation 2-8. The pressure energy or shear stress τ , necessary to deform a liquid, is calculated by the cone surface A and the measurable force F (equation 2-9).

$$\dot{\gamma} = \frac{du}{dy} \quad 2-8$$

$$\tau = \frac{F}{A} \quad 2-9$$

According to the Stoke's law, the friction force F is linear proportional to the dynamic viscosity and converted, the dynamic viscosity can be calculated by equation 2-10. Arrhenius states that the viscosity is temperature dependent. Therefore, viscosity measurements should be carried out at constant fluid temperature, achieved by continuous cooling of the measuring plate (Figure 2-7, right). An air bearing of the cone shaft enables the highly sensitive torque measurements resolving few nNm which are then converted in the corresponding shear force F using the cone diameter d_c .

$$\eta = \frac{F}{A} \cdot \dot{\gamma} \quad 2-10$$

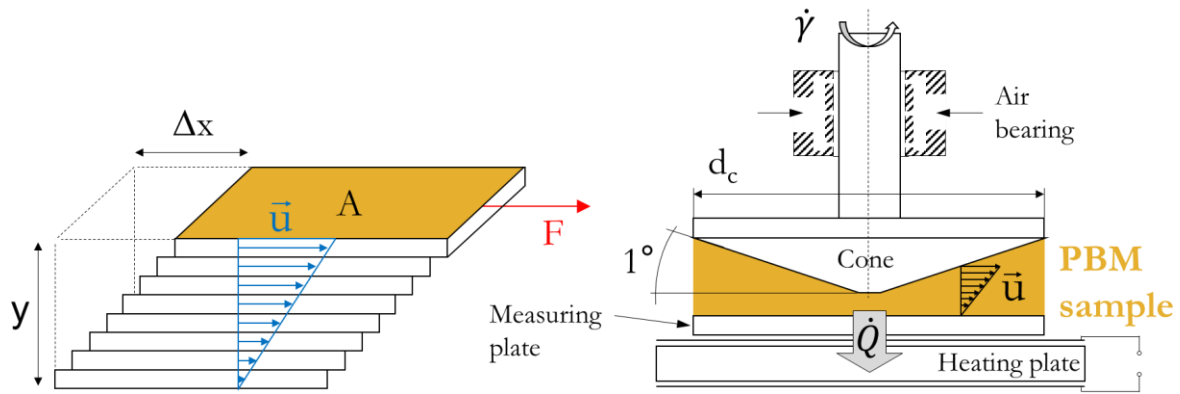


Figure 2-7 Principle behind viscosity measurements using a rheometer (cone and plate measurement)

Specifically, for membrane coating application, the capillary force between solid (membrane substrate) and liquid phase (coating material) affects the modification approach. Resulting from the cohesion, the capillarity (defined by equation 2-11) of very small membrane pores forces the liquid PBM to penetrate into the very same (Yoon, 2016). The capillarity h in mm represents the height of a liquid volume inside very small cavities as result of adhesion forces. Thereby, the depth of intrusion results from the capillary radius r , the fluid density ρ in $\text{g}\cdot\text{cm}^{-3}$ as well as interplay of wetting and wetted phase, described by the surface tension σ_{SL} in $\text{N}\cdot\text{m}^{-1}$. Once the liquid enters the capillary, it forms a meniscus at the solid surface with the angle φ in direction of the capillary. By replacing ρ with the kinematic and dynamic viscosity ν and η , respectively, the direct relation of the dynamic viscosity on the capillarity (membrane pore) intrusion depth can be established (Che Mat et al., 2019). g is the gravitational acceleration in $\text{m}\cdot\text{s}^{-2}$.

$$h = 2 \cdot \sigma_{\text{SL}} \cdot \frac{\cos(\varphi)}{g \cdot r \cdot \rho} = 2 \cdot \sigma_{\text{SL}} \cdot \frac{\cos(\varphi) \cdot \mu_{\text{L}}}{g \cdot r \cdot \rho} \quad 2-11$$

Pore intrusion is an effect limiting the membrane performance through pore clogging. It is thus of high interest to minimise the intrusion effect along with the coating layer thickness s_{m} (equation 2-1). These rheological considerations will be fundamental for major parts of this work. Limitations of present will be pointed out and approaches will be derived from equation 2-11. By means of a squared dependence to the membrane pore diameter d_{m} (equation 2-1), pore intrusion reduces the flux rate more significantly than the coating thickness s_{m} .

2.5.1.4 Durability

The environmental and operation conditions, the membrane is exposed to decide over the service life before being replaced. With the fouling type and extend, the intervals between the chemical cleaning methods change. Chemical cleaning affects the membrane structure and properties more or less. At best, the membrane material possesses excellent chemical resistance against highly oxidative cleaning agents and aggressive constituents present in the wastewater. Elevated temperatures are generally desired for membrane filtration processes (equation 2-4) as they improve the molecular diffusion. Hence, membrane science aims at higher temperature stability for the applied materials.

The mechanical strength of a membrane and assembled membrane module can change the operation scenario speaking of applied TMP and back-flushing options. The more resistant the material against mechanical stress, the higher the potential back-flushing pressure and the more effective the fouling removal and thus is the flux regain.

The discussed parameters above all have an influence on the membrane fouling behaviour and their improvement is in the great interest of the supplier. Within the last years, more and more researchers focused on developing new membrane materials. Executed as composites, layer-by-layer or one layer coatings on commercially available membranes, the filtration performance can be improved. Ultimately, higher arising specific production costs should be compensated with lower operation costs in the long-term.

2.5.2 Modification technologies

Louie et al. discovered that the surface roughness and charge of the membrane are main factors influencing the fouling propensity (Louie et al., 2006a). Therefore Shao et al. modified PVDF membranes with incorporated, hydrophilic TiO₂ nanoparticles. A “biological glue” consisted of a polydopamine (PDA) architecture. The result was remarkable: a substantially improved hydrophilicity reduced irreversible fouling propensity and promoted a flux recovery of around 90% (Shao et al., 2014). Lui et al. also worked with PSU substrates for composite membranes with a Polyamide-urea layer and embedded 5-isocyanato-isophthaloyl chloride (ICIC), m-phenylenediamine (MPD), and –NH groups. Slightly higher flux rates were gained. Mokhtari et al. moreover used salicylate-alumoxane nanoparticles as hydrophilic additives for PSU membranes. Within this work, AFM measurements showed an average surface roughness (R_a) reduction by 51%. Though, the additional membrane layer reduced the mean pore size by around 24% causing a general flux decline of around 40% (Mokhtari et al., 2017). For a better overview, Table 2-2 lists further studies about membrane modification procedures as well as their positive outcome.

Table 2-2 Excerpts of different membrane modification activities

Modification procedure	Result obtained	Reference
Entrapment of TiO ₂ nanoparticles in a casting solution as additional layer	Lower flux decline Greater fouling mitigation	Bae and Tak, 2005
Polyamide-urea composite membrane with 5-isocyanato-isophthaloyl chloride (ICIC) and m-phenylenediamine (MPD)	Higher flux recovery	Liu et al., 2006
Quaternary ammonium and phosphonium polymers	Enhancement of protein resistance	Hatakeyama, 2009
Copolymer hydrogel networks containing poly(ethylene glycol) diacrylate (PEGDA)	Improved fouling resistance against oily wastewater	Sagle et al., 2009
Extraction from natural wax (cabbage leaves - Brassica oleracea)	Increased protein rejection	Madaeni et al., 2011

Polymerisable bicontinuous microemulsion coating of polyethersulfone (PES) membranes	High antimicrobial activity against bacteria and fungi Reduced surface roughness Lower contact angle	Deowan et al., 2016 Galiano et al., 2015
Entrapment of quorum quenching bacteria into polymeric membranes	Lower fouling potential (stable TMP conditions in long-term operation)	Kim et al., 2015
TiO ₂ nanoparticles incorporation into a polydopamine layer onto PVDF membranes	Higher flux recovery	Shao et al., 2014
Functionalized PVDF flat sheet membrane by piranha reagent activation of labile groups, i.a -OH.	Production process investigation, more open, heterogeneous PVDF structure Higher water resistance with lower flux	Al-Gharabli et al., 2017
Novel high flux FO membrane by layer-by-layer self-assembled polyelectrolyte	Great separation properties High water permeability Low reverse salt diffusion	Pardeshi and Mungray, 2014
Alumina coating onto a diatomite-kaolin composite layer	Investigation of various coating parameters for an optimized production	Song et al., 2017
Structurally stable graphene oxide-based nanofiltration membranes	Reduced contact angle Increased flux and stability with bio-adhesive polydopamine	Wang et al., 2017

Although the listed research concluded a high benefit in low-fouling properties, the significant step towards applied research and pilot scale testing has barely been realised. Disproportionately high costs or high method complexity caused quality issues during upscaling. Accordingly, membrane modifications are not yet economical competitive but nevertheless are continuously being investigated worldwide due to their very high improvement potential.

2.5.3 Membrane coating technologies

Membrane surface modification can be executed in different ways. The approach and used coating material determine the final coating procedure. The next paragraphs list fundamentals of common membrane coating strategies and ultimately discuss their advantages and disadvantages relative to one another.

2.5.3.1 Spin coating

Spin coating techniques make use of the centrifugal force acting on a liquid on top of a spinning disc flywheel. Finally, the liquid coating covers the entire substrate surface. At the beginning of the discontinuous batch process, the liquid coating material is applied centrally. As the rotation begins, the liquid flows homogeneously across the substrate surface with a defined angular velocity. A thin film precipitates at constant rotation speed and excess material flows over the rim being collected and recycled for further production. Uniform film thickness ranges from 0.3 to 5 μm , respectively (Irzaman, 2017).

The initial wet layer thickness s_0 of added material reduces in time ($s(t)$) with the rotational speed ω acting as driving force, the rotation time t and with fluid properties such as density ρ and dynamic viscosity η following the equation 2-12.

$$s(t) = \frac{s_0}{\sqrt{1 + \frac{4 \cdot \rho_L \cdot \omega \cdot s_0^2 \cdot t}{3 \cdot \eta}}} \quad 2-12$$

Industrial processes applying spin coating are polymer electrolyte film coating (Kurzweil, 2015) or the solar thermal power branch (Stieglitz and Heinzl, 2012). The technology is limited to circular substrates only since an asymmetric shape causes uneven spinning with a resulting, inhomogeneous wet layer film.

2.5.3.2 *Dip coating*

Within dip coating, the substrate is dipped into a coagulation bath containing the coating liquid. Constant withdrawal speed and simple process control enables high reproducible coating layers. Environmental parameters influencing the precipitated film are temperature, pressure and oxygen content of the surrounding. According to equation 2-13, the coating film thickness depends on withdrawal velocity, density and dynamic viscosity. The relation also includes the surface tension σ_{LS} between the liquid and solid phase, and the gravitational acceleration g (Faure, 2013).

$$s = 0.94 \frac{(\eta \cdot v)^{\frac{2}{3}}}{\sigma_{LS}^{\frac{1}{6}} \sqrt{\rho_L \cdot g}} \quad 2-13$$

Common withdrawal speeds lay in between the range of 1-10 mm·s⁻¹ but can vary greatly up to minimum 0.01 mm·s⁻¹. The achieved wet film thickness can be 100 nm thickness and less (Brinker, 2013). Zhang et al. coated yttrium-stabilised zirconia (YSZ) electrodes/anodes for intermediate temperature-solid oxide fuel cells (IT-SOFC). The 20-30 μm thin, dense and crack-free film layers showed excellent surface roughness values. A modified assembly enhanced the common dip coating process, making use of capillary forces through the highly porous electrode material by an external pressure gradient (Zhang et al., 2004).

2.5.3.3 *Casting coating*

Among all membrane coating techniques, casting coating for membrane modification is regularly used due to the simply process execution, low excess material and good layer thickness control (Abrar and Bhaskarwa, 2019). Thereby – for solid substrate materials – the gap between the casting knife and substrate determines the final wet layer thickness. Uneven layers occur because of measurement tolerances for the casting equipment and machinery tool. A uniform coating layer required a steady casting coating speed and contact forces (applied pressure). Available coating tools are spiral casting knives or universal applicator with wet layer thickness adjustment. For spiral casting knives, film thickness is fixed resulting from the spiral diameter wrapped around a rod.

2.5.3.4 *Spray coating*

Contrary to casting coating, spray coating offers great benefits in system flexibility, coated surface area scalability, controlled film thickness, optimized material input and low membrane shear stress. Despite the apparent advantages, spray coating has been applied for small-scale membranes in lab tests only. For instance, membrane electrode assemblies (MEA) are major cost drivers for fuel cells containing platinum (Pt) as catalyst for the redox reaction at the electrodes. Aim is given at reducing material input to save investment costs by spraying the platinum with an ultrasonic nozzle on the electrodes which also results in thinner coating layers (Klinge et al., 2016). Sparks et al. and Li et al. produced super-hydrophobic surfaces on glass substrates with organic substances by using manually operated airbrush pistols (Li et al., 2013). Sparks et al. coated few square centimetres and further polymerised the material through UV-irradiation (Sparks et al., 2013). Existing literature extensively describes fundamentals using spray coating for very thin coating layers. Applications diverge and a specific spray mist and droplet size is required to obtain the desired final product. Some applications benefit from an optimum surface/volume ratio (combustion engine), while others aim at homogeneous distribution across a big surface area (fertilization by airplane; Nasr, 2002; membrane coating). However, spray coating is always based on the principle of atomisation which can be expressed by a high relative velocity between the sprayed material and its surroundings. As a result of high relative velocity, the liquid is atomised into small droplets changing in size and shape with the absolute velocity applied. The overall picture of all droplets together is the spray-mist (Wozniak, 2003). The basics about existing coating technologies are summarised in Figure 2-8. The overview also highlights the advantages of each method. A pictorial depiction further explains the process sequences. Since spray was considered as most promising coating technology, further fundamentals are listed below.

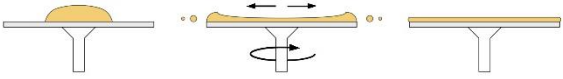
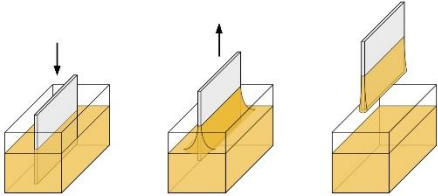
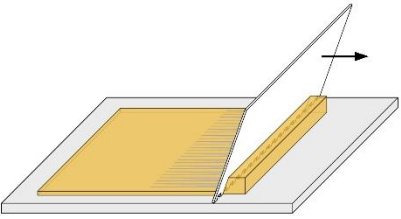
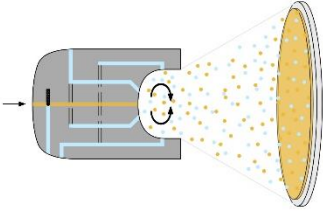
<p>Spin Coating</p>  <p>+ Highest homogeneity + Very good reproducibility</p> <p>- High material quant. required - High foot-print</p>	<p>Dip Coating</p>  <p>+ Good homogeneity + Very good reproducibility</p> <p>- High material quant. required - High foot-print</p>
<p>Casting Knife</p>  <p>+ Cheap and simple + Low foot-print</p> <p>- Mechanical stress on membrane - Potential for pore intrusion</p>	<p>Spray Coating</p>  <p>+ High control of homogeneity + No excess material</p> <p>- Higher invest costs - Potential for pore intrusion</p>

Figure 2-8 Comparison of existing membrane coating technologies

2.5.3.5 Basics of atomisation

When a liquid escapes from a capillary of a defined diameter, it will always form a smaller or bigger drop according to its surface tension (see section 2.5.3.4). Lefebvre and McDonell considered the viscosity as the most important fluidity characteristic for atomisation. The mean diameter of developing droplets changes with changing viscosity in the same way as with changing surface tension. Moreover, the viscosity directly affects the flow behaviour of liquid through a capillary or nozzle aperture which distinctively influences spray mist and spraying angle (Lefebvre and McDonell, 2017). Production of small droplets from a liquid bulk phase is only possible by additional energy input to overcome the surface tension to enable drop separation.

In general, two dimensionless key indexes describe the tendency of fluids to be atomised. The Weber number or Weber index We describes the atomisability as a ratio of aerodynamic forces with the density ρ_a of the surrounding medium, the relative velocity U_0 between the media and the liquid's surface tension σ as well as the initial drop diameter d_0 . Secondly, the Ohnesorge number Oh considers also the fluid properties kinematic viscosity μ_L and density ρ_L of the atomised fluid (equation 2-14 and 2-15). For Oh , however, the kinematic viscosity becomes negligible below $Oh < 0.1$ (Ashgriz and Yarin, 2011).

$$We = \frac{\rho_a * U_0^2 * d_0}{\sigma} \quad 2-14$$

$$Oh = \frac{\mu_L}{\sqrt{\rho_L * d_0 * \sigma}} \quad 2-15$$

Pressure atomiser

There are different ways of adding energy to the fluid phase. Pressure atomiser can be divided into sub-groups of changing construction but all use the pressure energy of pressurised liquid to obtain spray mists of small droplet sizes. Turbulence or jet nozzles eject a compact liquid jet of high impulse energy which can be used for surface cleaning and high-pressure cutting of e.g. during mining (Jiang et al., 2017). Deflection and channel rejuvenation break up the high kinetically energised jet through expansion, thus forcing the liquid to form fine droplets (Figure 2-9, elliptical opening). Lamellar nozzle types are different in aperture diameter and shape. As the subordinate body type, hollow cone nozzles make use of an eccentric inlet. This causes high turbulences and result in a liquid rotation and a highly homogeneous hollow circle form. Application are humidification processes, filter sprinkling and foam precipitation (Lechler, 2019). Flat jet nozzles are used for large wide coating areas whereas the aperture shape or a curved deflection surface define the ultimate spray shape.

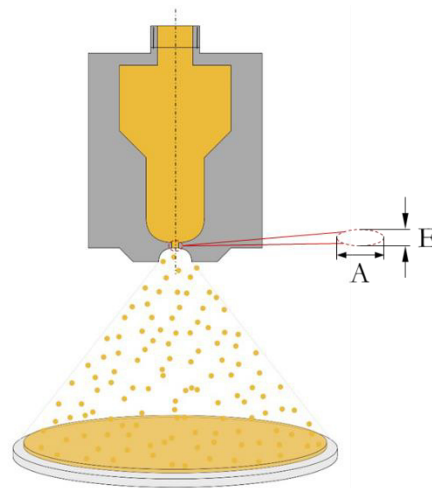


Figure 2-9 Jet nozzle for pressure atomisation

Valid for all pressure atomiser, the pressurised liquid is expanded and thus the pressure energy converted into high kinetic energy. The relative velocity in respect to the static environment is increased. Thereby, higher pressure levels result in higher kinetic energies; thus, higher relative velocities evoke smaller droplets and ultimately improve the spray mist homogeneity. The circumstance that the pressure is directly related to the sprayed quantity reduces the scope of use (relation shown by equation 2-16). Unique for each nozzle type, the manufacturer recommends a water-based pressure threshold below which no homogeneous atomisation is possible (Lechler, 2019). Consequently, the membrane coating layer character is limited by the jet nozzle geometry used.

$$\dot{V}_2 = \dot{V}_1 \cdot \sqrt{\frac{P_2}{P_1}}$$

2-16

Duel-fuel nozzle

Duel-fuel or twin-fuel nozzles are pneumatic atomisers where a pressurised gas assists droplet separation from a liquid bulk phase. Compared to pressure atomisers with a static surroundings and pressurised liquid, duel-fuel nozzles are mostly operated with pressureless liquids slowly supplied to the nozzle head. To achieve the required high relative velocity, a pressurised air duct with fast flowing air surrounds the liquid channel enabling the atomisation. Duel fuel nozzles – opposite to jet nozzles – are much more complex which is reflected by the high investment costs. The continuous supply of the assisting pressurised gas moreover increases operating costs (Lefebvre and McDonell, 2017).

Construction types differ from internal to external fuel mixing whereas internal mixing of the pressurised gas and liquid allows very high spray mist flow rates. Through internal gas mixture, at costs of greater wear and tear and shorter service life, a higher energy transfer into the fluid to be atomised can be obtained (premixing in swirl chamber; Hede et al., 2008). External mixing, as the name implies, is done outside of the nozzle head, and the atomised liquid commonly flows centrally, cylindrically surrounded by the assisted gas facilitating the atomisation (Figure 2-10). The nozzle integrity into the coating system can be realised with passive liquid feed making use of a pressure head (feeding by gravity). Additionally to the carburettor principle (self-priming), active liquid supply by a separate feed pump allowed dosing independent of other spray parameters (Lechler, 2019).

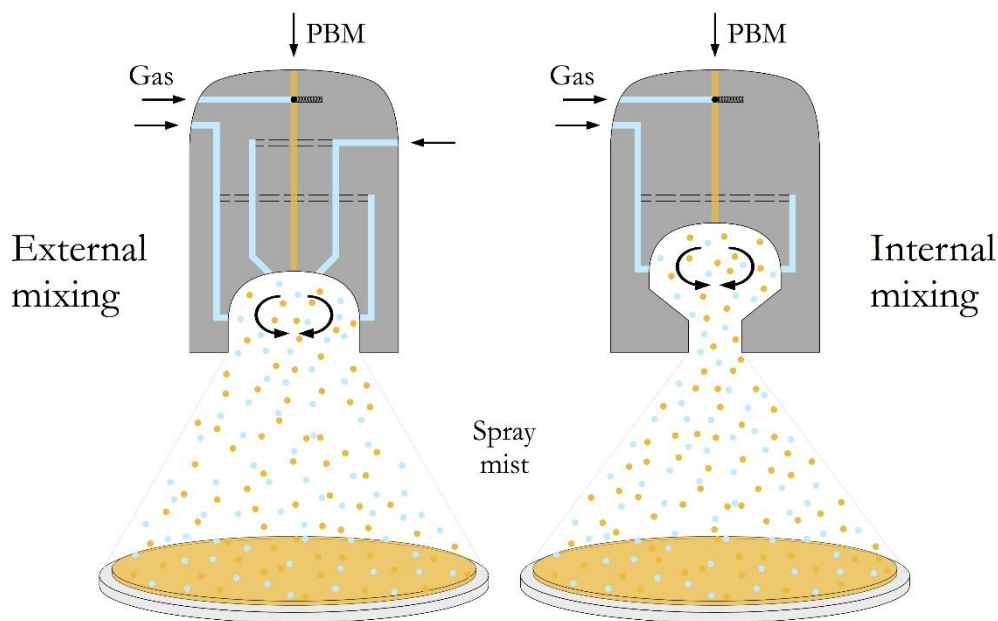


Figure 2-10 Duel fuel spray nozzles, internal and external fluid mixing

2.5.3.6 *Theoretical considerations about ultrasonic spray coating*

A complex construction and highly sensitive controlling characterise ultrasonic atomiser systems. Despite pressure driven spray application, piezoelectric elements excite a liquid until fine droplets separate from the bulk phase.

A piezo crystal makes use of the electric piezo effect changing its shape and/or its specific volume. Vice versa, applying certain deformation to the piezo crystal causes crystal lattice displacements. Some piezoelectric crystals are neutrally charged in itself.

Deformation exhibited by outer forces cause charge shifting (center of positive and negative charge) in the lattice creating microscopic dipoles inside the material. This results in an electric potential and generates a direct current voltage. The piezoelectric effect follows a linear progression between applied stress and polarisation/voltage whereas compression and tensile stress cause opposite polarity. The piezoelectric effect is more distinct for synthetic industrially produced piezoelectric ceramics such as lead zirconate titanate (PZT) or barium titanate (BaTiO_3 , Schneider, 2001)

Industrial branches make excessive use of this electric effect in controlling highly dynamic system parameters such as pressure, force, acceleration and distance measurements. Furthermore, piezo crystals are implemented in production lines replacing more and more conventional feed motors as fast and highly accurate linear motors. There are also piezoelectric pumps which supply the liquid through mechanical deformation. Likewise, in document printer, ink is injected onto the paper sheet. The impulse given by the deforming/vibrating piezo crystal causes the liquid flow through the injector needle (Waanders, 1991).

In terms of spray coating, the applied voltage and thus body deformations are created to release an impulsive energy into the wetting liquid above its surface energy. Droplets can separate from the liquid bulk phase which are subsequently carried away by the assisting gas stream. Ultrasonic atomiser are used for applications requiring very small and finely dispersed droplets, e.g. in medical use when being inhaled to cover the entire pulmonary lobe (Wozniak, 2003).

The generated droplets are of low energetic level. Technological advantages are thin and highly homogeneous coating layers and a very narrow droplet size distribution which is beneficial for membrane coating application (*Sono-TEK Corporation*). There are two types of ultrasonic systems, illustrated in Figure 2-11. Ultrasonic nozzles are used for coating application. Hereby, through the integrated piezo ceramic, the entire nozzle vibrates in longitudinal direction. The liquid coating is continuously fed by a pump through a small opening, coming out at the nozzle tip where it is pulverised. According to the applied frequency, energy is transferred from the vibrating body to the fluid forming standing waves at the tip. Above the critical frequency/energy, droplets separate from the bulk liquid phase and are carried away with an assisting gas flow. In contrast, submerged piezo elements (Figure 2-11, right) are used for air humidifiers (water, $1.9 \mu\text{m}$ @2 MHz). Placed just below the surface, the piezo element oscillates transferring the deformation energy into the liquid for droplet separation. The created free floating spray mist evaporates and is distributed to the environment with the assisting gas stream before the droplets can settle down again.

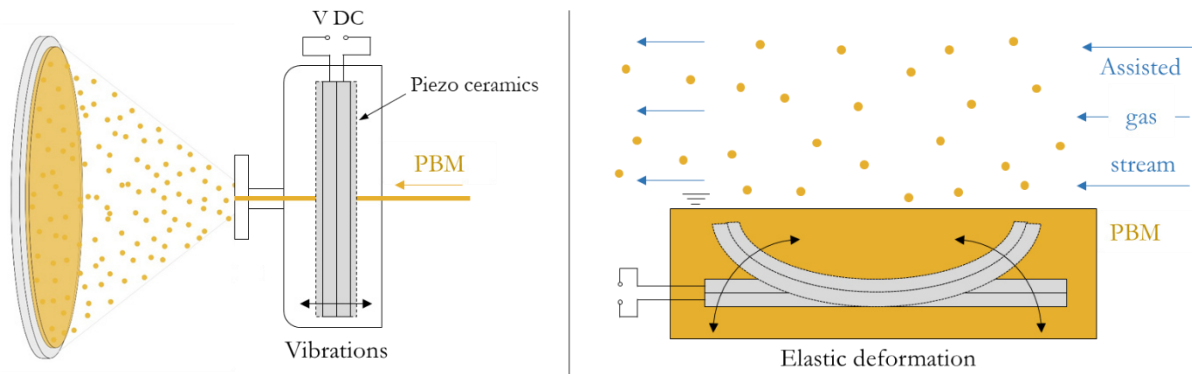


Figure 2-11 Ultrasonic system types, “stepped horn” using ultrasonic nozzle with integrate piezo ceramics (left) and submerged piezo ceramics (right)

There are basic relationships that need to be considered for suitable application. Yi et al. for instance studied the behaviour of basic parameter relations by computational modelling. He verified theoretical considerations with experimentally gained data for vascular stent spray coating using ultrasonic technology (Yi et al., 2011). Critical parameters were defined for droplet separation for different liquids. Below the critical parameters, instable droplet formation occurred and droplets collapsed before separation.

The droplet size is dependent on fluid properties, highlighted by equation 2-17 with the liquid surface tension σ_L and its density ρ_L . A further decisive operating parameter is the set frequency exciting the piezo crystal to a certain vibrational deformation. As it can be seen, the droplet diameter decreases with increasing frequency f_a . Considering DI-water (conductivity $<10 \mu\text{S}\cdot\text{cm}^{-1}$) with a surface tension of $72.9 \text{ mN}\cdot\text{m}^{-1}$ and a density of $1 \text{ g}\cdot\text{cm}^{-3}$, droplet size varies greatly from 22.5 to $1.9 \mu\text{m}$ for 50 kHz and 2 MHz , respectively. The latter are values usually found in humidifiers to improve air quality.

$$d_h = 0.73 \cdot \sqrt[3]{\frac{\sigma_L}{\rho_L \cdot f_a^2}} \quad 2-17$$

Moreover, the energy brought into the fluid determines whether critical parameters can be achieved. The higher the frequency and the lower the wavelength the higher the energy input. For the investigated materials, the critical frequency for jet atomisation (droplet separation) was defined with $f_{\text{crit}} > 20 \text{ kHz}$. The amplitude has little effect on the droplet diameter above the critical values which was found to be $>10 \mu\text{m}$. As it can also be extracted from equation 2-18, the surface tension has significant influence on the total volume flow of ultrasonic nozzles. The throughput of atomised liquid increases linearly with the effective area of the radiating surface (nozzle tip). It was also shown that the dynamic viscosity η has only minor influences on the droplet diameter (Yi et al., 2011).

$$V_{\text{unit}} = 0.041 \left(\frac{f_a \cdot \sigma}{\rho_l} \right)^{\frac{1}{3}} \quad 2-18$$

Typical parameters for stepped horn (Figure 2-11, left) water atomisers are: 53 kHz , 50 VAC , 6 W_{el} power input with a $2 \text{ L}\cdot\text{h}^{-1}$ water throughput containing droplets of $22 \mu\text{m}$ diameter.

The effective coupling factor k_{eff} as a ratio of the energy converted (from electrical to mechanical and vice versa) and the energy input determines the process efficiency and is $k_{\text{eff}}=0.2$ in this case.

There are major differences in critical parameters changing with the liquid to be atomised but also for the piezo element material. Different deformation/vibration in axial and longitudinal direction or bending in concave or convex ways are a material specific constant. Applied material pairing are diverse to match the exact requirements by adjusting ultrasound. Piezo oxides such as zirconated lead ($\text{Pb}[\text{Zr}_x\text{Ti}_{1-x}]\text{O}_3$) can be modified by appropriate doting changing the ratio between zirconium and titanium for $0 \leq x \leq 1$ (Waanders,1991). Described atomisation phenomena using ultrasonic show excellent properties for numerous industrial applications thanks to their high resolution parameters resulting in precise process control. Although studies showed that achievable surface smoothness is higher than for dip coating layers (Liu et al, 2016), benefits outweigh: a high transfer efficiency reduces material usage and an easily adjustable droplet size thanks to narrow droplet size distribution.

The alliance of the University Calabria (UNICAL), the Institute on Membrane Technology (ITM-CNR, Italy) and University Karlsruhe of Applied Sciences (HSKA) has been also committed to the goal of reducing membrane fouling potential. The innovative approach pursues the modification of – at first – UF PES membranes with a polymerisable bicontinuous microemulsion (PBM). The home-made AUTEAB surfactant showed high antimicrobial activity against gram-positive and gram-negative bacteria (Figoli et al., 2013; Mancuso et al., 2017). An incorporated co-surfactant contained a polar –OH group which is known to be hydrophilic (Rahimpour and Madaeni, 2010). Fouling propensity of commercial membranes were reduced, verified by SEM measurements (Galiano et al., 2015). Model foulant experiments in different concentrations further indicated higher fouling resistance visibly shown by differences in the membrane surface colour after testing with humic acid as brown dye (Galiano et al. 2018). The PBM layer showed a meandering pore structures so that spherical particles (for instance solids) only partially block the pores if they attach to the membrane surface, whereas circular pores in commercial membranes tend to be clogged pores completely. Previous membrane coatings have been consistently done by casting coating techniques using casting knives of different wet layer thickness. Spray coating technology has meanwhile moved into focus because of its very high homogeneous coating layer achieved, the simple scalability and the high material efficiency, also described by Susanto and Ulbricht (2009). This work also covers spray coating techniques for PBM membrane coating and its benefits relative to the casting coating.

3 Polymerizable Bicontinuous Microemulsion – Fundamentals and Literature Review

Most likely, Rodawald first industrialised the production of wax in water emulsions as floor polisher in the 1930s. The emulsion with small and stable droplet size facilitated a highly glossy floor through adequate light reflection with a high long-term stability (Bansal, 1977). First scientific reports have been published by Schulman and Hoar (1943) describing spontaneous formation of emulsions using water and oil with a strong surface-active agent. Schulman et al. later on (1959) intensified his work on transparent water/oil mixtures in multiphase systems using a surfactant and alcohol as co-surfactant (Eastoe, 2003). Simultaneously, Windsor (1954) classified microemulsions with changing phase equilibrium (Najjar, 2012). Starting in the 1970s and 1980s, driven by the global oil-crisis, microemulsion came under heavy focus as they effectively enabled oil recovery on a large scale (Paul and Moulik, 2001). Since then – despite their use as oil recovery tool – an ever-increasing interest in industrial and research work based on microemulsion technology has been observed. Nowadays, surfactants production for microemulsions serve a world market. Produced from crude oil or originated from natural resources, surfactants facilitate dirt removal or foam collapse and enable the miscibility of polar and nonpolar substances. In 2016, total worldwide sales totalled to around 31 Billion US\$ with an annual global growth rate of 3.1% (Ceresana Research Technologiezentrum, 2018)

3.1 Definition of microemulsion systems

Microemulsions are mainly composed of the two immiscible fluids oil and water. Adding surfactants of amphiphilic nature enable the miscibility between both phases by reducing the interfacial surface tension. Amphiphilic molecules are characterised by a lipophilic (nonpolar) and hydrophilic (polar) head. They can penetrate into the monolayer of both phases forming an interface of different micromolecular structures, also called micelle molecule complex (Schulman, 1959; Krause, 2001). The one continuous phase component surrounds the finely dispersed liquid phase. Micelles in microemulsion are of very small size preventing light scattering of spectral wavelength and thus appear transparent to the user.

Depending on the three-phase composition, either achieve oil-in-water microemulsions (O/W) can be produced where the amphiphilic micelles solubilise the monomers. In this way, oil droplets are easily entrapped within the hydrophobic tail region forming oil-swollen micelles (Mehta and Kaur, 2011).

Conversely, water solubilised in an oil phase forming water-swollen micelles are water-in-oil microemulsion (W/O). Best known examples for emulsions from daily life is ice cream where an oil in milk emulsion (O/W) is stabilised by the surfactant lecithin in the egg yolk. Further examples are milk, mayonnaise or various paints whereas margarine, lotions and facial creams are good examples of stabilised water in oil (W/O) emulsions. However, emulsions are not transparent since the dispersed phase commonly have macroscopic droplet sizes.

A third formulation is given as bicontinuous two-phase system, which is especially desired for membrane coating application where the two main phases coexist in interconnected domains (Galiano et al., 2015).

3.2 Thermodynamic background

A better understanding of transparent microemulsion formation can be obtained by equation 3-1. The Gibbs free energy is a thermodynamic potential and by considering the change in Gibbs free energy, a distinction can be drawn between spontaneous and non-spontaneous reactions. In thermodynamically closed systems of constant temperature and pressure, reactions are spontaneous if the change in free energy becomes negative ($\Delta G < 0$). Vice versa, reactions of increasing free energy ($\Delta G > 0$) are non-spontaneous and energy must be added to initiate the process. Considering microemulsions, the enthalpy difference term ($\Delta H = \Delta U + p \cdot \Delta V$) is nearly zero since no energy is added to the system; the pressure is constant (isobaric) as well as the change in inner energy (ΔU) remains nearly constant. The interfacial surface tension γ_{LL} between the oil and water phase becomes very small and as reported, can become even negative in equilibrium state (Kumar Rakshit, 2019). Consequently, by micelle formation, the surface area rises considerably depending on the surfactant used and amount added (see critical packing parameter). The smaller the droplets of the dispersed phase the bigger the surface increase ΔA relative to the state prior to initial phase separation. Even though there is a gain in surface area, the surface free energy $\gamma_{LL} \cdot \Delta A$ remains very small since the interfacial tension between the liquid phases can reach minimums of below $10^{-3} \text{ mN} \cdot \text{m}^{-1}$ (Figoli, 2001). As the two main components are promoted to finely disperse in each other, the entropy Δs increases and above a certain threshold, the disorder rises sharply strongly reducing the change in free enthalpy and – in case of microemulsions – ΔG becomes negative. Hence, the microemulsion forms spontaneously.

$$\Delta G = \Delta H + (\gamma_{LL} \cdot \Delta A) - (T \cdot \Delta s) \quad 3-1$$

It is assumed that the very large increase in entropy Δs is the dominant factor leading to a negative Gibbs free energy (Mehta and Kaur, 2011). Accordingly, only very small droplets can lead to spontaneous reaction as the disorder increases as necessary. Microemulsions are thermodynamically stable and can be stored for the long-term if kept in a dry, cold and dark place. Nevertheless the microstructure is often stabilized by a cross-linker which can be beneficial for specific storing conditions in case of long time use.

3.2.1 Comparing macro- and microemulsions

Macro- and microemulsions differ in droplet size. Whereas droplets in macroemulsions are of visible size, microemulsion contain much more finely dispersed droplets which do not reflect and scatter the light in visible spectral wavelengths (Schlüpen, 2000). The definition microemulsion does not imply an exact droplet size and thus different values are indicated in literature. For instance, Sharma and Shah defined microemulsions as a mixture of two immiscible liquids, containing a surfactant and co-surfactant of droplet sizes between 10-100 nm (Sharma and Shah, 1985), whereas different pertinent literature quote 10-200 nm (Schlüpen, 2000), 5-50 nm (Najjar, 2012), 2-30 nm (Figoli, 2001) or <100 nm (Khanjani et al., 2017). Anyhow, microemulsions lay within nanometres while macroemulsions are considerably bigger (>300 nm; Khanjani et al., 2017) and can reach up to 10 μm (Figoli, 2001).

Again, taken equation 3-1 into account, microemulsion formation is mainly driven by the increase of disorder. For macroemulsions, the interfacial surface free energy term is relatively big as the surface tension reduction achieved by the added surfactant is low. The surfactant cannot reduce the interfacial surface tension in such an amount that the increase in disorder $T \cdot \Delta s$ overrules the free surface energy term $\gamma_{LL} \cdot \Delta A$. For instance, microemulsion commonly show extremely low interfacial surface tensions up to 10^{-3} or 10^{-4} $\text{mN} \cdot \text{m}^{-1}$, which can be magnitudes above macroemulsions (Figoli, 2001). Ultimately, the change in free energy becomes positive resulting in a non-spontaneous emulsion formation. If additional energy is added to the system e.g. in form of mechanical stirring, the process can overcome the activation energy to form smaller dispersed droplets (Figure 3-1). Sudden stop in mixing movements provoke coagulation and coalescence, as the energetically more favourable lower surface-to-volume ration is naturally preferred. The water and oil phase separation begins. Such formulations are called kinetically stable. Macroemulsions have spherical droplets depending on the predominant phase and are formed according to the lowest surface/volume ratio. Kinetically driven processes lack available energy for overcoming big activation barriers prevailing for spontaneous reactions (final state of low system energy). Therefore, the least resistance, thus the lower required activation energy barriers is overpowered. Kinetic reactions are characterised by (1) low existing temperatures, (2) short reaction times or (3) are catalytically enhanced reaction types. By contrast, microemulsion formation is thermodynamically driven as enough energy is available to overcome desired energy barriers (Figure 3-1). Thermodynamic controlled processes are supported by high temperatures and long reaction times.

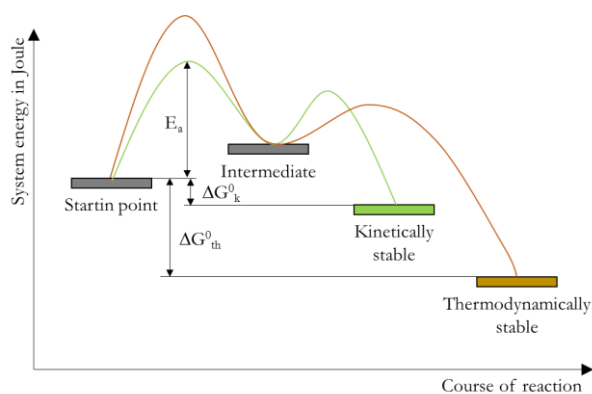


Figure 3-1 Thermodynamically and kinetically driven process

3.2.2 Critical micelle concentration and varying microstructures

When the amphiphilic surfactant is added to a single or multi-phase solution, the molecules first distribute across the liquid-air surface or the liquid-liquid interface. An increasing surfactant amount provokes a gradual reduction of the interfacial surface tension. This loss in surface tension follows the Gibbs adsorption isotherm (Bellmann, 2008). If more surfactant is added to water bulk solution it becomes energetically more favourable to aggregate as micelles inside the bulk phase. Micelles are not surface active and thus in the following course, the surface tension from this point – the so-called critical micelle concentration (CMC) remains nearly constant. Above the CMC, surfactant molecules keep forming micelle aggregates which shape and size changes e.g. with the surfactant type used. The polar head faces towards the aqueous phase. More specific, the micelle geometry changes with surfactant length (l_c), volume of aliphatic tail (v), effective head group area (a_0) and environmental conditions such as system temperature, pH value, conductivity (Figoli, 2001). By this mean, the critical packing parameter CPP (equation 3-2) has been defined to get a better quantitative idea of how the surfactant molecules aggregate as micelles.

$$CPP = \frac{v}{l_c \cdot a_0} \quad 3-2$$

As the ratio of the aliphatic tail volume to the effective head group area decreases with a bigger polar head, the amphiphilic surfactant aggregates in spherical configuration as it is energetically more favourable (for $CPP < 1/3$; Mehta and Kaur, 2011). Despite, surfactants form rod-like micelles at slightly higher CPP ($< 1/2$). High CPP are required for reversed rod-like micelles ($CPP > 1$). Lamellar micelle structures occur if the polar head relative to the aliphatic tail decreases further and the CPP becomes 1. For long nonpolar tails exhibiting small volumes relative to their length, the surfactant molecules tend to form a bicontinuous structure at $CPP \geq 1$. The Gibbs triangle phase diagram for multiphase components highlights possible formulations (Figure 3-2) and respectively shows micellar structures for the PBM used within this work (components listed in Table 4-1). Basic correlations between the CMC and the micellar structure has been clearly explained through transport and formation phenomena (Figoli, 2001).

For membrane coating application, in case of polymerisable microemulsions, a strong polymer layer at high porosity on top of commercial substrates is the suitable choice. In detail, a bicontinuous “sponge-like” structure offers both.

A high mechanical and chemical stability thanks to the highly interconnected water-polymer matrix as well as a high porosity emerging from the water which evaporates during the polymerisation process.

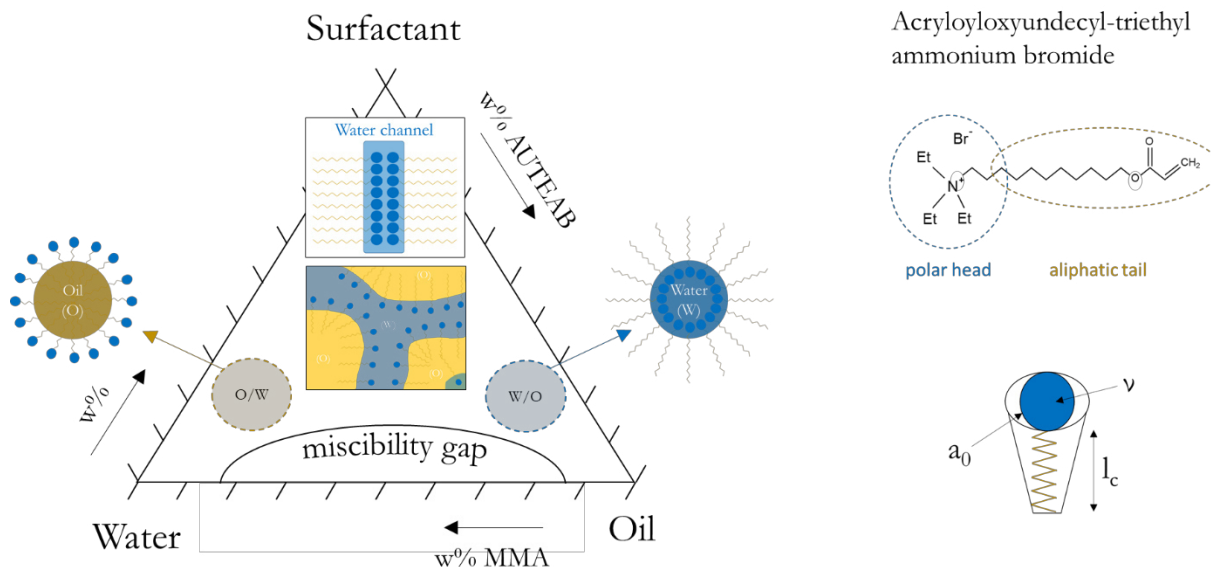


Figure 3-2 Gibbs triangle for multiphase components systems showing different micelle configurations for the PBM composition used within this work

A key challenge in applying microemulsion of a desired matrix lays in the identification of this very same. Gibbs triangles can be obtained by titration methods with occurring phasic regions identified for a specific composition. Many characterisation tools have been used for ultimate verification in case of quality control. Following a simple method, Gan et al. identified the three different microstructures W/O, bicontinuous and O/W microemulsion by conductivity measurements where the conductivity rapidly increased with increasing water ($1 \mu\text{S}\cdot\text{cm}^{-1}$) starting from 20 w% and dropped again at 70 w% (Gan et al., 1994). More accurate technologies are nuclear magnetic resonance (NMR) and infrared spectroscopy, small-angle X-ray scattering (SAXs), dynamic light scattering, neutron spin-echo spectroscopy or transmission electron microscopy (Najjar, 2012).

Microemulsion are highly dynamic systems and structural changes continuously appear resulting from molecule fluctuations (Krause, 2001).

3.3 Literature review

3.3.1 Microemulsion – scope of use

Microemulsion are mainly deployed for pharmaceutical use due to their affinity to carry hydrophilic (water soluble active) as well as lipophilic (oil soluble active) substances. This enhances solubilisation levels, biocompatibility and the skin-friendly appearance. They are an effective drug delivery system across the skin enabled through high skin permeability. For this reason, they are often used for dermal, transdermal and topical application.

The higher cumulative penetration quantity results in shorter treatment phases with reduced treatment costs and thus also less side effects. Concrete applications are: diabetic therapy, treatment of hereditary diseases such as androgenic alopecia, specifically breast cancer control due to a high anti-cancer activity, usage as anti-inflammatory agent and moreover as dexibuprofen for *E.coli* infections (Shukla T. et al., 2018). Kaur and Mehta focused their review on tween-based microemulsions and concluded research viewpoints investigating and evaluation the specific drug permeation, dissolution rate and adsorption capacity, also considering drug stability (Kaur and Mehta, 2017). Further reviews by Callender et al. conclude multi-drug delivery systems (to 79% lipophilic) targeting cancer treatment but also inflammatory and microbial infections as well as cardiovascular diseases (Callender et al., 2017).

The research of microemulsions as alternative fuels for compression ignition engines is going in a completely different direction. Diesel fuels are harmful since they emit exhaust gases irritating the mucous membranes and cause inflammations. In comparison, microemulsion fuels have shown reduced nitrogen oxide emissions (NO_x) and improved thermal efficiency due to the injected and vaporised water. These facts made microemulsion highly interesting as clean alternative to conventional fuels (Abrar et al., 2019). Starting in the 1970s with the first global oil crisis, microemulsion came under focus for enhanced oil recovery (EOR). Thereby, surfactant rich water is pumped into oleaginous rock to significantly reduce the interfacial surface tension and the oil is finally washed out from the geological structures. This procedure distinctly increases oil recovery relative to primary and secondary oil extraction methods (Paul and Moulik, 2001). A similar approach is used for environmental remediation for a highly efficient and eco-friendly soil washing. Thus, microemulsions are also a promising alternative to conventional soil cleaning and soil disposal.

Water-in-oil microemulsions (reverse micelles) are being used as lubricants within various industrial application. The water content compared to purely oil lubricants increases the heat capacity and therefore absorbs more heat, which is beneficial for reducing frictive dissipation in e.g. bearing cooling. Moreover, the surfactant can act corrosive inhibiting on top of common oil effects. Microemulsions are desired over macroemulsions due to thermodynamic stability required for CNC milling processes. Nevertheless, surfactant may cause corrosive reaction on the metallic surface wherefore its selection should be done with care (Paul and Moulik, 2001).

Applied to agrochemical use, microemulsions can help to reduce negative impact of solvent-based pesticides. As basic material for fertilizers, the entrapped oil solubilises trace metals, which can then be slowly adsorbed by plant leaves even under wet conditions as the oil sticks to leave surface. Used as detergent, the solubilisation of polar and nonpolar components is beneficial over traditional detergents based on organic solvents. Adding synthetic or natural additives can improve the washing performance by viscosity modification or temperature stability improvement (Nakajima, 2001). Microemulsions are also present in cosmetic applications e.g. giving the skin a nice and shiny glance. These products generally show faster uptake into the skin.

Incorporation of functional head groups contained in the surfactant makes microemulsions also attractive for hair care products by supplying certain vitamins to the applied area. For medical as well as body care products it is important to lower the applied surfactant to a minimum to reduce side effects as skin irritations (Nakajima, 2001).

Many more branches continuously seek for innovative products which could be covered by microemulsions due to their unique and unparalleled properties. The coating industry is a customer applying liquid microemulsion for high scrub resistant paints. Even more a high homogeneous coating layer with a better colour intensity also improves economic efficiency. Coatings of different kind have been realised using solid, polymerised microemulsions with excellent surface roughness and fast curing (Nakajima, 2001). These two reasons have resulted in further areas of application for microemulsions.

3.3.2 Polymerisable microemulsion systems in research and industry

Despite liquid microemulsions, solid (polymerised) microemulsions are formed as nano-particles or coating layers (Paul and Moulik, 2001). Polymerisable microemulsions are multicomponent systems forming a polymer architecture of strong covalent bonds after polymerising from the liquid into the solid state. The aim thereby is to preserve the micellar structure in the solid state. During polymerisation, the water evaporates leaving voids spaces in the polymer. In case of membrane modification using polymerisable bicontinuous microemulsion (PBM), the bicontinuous, and “sponge-like” porous structure is an additional selective layer on top of commercial membranes. In addition, solid plastic formation of nanoparticles is also a large field of application of PBM.

For the last decades, the interest in PBM has grown steadily. Various parameters affect the final polymer architecture and thereby the product quality. A beneficial change of polymer properties can be obtained by systematic and specific interference with the polymerisation propagation. For instance, Yan and Texer (2006) highlighted different ways to change the microstructure by temperature adaption and varying initiator amount. Moreover, Platkowski and Reichert (Platkowski and Reichert, 1999) successfully altered the polymer structure and polymer chain length of methyl methacrylate by polymerisation intervention (stopping and retarding) with the use of a strong radical inhibitor. In this way, Destarac (2010) created new plastic materials as customized modifications used for industrial application. Controlled or living radical polymerisation can be used to deliberately influence the chain transfer kinetics by atom transfer radical polymerisation (ATRP), reversible addition-fragmentation chain transfer (RAFT) or stable free radical polymerisation (SFRO). Different material properties can be obtained changing with each specific approach (Menter, 2000). The listed technologies will also serve as guideline for conducted pre-polymerisation experiments, further specified in chapter 4.3.2. Methyl-methacrylate polymerisation will be stopped and subsequently re-started in a targeted manner. The aim was to modify the viscosity of the PBM membrane coating material to reduce pore intrusion and improve the permeability.

Microemulsion sprays are mainly used for latex particle formation or combustion technologies (Paul and Satya, 2001; Narvaez et al., 2011). They gained more attraction for research activities and industrial application through studies carried out by Stiffer and Bone (1980). Focus was given on polymeric nanoparticle production of 10-100 nm size. Chew et al. (1998) first used polymerisable surfactants and incorporated them into the polymer chain. Mishra and Chatterjee (2011) achieved very homogeneous spray mists and droplet sizes resulting in reduced polymerisation times and material input of co-surfactants. Briceno-Gutierrez et al. (2015) and Balasubrahmanyam et al. (2006) reviewed spray coating application of common fluids. So far, no study is known giving strong emphasis on spray coating methodology used for PBM based membrane coatings.

So far, PBM coatings are still a niche sector for membranes modification. Li et al. (1997) produced PBM coatings for hollow fibre (HF) membranes by injecting a PBM directly into the fibres with subsequent REDOX polymerisation. Excess material was blown off between 1 and 5 min. Figoli took up the idea of forming PBM nanostructured liquid membranes for facilitated oxygen transfer based on the work by Gan et al. (1994; 1997). He examined the bicontinuous structure via conductivity measurements for different surfactants and co-surfactants. After polymerisation using UV-light and REDOX based initiation, he determined the polymerisation degree with weight loss measurements of the polymerised products (Figoli, 2001).

3.4 PBM modification based on UV-LED polymerisation

Within this thesis, the main surfactant used is the cationic, home-made acryloyloxyundecyldiethyl ammonium bromide (AUTEAB) with an ammonium bromide tail which is known to be antimicrobial (Mancuso et al., 2017). Unlike many other surfactants used for forming microemulsions, the AUTEAB is polymerisable and thus covalently bound into the PBM matrix. The co-surfactant 2-hydroxyethylmethacrylate (HEMA) entails a hydroxyl group (-OH) giving a more hydrophilic property (Rahimpour and Madaeni, 2010). Moreover, by adding the cross-linking agent ethylene glycol dimethacrylate (EGDMA), it promotes a thermodynamically stabilised microemulsion. The bicontinuous micelle structure is given by the water-surfactant-oil composition according to the tertiary phase diagram in Figure 3-2. Through the polymerisation, the coating layer forms a solid interconnected polymer matrix of bicontinuous “spong-like” structure with the benefit of being a high resistant coating with meandering shaped pores (Galiano et al., 2015).

Polymerisation becomes possible due to the reactive nature of the C=C double bond present in each component (other than DI-water) added to the microemulsion solution (composition listed in Table 4-1). In the process, monomers react with a previously induced radical and combine with a second monomer, finally forming the polymer network of finite number of monomers. The process initiation starts when an energy allowance is induced to overcome the activation energy for the specific molecule (initiator). Once this barrier is taken, the reaction is self-accelerating, supported by the increasing temperature as the exothermal process releases heat (Weiss, 1966, Stefan).

The two most relevant industrial polymerisation reactions are ionic polymerisation divided into cationic, anionic initiation and chemical reactions activated by radical formation. Industrial applications commonly desire radical polymerisation processes over ionic reaction types due to their higher thermal stability (Wicks et al., 2007). By reasons of temperature susceptibility of the PBM formulation due to weak C=O double bonds, this work is based on radical polymerisation only.

3.4.1 Radical polymerisation

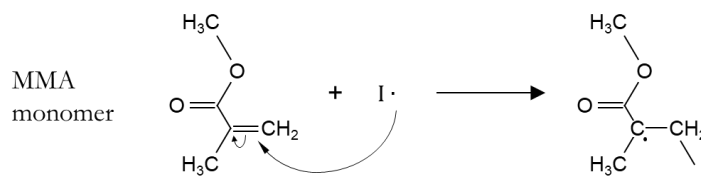
For the radical induced polymerisation, the chemical reaction starts either with a chemically induced radical decay or by light activation according to $h\nu_E$. Dependent on the principle used the solubility of the initiator changes. REDOX initiators are water-soluble whereas the used photo initiator (Table 4-1) has high solubility in the monomer phase. This could change the overall polymerisation time as the radicals for REDOX initiation first diffuse into the oil-swollen micelles before monomer chain growth can start (O'Donnell and Kaler, 2007).

Basic radical polymerisation follows the process sequences pointed out in more detail below. Divided into the individual propagation steps, a polymerisation propagation for methyl methacrylate (MMA) to solid polymethyl methacrylate (PMMA) is shown which is representative for the substances used herein.

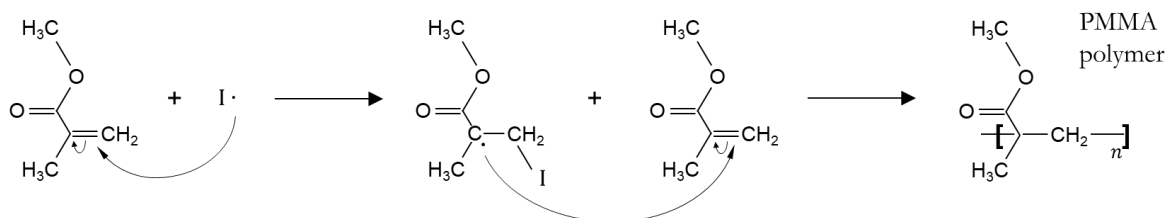
- (1) The activation of the initiator I (radical formation) by high energetic UV-LED light



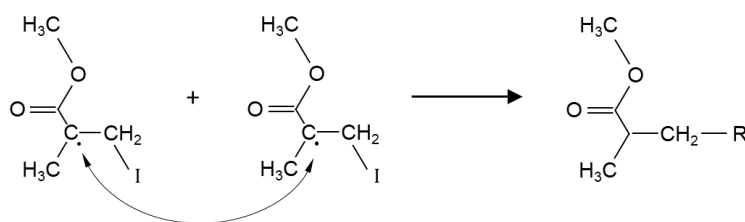
- (2) Initiated radical attacks the double-bond of a monomer (chain growth initiation)



- (3) Monomer-radicals further attack monomers resulting in a progressively growing polymer chain (propagation)



- (4) A polymer or monomer-radical attacks a chain transfer agent (chain transfer)
- (5) Two radicals, either an initiator or monomer, recombine (termination and disproportionation)



Ultimately, the resulting polymer structure comprises of many repeating, covalently bonded molecules of different molecular weight forming a very strong network.

3.4.2 UV-LED light induced polymerisation

UV light induced polymerisation has become indispensable for many technical applications thanks to the highly energetic radiation. Curing time for e.g. varnish and paint is thus reduced on a minimum. Reservations about an environmentally harmful technologies have been dispelled by introducing eco-friendly UV-LED light sources which more and more replace the outdated mercury (Hg) lamps. Mercury lamps emit wavelengths in a wide spectrum at temperatures up to 900°C and more (Hubergroup, 2012). After a long warm-up period, the highly toxic mercury is present as vapour phase and produces ozone during operation. First developments towards more ecologically friendly techniques have been realised by mercury emitter doping with iron (Fe), gallium (Ga), lead (Pb), cobalt (Co) or indium (In). In this way, a narrower emitting wavelength range at higher radiation energy is achieved. A reduction in operating temperature and shorter warm-up times ultimately lead to much lower energy consumptions. Nowadays, UV-LED radiators are state-of-the-art thanks to their outstanding performance and high efficiency. Based on semiconductor electronic, light emitting diodes (LED) are monochromatic radiators emitting wavelengths of only a very narrow range. UV-LEDs do not require any start-up time, have high specific energy consumptions thanks to a minimum heat generation and show considerably longer service life (Hubergroup, 2012). The emitting wavelength depends on the applied voltage which is unique for a specific semiconductor material. Common spectra range between 365 and 405 nm (Figure 3-3). The emitted wavelength penetrates into the polymerisable body superficial or deeper. Short-wave high-energy UV-C light (according to $E \sim \lambda^{-1}$) acts superficial whereas long-wave lower energetic UV-B and UV-A light penetrates into deeper areas (Wicks at al., 2007).

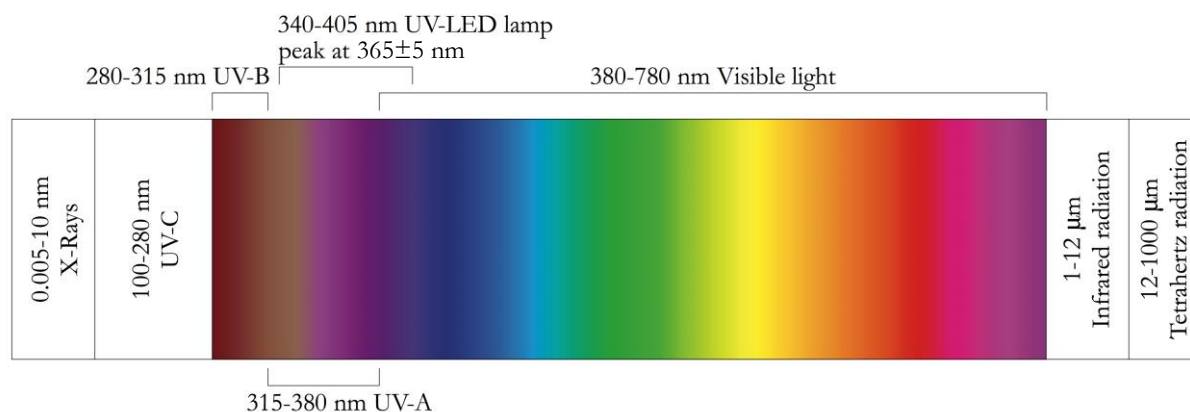


Figure 3-3 Spectral colours of electromagnetic radiation, UV-LED classification

Substances reflect and absorb spectral light at a distinct wavelength being characteristic for each molecular structure (Stowe, 1999). Substances with similar spectral absorptivity interfere with each other and the light stimulates all more weakly. In respect of PBM coating, this can be detrimental for polymerisation activation if different molecule absorptivity overlaps the absorption band of photo initiators as it reduces the intended activation energy. By this mean, components must be harmonised with each other for best radiation and thus polymerisation results. The adsorptive capacity of basic PBM component must diverge from the photo initiator which was validated first by UV/VIS spectrometry (Schmidt, 2016). Spectral analysis was executed to prevent interference above >360 nm for all components. In contrast, photo initiator with highest absorption capacities inside an emitting range of 365 ± 5 nm was selected for extensive polymerisation investigations (Schmidt, 2016). For specific UV-LED specifications see chapter 4.1.3.

3.4.3 Basic elements for the work carried out

In case of the herein used PBM composition (Table 4-1) and the targeted membrane coating layer, suitable UV-LED lamps and photo initiator were examined by Schmidt (2016) to select best-case options in terms of fast and complete PBM curing. Specifically, Schmidt worked on evaluating suitable UV-LED radiators being able to evenly irradiate big areas defined by the membrane area, given with ~ 0.11 m² (0.515 x 0.22 m). Oxygen inhibition generally occurs during polymerisation reactions if performed under atmospheric conditions. Oxygen molecules (O₂) react with available radicals during the polymer chain growth propagation and prevents or slows down further combination reactions (Wicks et al., 2007). Therefore, final polymerisation experiments were done under inert (N₂) conditions. Consequently, a closed environment was realised by a glovebox with inflated, dry nitrogen to keep the oxygen level on a minimum below <1 w%.

Schmidt (2016) tested potentially suitable initiators on their adsorption capability within the emitting wavelength of 365 ± 5 nm. In general, photo initiators can be distinguished on their initiation type, e.g. by molecule decay forming two radicals through α -splitting (Norrish type I) and initiators abstraction hydrogen atoms from adjacent molecules (Norrish type II, Hartley and Guillet, 1968). For this work, only Norrish type I was relevant. Schmidt did visible preliminary investigations to first evaluate the monomer/aqueous solubility and their influence on PBM transparency.

After pre-screening, Fourier transform infrared spectroscopy (FTIR) measurements were used to quantify the polymerisation degree for the PBM containing the pre-selected photo initiators.

As all used components contain the polymerisable C=C double bond (see Table 4-1), the reduction of R-C=CH₂ double bond indicates the polymerisation degree of the microemulsion formulation. In specific, during polymerisation, the R-C=CH₂ bond is converted into new R-CH₃ single bonds (section 3.4.1). Through the assessment of the R-H₃C/R-C=CH₂ conversion ratio the potential polymerisation capability could be evaluated. References were 0% (or “0” as liquid) polymerisation conversion and 100% (effectively “1” for solid) ensured with considerable long irradiation times, a high initiator amount and conducted under completely inert conditions. Conversion rate experiments were evaluated using peak interpolation within the reference range which corresponded to the specific polymerisation degree (Schmidt, 2016).

Finally, the best suitable photo initiator showing highest efficiency and effectiveness was selected. The initiator 1-Hydroxy-cyclohexyl-phenyl-ketone (Irgacure 184) is commonly used within a wide range of industrial applications and commercially available (BASF, 2012). These findings were taken as basis for the following polymerisation and membrane coating experiments within this thesis.

Previous layer coating was done by manual casting coating. As part of this work, an advanced coating technology was identified and evaluated. A big challenge for the implementation was the existing setup which limited the technology selection for PBM coating upscaling. In specific, the existing glovebox for inert conditions gave only very narrow useable space for the coating process. The glovebox outer dimensions were 1050 x 913 x 1000 cm (W x H x D). The commercial PES membranes had big rectangular areas of around 0.11 m² which excluded spin coating techniques (see chapter 2.5.3). Dip coating requires high amounts of liquid coating material for such big sample bodies. The PBM used contains the home-made AUTEAB surfactant, which was produced in the laboratories of the University Calabria. Production of small batches and manual synthesis greatly increased expenditures. The use of dip coating would cause huge scrap amounts and require big space for the coagulation bath. Therefore, only casting and spray coating were considered for producing large membrane coating quantities.

Casting coating is a simple technology, easy to handle and simply implemented into an automated coating machine, described in detail in chapter 4.3.3. Prior to upscaling, the spiral casting knife was compared with a casting coating applicator. Casting coating using a spiral casting knife was mainly used for preliminary experimental, PBM viscosity modification approach and the coating upscaling for pilot scale tests treating domestic wastewater. Limitations of this technique will be highlighted and the optimum parameters determined. Coating experiments done by spiral casting knives were:

- AUTEAB modification comparing the PBM coating quality
- Comparison of different casting coating knives
- PBM viscosity modification through controlled radical polymerisation
- Final membrane upscaling within the VicInAqua project for treating real domestic wastewater.

Spray coating technology represents a novelty in PBM membrane coating application. Therefore it was the objective to first deepen the knowledge about fundamental principles and identifying connected challenges. Atomisation brings many benefits for surface coating and is state-of-the art for many industrial processes. Studies about spray coating focused on:

- Approximate spray coverage for different fluids
- Spray coating layer surface characterisation using FTIR measurements
- Model foulant tests using humic acid and comparison with the casting coating method

Microemulsions are multi-phase components having many advantages over traditionally used liquids. Amphiphilic surfactants extremely reduce the interfacial surface tension and thus enable the miscibility of an oil and water phase. The result is a thermodynamically stable system of very small droplets. Polar as well as nonpolar properties combined with the possibility of incorporating numerous functional groups are the reason for this wide-spread technology. Added substances to the microemulsion mainly decide over the final performance characteristic. If polymerisable components are used and solidified on top of commercial membranes for water treatment application, fouling properties can be modified leading to a more sustainable filtration operation.

This thesis emphasises the polymerisation of PBM coating layers through UV-LED curing on top of UF PES membranes. Schmidt (2016) selected the most suitable photo initiator Irgacure 184 with an optimised 1.8 w% material input for complete polymerisation. The light activated initiator attacks C=C double bonds of monomers and initiates the polymer chain growth propagation. Irgacure 184 is oil-soluble and curing takes only seconds enabled by high irradiation intensities resulting in fast radical formation (Andrzejewska, 2015; Galiano et al., 2018). This basically enables large membrane coating quantities. However, first attempts using UV-LED induced polymerisation resulted in poorer membrane performance in terms of permeability. Despite a satisfying permeability, the REDOX curing time is significantly higher (>20 min) than for UV-LED activation (<60 s). This is the major benefit and reason industrial branches utilise UV-LED rather than REDOX polymerisation.

Therefore, it was part of this work to identify weak points and potentials of the photo-initiated PBM polymerisation. PBM coating upscaling from lab scale to pilot scale was defined as the target with highest possible permeability. Membrane coating for large scale application is challenging due to many facts. Published work on membrane coating are almost exclusively limited to small and lab scale application. Reasons were lacking reproducibility, disproportionally high costs in the course of upscaling or occurring technical issues during the implementation (Bae and Tak, 2005; Yu et al., 2005; Asatekin et al., 2006). In theory, four coating technologies were identified each having advantages over the other for specific application. Two methods were selected for extensive lab trials to establish a sustainable technology for best possible PBM coating results. An attempt of modifying the PBM properties will be discussed to improve the coating layer quality in regards of filtration capacity. Ultimately, a comparison between the used coating technologies as well as modified and reference PBM will be drawn.

So far, upscaling of UV-LED based PBM membrane coatings has not been realised. For conducted pilot scale experiments, membrane modules of in total 3.125 m² surface area were coated and tested in a submerged MBR treating domestic wastewater. The data yielded will be highlighted and assessed further within chapter 4.3.4 and 6.3.

4 Materials and Methods

The characteristics of the complex polymerisable bicontinuous microemulsion are defined by its precise chemical composition. Therefore, its application demands a tight production window. A better understanding of the polymer chemistry behind the coating process and the determination of material parameters is mandatory. An appropriately adaption of the PBM solution could help to achieve the coating properties demanded. The following chapter 4 describes prevailing preparation conditions and drafts the tools employed to study and investigate PBM membrane coating layers. With the aim upscaling, different ways to improve the performance of the coated membrane are proposed and later on evaluated. The basic membrane coating approach takes up previous examinations and considerations to achieve a long-lasting, efficient low-fouling membrane. Considerations have been adjusted from the work of Schmidt (Schmidt, 2016).

- The first part, **section 4.1** lists all the chemicals and materials used within this thesis. The exact PBM composition is shown for achieving transparent, thermodynamically stable bicontinuous formulations. Potential sources for production variances arising from systematic as well as random preparation and measuring errors are highlighted. Production tolerances also result from the UV-LED lamp operation settings which was used to polymerise the liquid PBM layer.
- **Section 4.2** deals with the characterisation of liquid as well as solid PBM and governs important material parameters. Ways to alter the PBM viscosity are discussed with the aim of reducing existing occurring membrane pore intrusion.
- **Section 4.3** includes the equipment used for PBM membrane characterisation. The investigation of molecular composition was carried out to identify successful polymerisation and determine the chemical stability of a solid PBM layer on top of the used UF PES membranes. Some analysing tools were used to acquire the membrane surface texture which is in important specification in regards to low-fouling behaviour. A possible way to quantify the pore intrusion depth is highlighted. Derived experimental setups are further highlighted. Laboratory setups for casting coating application are followed by an assembly to investigate the polymerisation propagation and to develop a protocol for successful PBM viscosity modification.

An automated casting coating machine was established necessary for coating upscaling. Subsequently, the pilot scale MBR is shown which was built up in order to test the novel PBM coating under real conditions treating domestic wastewater. Last of all, an automated spray coating unit is described in detail to achieve improved PBM coatings of higher permeability on lab scale.

4.1 Materials used

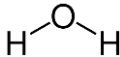
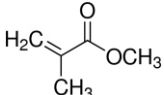
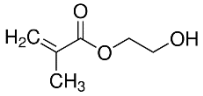
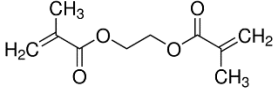
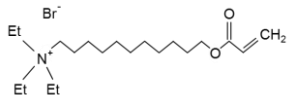
All chemicals used within the conducted work are specified and listed within the section. It is the aim to point out the systematic and measuring errors occurring in the overall process of PBM membrane coating. Starting with the chemical purities, the pipetting error affects the micellar formation according to the Gibbs phase diagram (Figure 3-2). Measuring errors occurring during the casting coating process are based on user handling, casting coating equipment and production tolerances of the UF PES membrane. Environmental influences will be further highlighted in section 4.3.

4.1.1 PBM composition

Table 4-1 and Table 4-2 list all chemicals required for forming the PBM formation: (1) the basic PBM components; (2) the photo initiator which was activated by UV-LED light; (3) chemicals used for REDOX initiation. APS radicals were activated by TMEDA; (4) the strong radical inhibitor TEMPO for stopping/retarding the polymerisation reaction.

Galiano et al. (2015) and Deowan et al. (2016) extensively studied REDOX initiation applied for PBM membrane coating. Within this work, only PBM viscosity modifications were done by REDOX initiation, further explained within chapter 4.3.2. Other examinations as well as re-initiation were done with the photo-initiation Irgacure 184, activated by UV-LED light. The TEMPO inhibitor was added in case of the viscosity modification approach only. All acrylates contain a C=C double bond and are also present in the home-made AUTEAB surfactant. Chemicals with this bond can be polymerised and since all listed products participate in the polymerisation reaction, a strong covalent polymer network was formed. Another characteristic bond present in the PBM components is the C=O bond. This will be used as characteristic fingerprint for identifying the polymerised PBM layer on top of the commercial PES membrane by using FTIR spectroscopy.

Table 4-1 Chemicals used for PBM preparation and their share of total mass

Substance	Acronym	Function	Mass fraction	Structure
Distilled water ¹	DI water	Water phase	41 w%	
Methylmethacrylate ¹	MMA	Oil phase	21 w%	
2-hydroxyethylmethacrylate ¹	HEMA	Co-surfactant	10 w%	
Ethylene glycol dimethacrylate ¹	EGDMA	Cross-linker	3 w%	
Acryloyloxyundecyltriethyl ammonium bromide ¹	AUTEAB	Main-surfactant	25 w%	

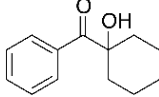
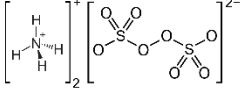
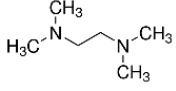
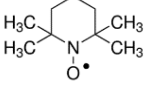
1-Hydroxy-cyclohexyl-phenyl-ketone ²	Irgacure 184	Photo initiator	1.8, 2.3, 5 w%*	
Ammonium persulfate ³	APS	REDOX initiator	0.12, 0.3 w%*	
N,N,N',N'-Tetramethylethylene-diamine ³	TMEDA	APS activator	2.7 w%*	
2,2,6,6-Tetramethyl-1-piperidinyloxy ⁴	TEMPO	Inhibitor	max. 0.1 w%*	
*of total PBM mass				

Table 4-2 Chemicals used within this work, purity and molecule information

Substance	Molecular formula	Molecular weight	CAS number	Purity
Distilled water	H ₂ O	18.02 g·mol ⁻¹	Millipore	<1.6 μS·cm ⁻¹
Methylmethacrylate	C ₅ H ₈ O ₂	100.12 g·mol ⁻¹	80-62-6	99%
2-hydroxyethylmeth-acrylate	C ₆ H ₁₀ O ₃	130.14 g·mol ⁻¹	868-77-9	≥99%
Ethylene glycol dimethacrylate	C ₁₀ H ₁₄ O ₄	198.22 g·mol ⁻¹	97-90-5	98%
Acryloyloxyundecyl-triethyl ammonium bromide	C ₂₀ H ₄₀ BrNO ₂	406.45 g·mol ⁻¹	Home-made	>90%
1-Hydroxy-cyclohexyl-phenyl-ketone	C ₁₃ H ₁₆ O ₂	204.26 g·mol ⁻¹	947-19-3	99%
Ammonium persulfate	H ₈ N ₂ O ₈ S ₂	228.20 g·mol ⁻¹	7727-54-0	≥ 98%
N,N,N',N'-Tetramethylethylene-diamine	C ₆ H ₁₆ N ₂	116.20 g·mol ⁻¹	110-18-9	~99%
2,2,6,6-Tetramethyl-1-piperidinyloxy	C ₉ H ₁₈ NO	156.25 g·mol ⁻¹	2564-83-2	98%
Humic acid (HA), crystalline powder	Not specified	Not specified	1415-93-6	min. 95%
Ethanol	CH ₃ CH ₂ OH	46.07 g·mol ⁻¹	64-17-5	≥99.8%
1-Octanol	CH ₃ (CH ₂) ₇ OH	156.25 g·mol ⁻¹	111-87-5	99%

All chemicals except the AUTEAB surfactant and DI water were purchased from *Sigma Aldrich* with the given purities shown in Table 4-1. AUTEAB is a home-made surfactant, synthesised by the *Department of Chemistry and Chemical Technologies* at the University Calabria in Rende (CS), Italy.

AUTEAB synthesis was done on a small scale in the laboratory and the production is time consuming and costly. Although the AUTEAB surfactant contributes to 25% of total PBM weight, its production costs represent nearly 80% of the total PBM costs considering small batch production².

² Excluding personnel costs

Therefore, cutting down on its price plays a fundamental aspect in the preparation and application of the PBM coating. A detailed execution of the AUTEAB synthesis can be found in the work of Galiano (2013). As part of the European funded project VicInAqua (2019), the AUTEAB production time was reduced through the elimination of an additional chromatographic purification step. During synthesis, to avoid spontaneous polymerisation, reaction steps contain the inhibitor 2,6-Di-tert-butyl-4-methylphenol (BHT). If not entirely removed, BHT could slow down or prevent polymerisation of the PBM. Additionally, a non-inert esterification (instead of inert) lead to further reduction in operating resources such as pressurised nitrogen and hermetical equipment. Through substituting the classic with this new modified AUTEAB, PBM costs could be reduced by over 50% (excluding workload). However, cost reduction must go hand in hand with an acceptable and sufficient product performance.

Different in purity, both synthesised surfactants will be compared by CAM, AFM and membrane performance tests using humic acid as model foulant. The evaluation will be further discussed in chapter 1. Polymerisation for both, the PBM prepared with the classic and the modified AUTEAB, were activated with the photo initiator Irgacure 184. The amount was slightly increased for the modified AUTEAB to compensate the higher impurities and obtain a similar polymerisation potential.

4.1.2 Pipetting errors and membrane properties

As stated, micellar structure changes with not only surfactant type and chemical properties but also with the microemulsion composition according to the Gibbs phase triangle. Not in focus of this research but for completeness, measurement deviations for pipetting and weighing are shown. Relative systematic and random measurement deviation of the pipettes used are listed in Table 4-3. All pipettes were purchased from *Eppendorf* (type *Research Plus*) with a maximum pipetting volume of 20 μL , 1,000 μL and 5,000 μL , respectively. To minimise the influence of pipetting deviation, at least 10 g PBM was prepared and stored in a dark, and cold place. The initiator was added just prior to the coating to prevent polymerisation inside the glass vessel.

Table 4-3 Pipetting errors for PBM preparation

Pipette volume	Rel. systematic deviation	Rel. random deviation
20 μL	$\pm 1.0\%$	$\pm 0.3\%$
100...1,000 μL	$\pm 0.6\%$	$\pm 0.2\%$
500...5,000 μL	$\pm 2.4\%$ (500 μL) $\pm 1.2\%$ (2,500 μL) $\pm 0.6\%$ (5,000 μL)	$\pm 0.6\%$ (500 μL) $\pm 0.25\%$ (2,500 μL) $\pm 0.15\%$ (5,000 μL)

An analytic balance (Denver Instruments) with a measuring resolution of 0.1 mg was used for weighing the solid substances AUTEAB, APS and TEMPO with weighing paper. Deionised water for PBM preparation had a conductivity of $<1.6 \mu\text{S}\cdot\text{cm}^{-1}$ (Millipore 3 UV, Direct-Q).

The membrane substrate has a high influence on the achieved coating layer quality. Membrane production is complex and the product properties can only be controlled within a certain area.

Thus, differences in coating layer characteristics were smaller or more severe. Table 4-4 shows the commercial UF PES membrane which was used as a coating substrate throughout all the conducted experiments.

Table 4-4 Product specification of UF PES membrane FM10 (*Martin Systems*) used as coating substrate

		Acronym	Unit	Value
Membrane material	Polyether sulfone	PES		
Backing material	Polyethylene/polypropylene	PE/PP		
Separation	Ultrafiltration	UF		
	Molecular weight cut off	MWCO	kDalton	150
Properties	Pore size, nominal	$d_{m,nominal}$	nm	35
	Pore size, maximum	$d_{m,max}$	μm	0.1
	Thickness	s_m	μm	230 ± 20
	Retention capability ^A	$\Delta C_{feed-permeate}$	%	90-98
	Permeability ^B	WP	$\text{L}\cdot\text{h}^{-1}\cdot\text{m}^{-2}\cdot\text{bar}^{-1}$	≥ 285
Allowable operation conditions	pH range	pH	-	0-14
	Processing temperature	T	$^{\circ}\text{C}$	5-95
Membrane sheet	Length	L	mm	515
	Width	W	mm	220
^A polyvinylpyrrolidone NKY® ^B clean water at 20°C				

4.1.3 Casting coating tool and UV-LED lamp

4.1.3.1 *Casting coating tool*

There are various casting coating applicators on the market, each suitable for a specific application. In the majority of cases, casting coating is used for single-component liquids spread over a dense, and solid support. For PBM membrane coating, a multiphase mixture is spread over a highly porous and soft membrane making the selection of best equipment more difficult. More specifically, a coating applicator with varying wet layer thickness (*ZUA 2000, Zehntner*) was compared with a spiral casting knife with a fixed $4 \mu\text{m}$ wet layer thickness (*AB305X, TQC*), depicted in Figure 4-1. The coating applicator offered the possibility to precisely change the wet layer thickness with two fine threaded adjusting screws. Possible layer thickness of the universal-applicator ranged between $0 \dots 3,000 \pm 10 \mu\text{m}$ with a 200 mm maximum film width. However, for PBM application and comparison with the spiral casting knife, the thinnest possible wet layer thickness was preferred.

The spiral casting knife has a fixed wet layer thickness but separate casting knives are available for $4 \dots 300 \pm 2 \mu\text{m}$ (different gradations) at wide coating areas up to 320 mm. The final wet layer thickness of a liquid casted on top of dense materials such as glass does not match the set value. For instance, Newtonian liquids settle and keep deforming after the shearing process.

For the spiral casting knife (*TQC*) with a spiral thickness of $8 \pm 2 \mu\text{m}$, the estimated wet layer thickness is $4 \mu\text{m}$ according to the manufacturer's information. For the universal-applicator (*Zehntner*), the final wet layer thickness is around 60% of the adjusted knife gap. However, data about the supplier's testing procedure including testing liquid and environmental conditions are confidential and therefore not further specified. Production tolerance also varies for the casting tools and the minimum possible gap height found for $17.5 \mu\text{m}$ for the coating applicator

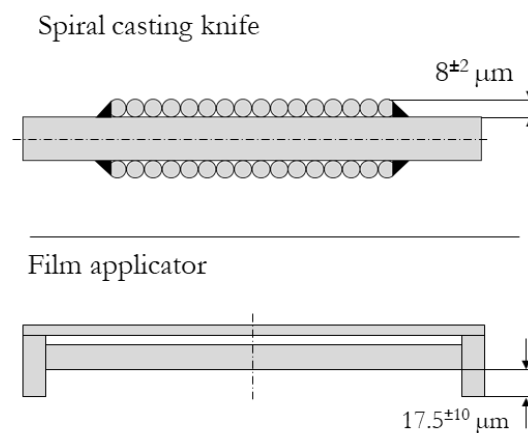


Figure 4-1 Schematic of cross section of the two used casting tools

4.1.3.2 UV-LED lamp

As verified extensively by Schmidt (2016), the air cooled UV-LED lamp, Series L (*Opsytec Dr. Gröbel*), offers suitable specific irradiation intensities for PBM coating application. The customised 250 x 550 mm exposure area emits a wavelength range of $365 \pm 5 \text{ nm}$. The spectral irradiance (Figure 4-2) matches the absorption band of the photo initiator Irgacure 184. The irradiation intensity changes with distance to the exposure area. Within the first 10 mm, the intensity drops significantly from 425 to $250 \text{ mW} \cdot \text{cm}^{-2}$ whereas at further distances, the slope reduces to around $0.4 \text{ mW} \cdot \text{cm}^{-2}$ per mm distance. Smallest exposure distances for highest possible irradiation intensities were desired to enable fast and effective PBM coating layer curing. Below the “critical” 4 mm, the membrane risked to stick to the UV-LED lamp due to slight curling effects.

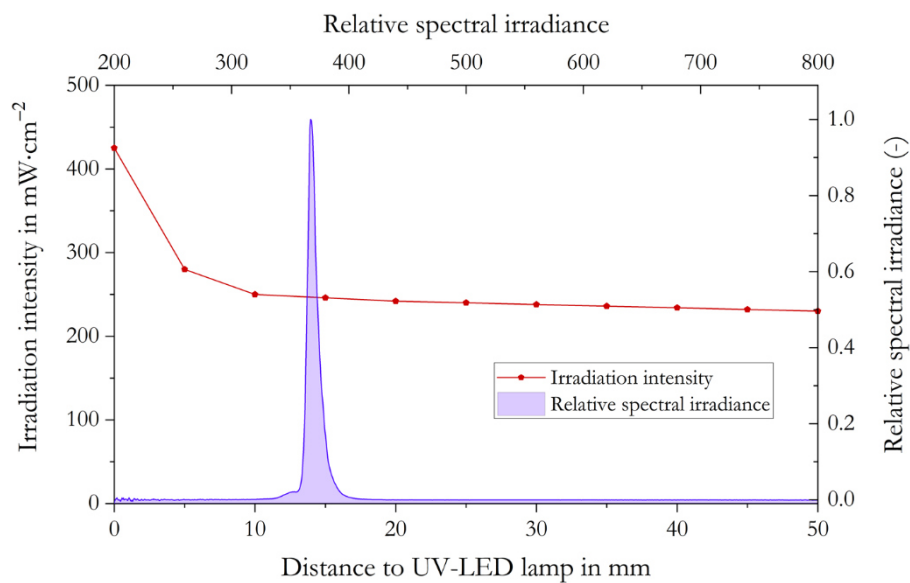


Figure 4-2 Characteristic of UV-A lamp used for PBM polymerisation (*Opsytec Dr. Gröbel*)

Throughout this thesis, polymerisation was executed at a 4 mm distance with $300 \text{ mW}\cdot\text{cm}^{-2}$ irradiation intensity. For all the experiments carried out, pressurised, dry nitrogen (N_2) was used with a $\geq 99.8\%$ technical purity including noble gases (DIN EN ISO 14175:N1).

4.2 Characterisation methods

4.2.1 Rheology

Rheological investigations were done using a rheometer (*HLAAKE RheoStress 1, Thermo Fisher Scientific*) with a 1° slope angle titanium cone with a 35 mm cone diameter. For the experiments, a Peltier element controlled the temperature of the measuring plate within $20 \pm 0.5^\circ\text{C}$. After dosing 0.25 mL of liquid PBM sample, a second tempering phase minimised temperature effects during the measurement procedure. Measurements followed a stationary step profile applied for precise measurements in equilibrium state. Incremental steps started from zero uniformly increasing the shear rates up to $7,000 \text{ s}^{-1}$ with an in total of 25 measuring steps. For one incremental step, the shear rate was taken after oscillation at constant conditions ($\Delta\dot{\gamma} \pm 0.05 \text{ s}^{-1}$). Maximum shear rate was maintained for 6 s before the cycle repetition in the same manner from $7,000 \text{ s}^{-1}$ to standstill. Total time of the experiment was 600 s. If the taken measuring points resulted in a linear curve when fit into logarithmic scale axis, PBM was a Newtonian fluid. Non-Newtonian fluids can be identified if changing viscosities for different shear rates occur. However, exact examination of experimental results is difficult for very liquid fluids such as water or PBM. The measuring signal is low and outer influences such as vibrations or random measuring errors become more significant. Further details will be given in chapter 6.2.2.

4.2.2 Modifying PBM viscosity

Pore intrusion is an effect limiting the membrane performance along with the coating layer thickness. Apparent into equation 2-11 three options can be excerpted to reduce the PBM penetration potential.

- (1) By lowering the surface tension between the solid surface (PES) and the wetting liquid (PBM)
- (2) By reducing the mean pore radius of the coating substrate
- (3) By increasing the density or dynamic viscosity of the PBM coating material

The complex nature of PBM limits implementation of option (1). First, adding components to the multiphase system could cause changes in microemulsion formulation according to the tertiary Gibbs triangle (Figure 3-2). E.g. nanoparticles represent impurities possibly interacting with the interfacial region of the water and oil phase. Depending on polar or nonpolar behaviour, different strategies can be pursued. The interplay between all the components remain unclear and is not predictable at this point. Further, altering the surface tension will not be part of this research. Option (2) was not feasible. The membrane substrate was delivered by the manufacturer (*Martin Systems*) who only offered a limited portfolio. UF membranes with smaller pore sizes and filtration properties were available only for different applications. This work aimed at UF membranes characterised by average pore diameters of 35 nm for wastewater reuse. A substitution with other substrate materials changes the electrostatic attraction between substrate and PBM due to different partial surface charges. This alters the material stability properties of the layer bonding and would require additional research capacity. In contrast, modifying the dynamic viscosity of PBM was a core element of this work (option (3)). A change in viscosity does not necessarily change the micellar structure.

However, if adding additives, either water or oil-soluble, the same uncertainties remain. The impact on the bicontinuous formulation is not trivial to solve.

A second strategy was found to be more relevant. Controlled radical polymerisation was studied as an innovative approach for viscosity modification. Controlled radical polymerisation describes ways to actively intervene polymerisation reactions to achieve desired intermediate products, e.g. for better storage properties. A precise change of molecular structure can be done by adding or removing molecule sequences. If modifying the PBM viscosity, the only additive used was an inhibitor to stop the chain transfer reaction after the PBM preparation and in chemical bound inside the polymer network. Further interactions with adjacent molecules were considered as not relevant. However, retarding or complete reaction stop can have major influence on the reaction product and polymer structure. Platkowski and Reichert (1999) investigated controlled retarding and stopping polyacrylic polymerisation by using 4-Hydroxy-Tempo inhibitor. The outcomes were used for a mathematical model development to predict polymerisation propagation and product structure. Menter (2000) altered the molecular chain length by changing the type and amount of photo initiator. Thereby, higher initiator amounts increase radical formation leading to shorter molecule chains and a highly linked polymer network. Moreover, diverse initiators of different activation potentials also affect the polymerisation speed, thereby significantly changing the final polymer structure.

With this in mind, investigations on how to adapt controlled radical polymerisation to PBM coatings were commenced. Controlled radical polymerisation holds the possibility to control the polymeric chain growth and thus the interconnected strong network. As the polymer chain changes in length, the polymer mesh is more or less dense which corresponds with the final porosity and ultimately the permeability of PBM coated membranes. This makes controlled radical polymerisation a useful tool for tailoring the coating layer to a desired point. Concretely, the process was initiated with REDOX chemicals (Table 4-1). After first using chemical initiators for the reaction start, the polymerisation was interrupted by adding inhibitor radicals. An intermediate chain termination provoked a higher molecular weight through formation of monomers into oligomers. Higher molecular weight refers to higher density and thus increased dynamic viscosities (Flory, 1939; Peticolas and Watkins, 1957). Supplementary, casting coating was carried out and finally cured by UV-LED light. Critical for this approach was the mutation of molecular structure which was likely to change with polymerisation interruptions and denser, highly interconnected polymer networks were expected.

Coatings were performed with the existing 4 μm spiral casting knife (*TQC*). Various coating attempts have been conducted and tested on their performance regarding permeability, visual examination of fouling behaviour and dynamic viscosity prior to the coating. How this contribute to the final membrane performance and correlate with the dynamic viscosity is discussed in chapter 6.2. A detailed elaboration of the test setup is shown in 4.3.2.

4.2.3 Surface tension measurements

Surface tension measurements were carried out using the pendant drop method (*OCA 15EC, DataPhysics Instruments*).

The measurement window ranges from 0.01-2,000 $\text{m}\cdot\text{Nm}^{-1}$ with a $\pm 0.01 \text{ m}\cdot\text{Nm}^{-1}$ accuracy. Calibration of the instrument was first done with DI-water (Millipore, $< 1.6 \mu\text{S}\cdot\text{cm}^{-1}$) also to confirm existing literature values. The dosing rate was set to the lowest suspending rate of $0.1 \mu\text{L}\cdot\text{s}^{-1}$ with a 1 mL disposable syringe (*SNP-D 183/136, DataPhysics Instruments*) and a 1.83 mm outer diameter ds. Dosing was stopped shortly before the drop dripped off from the capillary tip. Dynamic measurements started and the surface tension was calculated continuously. For DI water with a high surface tension, the measurement duration was prolonged since a higher volume could be suspended before drop separation due to higher surface forces (Saad et al., 2011). For the lower expected surface tension of the PBM (see chapter 3), higher sampling rates were chosen as the suspended volume and thus time of experiment was significantly shorter. Finally, DI water was measured with a 1 s^{-1} and the liquid PBM with a 5 s^{-1} sampling rate. Ambient temperature of the laboratory was constantly around $21^{\pm 1}\text{C}$. The *OCA 15EC* provided a database including various liquids but does not include the herein used PBM solution. Therefore, surface tension calculations were done with benzyl alcohol which has comparable properties for density $1.04 \text{ g}\cdot\text{cm}^{-3}$ and a dynamic viscosity of $6.44 \text{ mPa}\cdot\text{s}$. These PBM parameters were obtained prior to the experiments and are listed in chapter 4.3.3 and 6.2.2.

The surface tension has a high impact on liquid atomisation capability which was relevant for spray coating application. Determination of the exact value for the liquid PBM was thus an important parameter to adapt further research activities.

4.2.4 Molecular structure identified by nuclear magnetic resonance

Polymerisations using UV-LED photo-initiation (Galiano et al, 2018) show lower permeability than the PBM layer achieved with REDOX based initiation (Galiano et al., 2015). A denser architecture could be the reason for a lower permeability. It was expected that controlled radical polymerisation mutates the final network thus changing the membrane coating layer properties to a highly interlinked and denser polymers. Considering viscosity modification using controlled radical polymerisation, differently dense structures could also result depending on specific inhibition attempt (Platkowski and Reichert, 1999). By using spray coating application, the applied pressure could interfere with interfacial forces of the PBM breaking the existing formulation and thus alter the bicontinuous polymer structure. These facts led the research focus to nuclear magnetic resonance (NMR) spectroscopy. NMR examines the polymer structure and can distinguish differences of the polymerised molecules. Different polymerised PBM samples of 1.5 g volume were analysed and are listed below:

- REDOX initiated and fully cured PBM, following the approach of Galiano et al. (2015)
- UV-LED polymerised samples using 1.8 w% and 5 w% photo initiator amount to investigate the influence of a higher radical release
- Modified PBM produced with the established protocol in chapter 6.2
- Spray-coated PBM sample polymerised with UV-LED based initiation with a 1.8 w% photo initiator amount.

The sample analysis was done as follows. The ^{13}C solid-state NMR spectra were run with an *Avance 300* spectrometer (*Bruker*) at 75.5 MHz using magic angle spinning (MAS) and a spinning rate of 10 kHz cross-polarization (CP) (Laws et al., 2002). The ^{13}C MAS NMR spectra exploited the transfer of polarisation under Hartmann-Hahn conditions obtained by ramped amplitude variation of a spin locking field (RAMP; Metz et al., 1994) and TPPM decoupling (Samiulla et al., 2018). The contact time of 1 ms and a recycling delay of 4 s were used and typically, 2000 scans were acquired. For comparison, the spectra were also achieved without CP, with a HPDEC (high power proton decoupling) sequence with 2048 scans using a recycle delay of 2 s (Mauri et al., 2018).

4.2.5 FTIR measurements

By using Fourier-transform-infrared (FTIR) spectroscopy, the chemical composition and molecular structure of solids as well as liquid materials can be characterised. An emitted infrared beam excites present molecules and depending on their oscillatory capacity, molecule bond specific wavelength absorption occurs. This absorption band is visualised. In this work, membrane coating layers were analysed to obtain important information about coating layer homogeneity and layer stability after filtration and chemical resistance tests.

For PBM coating characterisation, the composition is defined and well known. A corresponding PBM “fingerprint” was previously defined (Galiano et al., 2015). Comparing the spectra of PBM coated and virgin PES membrane, the “finger-print” becomes clearly evident. According to information taken from Table 4-1, all components present in the PBM contain the C=O double bond with an adsorption peak at around 1726 cm^{-1} which stands out from the commercial PES structure. Assuming that all components are chemically linked in a polymer interwoven network, the peak provides a clear proof of the PBM layer (Figure 4-3). This holds the possibility of validating the PBM stability, for instance in course of a chemical cleaning by peak height. FTIR is a powerful tool and has been used to also quantitatively determine BSA fouling layer of PVDF coated membrane through FTIR mapping (Benavente et al., 2016). However, caution is advised making quantitative statements related to the PBM coatings applied by casting coating technique. The layer thickness may vary greatly due to high fluctuations of casting speed and contact pressure. A quantitative analysis for PBM coatings is limited as the membrane represents a multilayer system. Each layer varies in thickness (production tolerance) for each sampling spot and peak overlapping becomes arbitrary.

This changes the ratio between the three layers: (1) non-woven PE/PP support giving the mechanical strength; (2) the active PES membrane layer and (3); the PBM layer. Peak overlapping varies and becomes more dominant for bigger specimen clamping forces and higher squeezing factors.

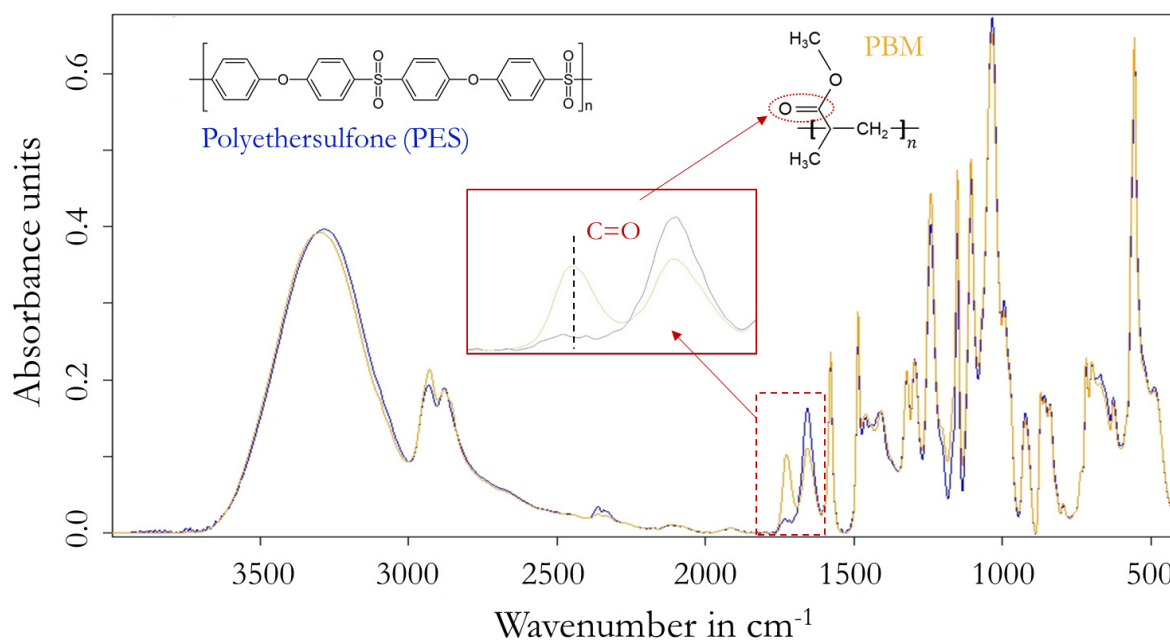


Figure 4-3 PBM fingerprint, C=O double bond at 1726 cm^{-1}

Characterisation was done with a FTIR spectrometer *Tensor II (Bruker)* using the Platinum ATR module with a diamond crystal, type *A225/QHP*, a MIR source and *RT-DLaTGS* detector. The spectral range was defined as 4,000-400 cm^{-1} . Sampling rate was set to 1 s^{-1} and 32 samples were taken per sampling point. Background measurements were first examined for atmospheric compensation of CO_2 and H_2O . After the background measurements the specimen was clamped manually between the diamond crystal with a 2.4 refractive index and the reflective specimen holder. The IR-beam was reflected through the diamond in such way that a 1.5 μm specimen depth could be resolved and analysed. Clamping caused squeezing the membrane specimen and in case of highly thin coating layers, more PES material gets in the absorption range. This overlaps the PBM spectra more thoroughly. Manual clamping also caused deviations due to changing clamping forces. This resulted in further measuring errors as the IR-beam penetrates deeper into the existing material for higher squeezed specimens. However, the latter could be minimised through built-in software functions but the impact of overlapping PES layers persisted.

4.2.5.1 Validating irradiation homogeneity

The homogeneity of the UV-LED exposure area was validated by polymerised drop investigations of the same volume at different spots below the UV-LED lamp. This was done to understand the influence of the LED-to-LED distance of the module. Assessed by the supplier, the irradiation distribution of one LED along the y axis shows high homogeneity between -40 to +40 mm from the LED centre (Figure 4-4). The uniformity stated by the manufacturer is >90%. In total, 512 UV-LED were installed in with a 16 mm distance between each other, both in longitudinal and transversal direction.

UV-LED show a very long cycle life with high cycle numbers. However, FTIR should confirm the homogeneity in irradiation capacity after three years of operation.

19 drops of 5 μL liquid PBM including the photo initiator were applied to a glass plate with a small capillary pipette. Deviations in shape and height were due to manual dosing and the very hydrophilic glass substrate. After polymerisation with 30 s irradiation time and $300 \text{ mW}\cdot\text{cm}^{-2}$ irradiation intensity, solid PBM drops were gently scrapped of the glass plate and investigated on their degree of polymerisation. In addition to potential deviations in polymerisation capacity, the impact of clamping force on the specimen alter the gained values, as described.

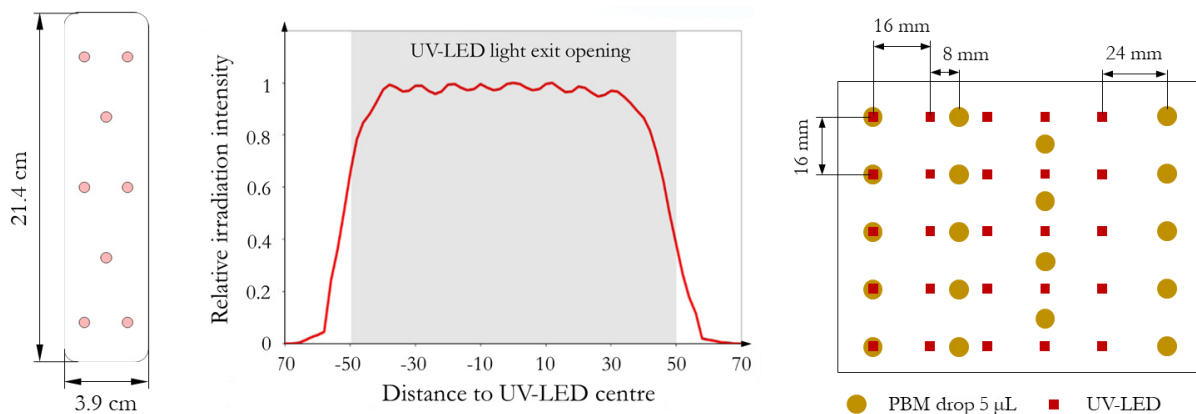


Figure 4-4 FTIR measuring template (left), drop investigation (right) and manufacturer specification about irradiation homogeneity (mid)

The conversion rate of $\text{H}_2\text{C}=\text{CH}_2$ double bond to the polymerised $\text{H}_3\text{C}-\text{CH}_2$ single bond was examined according to chapter 3.4. Besides relative, systematic errors caused by production tolerances of the PBM coating (microemulsion formulation), the membrane itself, and the operator handling caused relative random measuring errors within FTIR analysis. By using a measuring template for specific sampling points (Figure 4-4, left), FTIR reproducibility was enhanced. The software built-in normalisation functions reduce the impact of fluctuating specimen clamping force. This was specifically important for chemical cleaning tests as PBM detachments vary selectively with changing polymerisation degree and layer thickness.

The active filtration surface area of the membrane cuts used for performance and characterisation tests was 0.0085 m^2 in all cases.

4.2.5.2 *FTIR verifying chemical stability*

Type and extend of fouling during filtration dictate the chemical cleaning procedure and periodic time intervals. The need for chemical cleaning is indicated by a rapid pressure increase or decrease in permeability below a certain threshold. Specifically for UF membranes used in MBR application, the cleaning protocol contains different cleaning steps which were adapted for laboratory testing. A citric acid cleaning ($\text{pH}\leq 3$) followed an alkaline cleaning using sodium hypochlorite (NaOCl) and sodium peroxide (NaOH) at $\text{pH}=12$ and $\text{pH}\geq 8$, respectively. A more thorough cleaning with higher stress on the PBM layer was carried out with a protocol for industrial RO application.

A strong acid cleaning using a mixture of nitric acid (HNO_3) and phosphoric acid (H_3PO_4) was carried out at pH levels close to 1.

Last of all, the PBM coated membrane was soaked in a potassium hydroxide KOH solution at pH=13. DI-water rinsing was performed between each cleaning cycle and the PBM coated membrane submerged into the corresponding cleaning solution matching the times given by the manufacturer protocol. One cleaning cycle contained both protocols and were triplicated. Using the FTIR measuring template, 8 specific membrane spots were analysed on their C=O molecule bond peak height before and after the cleaning periods.

4.2.6 Contact angle measurements

Two different approaches were conducted validating the contact angle (CA) for PBM and PES surfaces. Membranes were rinsed three times for one hour in DI-water ($< 20 \mu\text{S}\cdot\text{cm}^{-1}$) to wash out present glycerol inside the membrane pores. For the first approach, the specimens were dried overnight in a drying oven at 35°C to remove total water residues before applying CA measurements. Secondly, wet membrane samples achieved through overnight soaking in DI-water were directly measured without drying. A pressurised air jet was used to roughly blow off water droplets from the surface. For both cases, removing the glycerol is essential as it falsifies the results due to the lower surface tension ($62.7 \text{ mN}\cdot\text{m}^{-1}$) relative to water ($72.1 \text{ mN}\cdot\text{m}^{-1}$, 20°C ; Kopczyńska and Ehrenstein, 2019).

Sampling method was analogue to Kertész et al. (2014). Within this work CA analysis was carried out by sessile drop method, executed by the *OCA 15EC (DataPhysics Instruments)* setup. Specimen strips were cut out of the prepared membrane sheet similar for PBM coated and PES membranes. Strips were then stuck on to the sampling plate using double-sided tape. This way specimen curling can be prevented which negatively affects the measurement result or even preventing the measurement. Sessile drop method works with grey level analysis requiring a clear contrast from the specimen itself and the liquid droplet. Curling prevents clear edges for a distinct analysis. DI-water (Millipore, $< 1.6 \mu\text{S}\cdot\text{cm}^{-1}$) of $5 \mu\text{L}$ volume was slowly suspended from a capillary syringe ($d_s=0.72 \text{ mm}$) precisely dictated by the liquid flow control. Once the drop reaches steady state, measurement was started. To reduce the influence of gravitational forces, the drop is gently collected by the sampling plate rather than dripped off the capillary.

In total, 9 randomly chosen measurement points were analysed for each membrane specimen stripe to minimise the impact of random measuring errors such as membrane architecture, impurities or electrostatic charge. The drop shape development was continuously monitored for one minute and finally, one frame each 10 s was taken for evaluating the drop shape progression and contact angle.

4.2.7 Atomic force microscopy

According to existing literature, the surface roughness greatly influences particulate attachments on the membrane surface (Johnson and Hilal, 2014). Thus, PBM coating aims also at smoothening the initial rough PES surface. Examining the surface roughness is therefore a basic technique in membrane coating characterisation.

Surface roughness measurements were carried out by atomic force microscopy (AFM), with a multimode AFM and a nonoscope *Illa controller* (*Veeco*). The tapping mode of a cantilever (*Bruker AXS*) reduced plastic deformation giving higher accuracies. The nominal spring constant (*TESP*) was 20-80 Nm. Evaluation followed using an image resolution of 512 x 512 pixels. Measurements were taken for PBM coated membrane samples of 4 μm and 20 μm wet layer thickness as well as for the commercial PES. Sampling was duplicated for the three sample types and measurements taken three times, finally giving the mean value and measuring deviation. The AFM software allows to derive various parameters from the measurements whereas the average roughness R_a and root mean square (RMS) R_q are mainly used to describe the surface morphology. R_a represents the arithmetic mean of all the values obtained within the sensing field. R_q is a statistic value gives the quadratic mean value of all surface values of the roughness profile. Experimental results in Chapter 6 highlight the R_q values for all three membrane types with an image size of 10 x 10 μm .

4.2.8 Scanning electron microscopy

Scanning electron microscopes are a perfect tool to investigate microstructure morphologies. Depending on the type of equipment, most advanced, extremely powerful tools can have magnifications up to 100,000x (<1 nm; Wang et al., 2007). SEM was used to study the surface morphology of different coating approaches.

Sampling was done with dry membrane samples still containing the glycerine which prevented the pore collapse. An approximate 1 cm^2 sample area was cut out and coated with an ultra-thin conductive gold cover using the automatic, rotary-pump coating system *Q150R S* (*Quorum Technologies*). Membrane polymers are non-conductive and SEM principle requires a conductive material which is sputtered on top of the surface prior to the measurement. Other conductive sputter materials can be used such as platinum (Pt) or silver (Ag). The sputtered film must be of very low thickness to prevent coverage of the ultrafine specimen structure. A typical range in practice lays between 2-20 nm but is entirely dependent upon the specimen characteristics (Höflinger, 2013). Subsequently, sputtered samples were analysed in the SEM *EVO MA 10* (*Carl Zeiss Microscopy GmbH*) using an acceleration voltage of 20 kV at a 50 pA current density. The magnification was adjusted to 15 and noise reduction parameters as well as contrast adjusted appropriately. The scanned surface area was 15 x 20 μm for each specimen.

SEM was used to characterise the membrane surface topography comparing commercial PES and PBM coated membrane. Likewise, differences in the PBM coating layer achieved by different coating approaches were examined. Concretely, it was expected that spray coating as well as PBM of different viscosity leads to a change in polymer architecture which was assumed to be visualised by SEM technology. A previously scanned specimen of a PBM coated served as a reference for the conducted work (Figure 4-5). However, the coating was done by REDOX initiated polymerisation and a change for photo-initiated polymerisation reactions expected. For instance, radical polymerisation by REDOX initiation takes comparatively long (>20 min) and the polymer chains grow slowly forming a wider polymer mesh. In contrast, the high irradiation intensity and thus fast radical formation during UV-LED polymerisation tends to lead to closely and strongly interlinked polymer structures.

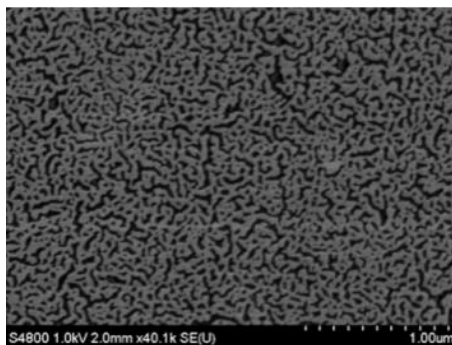


Figure 4-5 Bicontinuous surface texture of the PBM coating layer, achieved with REDOX initiation, with permission from Galiano et al. (2015)

4.2.9 Confocal light microscopy

Pore intrusion phenomena can only be quantified in the z-axis by validating the penetration into the pore depth. Fluorescence microscopy with high sensitivity is an excellent tool commonly used in analytical and biological analysis (Sanderson et al., 2014). The molecule species inside blood cells can be analysed and quantified by their fluorescence nature also used for malaria diagnosis (Hathiwala et al., 2017). Fluorescent microscopes are optical microscopes which use the fluorescence properties of investigated matter, addition to scattering, reflection and absorption effects. The material structures made visible in colour result in a 2-D or 3-D image with detailed information about the sample properties.

Discrimination between the PBM and PES membrane by fluorescent microscopy is generally not feasible since they do not show fluorescence. Instead, 30 mg fluorescent, home-made nanoparticles were added to 1 mL MMA prior to the PBM formulation production. Sample sonication inside an ultrasound bath for around 15 min prior to casting coating broke up existing agglomerates which enabled a finer distribution and prevented depositions. During membrane casting, the PBM and with it the nanoparticles were spread evenly across the surface. The nanoparticles are insoluble in all phases but through sonication homogeneously distributed and ubiquitous. Because the nanoparticles were smaller than the membrane pores ($d_{m,nominal} = 35 \text{ nm}$) they penetrated into the pores along with the liquid PBM. Subsequently, polymerisation entrapped the nanoparticles and analysing the pore intrusion became feasible through the cross-sectional view.

Following investigations were done by cutting specimens in cryogenic, liquid nitrogen. In this way a sharp and clear edge could be obtained giving a better view on the cross-section and thus making the investigations simpler. Various attempts were made to establish the best settings for pore intrusion investigations using the confocal microscope (*TCS SP8, Leica*). Final examinations were done with an excitement wave length of 561 nm within a 552-625 nm acquisition window. The specimens were immersed in DI-water ($<1.6 \mu\text{S}\cdot\text{cm}^{-1}$) to control refraction in the light path. The magnification range was 20x.

4.3 Experimental setup

The following section 4.3 covers the experimental concepts that have been developed. The research described focuses on deepening the knowledge of PBM coating applied on commercial membrane substrates. The main goal is the achievement of uniform coating layers with the possibility to make changes in thickness and structure. This section gives the end user clear guidance in obtaining a high-quality product matching his specific requirements of membrane performance.

- **Section 4.3.1** emphasis the membrane cross-flow test unit setup for testing 0.0085 m² membrane cuts. Besides the shown characterisation equipment, the membrane performance is the most important comparative figure. The permeability for pristine PES and PBM coated membranes was assessed and their performance evaluated within extensive filtration tests using humic acid as model foulant.
- **Section 4.3.2** highlights the setup which contributes to a better understanding of the complex polymer chemistry behind PBM curing processes. It moreover gives the idea of modifying the PBM viscosity to ultimately change the membrane performance.
- **Section 4.3.3** gives an insight into the automated coating machine designed for PBM coating upscaling within the VicInAqua project (see also chapter 2.3.3). It will give a clear explanation of challenges arising for coating upscaling of big membrane areas up to 0.11 m² for an industrial scaled application.
- **Section 4.3.4** outlines the pilot scale setup for testing upscaled PBM membranes with a total 3.125 m² coated surface area. Two PBM coated and commercial modules were compared under exact same boundary conditions using real domestic wastewater within the VicInAqua pilot system. The treated water was provided to an aquaculture hatchery farm as well as for agricultural purposes.
- Last but not least, **section 4.3.5** explains in detail how PBM spray coating can be achieved using two different types of spray nozzles. Concepts and challenges are highlighted and show restrictions for atomisation techniques using ultrasonic spray coating applied with piezoelectric ceramics. Pertinent literature about important parameters is concluded in chapter 2.5.3.

4.3.1 Membrane cross-flow test unit

Membrane characterisation is an essential part of research to assess the membrane performance. As described in chapter 2.5.1, various parameters influence the water filtration processes and make the examinations of exact relations very complex. Existing literature are numerous describing individual procedures acquiring greater knowledge about the interplay between membrane properties and wastewater quality. Sampling and analysing methods can vary greatly which results in high fluctuations making a direct comparison of studies difficult. However, what matters most is the membrane performance, specifically the permeability in $\text{L}\cdot\text{h}^{-1}\cdot\text{m}^{-2}\cdot\text{bar}^{-2}$ at constant flux ($\text{L}\cdot\text{h}^{-1}\cdot\text{m}^2$) or constant TMP (bar) conditions. For ecological considerations, besides capital investment, the water permeability is the most important comparative figure when membrane systems are implemented. A lower permeability requires larger membrane areas to achieve the similar capacity demanded. Moreover, decreasing permeability at constant flux refers to fouling as the TMP increases inevitably. This affects the energy consumption of permeate pumps to compensate for the higher pressure loss through the fouled membrane. Both aspects have to be considered within a system design phase.

Ultimately, lower permeability increases the specific energy consumption for membrane systems to achieve desired volume flow rates ($\text{m}^3\cdot\text{h}^{-1}$). Apparently, one membrane with a specific feature could work very well for one type of wastewater but for other compositions/level of pollution, might be less efficient or selective.

In case of PBM membrane coating, the performance was validated by model foulant water tests using humic acid (HA). Typical model foulants used for laboratory tests are also sodium alginate (SA) or bovine serum albumin (BSA). HA is brownish and provoked visible fouling layers changing in dark colour for thicker fouling layers. Therefore, HA indicated how the PBM layer can mitigate fouling relative to the commercial PES membrane. BSA is a protein ubiquitously present in many wastewater streams causing significant reduction in membrane filtration capacity (Le-Clech, 2015). Both, SA and BSA in solution are clear and a simple, visual examination of the fouling propensity is not possible. HA was used for all permeability lab tests shown in this thesis. The *SIMA-tec* double membrane cell cross-flow test unit allowed to simultaneously test two different membrane samples in series (Figure 4-6). Membrane samples were of 0.0085 m^2 size, cut out of the bigger membrane sheets delivered by the manufacturer. The cross volume flow was $28\text{ L}\cdot\text{h}^{-1}$ and kept constant for all experiments. The regulating valve installed in the concentrate line controlled the transmembrane pressure acting on the membrane. The installed magnetic inductive flow meters (*FEX300, ABB*) required a minimum conductivity of $20\ \mu\text{S}\cdot\text{cm}^{-1}$. The relative measuring error was 0.4% of the actual value. The measuring range of the pressure sensors was 0-6 bar- relative pressure (*Type A-10, WIKA*) with a 0.5% measuring tolerance. Temperature monitoring was done with a resistance thermometer type *TR3-W-Z (WIKA)* with a 1% deviation in the relevant range of $20\pm 1^\circ\text{C}$.

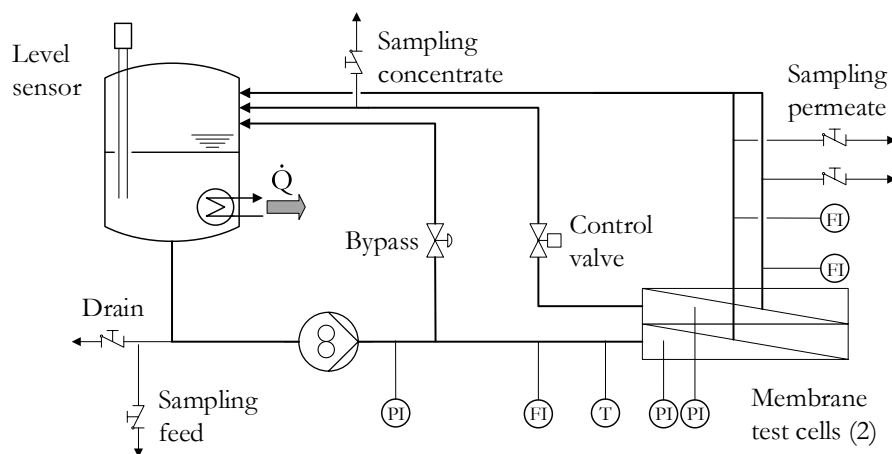


Figure 4-6 Double membrane cell cross-flow test unit (SIMA-tec GmbH)

For simultaneously testing two membranes, deviations occurred as the concentrate flow of the first membrane cell constitutes the feed flow of the second cell. Thus, the cross-flow velocity (CFV) was lower since the feed flow was reduced by the first cell permeate ($28 \text{ L}\cdot\text{h}^{-1} - \dot{V}_{P,1}$). Considering a maximum achieved permeate flow of $1 \text{ L}\cdot\text{h}^{-1}$, this deviation totals to around 3-4%. For constant volume flow trials, the system control setting did not allow simultaneous testing which would require a second feed pump and control valve for independent permeate flow control. For constant TMP tests, both test cells could be monitored simultaneously. Data were recorded for the TMP as well as each permeate volume flow with a 2 s^{-1} sampling rate. These tests were done since the permeability indicates the membrane porosity which was relevant for further investigations.

Before testing, each membrane sample was rinsed three times for one hour in DI-water ($<20 \mu\text{S cm}^{-1}$) to wash out the present glycerine in the membrane pores and to enable first pore-swelling. Pore swelling is the phenomenon of water molecules moving inside the void spaces of the membrane, enabling the substrate material to swell. As a result, the pores are tapered constantly reducing the permeability until steady state is reached. Membrane performance tests were carried out mostly in $100 \text{ mg}\cdot\text{L}^{-1}$ HA solution. HA solubility is dependent on the solvent type and its pH level. Dissolved and suspended fraction were analysed using the dissolved and total organic carbon of the solution used since different fouling phenomena (e.g. pore blockage, cake layer formation) may have occurred. Annex A.1, therefore, exhibits the essential properties of prepared HA solutions and their carbon analysis (figure A-2). The test protocol was determined for constant pressure and constant flux conditions. In both cases, further pore swelling was given by filtrating DI-water ($30 \mu\text{S}\cdot\text{cm}^{-1}$) prior to the tests (Figure 4-7). The test water was then replaced by a $100 \text{ mg}\cdot\text{L}^{-1}$ HA solution and filtration performed at 0.5 bar TMP. Once stable operation was reached, mean values were calculated from the last 20 frames of the recorded data. Figure 4-7 highlights in detail the procedure for constant TMP tests. Constant pressure mode was chosen specifically for PBM as the permeability at constant pressure gives an indication of structural layer density. The lower the permeability, the denser the layer texture. Moreover, pressure swing filtration between 0.5 and 2.2 bar with intermediate system rinsing using DI water at 0.5 bar indicated the regain potential after fouling.

TMP protocol was applied for commercial PES membranes as well as PBM coatings prepared with the classic and modified AUTEAB. Results are depicted in 6.1.1.

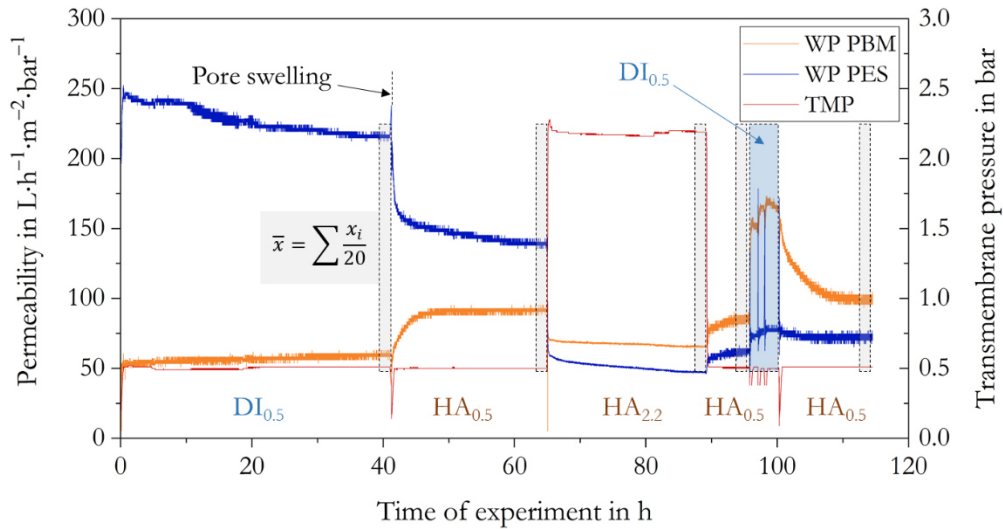


Figure 4-7 Test protocol for membrane performance tests with constant TMP conditions

Gradual incremental flux step tests (constant flux) were conducted to compare the membranes fouling propensity at comparable filtration conditions. Flux step tests started at lowest possible volume flows which was system-based and changed with the membrane porosity. For commercial PES membranes with a more open structure, flux steps started at around $0.3 \text{ L}\cdot\text{h}^{-1}$, whereas for PBM coated, more dense membranes slightly lower volume flows of $0.2 \text{ L}\cdot\text{h}^{-1}$ were set. The volume flow was then gradually increased by $0.1 \text{ L}\cdot\text{h}^{-1}$ up to $1.0 \text{ L}\cdot\text{h}^{-1}$, limited by the system pump pressure. The TMP was continuously recorded. Each gradual increment lasted for 40 min revealing the specific pressure increase to maintain the volume flow (Figure 4-8). A sharp increase in TMP indicated the exceeding of the threshold for critical flux values. However, defining a threshold for this application would be completely arbitrary. An evaluation was based on the last 20 values before parameter reset to a higher flux rate. After a sufficient system flush with three times DI-water, the membranes were removed to visually inspect their fouling state. Constant flux tests were done successively since the test unit could only control one permeate volume flow.

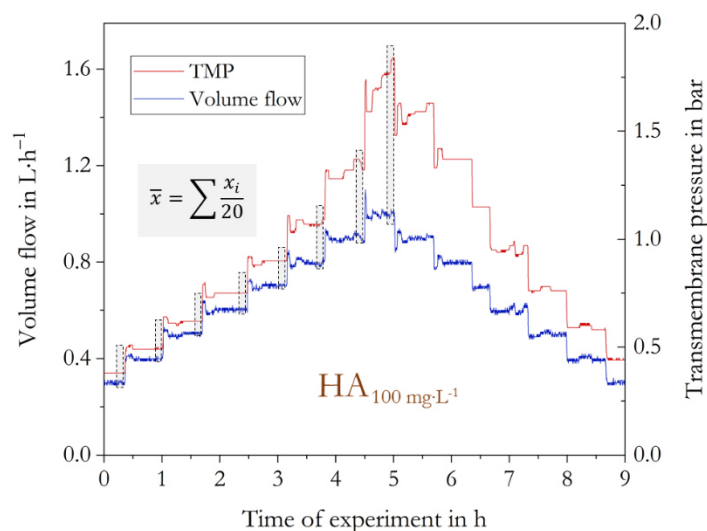


Figure 4-8 Flux step tests with incremental increase of 0.1 L·h⁻¹ (11.8 LMH)

Long-term tests at constant volume flow were carried out subsequently to an acclimation phase with DI-water ($30 \mu\text{S}\cdot\text{cm}^{-1}$) and humic acid solution ($100 \text{m}\cdot\text{g}\cdot\text{L}^{-1}$). The test unit was then restarted with a constant flux operation at $0.4 \text{L}\cdot\text{h}^{-1}$ which corresponds to a 47 LMH flux rate. This flux is much higher than the manufacturer's recommendation of 25 LMH. The guideline concerns a submerged membrane undergoing a suction filtration. The membrane cross-flow test unit however, applies a positive pressure to the membrane which changes the membrane performance contrary to expectations. Higher flux rates were used to simulate harsh filtration conditions in long time-scale. Permeability tests were done to characterise the PBM performance relative to the commercial PES membrane. Altogether, the experience from experimental data helped to identify the potential performance of PBM coated membranes under real conditions. Nevertheless, how well the laboratory conditions reproduced reality was extensively investigated during the pilot scale tests, further discussed within section 4.3.4.

Preliminary experiments confirmed high pore intrusion of the liquid PBM solution prior to the polymerisation (see chapter 5.6). Therefore, a possibility to improve the coating process by modifying the PBM viscosity was evaluated. Controlled radical polymerisation was considered as promising approach since a higher viscosity reduces the capillary force directly proportionally (chapter 2.5.1.3). The laboratory setup to investigate and evaluate this innovative procedure is described in detail below.

4.3.2 Modifying PBM viscosity by controlled radical polymerisation

Within this work, numerous experiments were executed for better understanding the complex chemistry behind PBM membrane application. Characterising the temperature progress during polymerisation lead to deductions for controlled viscosity modification approaches.

It is well known that temperature at elevated levels have a high acceleration characteristic on chemical reactions (Helfferich, 2004). Temperature monitoring and control is mandatory for nearly all chemical processes, endothermic as well as exothermic. In terms of microemulsion polymerisation, the reaction is exothermic and heat is released during the propagation (Helfferich, 2004).

This insight led to developing a viscosity modification approach. Figure 4-9 illustrates the basic idea of controlled radical polymerisation for PBM membrane coatings. During initial test series, the polymerisation propagation was characterised by temperature measurements (exemplary, left). The second test phase included the controlled interruption of polymerisation propagation at a certain polymerisation degree. This pre-polymerised PBM solution of higher viscosity was spread over the membrane and finally cured to a completely solid state, characterised by a second temperature rise (Figure 4-9 right).

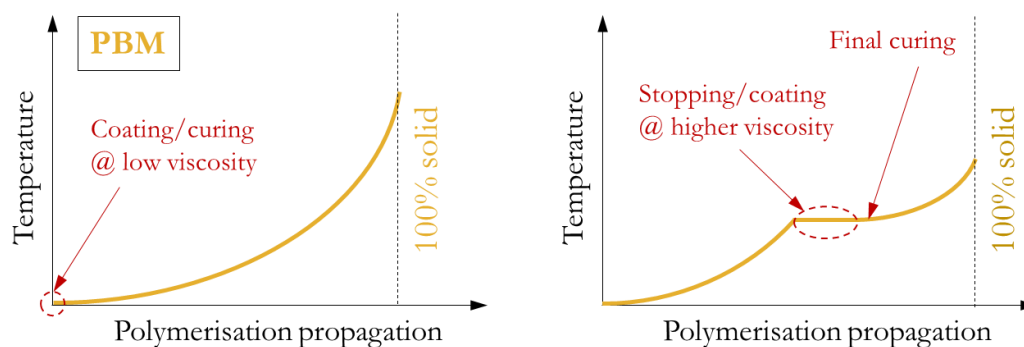


Figure 4-9 Basic idea of viscosity modification

Feasibility studies were carried out in two different polymerisation setups, also shown in Figure 4-10. In both cases, temperature measurements were done with thermocouples of type K with an accuracy of $\Delta T \pm 0.5^\circ\text{C}$ and a fast response time $t_{95} = 0.08$ s. Sensors were connected to a 20-bit data logger including processing (*USB TC-08, OMEGA*) for data evaluation using the *Logging Software (OMEGA)*. The illustrated setup (left) comprised of 5 thermocouples arranged in different spatial positions inside a flask containing 10 g liquid PBM. Polymerisations experiments throughout the viscosity modification tests were done with a nitrogen (N_2) overflow to facilitate inert polymerisation conditions. Flask size with integrated flea varied from initially 10 g PBM content to 1.5 g PBM with the option of continuous stirring. The second setup included the possibility to actively cool the PBM sample (Figure 4-10, right). The water bath contains a lamellar heat exchanger connected to a thermostat (*F35, Julabo*) to enable homogeneous temperature control, supported by an additional mixer. The setup was designed in such a way that thermodynamic conditions inside the flask could be evaluated which was a decisive factor for homogeneous polymerisation. The heat conductivity reduces significantly with a phase transition from liquid to solid and inhibits the chemical reaction due to a drop in heat release capacity. Strongly influenced by this Trommsdorff-Norish effect (Ozaki et al., 2015), a more spatial consistent polymerisation should be achieved by variations in mixing speed from 0, 1000 and 1500 rpm enhancing the turbulences inside the flask. Uniform coating layers and high reproducibility require pre-polymerised PBM free of partial polymerised PBM spots and agglomerates. Ambient temperatures were fixed at 22°C and water bath temperature varied between 15, 20 and 25°C , respectively. It was expected to have active control over the polymerisation process by improving the heat transfer inside the flask as well as from the flask through the glass and the circulating water. Experiments for temperature determination were triplicated.

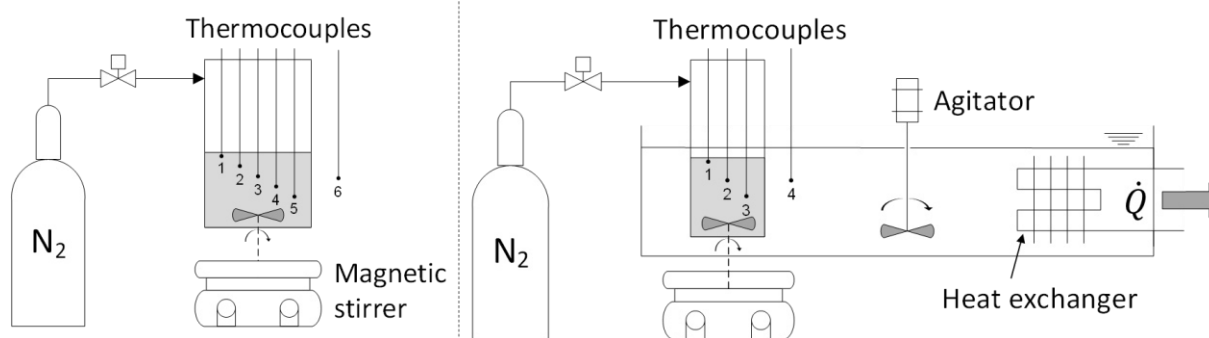


Figure 4-10 Schematic experimental setup for polymerisation characterisation and controlled radical polymerisation approaches, passive cooling (left), active cooling (right)

After the polymerisation characterisation, a protocol was developed to modify the PBM viscosity. Therefore, the approach of Platkowski and Reichert (1999) was adapted to the following steps.

First polymerisation was induced by REDOX initiation following Galiano et al. (see also Table 4-1). In terms of the 1.5 g PBM solution, around 1.85 mg APS was first added, dissolved and subsequently activated by the initiator TMEDA with a 40.5 μL dosage. Shortly after, controlled polymerisation reaction inhibition followed at defined inhibition times Δt_i after the first initiation. TEMPO delivered in solid form and finely grinded for these studies, is a strong inhibitor, preventing, for instance, OH-radical production from Fenton-reactions (Shi et al., 2017). By adding sufficient quantities of TEMPO to the polymerising PBM, the TEMPO-radical catches radicals and oligomers randomly resulting in termination reactions. Re-polymerisation potential was validated by simple storing the pre-polymerised PBM solution in a cold and dark place over night. If successful, re-initiation was done by adding the photo initiator Irgacure 184 and at first small amounts of APS as residual TEMPO radical catcher. After validating the feasibility, the material input was gradually reduced for the initiators as well as inhibitor to optimise the process since both are mutually influential leading to process delays and interruption. Finally, the optimum balance between lowest possible material inputs and most effective initiation as well as re-initiation was defined. The time of adding the TEMPO inhibitor after the polymerisation start was adjusted from time to time. Late times lead to higher viscous PBM, obviously, but could prevent homogeneous casting coatings in case of considerably high viscosities. Temperature monitoring in the flask centre was done continuously throughout the experimental phase. The basic idea of using temperature as control parameter for viscosity modification is the simple measuring principle and data evaluation and thus also simply system integration. Initially, point of adding TEMPO was defined at a 1.5 K temperature increase in reference to the point of initiation. This attempt should reduce the impact of material input variations and give allowance for changes in PBM formulation. Furthermore, a higher comparability between the experiments is given rather than by TEMPO dosing after a set time since impact of pipetting errors and environmental fluctuations are minimised.

Table 4-5 lists all conducted experiments including pre-trials, viscosity modification feasibility tests and the re-initiation potential for membrane coating application. Based on these experiments, the protocol was established. Interim times between stopping and re-starting were successively shortened and the material input optimised once again.

The modified, pre-polymerised PBM samples varying in time of inhibition (7, 8, 9, 10 min) thus changing in dynamic viscosity. Reference values were taken for the pristine PBM used for UV-LED polymerisation coatings. After a successful modification, 0.25 mg was taken for the rheological investigation. Dynamic viscosity measurements were duplicated and the mean value highlighted in chapter 6.2. With the remaining 1 g PBM, membrane coating with UV-LED re-initiation followed. 0.0085 m² membrane cuts were then classified on their performance inside the cross-flow test unit. Ultimately, membrane performance tests using the *SIMA-tec* test unit and humic acid as model foulant were performed. Examinations were also based on visual inspection of brownish appearance after removal of the test cell.

Table 4-5 Test series for polymerisation characterisation and PBM viscosity modification

Series No.	PBM amount	Approach	Objective
1	10 g	Passive cooling (ambient temperature) and 5 equipped thermocouples	Characterisation of spatial PBM polymerisation for stagnant solutions
2	10 g	Passive cooling (ambient temperature) and adjusted stirring speed	Investigation of turbulence effects on spatial distribution and temperature propagation
3	1.5 g	Passive cooling (ambient temperature) and 3 equipped thermocouples	Reproducing the results of (1) and (2) to minimise PBM material input
4	1.5 g	Passive cooling (ambient temperature) and inhibition using different TEMPO inhibitor amounts	Feasibility of inhibition approach with optimised material input
5	1.5 g	Establishing inhibition concept for passively and actively (water bath) cooled PBM	Identification of practical inhibition concept
6	1.5 g	Active cooling in a water bath for 15, 20 and 25°C water/liquid PBM temperature	Investigation of temperature susceptibility of PBM modification approach
7	1.5 g	Adjustment of inhibition time after polymerisation initiation Δt_i for 7..8..9..10 min	Identify latest possible stopping point for highest possible viscosities
8	1.5 g	Feasibility study of controlled radical polymerisation using UV-LED re-initiation	Weighing the potential for UV-LED based PBM membrane coating application
8	1.5 g	Membrane coating experiments at different viscosities and polymerisation temperatures	Establishing relations between inhibition time, viscosity and permeability
9	1.5 g	Final assessment of viscosity modification for PBM upscaling for pilot scale tests including comparison with pristine PBM.	

Highest priority was given to the evaluation of PBM viscosity modification concept for the membrane coating upscaling for pilot scale tests (see 4.3.4). Validating the concept on its reproducibility includes the relation between the parameters such as inhibition time Δt_i between initiation and stopping, the dynamic viscosity after stopping (modified PBM) as well as membrane permeability after UV-LED induced polymerisation (re-starting). As described in chapter 2.5.1.3, it was assumed that higher viscosities can potentially reduce pore penetration. The established relationship between these parameters could help to achieve deliberate changes in polymer structure being potentially beneficial for individual membrane separation applications.

4.3.3 Automated membrane coating system

Industrial membrane production thrives on high throughputs to meet high product demands. Production lines are mature enabling high reproducibility and consistent product quality. Manually conducted casting coatings caused inhomogeneity in the coating layer thickness first visually investigated; the concept can be derived from chapter 5.2. The reason lies in non-uniform movement patterns – coating speed as well as applied contact pressure – by the user leading to asymmetric layer properties. This not just reduced reproducibility but moreover highly affected characterisation results such as FTIR, SEM, AFM and coating thickness measurements. Not yet in focus but differences in coating thickness could also result in PBM detachments during filtration operation from the coated substrate if the thickest layers cannot be entirely polymerised. Therefore, and with a specific focus on the pilot scale tests carried out, an automated coating device was developed including appropriate controlling and sensor systems for process monitoring.

The basis for developing process was the customised UV-LED lamp (*L-Series, Opsytec Dr.Gröbel*, see chapter 3.4.2) and spatial boundary conditions given by the existing glovebox. Targeted parameters are based on preliminary works of Schmidt (Schmidt, 2016), given with:

- **300 mW·cm⁻²** irradiation time at a UV-LED-to-membrane distance of 4 mm
- **30 s**, respectively 60 s, irradiation time ensuring complete polymerisation
- **24±1°C** temperature valid for coating environment as well as UV-LED light source
- **Oxygen <1 w%** to avoid the majority of oxygen inhibition impact (Menter, 2000).

PBM coating material input orientated towards 4 µm wet coating layer using a stainless steel spiral casting knife (*TQC*). According to the used membrane cuts with dimensions of 0.515 x 0.22 m and around 0.11m² surface area (Table 4-4) 0.4 g PBM were required (1.03 g·cm⁻³). However, provoked by the described pore intrusion phenomenon (chapter 5.6), 1 g PBM was necessary to cover the whole membrane area.

For the design, small dimensions of the glovebox and the big membrane areas to be coated were major challenges making it impossible to use commercially available equipment. Limited budget moreover made the development process more complex.

4.3.3.1 Process parameters

Contrary to manual casting, automatic coating offers uniform coating layers which was required for the upscaling process. Adjustable and constant casting speed also resulted in faster production and shorter cycle times (see chapter 5.4). Some parameters were considered to be relatively stable but some require active control described within the next paragraphs.

Environmental influences

For preventing undesired oxygen inhibition reactions during polymerisation propagation, an air oxygen sensor based on amperometric liquid electrolyte principle was integrated into the glovebox.

The sample gas – in this case air inside the glovebox – flows inside the sensor casing where the oxygen diffuses through the polymer or typically ceramic sensor membrane according to its partial pressure. O₂ molecules are reduced at the cathode where released hydroxyl-ions (OH⁻) and electrons (e⁻) diffuse through the electrolyte to the anode and induce an electric current. The generated current is directly proportional to the converted oxygen and thus oxygen content of the sample gas (Barsan and Schierbaum, 2019). After converting the analogue value and digitally calculating the actual oxygen value, the coating process was started at oxygen levels below O₂<1w%. A software integrated, displayed digital and analogue warning message was implemented to avoid coating operations above this defined value.

Initially, to better understand the temperature distribution inside the glovebox (see below), 7 type K thermocouples measured the temperature at different locations, e.g. close to the radiator outlet, or the exposure area of the UV-LED lamp. Examinations showed that the temperature differs greatly with location but equalize in time. This information helped to adjust cooling/heating temperatures of the temperature control unit and optimize the coating upscaling process (time reduction between each coating). Identification of a representative measuring spots followed and subsequently, a PT1000 sensor was installed and replaced the existing temperature data logger including the 7 thermocouples.

Thermocouples and PT1000 thermometer are different in resolution, response time and accuracy. Thermocouples work according to the thermoelectric principle existing for various material pairing. If two joined conductive materials are exposed to a temperature whereby the loose conductor ends constitute the reference point inside a measuring cell, a thermoelectric potential/voltage is created between the loose ends, also called the “Seebeck-effect”. This voltage results from the difference in temperatures of joint and loose ends and is specific for each material pairing (*ifm electronic*, 2003). In contrast, PT1000 elements are resistance temperature detectors (RTD), mostly made of platinum, with changing resistance in direct correlation with the changing temperature at the sensor tip. PT1000 have higher resolutions relative to PT100 sensors since the reference resistance at 0°C is 10 times higher (1,000 Ω to 100 Ω) and thus the linear measuring curve gives significantly lower measurement falsification in combination with the sensor line resistance. Comparing both principles, PT1000 tend to have longer response behaviour (time t₉₅) due to the slow thermal process but show higher accuracies within the entire measuring range (*ifm, electronic*, 2003). The latter becomes more important for membrane coating processes as the nitrogen filling of the glovebox and air conditioning as well as the coating itself are comparatively slow processes.

A capacitive based hygrometer (handheld device) measured the **relative humidity** inside the glovebox. The response of the electric capacity inside the sensor tip changes with varying humidity in the air. As water gets adsorbed by a specific hygroscopic layer on top of a capacitor’s electrodes, its dielectric properties and thus the electric capacity changes. The exact relation is specific for each capacitor and also depending on the electrode coating material (Farahani et al., 2014). Measuring range of the digital thermo-hygrometer was $\phi_{rel}=100\pm 3\%$ (*type 625, Testo*). For phase-inversion techniques, the humidity has an impact on the membrane morphology since it acts as non-solvent for the cast polymer film (Marino et al., 2018). It was assumed that the impact of relative humidity on the PBM membrane coating production in terms of pore size, pore size distribution and permeability was of minor relevance.

However, the PBM coating upscaling and production of few square meters coating layer was done in a closed environment (glovebox). Thereby, the humidity increased substantially due to the water (41 w%) bound in the microemulsion solution which evaporated during the exothermal polymerisation. For future considerations, actions should be taken to not just monitor but also control the relative humidity of the coating environment. Some absorptive materials and a heating cartridge for desorption with successive aspiration out of the glovebox could be implemented.

Coating components and speed control

As preliminary tests revealed, the coating speed has a significant influence on the coating result (chapter 5.4). Considering casting coating, it also depends on coating material viscosity and flow behaviour (thixotropic, Newtonian). For instance, faster casting increases the shear force on the material and – assuming thixotropic behaviour – decreases the dynamic viscosity in course of the heat dissipation into the material. As a result, the dynamic viscosity decreases and according to equation 2-11, provokes membrane pore intrusion. For the final coating process, the casting speed was $6 \text{ cm}\cdot\text{s}^{-1}$ according to prior parameter examination and the motor rotational speed was adjusted accordingly. In general, speed control is commonly specified by the motor type and industrial scale. For high voltage current (400 VAC) and single phase (230 VAC) consumers, phase angle or phase-fire control (PFC) and frequency control (FU) is applied whereas consumers without blind power can be throttled with simply resistance control via a potentiometer. Motors supplied by 24 VDC and less are employed for electrical small-scale motors and sensors systems. Besides potentiometer regulation, pulse-width-modulation (PWM) can accurately set the voltage supply between zero and nominal voltage (0...24 VDC in this case). A hall sensor with integrated encoder into the 24VDC brush motor housing (*DC-max16S GB KL 24V, Maxon Motor*) provided feedback about the current rotational speed of the drive shaft and converted it into the current coating speed. This enables an accurate speed control. For this application, spindle drives were too costly or occupied too much space due to the construction with the motor behind the drive shaft.

Linear guidance beat other processes in terms of sliding properties and accuracy of the feed path (*Bosch Rexroth AG*; 2017). The driving force of the motor was transmitted via a toothed belt and thus constituted a compact solution to meet the space requirements. The major challenge was to comply with the tolerances for accurate parallel alignment for the guiding system and the orientation of the membrane and casting knife at the same time (explosion drawing illustrated in Figure 4-11). Differences can inevitably affect the homogeneity of coating layers additionally to the coating knife's rectilinearity and membrane thickness. The membrane support was a 250 x 550 mm glass plate as glass shows lowest thermal expansion coefficients and production tolerances. An integrated 24 VDC actuator (*CAHB 10, SKF*) moved a scissor lift up to the desired 4 mm distance to the UV-LED lamp. The lift contained the glass plate and the membrane which was fixed with double-sided tape.

Moreover, considering integration into continuous production conveyer, a minimum distance ensured sufficient clearance against belt conveyer vibrations.

Complete PBM polymerisation takes only 30 s (Schmidt, 2016) but was doubled to 60 s for the upscaling process to compensate systematic and random experimental errors (also see chapter 4.1). Subsequently, the actuator brought down the glass plate containing the cured PBM coated membrane in reverse direction. Unloading, process resetting and membrane re-loading was done manually.

Available, off-the-shelves coating systems did not match the requirements in terms of space limitation and particularly the lifting function to obtain the short distance for fast and complete PBM layer curing. Therefore, the developed and herein described coating unit was a custom-made, in-house developed product. Commercially available customised solutions were not considered due to considerable production costs.

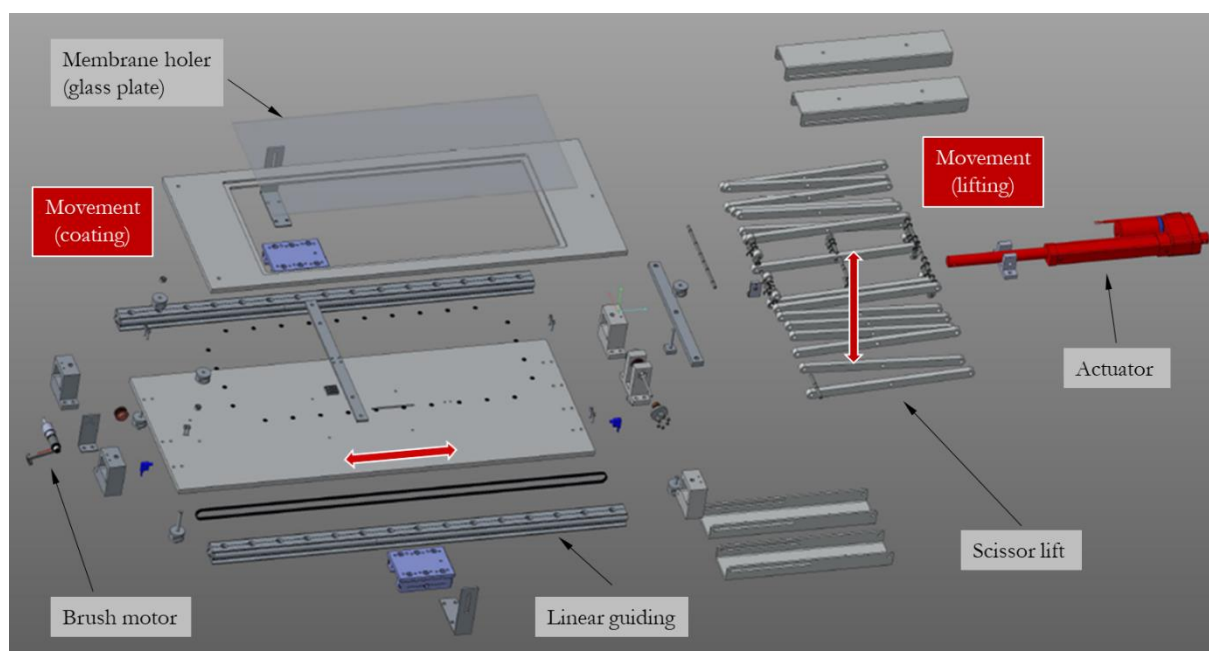


Figure 4-11 Automated membrane coating system, exploded drawing

Glovebox cooling system

Temperature fluctuations affect the polymerisation speed and can reduce the curing degree within the given time range (Schmidt, 2016). Shown by Platkowski and Reichert (1999), polymerisation duration also influences the final polymer structure (chain-length) to a wider or more closely interlinked network. Even temperature distribution inside the glovebox (538 L) was done with 3 parallel connected fans (*NF-F12, Noctua*) which also enhanced the heat transfer over the installed copper radiator. A connected thermostat (*F35, Julabo*) controls the radiator surface temperature by pumping the conditioned refrigerant (tap water) through the radiator on the liquid side. The glovebox temperature can be therefore controlled to $24 \pm 0.5^\circ\text{C}$. As explained before, 7 thermocouples of type K were mounted at several spots to examine the temperature profile. System configuration and design are based on the following calculations.

First of all, potential heat inputs were identified and quantified. This was vital as the result determined the installed system cooling capacity. The total heat input resulted from the sum of all individual heat inputs (equation 4-1). The UV-LED lamp provides the major share of heat (\dot{Q}_{LED}).

The maximum electrical input power including lamp cooling system and control element is given with 1,700 W_{el} . Independent measurements were around 1,500 W_{el} . Despite the minimum UV-LED efficiency of 30% (Muramoto et al., 2019), it was assumed that the energy consumed by the 512 UV-LEDs was nearly completely transformed and introduced into the glovebox. Heat losses and direct as well as reflected light absorption of the components present in the glovebox increased the temperature. Consequently, \dot{Q}_{LED} was 1,500 W_{th} and includes cooling system and supply of the control element. \dot{Q}_{PBM} was the heat input by the PBM in course of the exothermal polymerisation process releasing heat. Assuming a total mass of 1 g PBM per coating, this value is rather small and considered negligible compared to the LED heat intake³. The glovebox is made of PMMA and not insulated. Ergo, heat output through the walls were calculated according to Fourier's Law considering laboratorial conditions (equation 4-2). Total heat conduction coefficient was also derived from heat transfers air-to-PMMA and PMMA-to-air. Nevertheless, as the wall was the dominant resistance, the heat transfer coefficient of the 10 mm wall was considered only with $\lambda_{gb}=0.19 \text{ W}\cdot\text{m}\cdot\text{K}^{-1}$. With a total surface area $A_{ges}=4.26 \text{ m}^2$ and a $21^\circ\text{C}\pm 1^\circ\text{C}$ room temperature, \dot{Q}_{amb} comes to -155 W_{th} and the total heat input added up to approximately 1,345 W_{th} (equation 4-1). Other minor influences such as the user load through operating inside the glovebox were not considered for the system design.

$$\dot{Q}_{tot} = \sum \dot{Q}_i = \dot{Q}_{LED} + \dot{Q}_{PBM} + \dot{Q}_{amb} + \dot{Q}_{user} \quad 4-1$$

$$\dot{Q}_{amb} = \lambda_{PMMA} \cdot A_{PMMA} \cdot (T_{PMMA} - T_{amb}) \quad 4-2$$

The total heat input represented the minimum installed capacity of the cooling system and could be equated with the heat capacity of the radiator/heat exchanger \dot{Q}_{HX} (equation 4-3). \dot{m} is the refrigerant mass flow rate for tap water in $\text{kg}\cdot\text{s}^{-1}$ and defined by the mean mass flow rate of the connected thermostat. c_p is the heat or thermal capacity at constant pressure which is $4184 \text{ J}\cdot\text{kg}^{-1}\cdot\text{K}^{-1}$ (@ $T = 20^\circ\text{C}$) for water. A more detailed overview can be taken out of Figure 4-12 showing the heat balance and all boundary conditions.

$$\dot{Q}_{tot} = \dot{Q}_{HX} = \dot{m} \cdot c_p \cdot (T_{liquid,in} - T_{liquid,out}) \quad 4-3$$

$$\dot{Q}_{HX} = k_{tot} \cdot A_{HX} \cdot (T_{air,in} - T_{air,out}) \quad 4-4$$

³ Calculated with the reaction enthalpy of PBM components

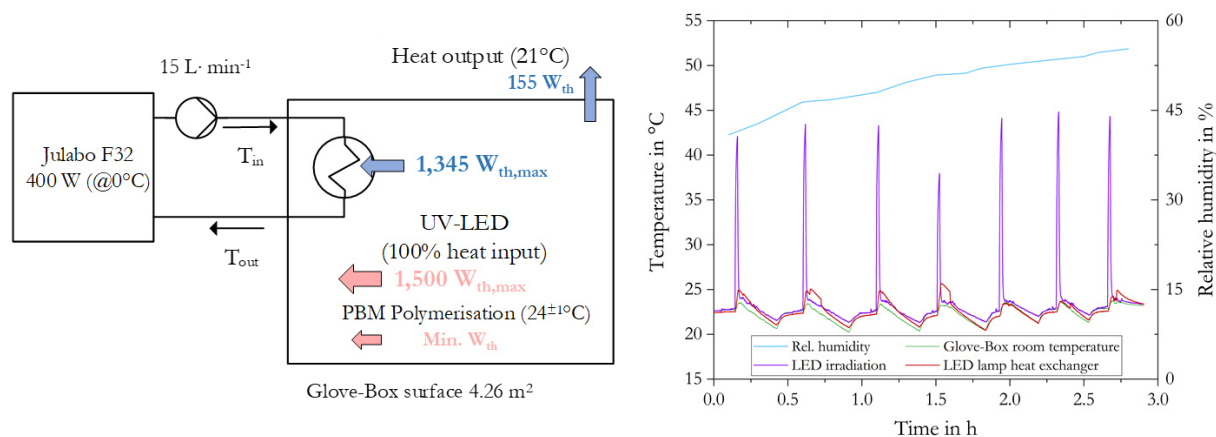


Figure 4-12 Heat balance of membrane coating system and considerations for cooling system capacity calculations (left), temperature and humidity during successive membrane production (right)

Finally, the following applies: the cooling system required time to cool down the large volume (538 L, >99 w% N₂) of the glovebox. Since the total heat input was 1.345 kW_{th} for 30-60 s irradiation, the total heat quantity becomes at maximum 22.4 Wh per coating. The 360 mm copper radiator (*NexXxoS XT45, Alphacool International GmbH*) cooling capacity was 0.45 kW but the thermostat limited the heat release to 0.4 kW_{th}. Therefore, it takes 22.4 Wh/400W=3.4 min for the cooling unit to reach initial state after each membrane coating. The heat amount seemed small but temperature inside the UV-LED lamp increased substantially in time and prevented continuous membrane production without active cooling. The actual cool down time differed with temperature inlet into the radiator and thus the setting of thermostat. Temperature control was done manually by regular inlet parameter adjustment (T_{in}) and due to thermal inertia, temperature conditioning took around 15 min before membrane production could continue (Figure 4-12, right). Bigger radiator surface areas and more powerful thermostats could shorten this cycle time with an automatic 3--point or PID temperature controller.

Altogether, the integrated cooling unit allowed for a production independent of environmental influences and a continuous membrane coating process.

4.3.3.2 *Control system for automatic membrane upscaling*

The control system was based on a semi-automatic operation. In this way, higher process control was given and the lower automation degree reduced installation expenditures and control complexity. Each control mode and the intersection will be outlined in more detail in the section below.

Implemented sensors were connected to a multifunction I/O-device *USB-6002* with a 16-bit ADC resolution and a maximum 50 kS·s⁻¹ sampling rate. Data processing took place via the graphical software *LabVIEW* and were stored on a PC for further evaluation (both *National Instruments*). Switching and actuation of relays, actuators and feed motor was done by an Arduino microcontroller. Arduino is a hardware and software manufacturer offering inexpensive controlling possibilities. Available open source software enabled the end user to program specific controlling environments from scratch.

Within this work, the microcontroller board *Arduino Mega 2560* had 54 digital input/output pins, 16 analogue inputs and other implemented ports. The resolution with the 8 bit controller was relatively low compared to other existing systems on the market but the accuracy was of no consequence to the membrane coating process.

The *Arduino mega 2560* received inputs from potentiometers determining the coating speed and exposure time for polymerisation; as well as buttons for motor actuation and integrated end-switches which gave feedback about the current process status. Arduino sent output signals to high current Darlington arrays of a *ULN2003* board, each containing seven open collector emitter pairs. In this way, higher currents above the Arduino output of 20 mA could be realised as npn-transistors were activated (Base, B) by the low *Arduino* current. This enabled a higher current (500 mA) with 24 VDC to flow through the transistor from the Collector (C) to the Emitter (E) and therefore actuated the relays. The exact process flow was determined by the individual code stored on the microcontroller itself. In addition, one output sent important information to a connected LCD-display making the monitoring simpler. Current coating status, coating speed and membrane exposure time were shown constantly. The whole implemented control and data evaluation implementation is depicted in the following Figure 4-13.

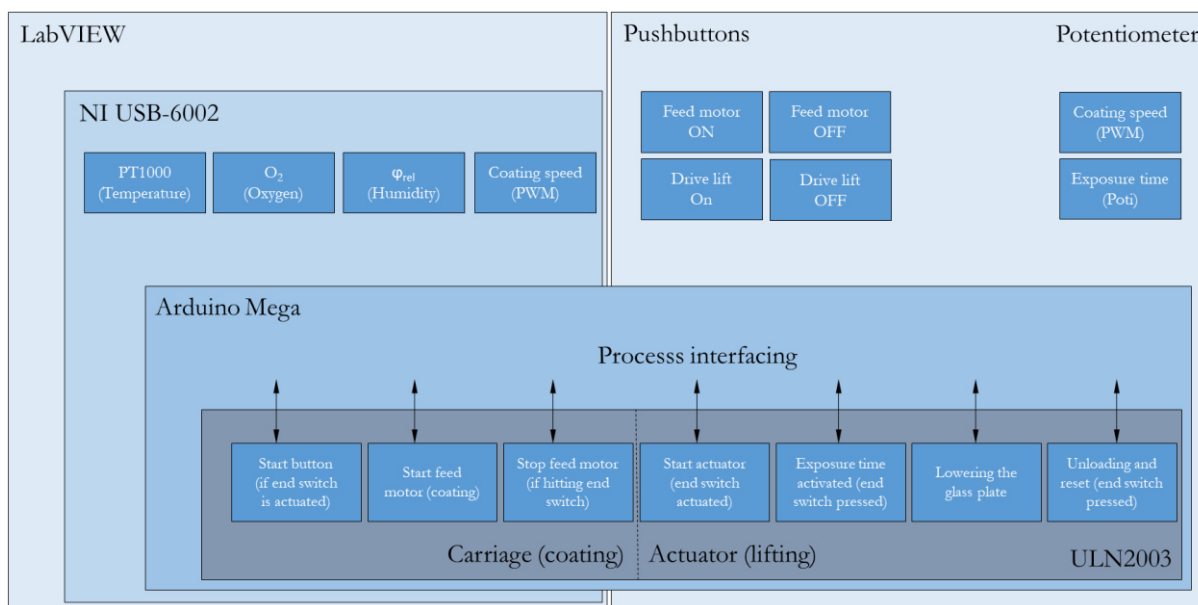


Figure 4-13 Intersection of the implemented control strategies

The system is modularly expandable with other sensors. Assuring manual control of the coating setup was important to avoid standstill of the coating production in case software errors. With this in mind, 10 k Ω potentiometers were implemented to adjust the coating speed as well as exposure time (time of lifted glass plate against the UVLED lamp) with simply accessing the PWM unit and counter relay. External interaction for process start and stop at any time could be done with pushbuttons which were connected to the *Arduino* microcontroller. Fans of the cooling unit could be manually controlled by a simple on/off switch integrated into the electronic cabinet. However, during membrane production fans remained on and temperature was controlled by changing the temperature inlet conditions into the radiator (thermostat control).

A fully automated cooling process would require a 2-point or – more accurate – a proportional-integral-derivative (PID) controller and interfacing the thermostat into the existing controllers.

Previous considerations about directly interfacing *Arduino Mega 2560* microcontroller with the *NI USB-6002* board was not realised due to major delays in response time. More precisely, there was a loss in synchronisation between *NI* and *Arduino* when the end switch status (on/off) changed.

Arduino offers only very small on-board memories (8 kB RAM) which limited the data rate transfer from the *LabVIEW* program and backwards. Severe control failures were determined. This fact clearly limits the application for such cheap and simple microcontrollers.

The rather robust semi-automated mode works with the end-switches connected to the *Arduino* microcontroller for activating and controlling the motor operation. Process/parameter monitoring was simultaneously done by the *NI* board only. The term “semi-automated” implies that the coating process was fully automatic but loading and unloading plus parameter resetting had to be done manually. Finally, all electric components were installed and connected inside a control cabinet in accordance with the existing regulations and safety aspects, including IP61 protection.

4.3.3.3 *Final assembly and coating sequences*

The production process follows the sequences: (1) manual membrane loading and preparation; (2) automatic casting coating; (3) automatic membrane lifting and curing process; (4) manual membrane unloading and parameter resetting. A separate membrane storage beneath the coating device enabled the coating of multiple membrane cuts without opening the glovebox. This processing helped to reduce pressurised nitrogen consumption and maintained environmental conditions. Continuous production required a precise and time-wise optimised coordination which was realised by interconnection of all sub-systems in an efficient and effective manner. Figure 4-14 highlights the complete setup for the automated membrane coating.

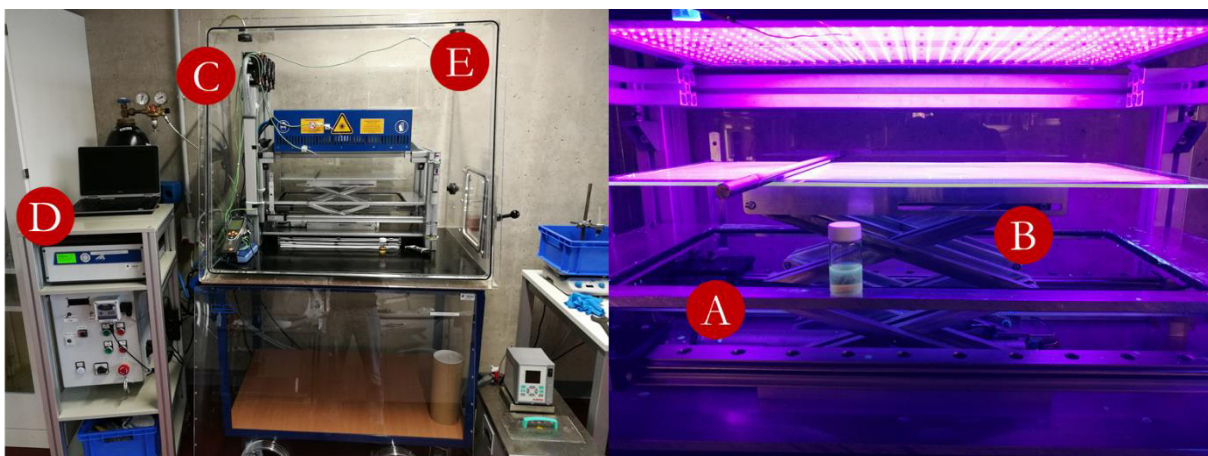


Figure 4-14 Membrane coating facility including (A) feed drive, (B) lifting platform, (C) cooling system, (D) electronic cabinet and (E) glovebox

The chosen design held the possibility of modular extension for further and different coating approaches.

For instance, as it was identified throughout extensive literature review, spray coating was expected to reduce pore intrusion and give high flexibility on the coating layer. This would enable coating several membranes and substrates independent of shape and size limited only by the maximum UV-LED exposure area of 250 x 550 mm. Various analogue and digital inputs/outputs of the A/D converter as well as Arduino microcontroller were vacant to implement e.g. a PBM feed pumps, feed motors and pressure sensors required for further upgrades.

4.3.4 Pilot scale setup

Using the automated machine, PBM coating upscaling was done within the VicInAqua pilot project, also listed in chapter 2.3.3. In total 68 membranes were coated and tested for treating domestic wastewater. One membrane module, comprising of 34 membrane sheets totalled to 3.125 m² active membrane area. Basically, extensive tests under real conditions were conducted to examine the PBM performance in comparison to commercially available PES membranes. Designed as flat-and-sheet (FS) module, the submerged MBR was integrated into a pilot plant next to the Lake Victoria in the East-African region. In Kisumu, Kenya, the MBR provided treated water for an aquaculture hatchery farm and agriculture land. Flux step tests were followed by a long-term operation at constant flux for two different PBM batches. Water samples were taken for a complete analysis at laboratories at the University Karlsruhe of Applied Sciences and the *DVGW-Technologiezentrum Wasser (German Water Centre)* to differentiate possible impacts of PBM coating the on-contaminant removal.

4.3.4.1 MBR setup and PBM module integration

The VicInAqua installation site was located in Kisumu, Kenya and setup next to a wastewater stabilisation pond (WSP) treating 29,000 m³ domestic wastewater on a daily average. The raw sewage was tapped and pumped into the MBR undergoing three stages of particulate removal. The first stainless steel strainer had a 2.5 mm mesh size followed by a plastic filter of 1-2 mm mesh size (excluded from Figure 4-15, right). Temporary buffering occurred in a 3 m³ tank which equated to the daily MBR capacity for the nominal load of 25 LMH. Before entering the MBR, a 0.8 mm cartridge pre-filter (*acuraline PBH 420, FUHR GmbH*) upfront the inlet removed smallest inorganic solids. Solid particulate removal is important for MBR long-term operation as abrasive particles damage the membrane, intensified by high cross-flow velocities (CFV) from the scouring process.

The MBR itself comprised of three treatment chambers merged to one cubic tank (illustrated also by Figure 2-4). Volumes for nitrification, anoxic and filtration chamber were 0.7, 0.44 and 0.56 m³, respectively. A static overflow between the chambers reduced auxiliary power units. Coming from the buffer tank, the raw sewage after solid removal was pumped inside the anoxic denitrification chamber. This was equipped with a mixer preventing sludge floc settling which supported homogeneous anoxic treatment. Subsequently, through overflow the wastewater flowed into the aerobic nitrification chamber. Aeration was done with a blower finely distributing the pressurised air via the installed diffusers to assure constantly good bacterial conditions.

One aspect was to guarantee enough dissolved oxygen that bacteria converted the present ammonium (NH_4^+) into nitrite (NO_2^-) and further to nitrate (NO_3^-). In addition, biodegradable processes crack C-components to a low molecular weight. The specified range for dissolved oxygen was given with 2-3 $\text{mg}\cdot\text{L}^{-1}$. This limited the energy input by the aerator since DO values above 3 $\text{mg}\cdot\text{L}^{-1}$ would not have beneficial impact on the biodegrading process, only unnecessarily elevating the energy consumption. DO values below 2 $\text{mg}\cdot\text{L}^{-1}$, however, stress the bacteria and causes EPS and SMP growth which can cause severe biofouling (further described in chapter 2.4.2). Aeration was done by simple on/off control.

The schematic diagram of the submerged MBR is depicted in Figure 4-15, excluding intake and permeate distribution. However, a UV-C lamp was installed downstream the sMBR to keep the option of sterilising the permeate water if required. A permeate pump connected to a 2 m^3 permeate collection tank finally distributed the clean water into the RAS and the agriculture. System control was done by a PLC system. The automated process kept the water recirculating between the three separated chambers. Capacitive pressure level sensors controlled feed and recirculation pump and switched of the filtration if the water level above the membrane modules dropped below a critical value. Table 4-6 lists the all energy consumers and installed sensors of the pilot MBR.

Table 4-6 Energy consumers and sensor system of the pilot MBR

QTY	Component	Model	Feature	Control mode
1	Sewer pump	<i>Pedrollo</i> VXCm 15/45	10..20 $\text{m}^3\cdot\text{h}^{-1}$	on/off
1	MBR feed pump	<i>Jung</i> U3KS	1.5..6.5 $\text{m}^3\cdot\text{h}^{-1}$	on/off
2	Level sensor (pressure)	VEGA WL52	0..4 m	
2	Level sensor (pressure)	VEGA BAR14	0..4 m	
1	Mixer	<i>Jebao</i> Jecod SW15	1..2..13 $\text{m}^3\cdot\text{h}^{-1}$	on/off
1	Redox sensor	<i>OxyGuard</i> K04GNV20RP	-600..+400 mV	
1	Air blower	Nitto LA 120	7.2 $\text{m}^3\cdot\text{h}^{-1}$	on/off
1	DO-sensor	<i>OxyGuard</i> D0243C	0.. 100% DO saturation	
1	Sludge pump	<i>Jebao</i> Jecod DCP5000	max. 5.5 $\text{m}^3\cdot\text{h}^{-1}$	on/off
1	Recirculation pump	<i>Jebao</i> Jecod DCP5000	max. 5.5 $\text{m}^3\cdot\text{h}^{-1}$	on/off
2	Permeate pumps	<i>Winter.Pumpen</i> GmbH	max. 7 $\text{m}^3\cdot\text{h}^{-1}$	PWM control
1	Air blower	LAM200	12 $\text{m}^3\cdot\text{h}^{-1}$	on/off
1	Air flow sensor	<i>Krohne</i> VA45 V/R,	1.7..17.0 $\text{m}^3\cdot\text{h}^{-1}$	
2	Cube® filters	<i>MARTIN Systems</i> , FM 611	2 x 3.125 m^3	
2	Filtration pressure sensor	VEGA BAR14	-1.0..+1.0 bar	
2	Permeate flow sensors	<i>IFM</i> SM4000	0.3..180 $\text{L}\cdot\text{h}^{-1}$	
1	PLC control unit	<i>Siemens</i> CPU 1510SP-1 PN	24 V DC; 0.6 A	

The hydraulic retention time (HRT) was 17 and 13.5 h for a 20 ($125 \text{ L}\cdot\text{h}^{-1}$) and 25 LMH ($156 \text{ L}\cdot\text{h}^{-1}$) operation, respectively. The HRT was calculated with the total volume of MBR with around 1,700 L.

It is well known to keep the mixed liquor suspended solids (MLSS) within an optimum range between 6-12 g·L⁻¹. Lower MLSS could result in a COD removal reduction but too high MLSS would increase the specific energy demand as the efficiency of aeration decreased due to higher sludge viscosity (MBR site, 2019). For the pilot tests, the MLSS ranged between 5 and 11 g·L⁻¹. Accordingly, the sludge retention time (SRT) was adjusted. Previous default settings of a daily 7% discharge (49 L) from the nitrification compartment were readjusted and sludge discharge controlled manually. The recirculation rate was set to 600 L·h⁻¹ (1200 L·h⁻¹, 50% operation time) from the nitrification into the filtration compartment. Higher flow rates would have caused substantial dissolved oxygen carryover into the anoxic denitrification compartment. Anoxic treatment processes are hampered above a 0.2 mg·L⁻¹ threshold. The installed REDOX sensor inside the anoxic chamber measured values between -520 to -440 mV indicating a highly reduced conditions for an effective denitrification (Gallert et al, 2015).

Figure 4-15 (left) shows the membrane sheets laminated to black frames which together made up a membrane module of in total 3.125 m² active membrane area. The installed FM 611 modules are usually supplied ex works with a 6.25 m² surface area but for pilot trials, every second laminated frame was a blank frame to reduce the installed capacity. Likewise, the manufacturer (*Martin Systems*) produced two batches of 34 PBM coated membranes. Lamination temperature was >200°C to meld the membrane polymer onto the frame margins with subsequent compression and a cool down under ambient conditions. The customized design was characterised by two paralleled membrane modules with a separate permeate line each. Performance monitoring was done with capacitive pressure sensors continuously recording the TMP of both suction lines. Magnetic inductive flow meters controlled the permeate pump speed to maintain the flux rate. For remote data processing and evaluation, the PLC was interconnected with pacific units (*OxyGuard*) transferring the readings to the *Nautilus* interface (*OxyGuard*). For type and manufacturer see Table 4-6.

Parallel installation allowed for accurate comparability. Both modules were exposed to the same environmental conditions including biological processes, sludge quality and hydrodynamic conditions. The FS membrane modules were not suitable for operative back-flushing. Adequate fouling mitigation was realised by an alternating operation set to a 12 min suction followed by a 3 min relaxation period to reduce membrane stress and enable higher scouring effectivity. CFV was high, induced by a 12,000 L·h⁻¹ air flow finely distributed with the diffusers as fine bubbles along the entire membrane module inflow. The blower cycle operation consisted of 9 min aerating and 1 min standstill.

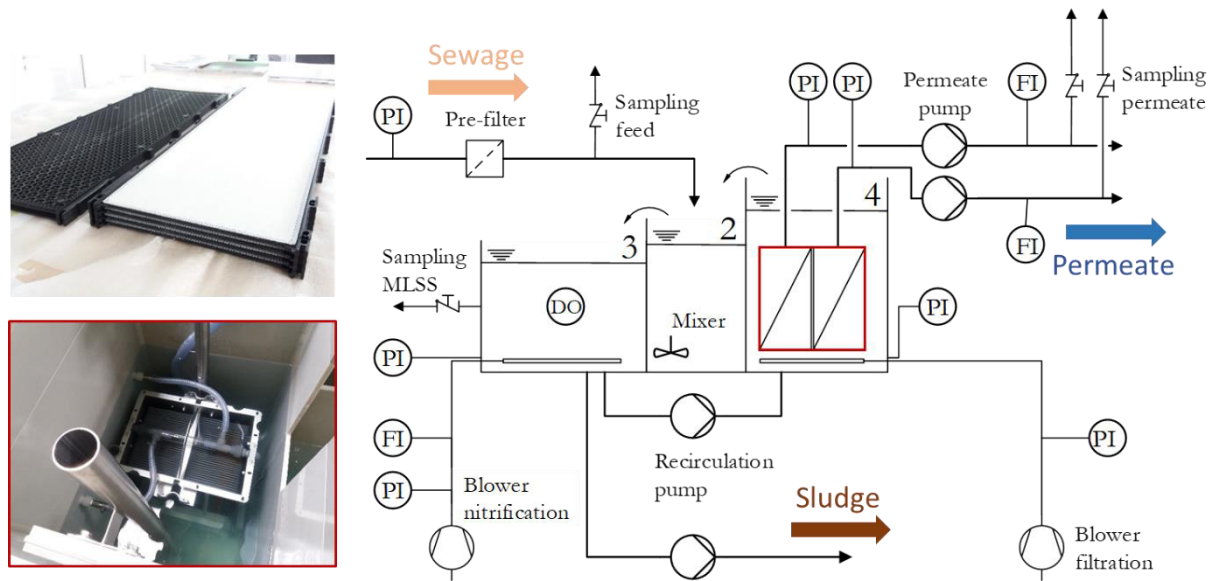


Figure 4-15 MBR schematic diagram (right) and PBM module integration

4.3.4.2 Methodology

Membrane performance tests

As described, two different membrane production batches were laminated and their performance studied by flux step tests methodology based on pertinent literature (Le Clech et al., 2003; Monclús et al., 2011) and for constant flux conditions. Moderate flux rates of 20 LMH ensured acclimation of membrane pores for both cases prior to actual testing. An in-situ cleaning was done prior to the test to achieve virgin membrane conditions. The flux step tests started after a 30 min module relaxation phase. Thereby, the flux was gradually increased by 5 LMH for each step covering a total test range of 5-50 LMH. One step contained two cycles of 12 min suction and 3 min relaxation. TMP was recorded continuously with a 10- samples·min⁻¹ sampling rate. Ultimately, the specific pressure increase was calculated following equation 4-5, also illustrated by Figure 4-16. Starting and end value of each cycle gave the average increase per cycle $dTMP_n$. With the reproduced second cycle $dTMP_{n-1}$, the average, time depended specific transmembrane pressure increase was calculated. By applying high stress, also in terms of enforced fouling, it was a first indication of how the membrane operated in the given environment. A basic trend of the critical flux value was also derived.

$$\frac{dTMP}{dt} = \frac{dTMP_n - dTMP_{n-1}}{dt} \quad 4-5$$

Flux step tests were duplicated after a second thorough in-situ alkaline cleaning using 1000 mg·L⁻¹ sodium hypochlorite (NaOCl) and 2,000 mg·L⁻¹ sodium hydroxide (NaOH) followed by an acid cleaning using 4.8 g·L⁻¹ citric acid. Residual chlorine neutralisation was performed with roughly 100 mg·L⁻¹ hydrogen peroxide (H₂O₂) solution. A gentle recirculation through the membranes enabled internal pore cleaning. The procedure followed the official recommendation for submerged membrane cleaning given by the manufacturer (*Martin Systems*).

The harsh chemical cleaning in combination with the high stress during the flux step tests at high flux rates of 50 LMH was a serious stress test for the innovative low-fouling coating.

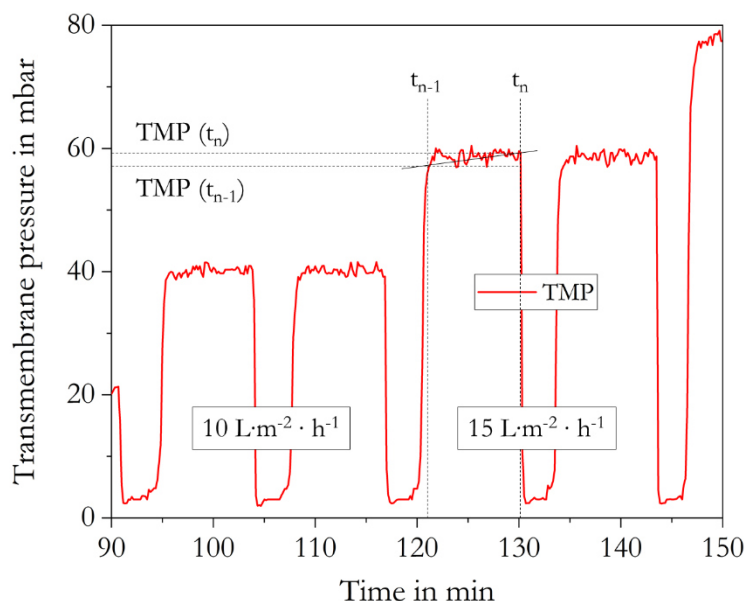


Figure 4-16 Methodology for flux step tests and long-term operation

After testing the first batch, both modules were replaced by the second PBM batch as well as a virgin PES module to obtain comparability. Long-term-tests at constant flux conditions were carried out after a short pore acclimation at 10 and 15 LMH. The flux rate was increased from 20 LMH to 25 LMH and pilot scale tests covered a 137 days operation period. Subsequently to the tests, the membrane modules were disassembled and membrane samples cut out for a final assessment. Focus was given on the PBM stability validated by FTIR measurements and filtration performance tests in the laboratories of the *University Karlsruhe of Applied Sciences*. The Mixed liquor suspended solids (MLSS) was around $6 \text{ g}\cdot\text{L}^{-1}$ for the flux step tests measured prior to the experiments and between $5\text{-}11 \text{ g}\cdot\text{L}^{-1}$ in the long-term.

Water analysis

Comprehensive water analysis for the MBR inlet and the permeate quality for both modules were conducted at the laboratory of the *Karlsruhe University of Applied Sciences* and the *DVGW-Technologiezentrum Wasser (German Water Centre)*. It was presumed that PBM coating could result in better contaminant removal due to the additional layer resistance and the denser structure. Ion measurements were done after sample-pre-filtration using $0.45 \mu\text{m}$ filter mesh with the ion chromatograph *Metrohm 883 Basic IC plus* (column: *Metrosep A Supp 4*). The total organic carbon analyser *TOC-L CPH/CPN (Shimadzu)* concluded the analysis with TOC, TIC and TN measurements. Electrical conductivity measurements and pH level was measured by handheld units type *Cond 315i* and *pH 325 (WTW)*, respectively. COD analysis was done with cell tests (1.14541) using the spectrophotometer *Spectroquant® NOVA 60 (Merck KGaA)*. MLSS samples were taken from the nitrification chamber (Figure 4-15, right) after 2 min of continuous aeration to maintain a homogeneous sludge distribution. Weight of dry residues of both, the nitrification chamber (total solids, TS) as well as the permeate line (total dissolved solids, TDS) was taken with the balance *DELTA-500* (max. $500^{\pm 0.1} \text{ g}$).

Subtraction of both values gave the MLSS inside the nitrification chamber. In addition, water analysis on heavy metals and antibiotics was conducted. The analysis equipment and analysed parameters are listed in Table 4-7.

Table 4-7 Permeate analysis on heavy metals and antibiotics

Parameter	Unit	Equipment	Standard deviation STD	Detection Limit DT
pH	pH scale	Handheld sensor, Cond 315i, <i>WTW</i>	±0.1	
El. conductivity	µS·cm ⁻¹	Handheld sensor, pH 325, <i>WTW</i>	±10	
COD	mg·L ⁻¹	COD cell tests (1.14541), spectrophotometer Spectroquant ® NOVA 60, <i>Merk KGaA</i>	±4.9	
TOC	mg·L ⁻¹	Total Organic Carbon analyzer (Model: TOC-L CPH/CPN, <i>Shimadzu</i>)	±0.5	
TIC	mg·L ⁻¹		±0.5	
NH ₄ ⁺	mg·L ⁻¹	Ion chromatograph Metrohm 883 Basic IC plus; column: Metrosep A Supp 4	±0.14	
NO ₃ ⁻	mg·L ⁻¹		±0.8	
TN	mg·L ⁻¹	Total Organic Carbon analyzer (Model: TOC-L CPH/CPN, <i>Shimadzu</i>)	±1.0	
PO ₄ ³⁻	mg·L ⁻¹	Ion chromatograph Metrohm 883 Basic IC plus column: Metrosep A Supp 4	±0.1	
SO ₄ ²⁻	mg·L ⁻¹		±0.8	
Cl ⁻	mg·L ⁻¹		±0.5	
Na ⁺	mg·L ⁻¹		±0.1	
K ⁺	mg·L ⁻¹		±0.1	
Mg ²⁺	mg·L ⁻¹		±0.5	
Ca ²⁺	mg·L ⁻¹		0.5	
Cd	mg·L ⁻¹		7900 ICP-MS, <i>Agilent</i>	±6.4% ^a
Cu	mg·L ⁻¹	±7.9% ^a		0.01
Zn	mg·L ⁻¹	±7.0 % ^a		0.02
Pb	mg·L ⁻¹	±7.0% ^a		0.001
Hg	mg·L ⁻¹	AAS Hg-Analysator, <i>Mercur</i>	±11.1% ^a	0.00005
Ciprofloxacin	ng·L ⁻¹	Chromatograph HPLC 1200 Series, <i>Agilent</i> Detector triple quadrupole mass spectrometer 4500 MS/MS (ESI) (positive mode), <i>AB Sciex</i>	±9.5/20.1% ^a	100
Metronidazol	ng·L ⁻¹		±13.8/42% ^a	50

^aExtended measurement uncertainty (STD, pipetting errors including random measuring errors)

Within chapter 6.3, a detailed water analysis including comparison of both modules, PES and PBM, is given.

4.3.5 *Spray coating setup*

Different approaches were sought to solve the issue of membrane pore intrusion. Supplementary to the PBM viscosity modification using controlled radical polymerisation, the application of spray coating was studied. Contrary to casting coating knives exerting pressure and friction forces on the PBM, the atomised PBM droplets settle smoothly on the membrane surface, only driven by the kinetic and gravitational energy. Hence, the coating material was not pushed into the membrane pores which potentially resulting in lower pore intrusion levels.

Until now, to the author's knowledge, no studies have been published about PBM coatings applied with an automated spray coating device. To assess the feasibility and verify the process more thoroughly, the described jet and duel fuel nozzles were studied, the relevant parameters for each system tested and finally compared.

Experiments were conducted in a separate glovebox. This reduced the construction expenditure for integration into the existing automated coating machine. Nevertheless, the spray coated membrane was put into the nitrogen inflated glovebox and polymerised as customary with the UV-LED lamp. Prior to the membrane coating with PBM, preliminary investigations were performed:

- (1) to achieve first visual impressions about microemulsion formulation as a result of the PBM pressurisation
- (2) to verify the stability by FTIR analysis comparing the liquid PBM before and after spray coating. Therefore, peak shifts in absorbance spectra would indicate phase separation (reference see Figure 4-3)
- (3) to evaluate both concepts for PBM coating feasibility.

The setup was designed in such way that integration into the existing automated coating machine was generally possible. System parameters were taken from the automated casting coating attempt. Thus, the target wet coating layer thickness was 4 μm , the total coating area 0.11 m^2 and the feed speed of the carriage 6 $\text{cm}\cdot\text{s}^{-1}$ for homogeneous spray layers. This resulted in a 3 $\text{mL}\cdot\text{min}^{-1}$ and 10 $\text{mL}\cdot\text{min}^{-1}$ nozzle throughput for corresponding 0.4 mL and 1 mL PBM coating material, respectively (therefore see section 4.3.3).

4.3.5.1 *Pressure nozzle*

The jet nozzle for pressure atomisation has an elliptical bore defined by the equivalent bore diameter A (0.2 mm) and the narrowest cross-section E (0.12 mm; also see Figure 2-9). The very small opening makes the nozzle susceptible to blockage e.g. by impurities and foreign matter. The starting value for the parameter investigation was calculated using equation 2-16 and data given above. For directly comparing spray and casting coating, the volume flow should be assumed to be maximum $\dot{V}_2=10 \text{ mL}\cdot\text{min}^{-1}$ which is the required volume for one membrane coating. \dot{V}_1 and p_1 could be obtained from the manufacturer's data sheet with 50 $\text{mL}\cdot\text{min}^{-1}$ at 2 bar. This results in a 0.8 bar pressure (relative) for a 1 mL PBM coating using the jet nozzle.

$$p_2 = \left(\frac{10 \frac{\text{ml}}{\text{min}}}{50 \frac{\text{ml}}{\text{min}}} \right)^2 \cdot 2 \text{ bar} \rightarrow p_2 = 0.8 \text{ bar}$$

Yet, the manufacturer's guideline was given with $p_{\min}=2$ bar for a homogenous droplet formation. Thereby, the desired $10 \text{ mL}\cdot\text{min}^{-1}$ volume flow was not applicable. To meet the manufacturer's recommendation, a $50 \text{ mL}\cdot\text{min}^{-1}$ volume flow theoretically results in a $67 \mu\text{m}$ wet coating layer thickness. This would increase the resistance of the generated PBM coated membrane considerably (equation 2-2). However, to deepen the knowledge about this technology and to better understand the hydrodynamics of different spray principles, pressure atomisation was included into preliminary investigations.

Figure 4-17, left, depicts the implementation of the jet nozzle as pressure atomiser into the existing setup. It was directly connected with a reservoir serving as pressurised PBM buffer, similar to common rail injection systems. The PBM was filled in the "rail" from the top and was sealed with a screwable end-cap. The nitrogen bottle ($50 \leq x \leq 200$ bar) was opened to start the coating process, whereby the pressure regulator throttled the nitrogen inflow to the desired pressure ($p_{\min}=2$ bar for jet nozzle). The PBM reservoir and main connections were designed as quick couplings for possible constructional changes and cleaning purposes. A magnetic valve to start and stop the spray process was connected upfront the reservoir to avoid pre-expansion/atomisation by cross section rejuvenation as existing in the magnetic valve.

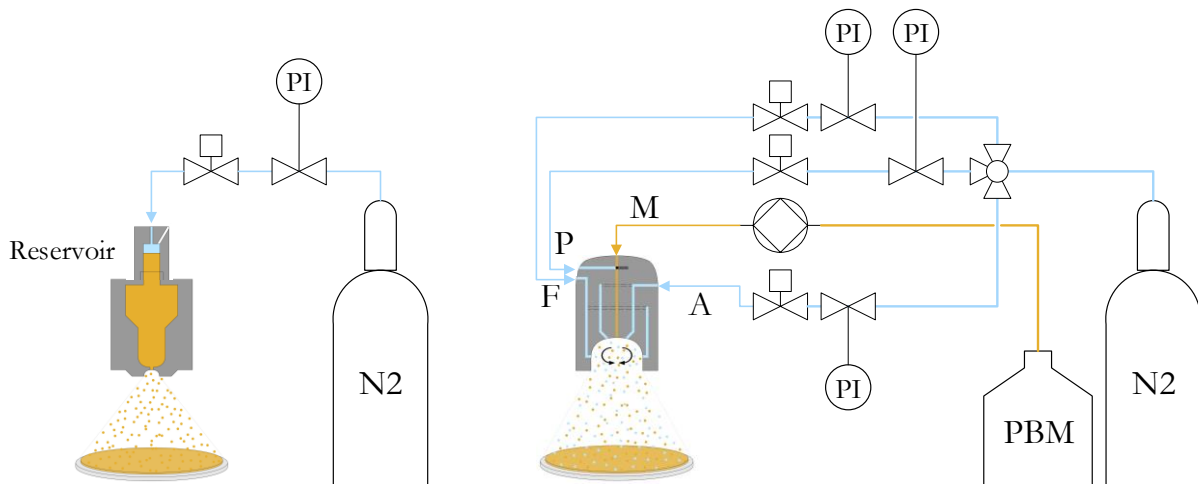


Figure 4-17 Spray coating setup with implemented pressure atomiser (left) and duel-fuel nozzle (right)

4.3.5.2 *Duel-fuel nozzle*

The extreme low throughputs limited the operational scope of the chosen equipment, likewise for the duel-fuel or assisted nozzle. Considering upscaling to industrial scale and integration into given membrane production lines, higher flow rates were expected depending on membrane width and coating thickness.

Lechler GmbH offers a relatively inexpensive but high quality *ViscoMist* duel-fuel nozzle with high flexibility in spray mist configuration. The spray cone shape could be adjusted with the four connection ports; the piston port (P) to close the nozzle aperture for protection; the liquid port (M) for continuous spray material supply; the atomisation port (A) which determines the overall droplet size; and the fan air port (F) which influenced the cone width.

With this approach, it was possible to finely adjust and independently set the droplet diameter, diameter size distribution and mist width (Figure 4-18, right). Independent parameter setting was achieved with the separate air inlets for the assisting pressurised gas (dry nitrogen, N_2). Each line was equipped with a pressure regulator and indicator. The cone shape varied greatly with the distance of the nozzle head to the membrane. Corresponding values for water at 20°C and variations in the spray parameters are highlighted below in Figure 4-18.

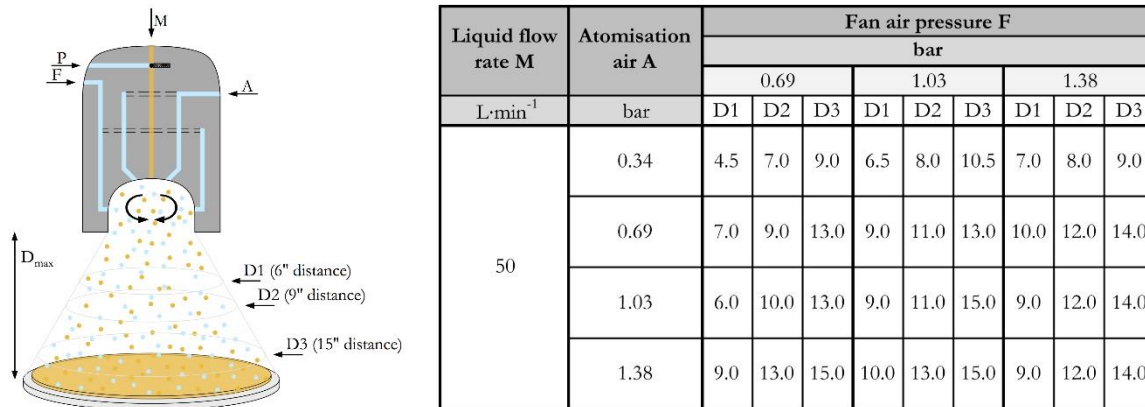


Figure 4-18 Approximate spray coverage at specific nozzle distances, parameter pairing (adapted from Lechler, 2019)

4.3.5.3 *System description*

Each inflow required a separate pressure regulator and a solenoid valve for actuation (type *M214 ES 24V*; NC=normally closed). It was the goal to ultimately integrate spray coating into the existing automated coating process. 24 VDC magnetic valves were connected to a Darlington array to enable controlling via a separate *Arduino* microcontroller, as illustrated by Figure 4-19. The *Arduino* microcontroller triggered the transistors by sending a 5 VDC signal with a small 50 mA current. This current opened the transistor gates and enabled a bigger current (24 VDC) to flow through the transistor and actuated the installed valves. With the additionally integrated manual pressure regulators *EN 837-1 (WIK)* the spray parameters P, A and F could be adjusted within a given range of 0-2.5 bar absolute. A venting valve in port P could release trapped air inside the nozzle head after process shutdown. The applied pressure to port (P) did not have any further effect on the spray mist generation contrary to the spray pressure (A) and (F).

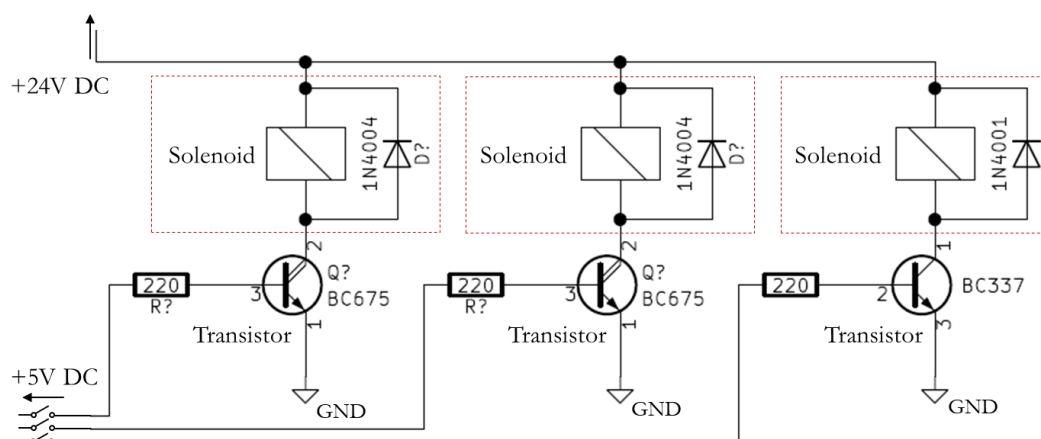


Figure 4-19 Electric circuit for solenoid valve actuation (spray mist control)

Besides the spray pressure control unit, the liquid flow rate to port M was continuously provided with an adjustable, peristaltic pump (*EcoLine VC-MS/CA8-6, Ismatec*).

Possible volume flow rates were $0.005\text{--}150\text{ mL}\cdot\text{min}^{-1}$ depending on motor circulation speed and hose inner diameter. Basic electronic installations were performed for a 0-230 VAC supply and could be controlled manually with built-in push buttons or via the Arduino board, connected via an external analogue connection. The entire circuit diagram can be found in annex A.3.

The pump head was equipped with an 8-channel system which enabled the liquid supply of up to 8 different nozzle heads. This is highly beneficial in terms of spray coating upscaling to even larger membrane areas. Despite the modification with a second spray nozzle, a linear guidance two-axis (xy-) system could move the membrane below the nozzle to achieve complete surface coverage. Installation of a moveable spray nozzle in three dimensions (x-y-z) was found to be too complex and less space-saving. In case of the herein used setup, a one axis linear guidance system *ZLW-0630-B (igus® GmbH)* moved the membrane below the nozzle head in y direction. The feed speed range was comparable with the preferred casting speed. The direct current motor *MOT-DC-37-M-A-B (igus® GmbH, 0.3 Nm)* came with a gearbox and 24 VDC PWM control. The feed speed was adjustable within the range of $5\text{--}25\text{ cm}\cdot\text{s}^{-1}$. However, for initial tests, $6\text{ cm}\cdot\text{s}^{-1}$ were chosen which correlated to the casting coating speed of the automated coating machine. The linear guiding system with a toothed belt had a 600 mm total stroke to coat the membrane in full length. Subsequently, the sprayed PBM coating was polymerised in the separate glovebox with the UV-LED lamp.

Similar than for the automated casting coating machine, an implemented display showed the current status of the spray coating process. To give the reader a better overview, Figure 4-20 shows the final spray coating setup including all described components. Atomisation was also done in a completely sealed glovebox to avoid distribution of very fine droplets inside the laboratory.

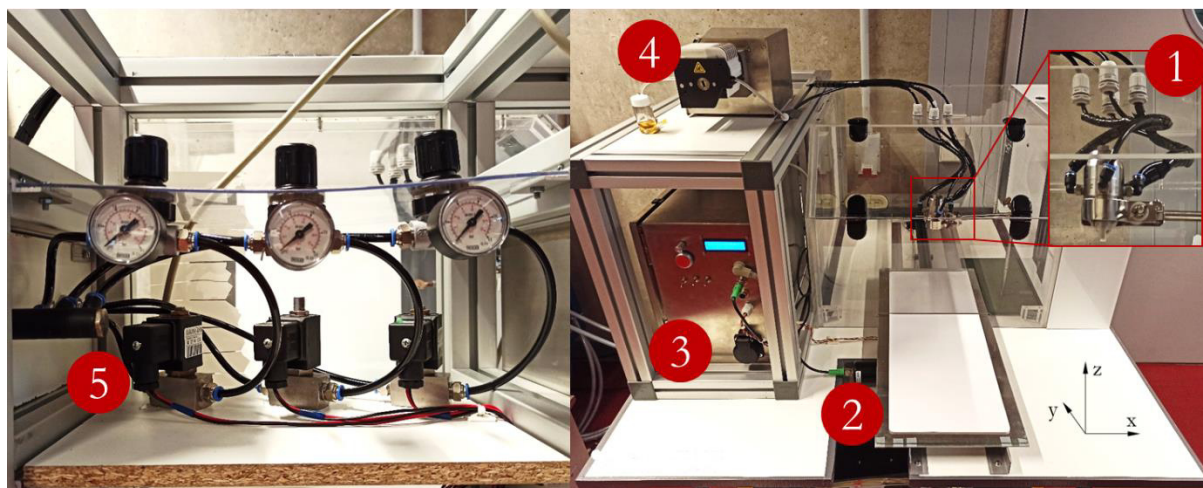


Figure 4-20 Spray coating setup with (1) duel-fuel spray nozzle (2) feed drive (3) control cabinet (4) PBM supply pump (5) pressure regulation system

Duel fuel-nozzles enable a flexible spray cone shape and thus a change in the substrate coverage. For the lab experiments, the spray parameters A and F were successively adjusted from 0.5 to 1.8 bar (absolute). The aim was to achieve complete membrane spray coverage in the membrane width (x-axis). The liquid PBM flow rate was calculated with a 1.5 g total spray volume for a total membrane coverage within 9 seconds ($6 \text{ cm}\cdot\text{s}^{-1}$). The distance from membrane to the nozzle opening was held constant at 21.5 cm.

Since large coating quantities should be produced on a high homogeneity level, the spray mist shape was quantified with other liquids first. Pre-trials were carried out with DI-water, ethanol ($\text{C}_2\text{H}_6\text{O}$) and 1-Octanol. Water and ethanol show similar dynamic viscosities with 1 to 1.26 mPa·s. According to pertinent literature, ethanol however has a three times lower surface tension with 21.6 to 72.1 $\text{mN}\cdot\text{m}^{-1}$ for DI-water (20°C). In this way, the influence of surface tension on the spray coverage was examined. 1-Octanol has comparable values than the pristine PBM, as validated within chapter 5.7 and 6.2.1, with 7.5 mPa·s (25°C) and 27.6 $\text{mN}\cdot\text{m}^{-1}$ (20°C). The results obtained should give a better understanding to set appropriate parameters for atomising the PBM solution. The testing procedures followed the manufacturer guideline (Figure 4-18, table on the right) for water. The table lists the parameter pairing for the approximate spray coverage at specified distances from the nozzle aperture to the substrate (membrane).

The studies for homogeneous spray pattern was inspired by the work of Wei et al (2009). The examination of spray coverage along the membrane width (20.5 cm) was conducted using 9 flasks in a 2.5 cm distance to each other, placed below the nozzle (Figure 4-21). For the spray coverage tests, the distance between centred nozzle and membrane was $D=14.2 \text{ cm}$ resulting from test setup construction and test tube height. The experimental duration was 5 min and the liquid was continuously sprayed to get high spray volumes for all measured spots and reduce the influences of measurement inaccuracies. Each sample was weighed before and after the spray tests to precisely determine the sprayed volume as a function of centre distance. Reference values were taken for DI-water first.

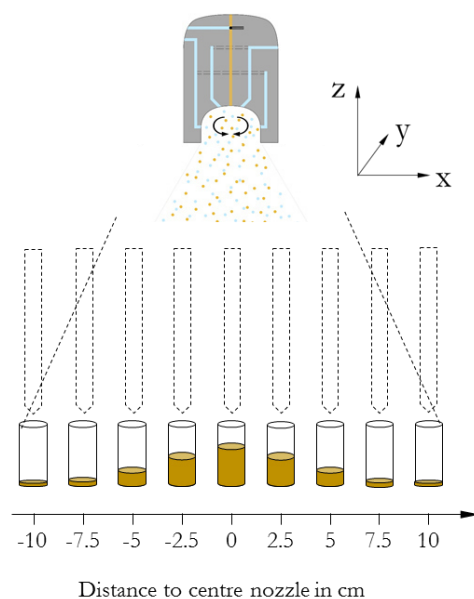


Figure 4-21 Validation of Spray coverage, adapted from Wei et al. (2009)

4.3.5.4 *Challenges for PBM atomisation using piezo ceramics*

Microemulsion generally shows a low surface tension compared to water (Prince, 1977). This enables much smaller droplet sizes at similar frequencies but smaller volume flows can be achieved according to equation 2-18. To increase the volume flow to the required 0.4 and 1 ml per coating, respectively, the effective nozzle tip area and energy input has to increase substantially.

Considerably more challenging is the concurrent atomisation of all components present in the PBM to avoid phase separation. As described, one defined system setting refers to one application using one liquid phase only. More specific, the chosen piezo ceramic element vibrates at a defined frequency and would differently excite the water, oil, surfactant, co-surfactant and cross-linker phase. When the critical frequency of one component is reached, droplets of this specific liquid only separate from the PBM bulk phase. Others are only excited into instable atomisation levels without droplet separation and droplet collapse occurs. Whereas for MMA ($41.6\text{--}42.5 \text{ mN}\cdot\text{m}^{-1}$) the critical frequency is lower, water ($72.9 \text{ mN}\cdot\text{m}^{-1}$) shows much higher values (Polymerdatabase, 2019). Therefore, it is much likely to have phase separation breaking the bicontinuous or micellar structure which would change the microemulsion formulation. The actual phenomena clearly depend on the interfacial tension and the actual microscopic forces in the interfacial section.

These are considerations made during PBM spray coating developments and imply the complexity of ultrasonic systems. For the future, it might be wise to exactly define material-specific values such as critical frequency and the achievable droplet size for each PBM component. An initial evaluation of the PBM formulation performed before and after ultrasonic application would help to identify possible phase separation using FTIR analysis. This approach was also used for the duel fuel spray coating technology. However, due to the described key challenges this approach was not further investigated and is moreover presented for the sake of completeness covering possible spray coating attempts.

5 Preliminary Experimental

The study of relevant coating parameters and conducted experiments focused on testing the PBM coating on larger scale, treated raw domestic wastewater. To better understand the author's intentions behind the developed experimental setups, chapter 5 gives a comprehensive explanation of preliminary investigations and the findings stemming therefrom. Preparatory measures were taken to obtain a high qualitative coating layer with a high reproducibility. Specifically, FTIR analysis focused on the polymerisation degree of PBM drops polymerised at different spots below the UV-LED lamp to validate the uniformity of layer polymerisation. The need for an automated coating machine is discussed. Manual and automated casting coating were compared by the visual contrast of a food dye, wet layer coating film. Moreover, the influence of casting coating speed and contact pressure of the casting knife to the membrane was tested on their coating layer integrity using food dye. Two casting knives of different principle were examined to select the optimum one for further test series. Confocal light microscopy was used to quantify the pore intrusion depth into the PES membrane structure using fluorescent nanoparticles. They were finely dispersed in the PBM prior to the coating procedure. Pre-trials and the identification of the best possible setting for membrane upscaling were vitally important. Subsequent sections will therefore highlight important information about considerations which led to further research activities.

5.1 Polymerisation homogeneity measured with FTIR

Results for the conducted drop polymerisation at different distances to the LED focal points are shown in Figure 5-1. The software in-built normalisation methods analysed the entire absorption spectrum and examined each peak in relation to every peak in the measured spectrum. Since measurements were taken for one material composition only, correlations between each measurement could be established and the peak height was adjusted. This procedure was done for the $\text{H}_2\text{C}=\text{CH}_2/\text{C}-\text{H}_3$ ratio which changed during the course of the polymer change growth. Figure 5-1 contains the results after normalisation for the $\text{H}_2\text{C}=\text{CH}_2$ molecular bond at around 813 cm^{-1} which decreases in the course of the polymerisation (left). Despite the polymerisation of 19 drops, only 16 were analysed due to material loss during the scraping off. In overall, the degree of polymerisation calculated by the present peak height was $>90\%$ for 75% of the drops. Maximum deviation from the reference value (“1” as 100% conversion rate) was calculated to an 81% conversion rate. Overall, the data were mostly in line with the manufacture’s indication of a $>90\%$ uniformity in irradiation distribution, given at the centred focal point of 10 mm UV-LED distance (chapter 4.2.5). The $5\text{ }\mu\text{L}$ drops were applied manually and were different in shape and thus drop height due to a highly hydrophilic glass plate and a possible electrostatic charge. Moreover, scraping of the polymerised PBM drop from the glass plate caused small cracks inside the solid material. This was an indication of complete polymerisation but cracks interrupted deflection of the infrared beam which was caused variations in the FTIR spectrum.

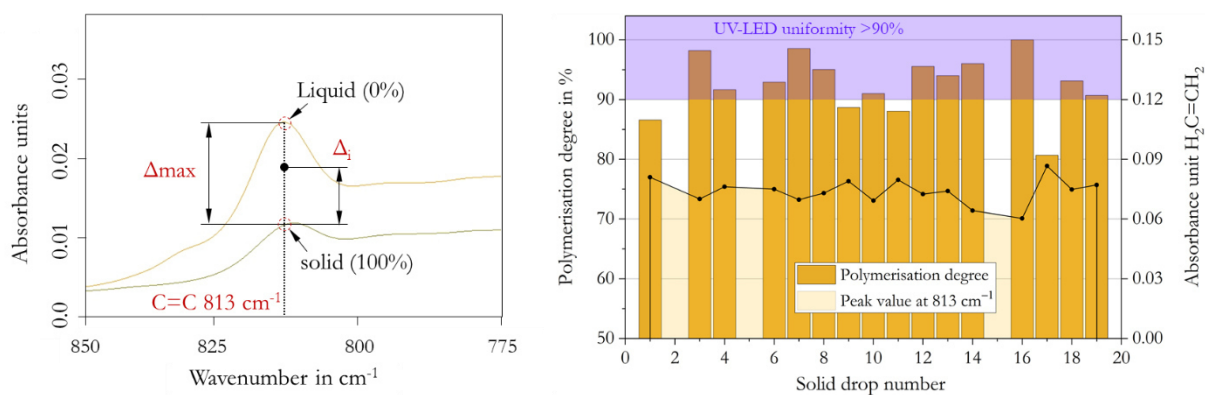


Figure 5-1 FTIR measurements for polymerised $5\text{ }\mu\text{L}$ PBM drops, peak analysis at 813 cm^{-1} ($\text{RC}=\text{CH}_2$ bond)

The results have satisfyingly high reproducibility considering the measuring errors resulting from the equipment used (see Table 4-3). Therefore, irradiation distribution of the UV-LED lamp was further regarded as reasonably constant and the deviations considered to be of no significant influence to the polymerising PBM layer. However, the polymerisation time was extended from 30 s to 60 s to achieve complete and even polymerisation in regards to the few larger deviations occurring in the measurements.

5.2 Uneven coating layer

Initial casting coatings were done manually. The applied layer was found to be highly inhomogeneous in wet film layer thickness across the membrane surface.

This was demonstrated with visual experiments using food dye solutions of different viscosities. In all cases a wave-shaped height profile occurred, highlighted by the varying contrast in Figure 5-2, left.

These irregularities were an obstacle for the high reproduction goals, and specifically for membrane characterisation. Large changes in coating layer thickness make punctuated investigations arbitrary. On the opposite side, similar experiments conducted with the automated coating machine showed evenly smooth surface layers achieved by a steady casting speed and contact pressure (Figure 5-2, right). This was clearly indicated with the even contrast along the entire coated membrane surface. The experiments were reproduced with different food dye to get the highest possible ink coverage. In the shown case, the black and white illustration was chosen to increase the contrast for a better visualisation.

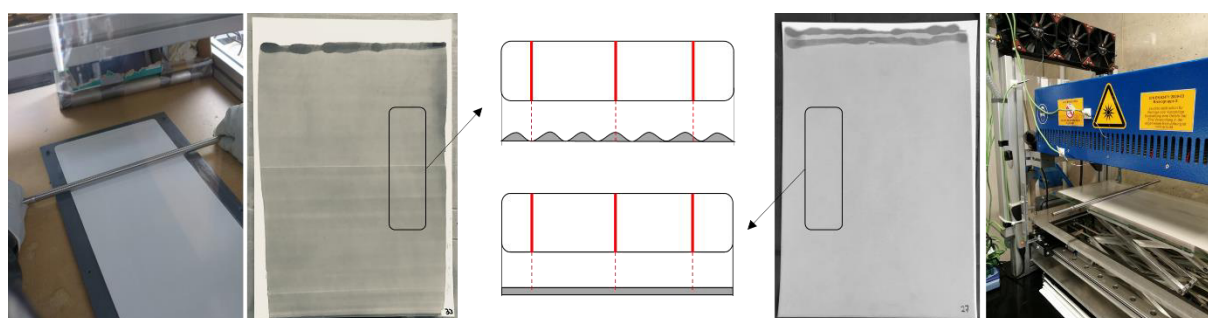


Figure 5-2 Coating layer thickness with manual (left) and automated (right) casting coating, visualised by food-dye experiments

Hence, automated coating is a great tool to maintain constant coating quality and high reproducibility for any characterisation method applied. The more uniform coating layer thickness could also improve the low-fouling properties as punctual fouling is reduced for very thin coating layer spots. Inhomogeneous fouling propagation can ultimately result in a sudden TMP jump, as explained before in chapter 2.4.3. Contrarily, spots of very high layer thickness might not become completely cured which could then cause partial detachment of PBM from the membrane during the water filtration process.

5.3 Casting coating tool

Figure 5-3 displays permeability values for DI-water and humic acid solutions for commercial as well as the two PBM membranes coated with two different casting tools. The experiments were conducted at 0.5 bar TMP. The results show that the deviations between the spiral-casting knife (8 and 4 μm , respectively) and the film applicator (17.5 and 10 μm , respectively) were negligibly small and within the given tolerance. However, the comparable high production tolerance of $\pm 10 \mu\text{m}$ for the universal applicator reduced the smallest possible layer thickness to 17.5 μm . Slight curling and wave movements of the membrane during the casting coating procedure prevented a further reduction since large surface areas would remain uncoated. It should be pointed out that thicker membrane coating layers should also result in a drop of permeability (see equation 2-2). However, this was not the case which indicated a difference in the casting process. The spiral-casting knife maintained direct contact with the surface along the entire membrane width. This was beneficial for a highly homogeneous wet film thickness.

The manufacturer (*TQC*) states very low production tolerances of $\pm 2 \mu\text{m}$ for this casting tool. In comparison, the film applicator (*Zehntner*) only contacted the membrane with the two lateral slides (Figure 4-1). This construction reduced the friction between applicator, liquid PBM and solid membrane. This positive influence on the coating dynamic could prevent the PBM to “be pushed” inside the membrane pores. The higher occurring friction and potentially higher pore intrusion caused by the spiral casting knife might be the reason for similar permeability of around $96^{\pm 18}$ to $98^{\pm 12} \text{L}\cdot\text{h}^{-1}\cdot\text{m}^{-2}\cdot\text{bar}^{-1}$ despite a thinner wet layer film thickness. Figure 5-3 also shows mean values for the commercial UF PES membrane which is significantly higher for clean water tests but shows a steep drop to $138^{\pm 29} \text{L}\cdot\text{h}^{-1}\cdot\text{m}^{-2}\cdot\text{bar}^{-1}$. Humic acid fouling is stronger at a comparable TMP as higher flux rates prevail for the more porous separation layer (PES).

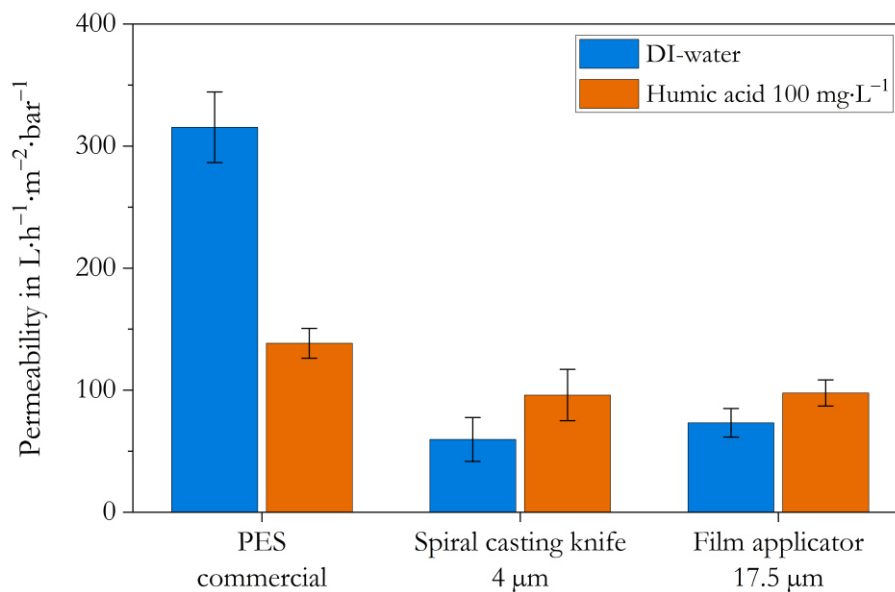


Figure 5-3 Permeability test for different casting coating tools (left)

Casting coating attempts showed comparable permeability for both tools. Nevertheless, despite the assumption of a higher pore intrusion provoked by potentially higher friction forces, all listed casting coating experiments were conducted with the spiral-casting knife only. Several benefits can be highlighted:

- A highly controlled wet film thickness and a low tolerance of the fixed spiral wire thickness resulting in high reproducibility
- Simple implementation into the automated coating assembly (no additional guidance required)
- Commercially available spiral casting knives cover the entire 205 mm membrane width. For film applicators, this special coating area required customised products of considerably higher invest costs.

Figure 5-3 clearly shows an increase in permeability for the humic acid solution (orange columns, $100 \text{ mg}\cdot\text{L}^{-1}$) relative to the clean water filtration, represented by the blue columns. This effect has been observed more or less pronounced through entire UV-LED initiated casting coatings but the mechanisms behind still remain unclear. Contrarily, REDOX polymerised coating layers showed a drop in permeability for model wastewater tests (Deowan, 2013; Galiano, 2013).

It was suspected that the exceptional rise was provoked by a different polymer structures which were shown to deviate with the polymerisation approach (SEM, NMR).

5.4 Casting coating parameter adjustment

The coating speed was a decisive parameter for thin and homogeneous coating layers. The optimum feed speed changed with the coating substrate and in specifically the coating material itself. Bearing this in mind, for this study, it was deemed useful to investigate and verify adequate casting coating speeds for PBM coating on top of the commercial UF membranes. Different casting speeds were set and the ability for complete surface coating evaluated. A coating degree was defined to better compare different attempts on their coating integrity. Therefore, the coating degree ζ (equation 5-1) was defined as the ratio of the coated area A_{coated} to the total membrane area A_{membrane} .

$$\zeta = \frac{A_{\text{coated}}}{A_{\text{membrane}}} \quad 5-1$$

During these preliminary experiments, the coating speed, contact pressure and thus friction between coating material and substrate were varied to better understand the casting process. Finally, the settings of the automated coating machine for upscaling PBM coatings were adjusted accordingly. The results are shown in Figure 5-4. The membrane surface was divided into 154 segments and the coating degree manually counted. Casting speed variations were done by changing the motor voltage between 5, 10 and 24 VDC. The results gave a higher coating degree for the highest casting speeds, indicated by the degree factor $\zeta=0.85$, 0.88, 0.92, respectively. A 5% surface loss was considered for the edge losses of the highest speed when manually applying the food dye. Contact pressure variations were achieved by using aluminium knife holders of different sizes and thus weight. Values in Figure 5-4, bottom-right, are production-related and result from the density of aluminium.

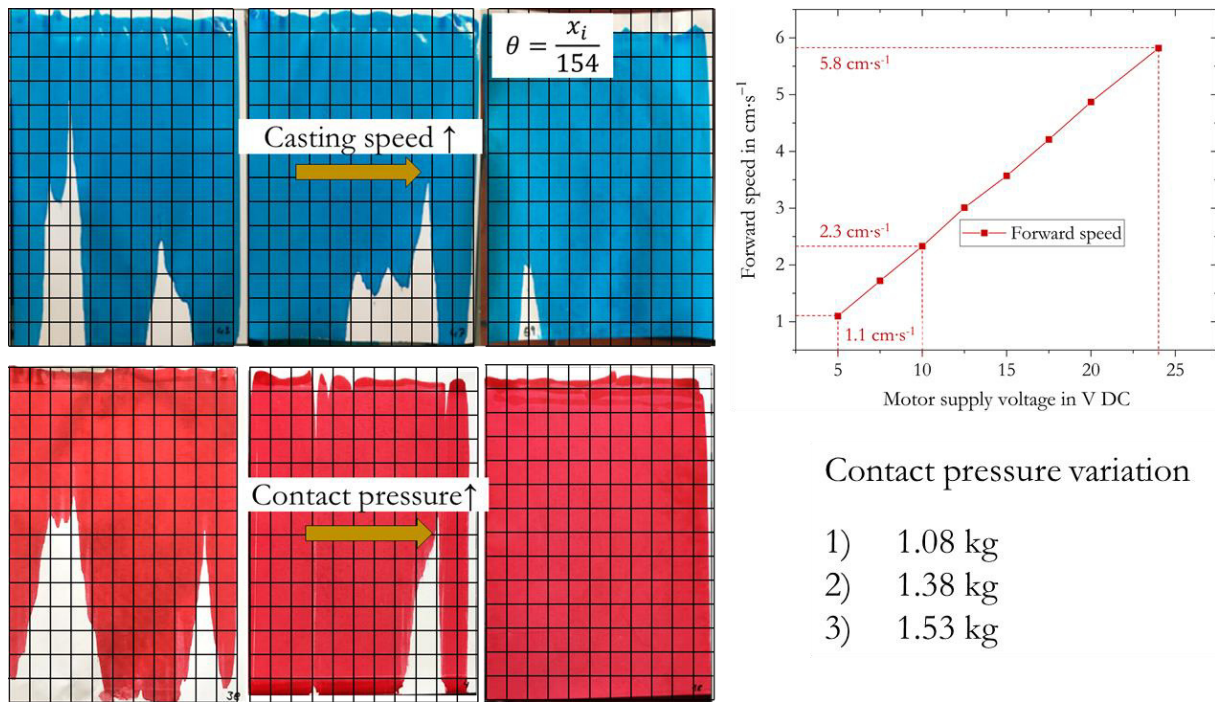


Figure 5-4 Coating degree ζ increasing with higher casting speed and higher contact pressure

In summary it can be stated that higher casting coating speeds and pressures generally yield higher coating degrees ζ .

These pre-tests were done with the spiral casting coating knife of 20 μm thickness (*TQC*) to get a higher ink coverage resulting in better contrast for the evaluation. Food dye viscosities were adjusted to the virgin liquid PBM using an Ubbelohde viscometer (PBM values given in chapter 6.2).

5.5 Membrane pore intrusion phenomenon

PBM pore intrusion was visually measurable and was first confirmed by manually coating of two PBMs with varying viscosity. First studies for modifying the PBM intrusion were inspired by Schmidt who used polyethylenglycol (PEG, $\text{C}_{2n}\text{H}_{4n+2}\text{O}_{n+1}$) of different molecular weights as a viscosity enhancer. He concluded that PEG 20,000 reduced pore intrusion successfully if used in very high amounts (15 w% of PBM). However, this came at a cost of very poor membrane performance as the PEG created highly dense membrane coating layers (Schmidt, 2016). PEG is water-soluble and is theoretically washed out during the filtration. The higher the molecular weight, thus longer molecular chain length, the higher the risk of interference with the prevailing interfacial forces between the water and oil (MMA) phase in the PBM. Therefore, a short-chain polymer PEG 400 was dissolved in the PBM for the herein described tests. The pristine and modified PBM were manually suspension on the PES membrane and Figure 5-5 highlights the visual inspection of the membrane's front and backside. When suspended on the front the differences in pore intrusion levels is obvious, indicated by the more or less transparent appearance of the active PES layer. The backside revealed the real extent of pore intrusion. The modified PBM did not penetrate as deep as the virgin PBM.

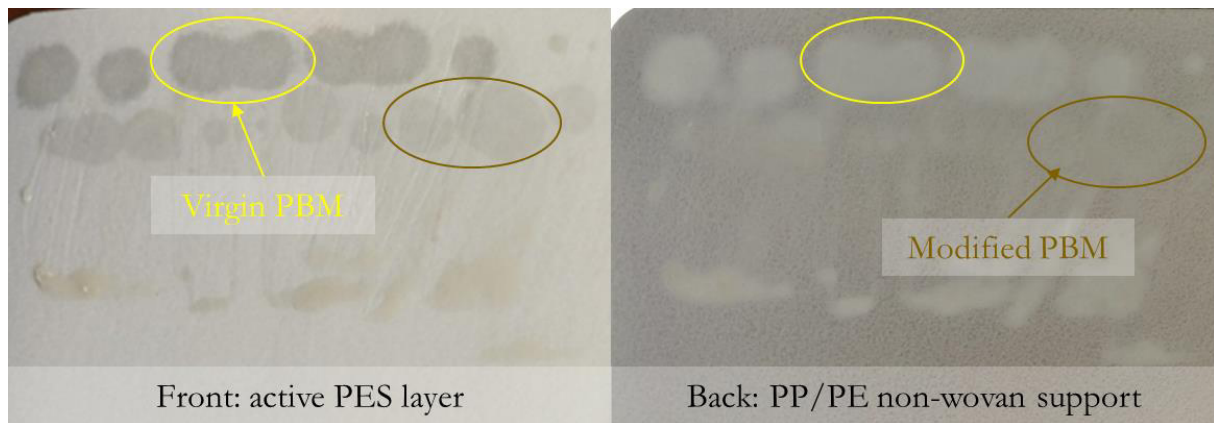


Figure 5-5 PBM pore intrusion for virgin and modified PBM using 15 w% PEG 400 as viscosity enhancer

High absorption of the pristine PBM led to membrane curling which was detrimental to production handling. As explained in chapter 2.5.1, pore size and pore size distribution have a major impact on the membrane properties but was well as pore intrusion of liquid coating materials. Curling for different membrane substrates could be an avenue for future research exploration. The *FM10* membrane cuts (*Martin Systems*) cuts were delivered in soaked glycerine added after the production to prevent pore collapse during transportation and further processing. FTIR confirmed the glycerine/glycerol ($C_3H_8O_3$) in pristine membrane specimens. It was assumed that glycerine present inside the capillary pores prevented higher pore intrusion in contrast to dry delivered membranes.

In addition to these observations, pre-tests followed with the usage of glycerine as a PBM viscosity enhancer. Glycerine has a much higher viscosity at a smaller molecular weight (1480 mPa·s) than PEG 400 (105-130 mPa·s). Hence, a lower material input resulted in a greater viscosity influence. However, similar to PEG, glycerine was not suitable as a viscosity enhancer for the given application. In this case, the PBM transparency changed and serious permeability drops close to zero were examined with the cross-flow unit of setup (chapter 4.3.1). Hence, the filtration tests for the described pre-trials were excluded.

Finally, it is pointed out that virgin PES membranes were pre-treated with PEG 400 and glycerine by submergence in a PEG and glycerine solution (10, 25 and 50%) prior to the PBM coating. The intention was to fill up the pores prior to the coating process to prevent liquid PBM entry into the void spaces of the porous membrane. However, as the entire membrane came into contact with the solution bath, PEG and glycerine was also present on the PES membrane surface making PBM casting coating impossible.

These findings were ground-breaking and led to a focus shift which influenced the further research work. From here on the solution for PBM pore intrusion reduction was sought out to ultimately improve the coated membrane performance.

5.6 Observations by confocal microscopy

Before establishing techniques to prevent PBM pore intrusion, confocal microscope investigations were carried out for scientific confirmation and quantification.

The data evaluation is shown in Figure 5-6 below, with the cut specimen on the very far right and the fluorescence 2-D image taken at the marked spot; the nanoparticles are indicated in green. Considering the absolute pore intrusion between 60-80 μm and the PBM wet layer thickness of 4 μm (spiral casting knife), pore intrusion was a minimum of 56-76 μm at this spot of coating. The hereby coated PES membrane had a 230 ± 20 μm thickness including active membrane layer and non-woven support. Nevertheless, it became clear that this very deep penetration led to a substantial decreased in water permeability. The membrane resistant not only increased due to the thickness of coating layer but also decreased due to a sharp pore size reduction. In fact, pore intrusion altered the porous structure of the PES membrane support and thus deteriorated the performance.

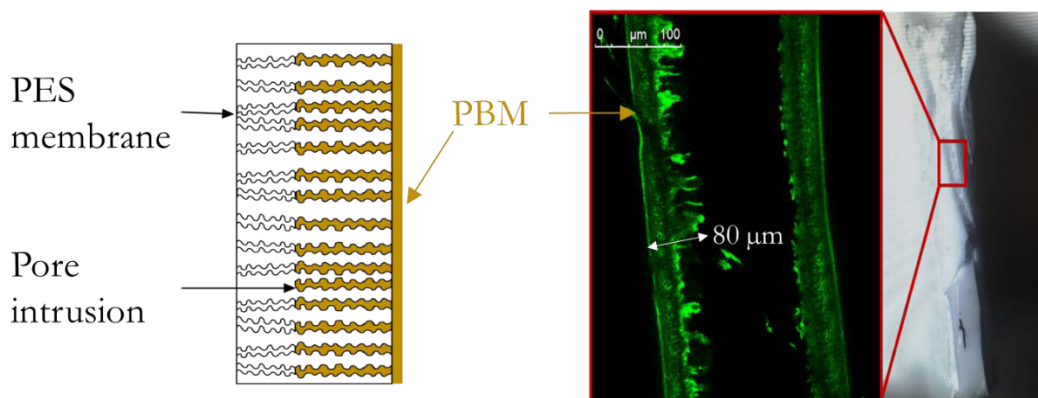


Figure 5-6 Cross-sectional view of the PBM coated membrane, schematically (left) and visualised by fluorescent microscopy (right)

The PBM coatings achieved with UV-LED polymerisation showed considerably lower permeability than previous REDOX initiated polymerisations (Galiano et al., 2015; 2018). Despite potential structural differences in the polymer matrix, further described in chapter 4.2.2, the REDOX initiated PBM solution had a slightly higher viscosity at the moment of coating. After activating the initiation, the PBM solution was spread over the membrane after a 5.5 min dwelling time. This resulted in a pre-polymerised PBM solution with a higher viscosity. Continuous flask shaking reduced inhomogeneity in polymerisation which could cause agglomerations and solidified clusters. Relations between viscosity and capillarity were discussed in chapter 2.5.1. Conclusively, lower capillarity was obtained by higher viscous liquids (Weiss, 1967; Che Mat et al., 2019).

This basic reflection pushed the research towards modifying the PBM viscosity. Measures were aimed at achieving PBM viscosity similar to REDOX based polymerised coating and beyond to get a better view of the polymer chemistry behind it. It was assumed that pore intrusion was not only caused by low viscosities but also considerably by the applied friction and pressure forces during the casting coating using spiral casting knives. The works listed here are aimed at different ways to reach the goal of better PBM coated membrane performance, also by reducing the capillarity effect.

5.7 Surface tension

Equivalent to the viscosity, the surface tension is a crucial characteristic of liquid materials for coating application, especially for the herein studied atomisation. Surface tension measurements were carried out as described and the results depicted in Figure 5-7. Different syringe diameters were available and before running PBM tests, the equipment was calibrated with DI-water. Recommended outer needle diameters for the pendant drop method for water ($72.8 \text{ mN}\cdot\text{m}^{-1}$ at 20°C) are in between 1.65 and 3.4 mm. Therefore, reference measurements were done with a 1.83 mm outer needle tip diameter and the values taken for the beginning of drop suspension until tearing off (blue curve). Within the initial measurement phase, values are small and ascend gradually. This is in line with pertinent literature. The accuracy of pendant drop method reduces significantly for incomplete drop shapes as it is the case in the beginning of each liquid suspension. Once a clear elongated drop developed, values stabilised and the measuring accuracy increased.

The measured $72.7 \pm 0.1 \text{ mN}\cdot\text{m}^{-1}$ is in line with the expected value. PBM measurements followed with the same equipment and the results highlighted in dark orange. Two special characteristics can be seen. A sudden jump of in the surface tension at second 3.4 represents a backflow of the liquid PBM up along the needle surface due to the relatively small surface tension. The result of a change in drop shape influenced the surface tension calculation. A second change in drop shape at second 7 was caused by a slightly tilted needle tip and a resulting more spherical drop shape. Afterwards, a perfect elongated drop developed and thus the surface tension value stabilised at around $30.1 \pm 0.3 \text{ mN}\cdot\text{m}^{-1}$ before completely tearing off. The two measured drops clearly deviated in their final drop shape, drop volume and thus measuring duration ($1 \mu\text{L}\cdot\text{s}^{-1}$ suspension speed). For liquids with higher surface tension, the force resulting from the surface tension was more dominant relative to the gravitational force acting on the hanging drop. This was indicated by smaller bond numbers $Bo = F_{\text{volume}} \cdot F_{\text{surface}}^{-1}$. With regards to the PBM drop, a larger drop volume was achieved before the drop teared off due to the increasing gravitational force. This is shown by the rather spherical drop compared with the PBM.

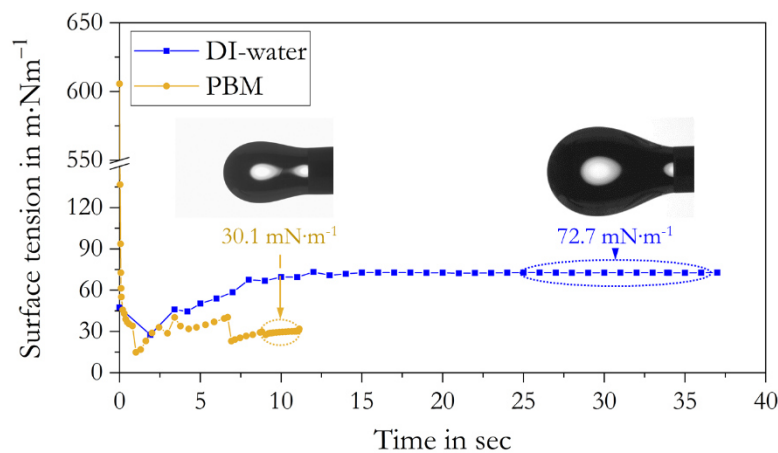


Figure 5-7 Pendant drops for water (blue, right) and PBM (orange, left) during surface tension measurements

These findings were crucial for further atomisation tests. Atomisation level and spray cone shape highly depended on the surface tension as well as viscosity. To save liquid PBM for spray coating pre-trials Octanol-1 was used as it showed comparable surface tension properties with $27.6 \text{ mN}\cdot\text{m}^{-1}$ (20°C , *Carl Roth*).

The spray volume and spray coverage were evaluated for different spray parameters. Random measuring errors were the occurring vibrations which interfered with the static grey level analysis. Moreover, environmental parameters such as humidity, electrostatic charge and air movements led to measuring deviations. Impurities inside the liquid drop could also reduce the surface tension and might vary for different PBM batches (AUTEAB purity, microemulsion formulation).

As an outcome of the findings of preliminary experiments in chapter 5, the experimental setups described in detail in 4.3 were designed. The approach of viscosity modification was developed and adjusted to the PBM polymerisation. Casting coating parameters such as casting speed were set and later on used for the upscaling procedure as well as the linear guidance for spray nozzle application. Determining the PBM surface tension was a necessary step for upcoming spray coating experiments. With the characterisation of PBM properties, fluids of comparable viscosity and surface tension were used to investigate spray parameters on the approximate membrane surface coverage. PBM was costly due to the manual AUTEAB batch production and the material input should be kept at a minimum.

6 Results and Discussion

This chapter presents the experimental data obtained with the experimental setups of chapter 4. Study parameters and environmental conditions were set based on the outcome of preliminary investigations and previously conducted work.

- The first **section 6.1** emphasises the investigation of PBM coatings containing the modified AUTEAB surfactant in order to verify the quality comparability to the PBM prepared with the highly pure classic AUTEAB. The obtained PBM layer through casting coating was characterised using AFM analysis for two different wet layer thicknesses. In combination with contact angle measurements and model foulant tests using the membrane cross-flow test unit, the results decided over the feasibility of modified AUTEAB surfactant for the upscaling procedure. Prior to the large PBM production quantities, the critical flux for PBM and PES membranes were examined using flux step tests on lab scale.
- Viscosity modifications in **section 6.2** were based on the crucial findings about membrane pore intrusion highlighted in chapter 5.6. The controlled radical polymerisation approach was inspired by industrially produced polymers of different architecture. With the knowledge gained through extensive pre-trials including polymerisation propagation investigations, the protocol for the viscosity modifications was established. Rheological investigations were carried out for PBM solutions of varying inhibition times. Finally, permeability tests using humic acid as model foulant followed and correlations between the time of polymerisation inhibition, dynamic viscosity and permeability were developed. At last, a comparison to the pristine PBM was drawn and the most suitable viscosity for the pilot scale production selected.
- Controlled environmental casting coating conditions and the preselection of optimum PBM viscosity allowed for the automated production of large PBM membranes required. The pilot scale trials for domestic wastewater reuse are depicted in **section 6.3**. Results are shown which were yielded with the pilot MBR within the decentralised VicInAqua project in Kisumu, Kenya. Flux step tests involved two in-situ chemical cleaning procedures and were carried out as short-term stress tests. A constant flux tests followed with a 137 day trial period at 25 LMH for a second PBM module batch.

The last part highlights PBM stability tests of samples taken from the pilot MBR subsequent to the field trials. FTIR measurements and permeability tests are shown and both, lab scale and pilot scale experiments were compared.

- The feasibility study of spray coating application using pressure-based and assisted atomisation is illustrated in **section 6.4**. Pre-tests are shown which compared both spray principles including spray mist homogeneity. The nozzle type for final tests was selected. Main tests were conducted with water, including the investigations of spray pattern and also membrane surface coverage depending on fixed spray parameters. It is shown how the surface tension had a high influence on the spray cone shape. Optimum spray parameters for PBM coating were derived from these tests and final curing was done with UV-LED light. Spray coverage and thus the coating layer thickness for the PBM fluid was examined with FTIR analysis along the membrane width. Ultimately, the FTIR peak height was put in correlation with the permeability and examined with a cross-flow test unit.
- The last **section 6.5** depicts the comparison between PBM coated membranes achieved with casting coating and spray coating technology. Various permeability tests were conducted for both and the mean value as well as production tolerances were evaluated. For the final assessments, SEM and NMR spectroscopy were used to analyse the surface texture and polymer structure. The data acquired gave a brief insight into the mechanisms responsible for the differences in the coating results.

6.1 Casting coating application

Following casting coating experiments were all carried out with a spiral casting knife of 4 μm coating thickness. As previously described, the coating thickness has a direct impact on the membrane permeability. The total membrane resistance increases according to equation 2-1 and 2-2. Therefore, the thickness is kept at a minimum since an improvement of low-fouling properties with increasing thickness could not compensate the higher resistance (Schmidt, 2016).

6.1.1 Classic and modified AUTEAB

AUTEAB synthesis is complex and requires a high level of chemical knowledge to produce a high quality powder for the PBM formation. Since it was the goal to upscale low-fouling coating also beyond this work, slashing production costs was a major concern. Currently, the AUTEAB surfactant is synthesized in the laboratories of the *Department of Chemistry and Technical Technologies (CTC)* at the University of Calabria. The synthesis steps are conducted as a successive manual batch process with labour costs being the highest cost share. Material costs were calculated for small chemical quantities and thus, AUTEAB production represents 77% of total PBM costs (Mancuso et al., 2018). The potential for price reduction was high for large scale batch production. To satisfy the amounts that were required for upscaling PBM coatings within the VicInAqua pilot project (2 x 3.125 m² coating area), few synthesis steps were modified to reduce the production time considerably. The modification included (1) esterification under atmospheric conditions instead of inert-conditions reduced the operating costs for pressurised nitrogen (N₂) and increased operation simplicity (e.g. flask sealing); (2) the elimination of a chromatographic purification step substantially optimised the overall synthesis time. The adapted production flow changed the AUTEAB surfactant purity. The PBM solution appeared yellowish; however, a clear microemulsion formulation was still given. Chromatographic purification (2) reduced the amount of butylhydroxytoluol (BHT) inhibitor which was added to the synthesis to prevent spontaneous polymerisation of products. Moreover, small impurities of the chemicals used remained inside the produced AUTEAB powered which led to the yellow-brownish appearance (Figure 6-1). Exact details of the AUTEAB synthesis can be taken from Galiano (Galiano, 2013).



Figure 6-1 Clear and yellowish appearance of transparent PBM formulation

The comparison of both synthesised surfactants, modified and initial classic AUTEAB, was part of this study. It included surface characterisation by CAM, AFM and membrane permeability tests.

Impurities present in the modified product could act as polymerisation inhibitor and thus the photo initiator amount was slightly increased from 1.8 w% to 2.3 w% to achieve fast and complete polymerisation of the PBM layer.

6.1.1.1 *Contact angle measurements*

The contact angle (CA) between a solid and liquid surface indicates whether the wetted solid substrate is hydrophobic ($>90^\circ$) or hydrophilic ($<90^\circ$). According to equation 2-7, the liquid entry pressure (LEP) becomes negative for $<90^\circ$ resulting in spontaneous membrane pore entry of the liquid. For wastewater treatment application, hydrophilic surface properties are desired to enhance the repulsion of hydrophobic foulants.

Results are shown for measurements of dry membranes only. Figure 6-2, on the right side, exemplarily depicts the grey level analysis for CA calculations for a PBM coated membrane sampling spot at 0 s and 50 s, respectively. Over time, the contact angle reduced due to the liquid pore entry and the wetting behaviour of the surface. The impact of evaporation was negligible as the experiment duration was short. The diagram shows the CA as a function of time, including the deviation band of the measuring errors. For all PBM coated samples, the CA progression, the absolute contact angle as well as the measuring tolerance show lower values than the commercially available PES membrane (blue). It is interesting that the CA for the PES had high deviations with maximum $\pm 12^\circ$ at second 30. High deviations for CA measurements exist throughout existing literature. For instance, Levitsky et al. (2011) indicated a hydrophobic 100.6° CA for UF PES membranes, whereas Kertész et al. (2014) measured very high hydrophilic values of around 64° . This huge discrepancy shows the real difficulty of CAM measurements. Despite varying membrane architecture which highly differs for each manufacturer, sampling preparation methods as well as the equipment used can greatly affect the test results. Worth particular mentioning the varying suspended drop volumes, membrane conditions (either dry or wet, also see 4.2.6) and equipment calibrations (*DataPhysic Instrument*, 2019). When comparing the PBM with the PES, generally less deviation can be observed from Figure 6-2. An explanation could be the very broad production-related pore size distribution for PES membranes. Once the solid coating layer was applied, it became the dominant resistance factor for the filtration process and the characterisation. Considering similar coating and thus polymerisation temperatures and, despite present deviations in PBM preparation, a uniform polymer network was created. This could lead to the much smaller tolerances with maximum $\pm 4.7^\circ$, $\pm 5.8^\circ$ and $\pm 7.1^\circ$.

The classic AUTEAB (light yellow, Figure 6-2) showed lowest values with 54° representing a 42% reduction relative to the starting value at 0 s. Values of the PBM coatings with the modified AUTEAB are 68° with a percentage reduction of 31% for the lower 1.8 w% photo initiator amount (light orange line). Conclusively, the PBM achieved with 2.3 w% initiator had slightly lower values with 59° (at second 50) with a 37% declining CA relative to the starting point at 0 s (dark orange line). Values for the classic AUTEAB surfactant were taken from Schmidt (Schmidt, 2016).

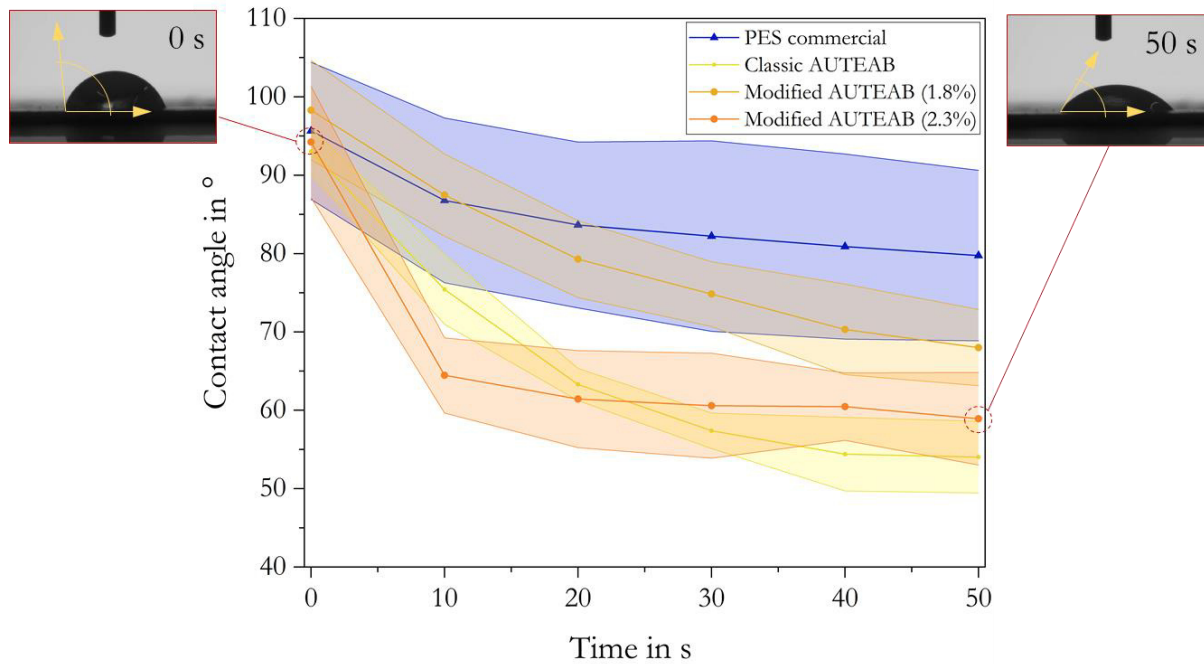


Figure 6-2 Contact angle measurements (left), and schematic of grey level drop shape analysis (right)

With both, the classic and modified AUTEAB surfactant, PBM could improve the hydrophilic surface properties of the UF membrane. The deviation bands of both modified AUTEAB (1.8 and 2.3 w%) overlapped and thus showed insignificant differences in hydrophilicity. Therefore, in terms of hydrophilicity, the polymerised PBM layer achieved with the modified AUTEAB surfactant could compete with the classic and more expensive one. Slightly higher initiator amounts (0.5 w%) were used compensating higher impurities in the AUTEAB powder. The Measurement results overlap and considering the highly sensitive CAM analysis, there was no significant difference.

6.1.1.2 *Atomic force microscopy*

Atomic force microscopy (AFM) showed on average a -58% smoother surface for the PBM coated membranes (Figure 6-3). Differences which arose from the coating layer thickness 4 and 20 μm , respectively, have a minor impact on the results. The first measurements with 4 μm (Figure 6-3, mid-left) were considered an outlier since many impurities were present on the surface prior to the measurements. This was also indicated by the very high deviation ($17.43^{\pm 6.7}$ nm, 4 μm). All measurements showed the root mean square (RMS) value R_q . The results were in line with previously conducted experiments (Galiano et al., 2018) showing a -79% reduction compared to the commercial UF PES membranes. PES roughness highly varies in literature and measuring errors for AFM are comprehensive and in sum can strongly affect the results (Johnson and Hilal, 2017). Nevertheless, there was still a clear trend and the modified AUTEAB surfactant (1.8 w% photo initiator) used for PBM preparations does result in significant surface roughness reduction which is beneficial for mitigating fouling phenomena (Yoon, 2016).

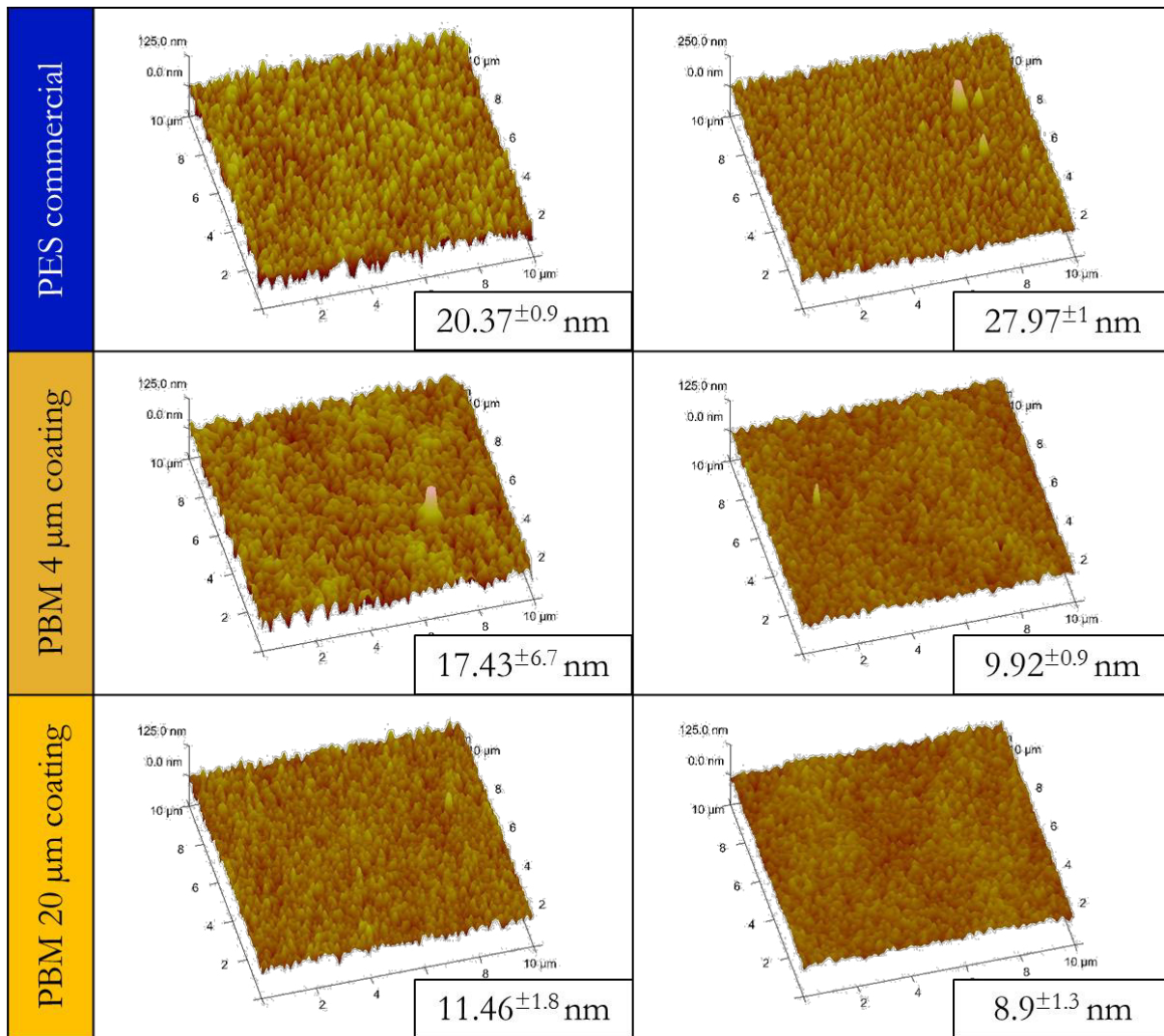


Figure 6-3 AFM measurements of commercial PES and PBM coated samples using the modified AUTEAB

6.1.1.3 *Model foulant tests comparing classic and modified AUTEAB*

Figure 6-4 depicts the permeability for the coated membranes with different AUTEAB quality relative to the commercial PES membrane. The shown values were determined with the protocol developed in chapter 4.3.1 and tests were carried out at constant TMP. It can be seen that the value of the PES membrane drops significantly in the course of laboratory test. Since the pristine membrane was much more porous than the coated membranes, the obtained flux rate and thus permeability is around 4 times higher for clean water tests. Higher volume flows through the membrane also resulted in higher concentration polarisation and thus elevated fouling rates. As a result, the drop in permeability was much higher than for the coated PBM membranes. Similar explanation also applied for the pressure increase from 0.5 to 2.2 bar. In the further filtration process, the commercial PES membrane could not recover to its initial performance due to the big cake layer formed on the surface. Although constant TMP tests are not properly suitable for comparing membranes of different resistance, the obtained values provide a relative efficiency to each other. Focusing on the PBM membranes prepared with the classic and modified AUTEAB, only small differences could be identified and were mostly within the measuring and production tolerance. The ratio of clean water and humic acid permeability at 0.5 bar remained constant for all membranes.

The permeability within the HA experiments dropped at a TMP of 2.2 bar compared to the values obtained for 0.5 bar as expected. Regain potential for the classic and modified (1.8 w%) AUTEAB after three rinsing steps with DI-water was higher than for the coating prepared with the modified (2.3 w%) AUTEAB surfactant. The reason could be the higher fouling state caused in the first part of the experiment. Higher permeability at constant TMP show higher flux rates which aggravates the cake layer growth (see Equation 2-3). Cake layer removal by clean water rinsing became more difficult. A loss of layer material by washing off was unlikely since the filtration conditions are rather low.

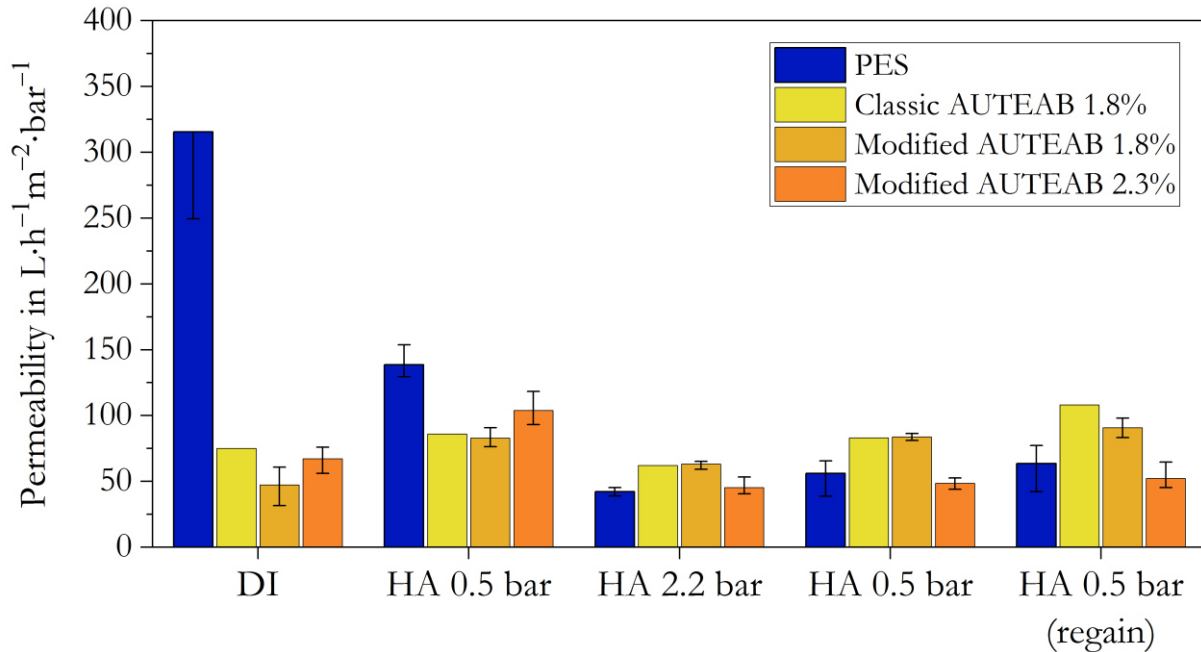


Figure 6-4 Permeability tests for PES and PBM prepared with classic and modified AUTEAB at constant TMP operation

6.1.2 Constant flux operation on lab scale

As a consequence from these conducted tests, the PBM solution was prepared with the modified AUTEAB only since no significant difference to the classic AUTEAB was observed. A 1.8 w% photo initiator was utilised since the benefit of a 0.5 w% higher amount was not evident throughout the tests. Subsequently, constant flux tests performed and assessed to determine the filtration performance comparatively to the pristine PES membrane. The flux step test protocol was explained before (chapter 4.3.1) and the results are highlighted in Figure 6-5. In the first phase of the test, a much higher TMP for PBM coated membrane prevail up to around 1 bar. Within this phase, the beneficial low-fouling properties could not compensate for the higher membrane resistance and the larger pressure loss. However, in the further course of the experiment, the blue (PES) and orange (PBM) meet at the “intersection point”. From that point, at TMP=1.1 bar and 96 LMH, the PBM showed a better performance with lower TMP values. The results indicated that the PBM coating had a higher critical flux which would extend the operation time between cleaning intervals in long-term. However, it should be considered that industrial scale aerobic iMBR for wastewater treatment operate at much lower flux rates, commonly below 40 LMH (Hai et al., 2019).

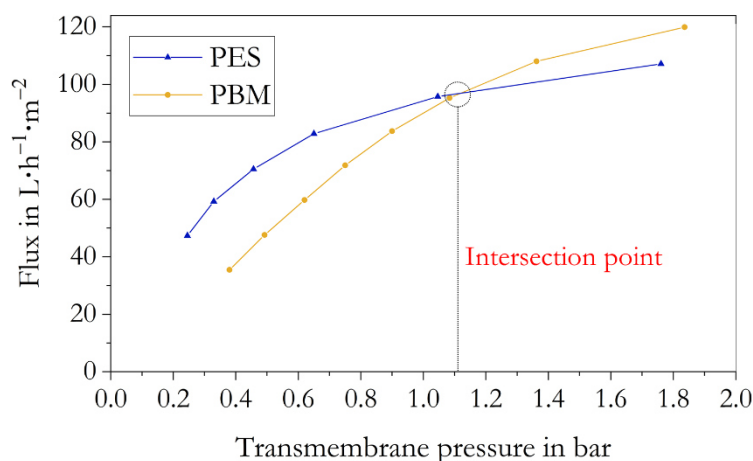


Figure 6-5 Flux step tests using membrane cross-flow test unit

These results indicated a higher critical flux and thus a reduced fouling mitigation for the PBM coating at harsh filtration conditions. In contrary, the commercial PES membrane showed a higher fouling propensity at laboratorial conditions.

6.1.3 Chemical resistance tests

The polymerised PBM is a covalently bonded nanostructured, interconnected polymer network. Covalent bonds vary in strength with the participating atom pairs as the distance to the sharing electrons changes proportionally with the atom diameter. The binding energy in $\text{kJ}\cdot\text{mol}^{-1}$ is high and thus is the resistance against external factors. The prevailing binding forces between the PBM layer and the PES substrate are cohesion forces and result from the different partial surface charge. This electrostatic bond also depends on the polarity of the atoms involved (Nilsson and Pettersson, 2008). However, the binding energy is substantially lower than for a covalent bond and the chemical stability decreases. Accordingly, an extensive chemical cleaning cycle was triplicated under laboratorial conditions prior to the upscaling process in order to study chemical stability of the PBM layer. FTIR measurements were taken between and after each cycle to investigate potential detachments of the PBM from the PES membrane. The protocol was described in chapter 4.2.5.2 and the results of the tests shown below in Figure 6-6. In total 8 defined spots of the coated membrane were measured using a template. This approach ensured that the same coating points of a constant coating thickness were measured repetitively. Two selected measuring spots are depicted. The different colours represent the measurement, before the chemical resistance test (reference, green) and the measurements after each cleaning cycle (purple, blue and yellow). The peak height between the reference and 3rd cleaning cycle reduces for both sampling points but remained roughly constant for the 2nd and 3rd cleaning cycle. According to previous explanations, a peak height reduction and material loss could not be quantitatively correlated for PBM coatings. If a multilayer specimen with varying production tolerances for all three layers exist, the layers interfere and overlap with each other independent of the applied clamping force. Nevertheless, for the results shown in Figure 6-6., the PBM could be considered as chemical stable for the three cycles conducted.

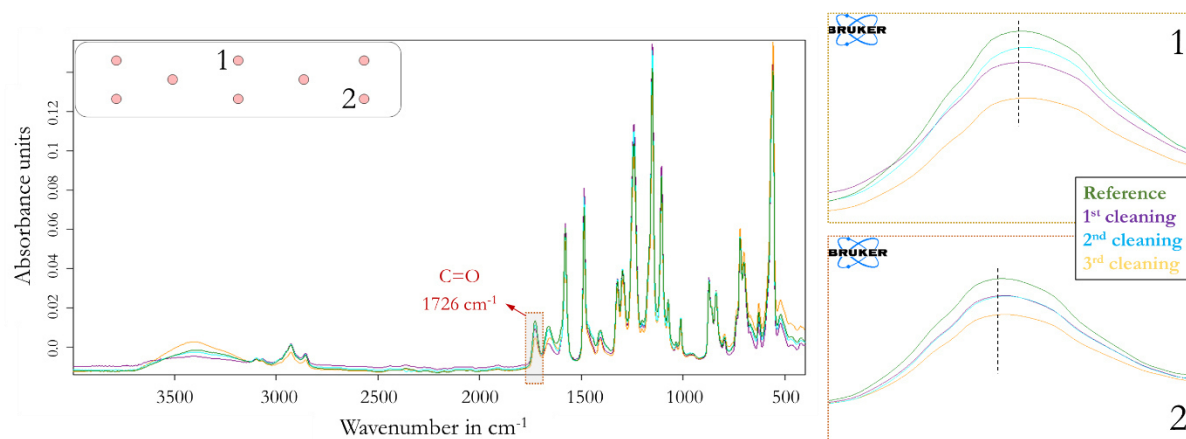


Figure 6-6: FTIR measurements validating chemical stability of PBM layer in the course of a chemical cleaning procedure

It should be pointed out that the protocol also included a very harsh test at pH 1 and pH 13 levels. This is common for membrane cleaning in desalination application and potable reclamation. PES membranes in wastewater reuse are exposed to moderate conditions, limited to pH 3 and pH 11 using less aggressive chemicals. In conclusion, only a long-term filtration of real wastewater streams including chemical cleaning steps could finally and quantitatively define the chemical resistance of the PBM coating.

Considering the chemical stability within the pre-trials in combination with AFM, CAM and permeability tests, the modified AUTEAB surfactant showed similar performance as the classic AUTEAB. It was concluded that the slightly lower purity was of no negative consequence for the PBM coated membrane. Therefore, production expenditures for the AUTEAB synthesis could be reduced substantially which was a major step towards industrial upscaling procedures. From this point on, the entire coating production shifted to a PBM prepared with the more favourable modified AUTEAB.

6.2 Feasibility of PBM viscosity modification for UF application

6.2.1 Protocol development

Figure 6-7 shows several experiments with the temperature measurements representing the polymerisation propagation. These pre-tests were done to better understand the polymerisation for active process control. The results from bigger PBM masses were reproduced with smaller amounts to reduce material input and increase the number of experiments. The left side highlights a 10 g PBM solution whereas the right side depicts 1.5 g test mass in a smaller test tube. All experiments were carried out at ambient temperatures of $22 \pm 1^\circ\text{C}$ with passive convection. The temperature differences in spatial resolution is given with the deviation band, with the black line representing the mean value. The spatial temperature deviation for all temperature progressions inside the large 10 g PBM solution were higher pronounced than for the smaller 1.5 g quantities (Figure 6-7, right). The following reasons can be stated. For smaller PBM masses, the reaction enthalpy ($\text{J}\cdot\text{mol}^{-1}$) was correspondingly lower and a lower heat quantity was dissipated. On top, higher heat outputs (faster sample cooling) were achieved due to a higher surface-to-volume ratio of the smaller test tubes. At comparable stirring speeds, turbulences in the smaller test tube were higher compared to the bigger volume. Altogether, the prevailing thermodynamic conditions supported homogeneous sample cooling and minimised the so-called Trommsdorff-Norish-effect (Ozaki et al., 2015). In the course of exothermal polymerisations, the viscosity increases over time along with the temperature. As the temperature rose, the higher viscosity reduced the heat transfer coefficient and thus the cooling effect of the surrounding air. At the same time, higher viscous liquids inhibited the movement of oligomers and radicals. This reduced the change of polymer chain recombination and termination. Both phenomena accelerated the polymerisation reaction and provoked the exothermal propagation (Ozaki et al., 2015).

Moreover, the influence of varying turbulences inside the test tube containing the polymerising PBM was evaluated. The turbulence was increased from the top to the bottom (Figure 6-7) for a stagnant solution (0 rpm), a turbulence flow at 1,000 and 1,500 rpm stirring speed. As mentioned above, turbulence effects improved heat dissipation into the surroundings and the deviation band became narrower. For 1.5 g PBM masses, however, no large difference could be observed as the heat output was relatively high for stagnant solutions. In all cases, maximum deviations of around ± 1 K could be measured. For the stagnant 10 g PBM (top-left) the deviation represented by the light orange deviation band was at a maximum ± 14.5 K whereas the 1000 rpm mixed PBM (mid-left) showed maximum deviations of only ± 6.5 K. With the further increase of turbulences by 1,500 rpm, a certain phenomenon could be observed for both PBM quantities (bottom side). This time, both experiments showed similar tendencies. A very high forced convection inside the polymerising PBM test tube prevented complete polymerisation, implicated by the nearly constant temperature within the first 60 min. After a stirring speed reduction to 1,000 rpm, the self-accelerating polymerisation took place as usual. This is clearly shown by the sharp temperature increase. The polymerisation was initiated by a REDOX attempt using an APS initiator and TMEDA activator.

It was expected that a significant increase in turbulent flow inside the test tube impaired the diffusion from TMEDA radicals to the APS molecules and in the same way, APS radical diffusion into the monomer-swollen micelles.

Hence, chemical reactions decayed and complete polymerisation did not occur in the short term. Once turbulences were reduced, diffusion became more dominant and complete polymerisation occurred. The temperature development was not as pronounced as for spontaneous polymerisations at moderate turbulences. This could be explained by minor pre-polymerised polymers during the first phase at 1,500 rpm, indicated by the slight 0.8°C temperature increase from the initial 28.8°C to 29.6°C at minute 30 (Figure 6-7, bottom-left). Most likely, some random radical polymerisation took place as the reaction probability was highly reduced but not prevented entirely. This assumption was also supported by the significantly lower temperatures during the final polymerisations. Whereas stagnant and 1,000 rpm stirred PBM solutions showed peak temperatures of 69.6°C and 71.3°C, respectively, the delayed polymerisation for 1500 rpm had moderate 55°C peak values. Lower temperature development refers to lower heat generation and thus pre-polymerisation must have taken place. More specifically, since similar PBM with equivalent reaction enthalpy were used, heat generation was the same throughout the experiments. The differences in peak values for the stagnant and 1,000 rpm stirred PBM are within the systematic and random experimental errors. The same behaviour was also confirmed for the experiments with 1.5 g PBM test tubes (Figure 6-7, right).

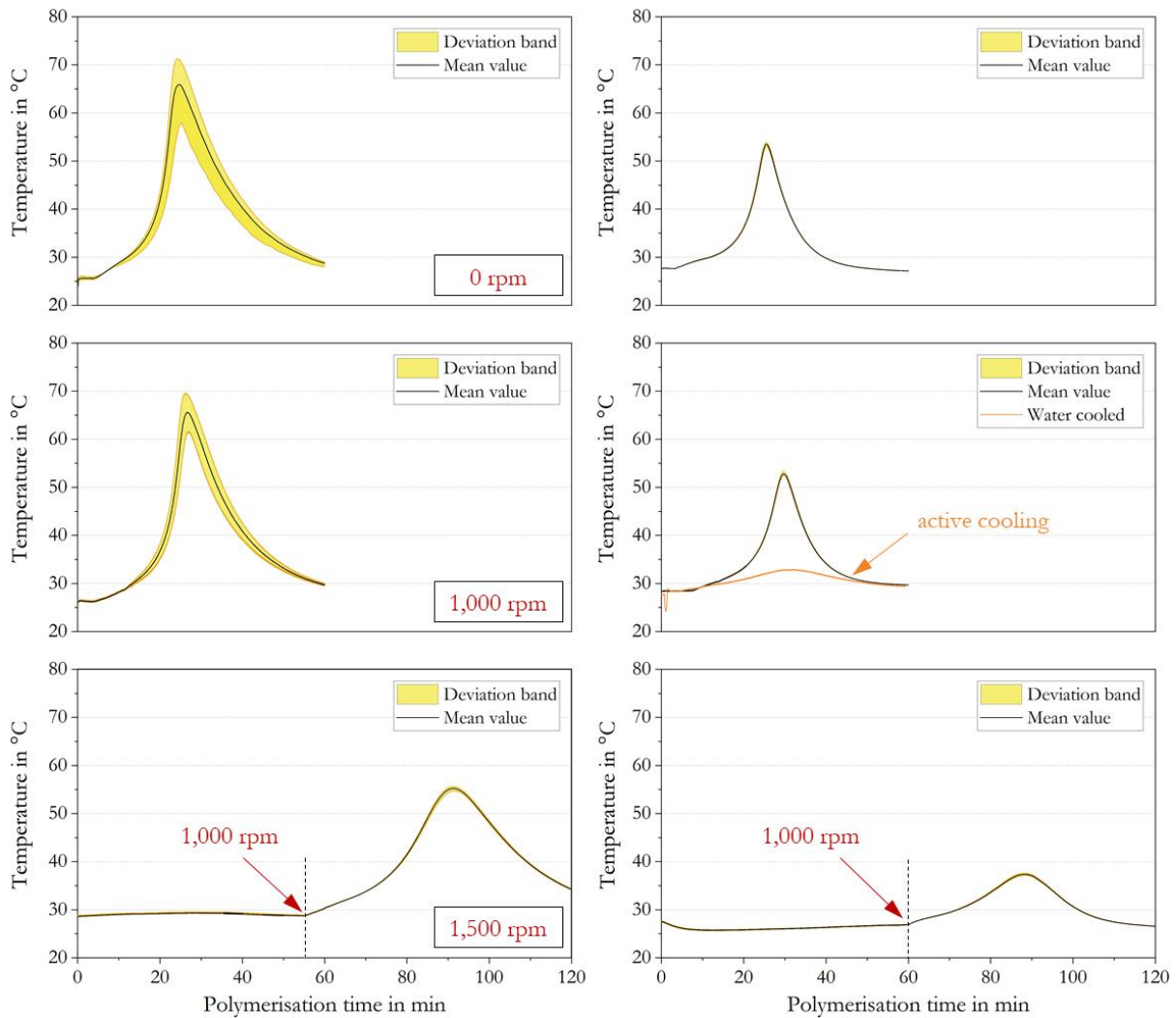


Figure 6-7 Temperature propagation during polymerisation, different turbulences and varying PBM mass

Further studies included polymerisation of 1.5 g PBM only due to a much lower spatial polymerisation deviation resulting in a higher product homogeneity.

Feasibility studies about polymerisation inhibition followed with adding the finely grinded radical inhibitor TEMPO to the polymerising PBM solution. First, starting at 0.5 mg the TEMPO amount was slowly increased to get a threshold for a possible polymerisation stop (Figure 6-8). By using 0.5 mg TEMPO, the polymerisation could not be inhibited, as shown, and the polymerisation restarted spontaneously after 15 min to the inhibitor dosing. By doubling the amount up to 1 mg, a successful polymerisation stop was achieved (right). Re-polymerisation potential was double-checked by PBM storage in a cold and dark place over night. Through final adjustments, 0.9 ± 0.1 mg was set as threshold for a successful polymerisation inhibition. The reduction in peak temperature of the final curing could be interpreted that a previous polymerisation took place. This corresponded to higher viscosities than the pristine PBM which was later on also confirmed by rheological investigations.

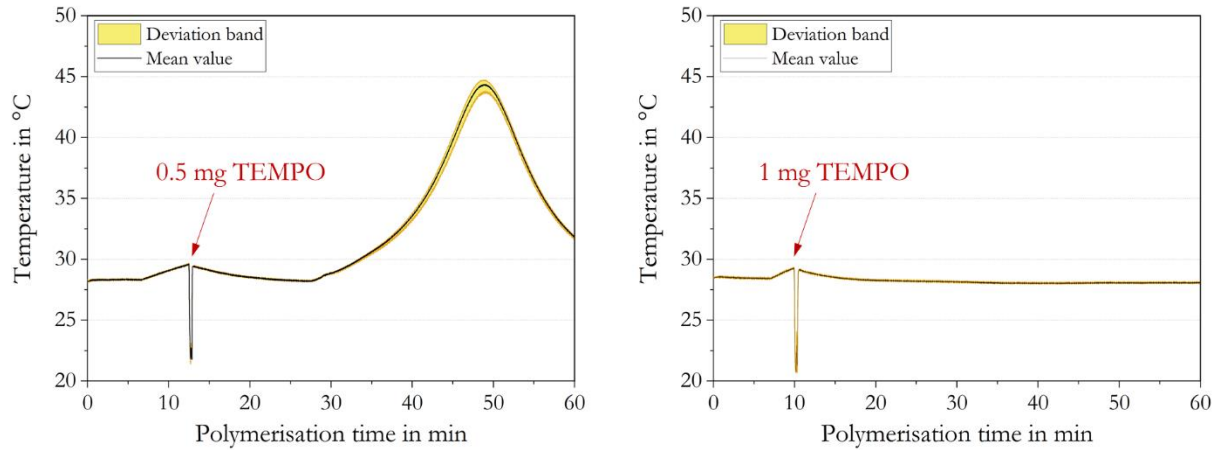


Figure 6-8 Polymerisation inhibition experiments using adapted amounts of the radical inhibitor TEMPO

Besides inhibitor amount adjustments, two different inhibition concepts were the research focus (Figure 6-9). Therefore, a passively air cooled (left) and an actively cooled test tube inside the water bath (right) were studied and compared. The first attempt included a reaction inhibition at a specified temperature increase relative to the ignition temperature of $\Delta T = 1.5$ K. By this method, the impact of pipetting and experimental errors such as ambient temperature should be minimised. Higher differences in the set point resulted in spontaneous polymerisation as the self-accelerating polymer chain growth was already too powerful. Active cooling with the water bath further enhanced the heat transfer from the PBM into the coolant. This further reduced the Trommsdorff-Norish effect and supported a more homogeneous polymerisation which resulted in a very small temperature increase of maximum 4.6 K (right). The first inhibition attempt using a defined temperature difference was not practical owing to a delayed dosage. For this reason, the second inhibition attempt involved the addition of TEMPO powder after a defined time Δt_i after the initiation. This was also evaluated as most promising attempt for modifying the PBM viscosity. Step by step, the inhibition time was extended to identify the latest possible time of a sustainable polymerisation stop. Results showed that reproducible results were achieved with at most $\Delta t_i = 10$ min which was then defined as maximum time of possible inhibition for desired viscosity modifications.

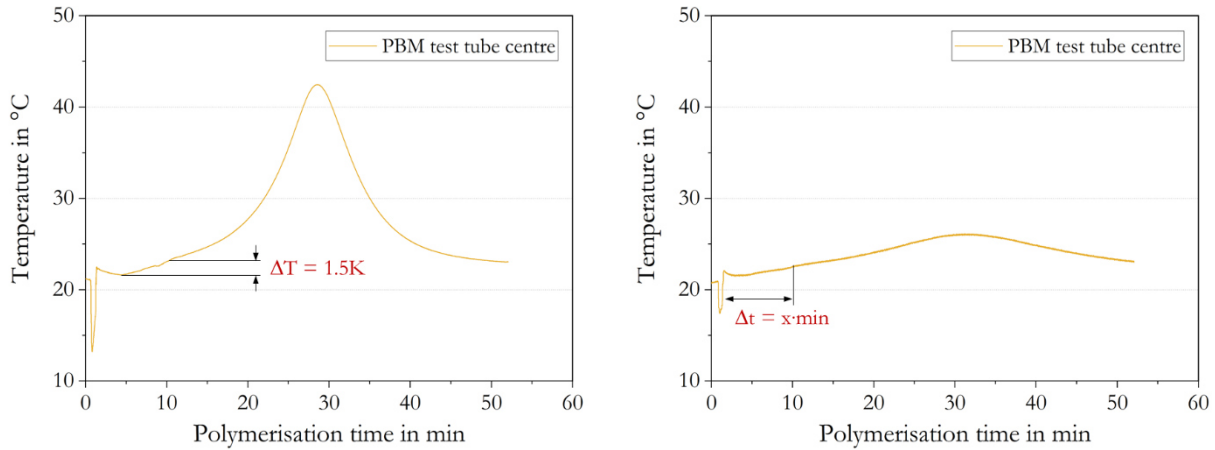


Figure 6-9 Polymerisation inhibition concepts, dosage after a specified temperature (left), inhibition after a specific inhibition time (right)

Based on these studies, the final viscosity modification protocol was developed. The concept of PBM viscosity modification thereby includes the time-dependent polymerisation inhibition and the entire process chain is given in Figure 6-10 which follows 5 basic steps:

- (1) Polymerisation initiation of 1.5 g PBM using $1.8^{\pm 0.2}$ mg APS activated by $40.5 \mu\text{L}$ TMEDA in a temperature controlled water bath with temperatures between 15...20...25°C
- (2) Inhibition of chemical reaction by adding $0.9^{\pm 0.1}$ mg finely grinded TEMPO for quick dissolving. Dosage was done at inhibitions times $\Delta t_i = 7 \dots 8 \dots 9 \dots 10$ min, respectively
- (3) Rheological investigation using 0.25 mL of pre-polymerised PBM solution. Viscosity measurements were reproduced
- (4) Casting coating with the remaining pre-polymerised 1 g PBM and re-initiation with 75 mg Irgacure 184 for UV-LED polymerisation. 5 mg APS were added as TEMPO radical catcher which would potentially decay the polymerisation reaction⁴
- (5) Ultimately, membrane performance tests with a humic acid solution ($100 \text{ mg}\cdot\text{L}^{-1}$).

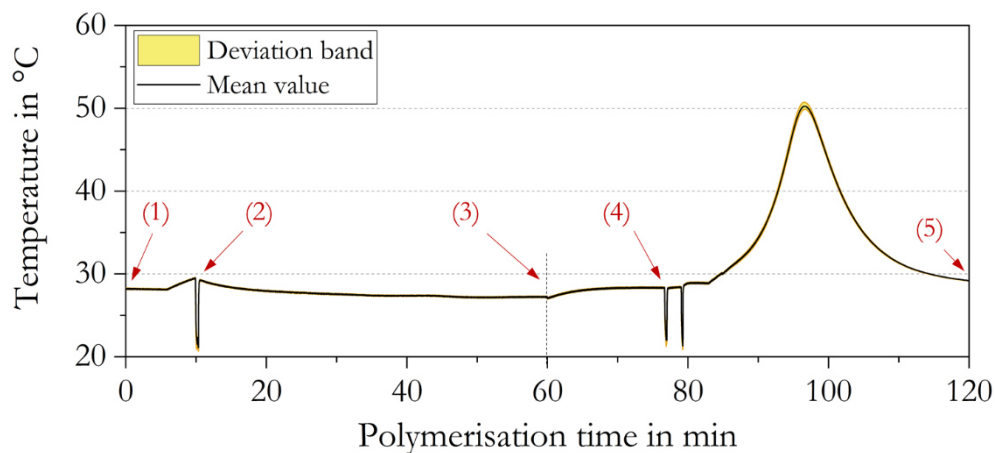


Figure 6-10 Procedure of pre-polymerisation for membrane coating with PBM of modified viscosity

⁴ For a better visualisation the temperature measurements are highlighted for a passive cooled PBM

6.2.2 Rheological examination

Validating the PBM viscosity was of prime importance for improving the coating process and the membrane performance. Figure 6-11 highlights the measurement evaluations for the pristine PBM as well as for pre-polymerised PBM for a different inhibition time Δt_i . The diagrams show the progression of dynamic viscosity η and the shearing stress τ depended on the changing shear rate $\dot{\gamma}$. The experiments for the pristine PBM (top-left) were carried out with a slightly different gradual increases revealing prevailing marginal phenomena. For instance, the inertia of the equipment and the PBM liquid caused the initial fluctuations up to around 20 s^{-1} . Moreover, starting at shear rates of $6,000 \text{ s}^{-1}$, slightly elevated values could be observed. For very liquid testing fluids, centrifugal forces acting at very high shear rates could overrule friction forces inside the liquid and between the cone and measuring plate. In this case the fast rotational movement pushed parts out of the cone and plate gap. The torque response and thus the measuring signal was thereby reduced which falsified the result. Lower torque correlated with lower viscosities since the resistance by the flowing fluid was smaller. This reduction in measuring signal could also be caused by a gap under filling which would be a handling error by the user.

In contrary, the modified or pre-polymerised PBM solutions all showed a slight decrease in dynamic viscosity above shear rates of around $5,000 \text{ s}^{-1}$. Shear thinning effects could explain the higher signal response at higher shear rates/high shearing stress. Shear thinning occurs for liquids which show lower liquid behaviour than in dormant states. For instance, this effect could be noticed in body lotions or Ketchup. Stored in plastic tube, they are pressed out before applied to the skin. These liquids are also called thixotropic and are non-Newtonian fluids (Pritchard et al., 2016). In terms of decreasing viscosity for the PBM, shear thinning could be explained by a phase separation and change of micellar structure. Bicontinuous formulation tend to show higher shear resistance whereas frictional forces between spherical micelles are lower (Zhang et al., 2017). However, PBM is a thermodynamically stable system and segregation unlikely. For stable liquid formulations, despite developing hysteresis, the shear strain reaches zero after the experiment and descending step function. This was the case for all the PBM solutions, either pristine or modified. Effects of a measurable variation in signal response could also be caused by a cone and plate gap overfilling. A marginally higher torque response could be provoked if excess sampling material flowed out of the gap, around the cone and measuring plate edge. Increasing contact areas thereby increased the response signal distorting the real value. Nevertheless, during extensive measurements, the sampling volume was regularly adjusted to avoid negative gap filling effects.

For the pristine PBM solution, a constant 7.03 mPa s dynamic viscosity was measured whereas the modified PBM all show higher values as expected. All measurements showed constant dynamic viscosities independent of the shear rate within the representative range. Constant dynamic viscosity at increasing shear rates validated the PBM to have properties of a Newtonian fluid. In the same manner, the shear rate showed linear proportional behaviour for the ascending step phase (Viswanath et al., 2007). Since the PBM basically comprised of Newtonian fluids such as water and oil phases (MMA, surfactants), the final composition had equal flow character.

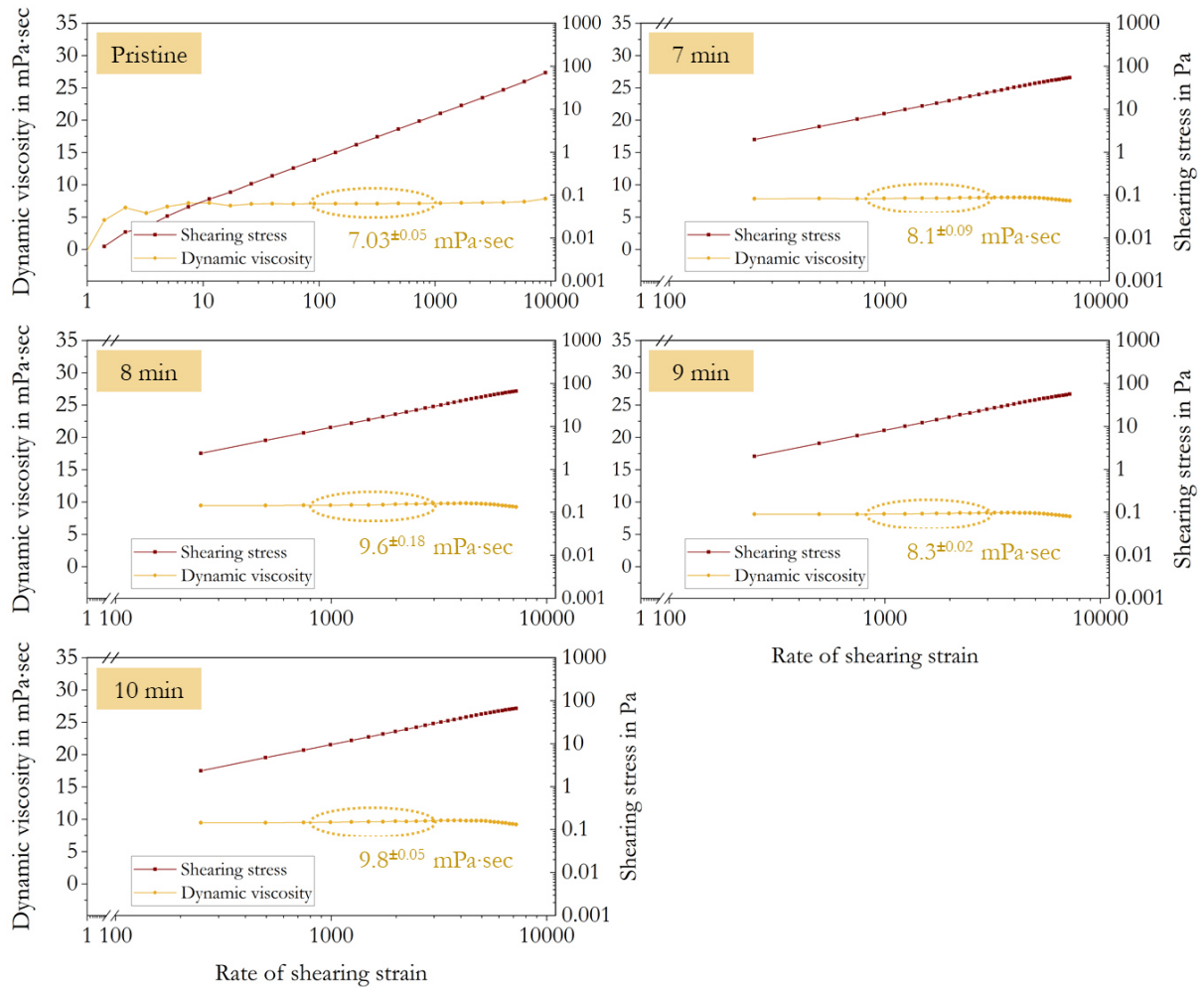


Figure 6-11 Viscosity measurement for the pristine and modified PBM using a rheometer

The cone diameter had a high impact on the measuring result. Too small cone shapes for a given viscosity significantly falsified the response signal as the cone diameter is squared included in the measurement result ($A = \pi \cdot 4^{-1} \cdot d^2$, see equation 2-10). Large fluctuations in shear stress τ and dynamic viscosity η were expected in this case. Consequently, bigger cone diameters should be preferred over smaller diameters independent of the expected viscosity.

Additionally, tests examined the viscosity relation to the water bath temperature, respectively the initiation temperature for polymerisation inside the test tube. The results (Figure 6-12) indicate an independence of both parameters. For water bath temperatures at 25°C significantly high deviations were observed. As previously stated, a precise control of the polymerisation propagation remained difficult with the given experimental setup. Moreover, the acceleration nature of higher reaction temperatures of 25°C aggravated this circumstance. As a result, an uncontrolled inhibition of the self-accelerating polymerisation reaction led to higher inhomogeneity of the modified PBM solution. In general, an instantaneous inhibition was not given since the TEMPO – despite finely grinded – requires a relatively long dissolving time. Complete reaction termination through radical catch was delayed.

Consequently, material input for initiator as well as inhibitor would have to be adapted for smaller deviations. As smaller deviations in the sample preparation were achieved close to room temperature, the next membrane coatings were prepared with modified PBM at 20°C. Dosage of the TEMPO radical for controlling the chemical reactions could change the micellar formation considerably. Therefore, nuclear magnetic resonance (NMR) were carried out for pristine and modified PBM (see 6.5.3).

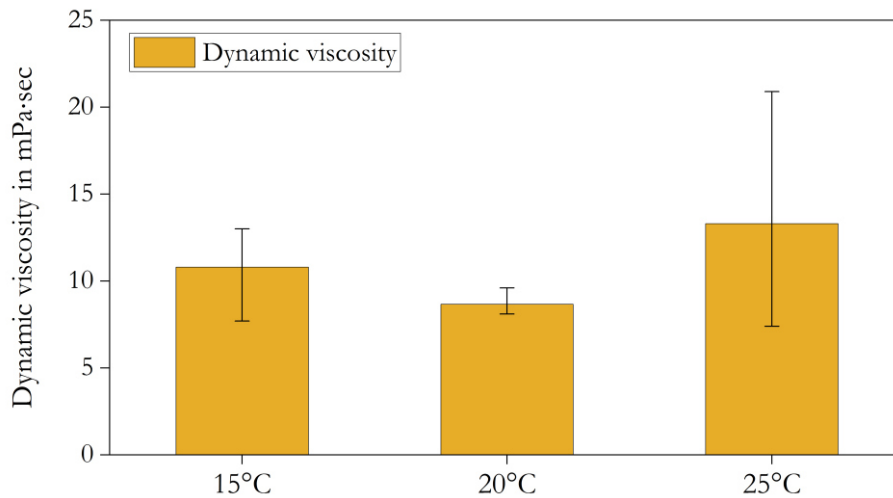


Figure 6-12 Viscosity dependency of the water bath temperature at the start of polymerisation

6.2.3 Verifying the feasibility for pilot scale trials

Figure 6-13 shows the parameters from the viscosity modification experiments. Tests were performed with a humic acid solution according to Figure 4-6 for 0.5 bar TMP after an acclimation phase. Contrary to expectations, the water permeability (orange line) decreases with increasing dynamic viscosity (brown line) relative to the pristine PBM. The reference dynamic viscosity was 7.03 mPa·s giving a 96 L·h⁻¹·m⁻²·bar⁻¹ permeability. As can be seen, there was no direct correlation between the viscosity and permeability for the modified PBM. The shown REDOX values were not included in the trend line. Deviations are high for pristine, REDOX and 7 min modified PBM, indicated by the error bars. The reason was that separate casting coatings were conducted for different coating and modification attempts, thus varying distinctly. In contrary, other rheological investigations were duplicated with the same modified PBM solution. Figure 6-12, on the right side, shows the humic acid fouling layer after the experiments. There was a clear change in brownish colour of the humic acid fouling layer. More dense membrane layers reduced the flux at a comparable TMP. As consequence, fouling was less pronounced over time. This effect was explained in chapter 2.2 according to which the flux rate plays a much more significant role in fouling phenomena. Nevertheless, the experiments pointed out differences in the permeability at the given 0.5 bar TMP. Conclusions could be drawn about the porosity of modified PBM membranes and the data demonstrated the filtration capacity at a comparable TMP.

In case of later polymerisation interference at longer inhibition time Δt_i , polymer chains had more time to propagate. This resulted in different polymer networks, also when reinitiated with the photo initiator activated by the UV-LED light.

Utilising nuclear magnetic resonance (NMR) spectroscopy this assumption was verified, see section 6.5.3. The further indication was the surface structure, which was visualised by scanning electron microscopy (SEM), see chapter 6.5.2. Additional experimental errors were the dosing speed of the initiator as well as inhibitor which potentially affected the polymer architecture. Minor deviations of measuring errors from temperature measurements (± 0.5 K) and weighing errors (± 0.2 mg) were considered to be negligible for PBM viscosity modifications.

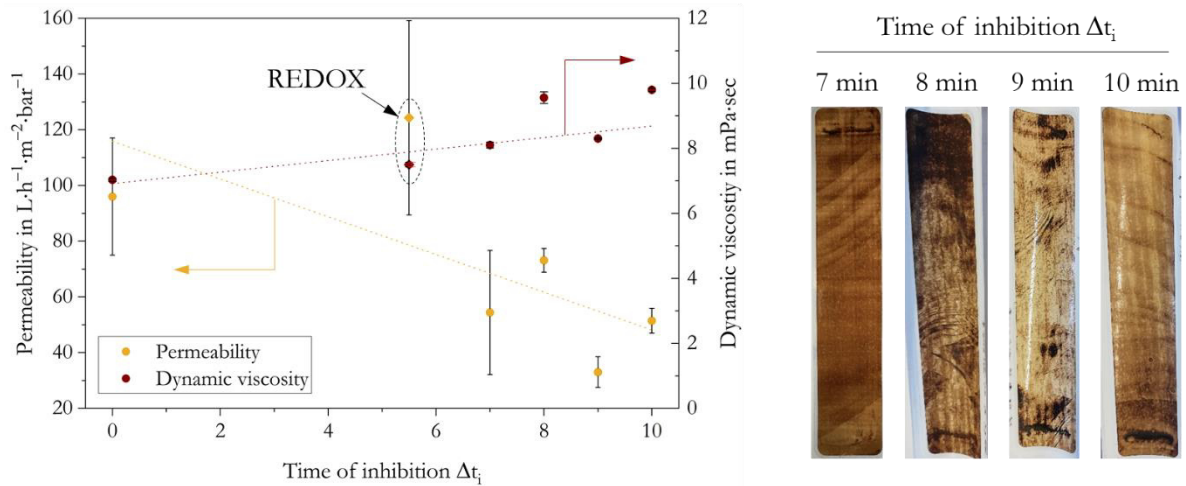


Figure 6-13 Membrane performance tests for different PBM viscosities, achieved by varying inhibition time

In conclusion, modifying the PBM viscosity through controlled radical polymerisation is a complex procedure. Results showed that despite previous assumptions, the permeability of final coated membranes decreased substantially compared to the pristine PBM. For pilot scale trials treating domestic wastewater, the innovative PBM coating had to compete with commercial PES membranes showing high permeability during lab scale tests (section 6.1). Fouling propensity within domestic wastewater treatment is known to be less critical for membranes in general. Therefore, highest possible permeability of the PBM coating was the main target with low-fouling properties coming in second.

Consequently, pilot scale trials were conducted with casting coatings using the pristine PBM.

6.3 PBM upscaling for pilot scale domestic wastewater treatment

Based on preliminary investigations with reproduced values of Schmidt (Schmidt, 2016), the optimum coating strategy was developed for PBM upscaling using UV-LED polymerisation. Table 6-1 lists the coating parameters and includes boundary conditions for the pilot MBR. Research activities were part of the European funded *VicInAqua* project located in Kisumu, Kenya. The MBR supplied 3 m³ treated domestic wastewater per day to an aquaculture hatchery and agriculture. Following results compared two batch produced PBM coated membrane modules with a virgin commercial UF PES module of 3.125 m² membrane area. First and foremost, membrane performance tests are discussed and a complete water analysis demonstrates the achieved water quality.

Table 6-1 Optimum parameters used for PBM upscaling

	Parameter	Symbol and unit	Value
PBM membrane casting coating	Viscosity of pristine PBM	mPa·s	7.03
	Temperature	T in °C	24±1
	Oxygen level	in %sat	< 1
	Irradiation intensity	mW·cm ⁻²	300
	Irradiation time	T in s	60
	Humidity	φ _{rel} in %	40-60 %
	Wet layer casting thickness	μm (spiral casting knife)	4
MBR operation conditions	Mixed liquor suspended solids	MLSS in g·L ⁻¹	6-12
	Dissolved oxygen	DO in mg·L ⁻¹	2-3
	Flux (module volume flow)	LMH in L·h ⁻¹ ·m ⁻²	20 and 25
	HRT	h	17 and 13.5
	Average water temperature	°C	25

6.3.1 PBM performance tests treating real domestic wastewater

The initial acclimation phase of the pilot MRB included functionality tests using clean tap water and 2 x 3.125 m² commercial PES modules *FM 611 (Martin Systems)*. The capacity sensor of permeate line 2 had a 14 mbar offset which was autocorrected during the data evaluation. First PBM tests were performed using production batch 1, installed in parallel with one virgin PES module. Data was recorded at a 1 min⁻¹ sampling rate for long term tests and a 6 min⁻¹ sampling rate for the conducted flux step tests.

Membrane pore swelling and membrane adaption was enabled by slowly increasing filtration capacity from 10 LMH to 15 LMH and 20 LMH in a two-day cycle. Once the commercial PES module reached steady state filtration (Figure 6-14), an extensive chemical in-situ cleaning was carried out following the official protocol, given in chapter 4.3.4. The first flux step test on day 7 was conducted and reproduced after a second in-situ cleaning on day 8.

The flux was then gradually increased to nominal operation (20 LMH) on day 11. As shown, the PBM coated membrane module could not compete with a commercial version. After acclimation, the PES stabilised at around $440 \text{ L}\cdot\text{h}^{-1}\cdot\text{m}^{-2}\cdot\text{bar}^{-1}$ which was significantly higher than the PBM permeability of approximately $63 \text{ L}\cdot\text{h}^{-1}\cdot\text{m}^{-2}\cdot\text{bar}^{-1}$. Reduced permeability was expected as the PBM coating layer increased the total membrane resistance R_{tot} (equation 2-2) through an increased membrane thickness and by pore intrusion.

Throughout the flux step tests (Figure 6-15), the PBM module shows a sharp specific TMP increase up to a 50 LMH flux rate. Large deviations relative to the commercial PES module started at 30 LMH and the TMP quintupled from around 8.5 to $43.5 \text{ mbar}\cdot\text{min}^{-1}$. On the contrary, the specific TMP increase for the commercial PES showed a moderate rise in the pressure progression and only tripled within the critical phase of 30 LMH ($3 \text{ mbar}\cdot\text{min}^{-1}$) and 50 LMH ($9.5 \text{ mbar}\cdot\text{min}^{-1}$). Interestingly, for both modules, the reproduced results in overall show much smaller specific TMP increase through the entire test progress. It was assumed that very high stress levels on the membrane pores at 40 LMH ($125 \text{ L}\cdot\text{h}^{-1}$) and above caused irrecoverable pore expansion. The permeability increased due to lower pressure drops caused by the membrane. Figure 6-14, left, shows that after two flux step tests including two chemical cleanings and regaining up to 20 LMH, PES values were around $1000 \text{ L}\cdot\text{h}^{-1}\cdot\text{m}^{-2}\cdot\text{bar}^{-1}$ which was far above manufacturer's recommendation of $>250 \text{ L}\cdot\text{h}^{-1}\cdot\text{m}^{-2}\cdot\text{bar}^{-1}$. Similar behaviour was shown for the PBM module reaching stable permeability of around $380 \text{ L}\cdot\text{h}^{-1}\cdot\text{m}^{-2}\cdot\text{bar}^{-1}$. A reason could be that the PBM coating was washed off by the chemical cleaning procedures combined with high membrane stress levels. By comparing both progressions, an increase of factor 2.2 and 6 could support this expectation. However, contrary to this opinion, PBM showed stable values within the last three days of stable flux operation before replacement. Since the PBM attached to the PES with electrostatic forces (cohesion) only, the thin PBM layer could have expanded more extensively. Nevertheless, supplemental FTIR measurements should be examined to investigate the PBM stability for these flux step tests.

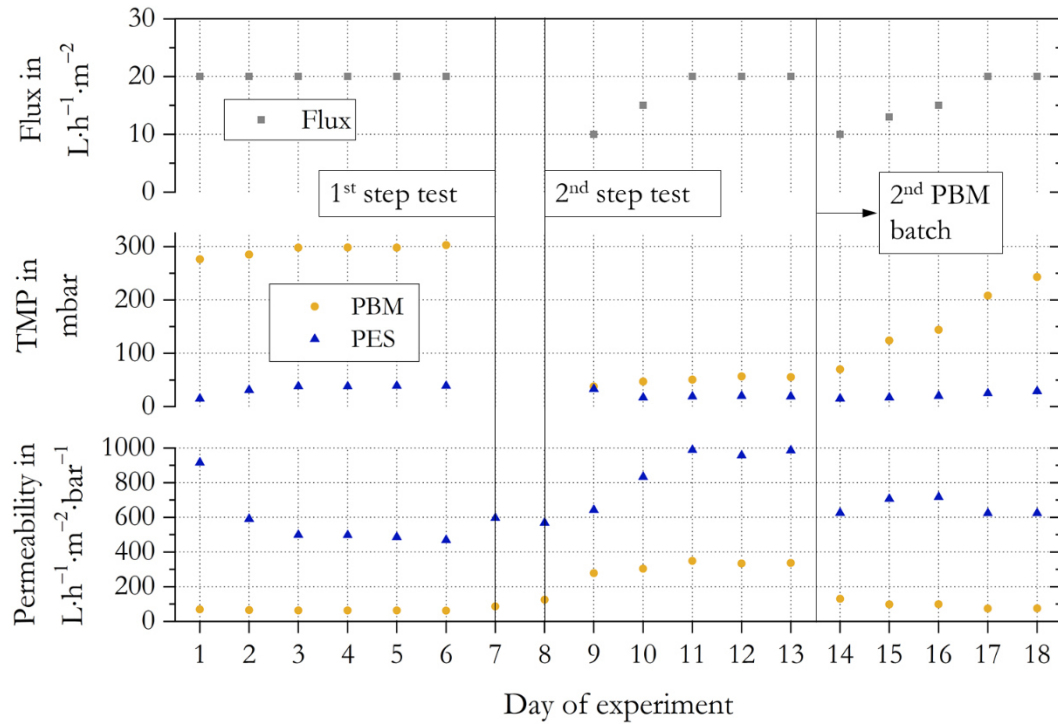


Figure 6-14 Testing phase of 1st PBM batch with duplicated flux step tests on day 7 and 8

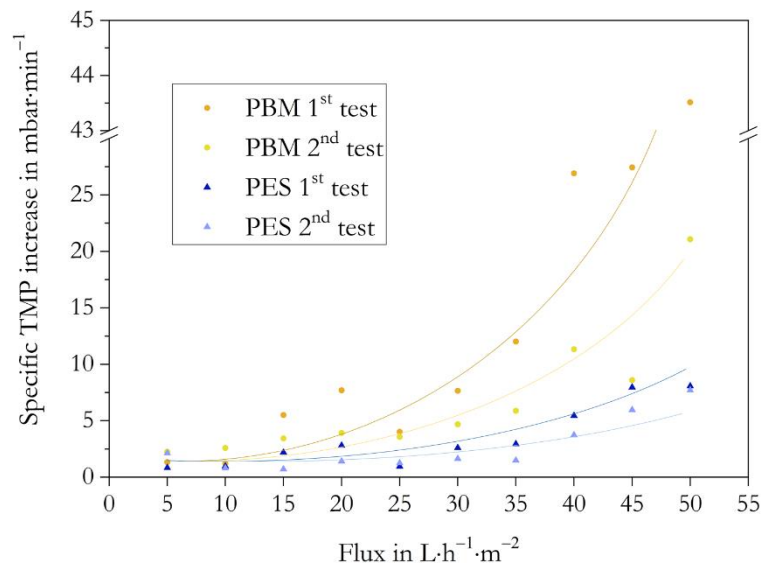


Figure 6-15 Specific TMP increase of 1st PBM batch and PES module during the conducted flux step tests

Supplementary to the flux step tests, constant flux operation was done with the second PBM batch and a separate virgin PES module to re-establish comparability. Long-term tests at a constant flux started for a 137 day period (Figure 6-16). Initially operated at 20 LMH, the flux was increased to 25 LMH ($78 \text{ L}\cdot\text{h}^{-1}$) after 19 days. Some commercial system may reach flux rates of 35 LMH in the long-term, which highly depends on the end user application including wastewater composition and contaminants. Domestic wastewater is commonly low-strength wastewater (see Table 6-2) and was of no challenge for commercial PES membranes. Poorasgari et al. (2015) reviewed studies investigating cakelayer formation effects in submerged MBR systems (iMBR).

He defined the threshold range for TMP values below which no cake layer occurred with 4978 mbar (vacuum). In regards to the domestic wastewater filtration in Kisumu, almost no fouling propensity of the commercial PES membranes was anticipated for the <50 mbar operation throughout the 137 day trial period. After the membrane pore acclimation phase, the permeability dropped from around $900 \text{ L}\cdot\text{h}^{-1}\cdot\text{m}^{-2}\cdot\text{bar}^{-1}$ to below $600 \text{ L}\cdot\text{h}^{-1}\cdot\text{m}^{-2}\cdot\text{bar}^{-1}$ which was still significantly higher than the manufacturer's recommendation. The permeability of the first batch with in average $63 \text{ L}\cdot\text{h}^{-1}\cdot\text{m}^{-2}\cdot\text{bar}^{-1}$ was confirmed with the second PBM permeability of around $66 \text{ L}\cdot\text{h}^{-1}\cdot\text{m}^{-2}\cdot\text{bar}^{-1}$. In terms of both batch produced PBM modules, the average permeability was $64.5 \text{ L}\cdot\text{h}^{-1}\cdot\text{m}^{-2}\cdot\text{bar}^{-1}$ at a 20 LMH flux rate. This made a production tolerance of $\Delta\text{WP}=\pm 2\%$ showed the narrow production quality the coated membrane could be produced in. The very low deviation resulted from the homogeneous coating layer achieved with the automated coating machine with implemented accurate casting process control.

One important finding was the almost constant operation of the PBM module within the entire 137 days. This is a clear indication that the PBM layer was not washed off during the normal operation mode which is very important for novel membrane coatings. Comparing both modules, the commercial PES showed a slightly lower specific TMP increase over time with around 0.4 to $0.7 \text{ mbar}\cdot\text{day}^{-1}$, respectively.

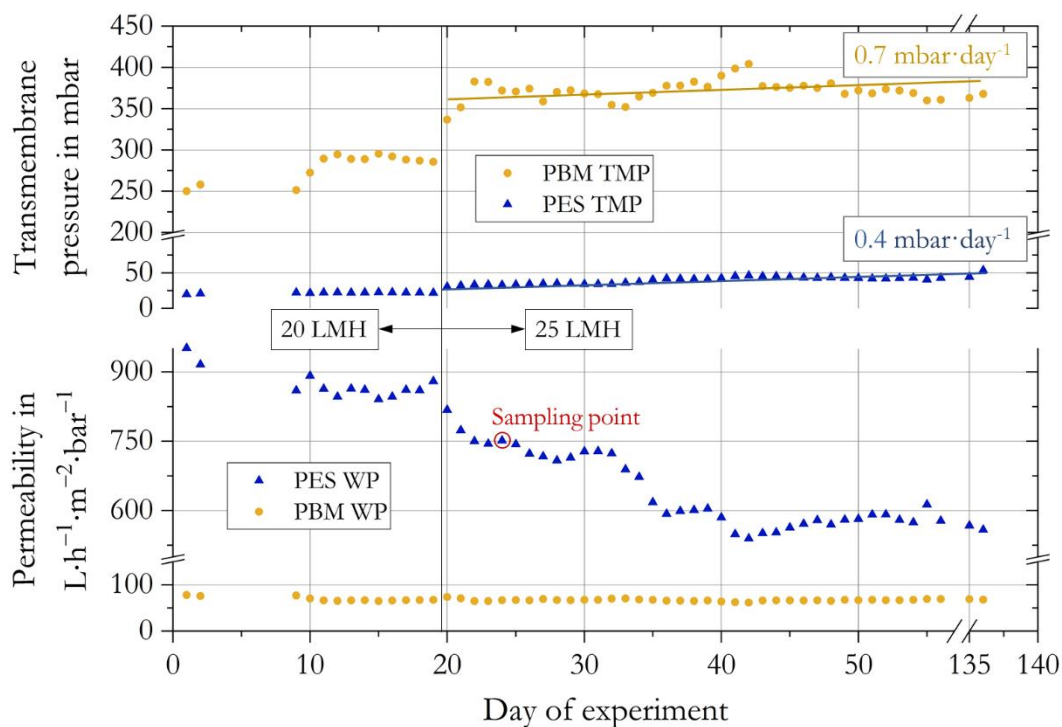


Figure 6-16 Long-term comparison between the 2nd PBM batch and PES module

In summary, as expected, the PBM performance was worse than the commercial PES. The PBM coating also did not show benefits during the flux steps tests contrary to lab scale trials. It is important to state that domestic wastewater generally exhibits very low-fouling propensity. Therefore, the PBM coating could not reach its full potential.

Overall, the advantage of low-fouling behaviour through the incorporated antimicrobial AUTEAB surfactant and co-surfactant HEMA could not compensate the disadvantages of additional layer resistance.

Lab scale experiments previously showed better surface characteristics in terms of lower contact angles and a smoother surface (average roughness R_a). Structural differences revealed by NMR (Figure 6-31) yielding from the different initiation type were most likely the reason for poorer filtration performance in relation to previously conducted REDOX initiation coatings (Galiano et al., 2015). Different structures of the polymerised, solid PBM, validated by SEM experiments supported this assumption, see Figure 6-30.

However, it was anticipated that better filtration performance compared to commercial membranes could be achieved at a high-strength water pollution with higher fouling propensity. In particular, Deowan et al. demonstrated a higher critical flux in the long-term when he used a 0.33 m² PBM coated UF PES membrane module for treating textile wastewater (Deowan et al., 2016).

6.3.2 Comprehensive water analysis

A water sample was taken at day 24 and the parameters listed in Table 6-2 analysed. MBR feed was the raw domestic waster after the three-stage solid removal before entering the denitrification tank (details shown in chapter 4.3.4). Permeate samples were taped directly at the permeate pump outlet. Sampling points are shown in Figure 4-15. The feed COD was with 438 mg·L⁻¹ in the typical range of domestic wastewater which is 200-800 g·L⁻¹. The COD in both permeates for PES and PBM module was typically <100 mg·L⁻¹ resulting in overall COD removal efficiencies of >80%. The hydraulic retention time (HRT) was increased from 17 h (20 LMH) to 13.5 h (25 LMH). The calculations were based on total MBR volume of 1.7 m³ (three compartments) and the suction-to-relaxation ratio of 12min:3 min (also see chapter 4.3.4). Mixed liquor suspended solids (MLSS) measured inside the nitrification chamber fluctuated between 5-11 g·L⁻¹. MLSS values typically range between 6-12 g·L⁻¹ (MBR site, 2019). Ammonium NH₄⁺ is a fish toxic cation and a critical parameter in aquaculture systems. Elevated ammonium displaces K⁺ and prevents oxygen uptake of the fish gills. This can eventually cause cell death in the central nervous system (Randall and Tsui, 2002). Therefore, official guidelines recommend a total ammonium level in aquaculture below 1.5 mg·L⁻¹ (Bregnballe; 2015). The conspicuously high nitrate NO₃⁻ values could be caused by high dissolved oxygen levels inside the anoxic denitrification chamber preventing the bacterial nitrate decomposition. Nevertheless, nitrate is less critical regarding fish toxicity. According to existing guidelines, nitrate should not exceed 500 mg·L⁻¹ in aquaculture systems for juvenile tilapia farming (Monsees et al., 2017). Orthophosphate PO₄³⁻ has no known toxic effects on fish. However, orthophosphate causes eutrophication which leads to elevated algae growth (Effendi et al., 2018) and can affect the dissolved oxygen balance of the RAS. If there is a need, the addition of Al₂(SO₄)₃ as a chemical coagulant into the MBR tank could further reduce orthophosphate removal (Mburu et al., 2019).

Table 6-2 Comprehensive water analyses comparing both membrane modules

Parameter	Unit	Day 24 of operation (Figure 6-16)		
		MBR feed	Commercial Membrane module	PBM modified membrane module
pH	pH scale	7.5 ^A	7.9	7.9

El. conductivity	$\mu\text{S}\cdot\text{cm}^{-1}$	856 ^A	654	654
COD	$\text{mg}\cdot\text{L}^{-1}$	438 ^A	68	70
COD _{Removal}	%		84	84
TOC	$\text{mg}\cdot\text{L}^{-1}$	70.8	4.5	5.7
TIC	$\text{mg}\cdot\text{L}^{-1}$	74.9	15.7	16.3
NH ₄ ⁺	$\text{mg}\cdot\text{L}^{-1}$	46.5	0.111 ^A	0.075 ^A
NO ₃ ⁻	$\text{mg}\cdot\text{L}^{-1}$	BDL	117.7	116.5
TN	$\text{mg}\cdot\text{L}^{-1}$	65.1	33.7	32.2
PO ₄ ³⁻	$\text{mg}\cdot\text{L}^{-1}$	14.3	11.9	13.1
SO ₄ ²⁻	$\text{mg}\cdot\text{L}^{-1}$	43.0	69	76.5
Cl ⁻	$\text{mg}\cdot\text{L}^{-1}$	75.0	73.6	74.2
Na ⁺	$\text{mg}\cdot\text{L}^{-1}$	88.3	83.9	85.4
K ⁺	$\text{mg}\cdot\text{L}^{-1}$	33.9	31.5	32.6
Mg ²⁺	$\text{mg}\cdot\text{L}^{-1}$	16.0	14.0	12.9
Ca ²⁺	$\text{mg}\cdot\text{L}^{-1}$	74.1	52.6	54.2
MLSS	$\text{g}\cdot\text{L}^{-1}$	5 – 11 ^B		
^A Cell test Merck KGaA 1.14739.0001				
^B MBR nitrification tank				

In general, heavy metals occurred in very small quantities and did not require any further treatment. Slightly elevated values of Ciprofloxacin were detected. Listed values in Table 6-3 showed a 19% higher removal efficiency for the PBM module relative to the commercial PES module but this was within the extended measurement uncertainties (see Table 4-7). Besides the shown values in Table 6-3, other antibiotics could not be found. Further analysis was performed for common penicillin such as Amoxicillin, Cloxacillin, Dicloxacillin, Nafcillin, Oxacillin, Penicillin G and Penicillin V. It was important to keep track on the antibiotics and to observe absorption in fish tissue. Also, the uptake of contaminants and antibiotics of the plants have to be studied further.

Table 6-3 Water analysis on heavy metals and antibiotics

Parameter	Unit	Value			
		Raw sewage	MBR feed	PBM coated module	PES commercial module
Cd	$\text{mg}\cdot\text{L}^{-1}$	< BDL	< BDL	< BDL	< BDL
Cu	$\text{mg}\cdot\text{L}^{-1}$	0.02	0.07	0.02	0.02
Zn	$\text{mg}\cdot\text{L}^{-1}$	0.07	0.06	0.06	0.06
Pb	$\text{mg}\cdot\text{L}^{-1}$	0.005	0.002	< BDL	< BDL
Hg	$\text{mg}\cdot\text{L}^{-1}$	< BDL	0.000057	< BDL	< BDL
Ciprofloxacin	$\text{ng}\cdot\text{L}^{-1}$	1430	980	640	790

Metronidazol	ng·L ⁻¹	< BDL	< BDL	66	67
BDL = Below detection limit					

The result did not show a clear distinction of the achieved permeate water quality for PBM coated and commercial PBM membranes. The measured differences were all within the measuring errors. It was expected that the denser structure indicated by the rather low permeability compared to commercial PES membranes resulted in higher rejection rates. However, studies have shown that differences in average mean pore size and pore size distribution did not necessarily change the retention capability (Yoon, 2016). Projected to this case, denser PBM structure did not necessarily improve the water quality in the long-term.

6.3.3 PBM stability validated by FTIR measurements

After the long-term operation at a constant 25 LMH flux rate, the second PBM batch and operated PES module were dismantled. The modules were opened in the centre and in the external section. Rough cleaning was conducted with a water jet and a cloth, wiping off activated sludge between the laminated frames. The view depicted in Figure 6-17 confirmed the data values. The PES membranes did not show significant irrecoverable fouling (left). The PBM coating layer was clearly visible showing a light brownish colour. Galiano et al (2018) determined a different surface charge for the PBM, also provoked by the positive quaternary ammonium salt group of the AUTEAB surfactant. Specifically, the ZETA potential shifted from negative to more positive values. As explained in chapter 2.5.1, membrane surface characteristics have a big influence especially on the first fouling propagation phase where adsorptive processes prevail. There are numerous organic particles such as proteins, lipids, phenolics or polysaccharides but also diverse bacteria present in domestic wastewater. Certain contaminants could therefore favour an attachment to the PBM coating layer which are unlikely to get absorbed by the PES surface. Moreover, most probably there was no internal fouling for the PBM since the permeability was stable throughout the experiment. This again confirmed the theory of surface property contribution to the selective process only in the beginning of the filtration.

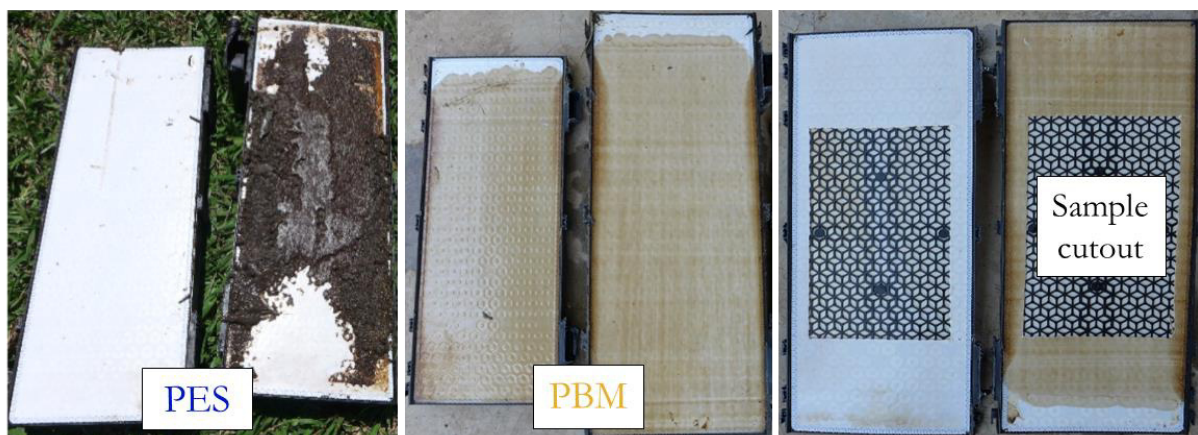


Figure 6-17 Dismantled membrane sheets after a 137 days trial period, sample collection (right)

Different sample cut-outs were taken for further characterisation at the laboratory of the *University Karlsruhe of Applied Sciences*. Again, samples were roughly cleaned with a DI-water jet with a subsequent, gentle surface cleaning with a fibre-free cloth. Prior to an FTIR analysis, specimens from different membrane sheets were dried in a drying oven at 35°C over night.

Focus of the assessment was placed on the C=O double bond peak height. In all cases, a distinct absorbance peak indicated the presence of the PBM coating (Figure 6-18). The values from the left measurement series were taken from the centred module frame and the right values highlight the measurement series of a rather external membrane sheet of the module. The comparison of all peaks did not provide an absolute value but the trend of a stable PBM layer was confirmed. Additionally – despite rough sample cleaning – certain level of surface fouling still persisted as thin cover on top of the PBM layer. The emitted infrared beam also exited molecules of this fouling cover which then individually oscillated. This absorbance peak could interact with neighbouring peaks of molecules in the PBM. If strong overlapping took place, a quantitative C=O peak height identification became impossible (see also chapter 4.2.5). Molecular bonds with higher degree of freedom show more than one peak, for instance as a longitudinal, twisting, or wagging movement which further provoked this phenomenon.

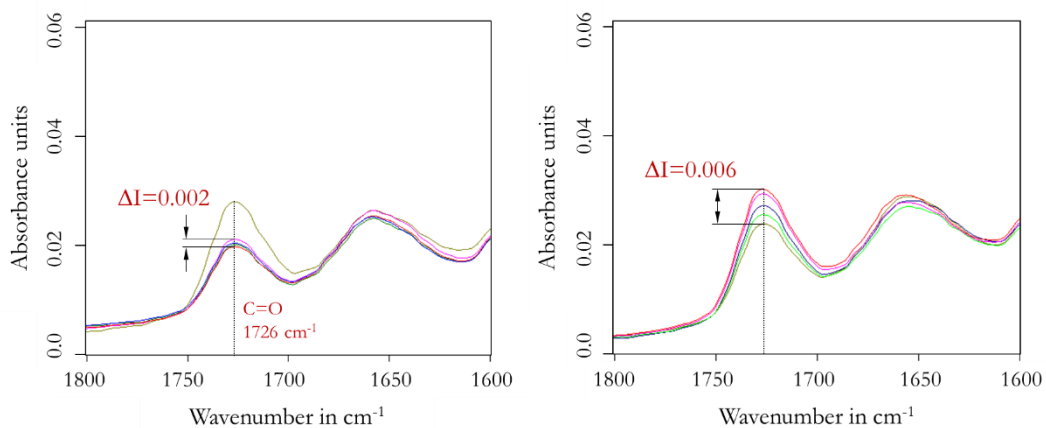


Figure 6-18 FTIR measurements of second PBM batch confirming stability after 5 months long-term operation at 25 LMH

Together with the stable operation at around $67 \text{ L}\cdot\text{h}^{-1}\cdot\text{m}^{-2}\cdot\text{bar}^{-1}$ and the chemical resistance tests under laboratory conditions (6.1.3), the FTIR tests are a further indication of the PBM coating layer stability on top of UF PES membranes. It should be again pointed out that the requirements for domestic wastewater filtration were low and thus only a gentle in-situ cleaning using 500 ppm NaOCl within the 137 day operation period was conducted. Considering the contradictory results of flux step tests including two extensive chemical in-situ cleanings, further extensive resistance tests must follow to validate the PBM stability.

6.3.4 Comparing lab scale with pilot scale

Long-term tests followed for the used PES and PBM cut-outs at a constant $0.4 \text{ L}\cdot\text{h}^{-1}$ volume flow, corresponding to 47 LMH. Both membranes were tested successively to ensure a proper comparability between different membrane sheets. The membrane cross-flow test unit could only control one permeate volume flow and thus, the corresponding pressure of the first membrane would dictate the pressure for the second membrane.

In this case, similar TMP would highly influence the result as the denser (PBM) or more porous (PES) membrane would have a change in volume flow. The following Figure 6-19 highlights similar behaviour than the flux step tests described above (Figure 6-5). Apparently, the PES membrane showed a lower TMP in the very beginning but sharply increased over time. At hour 86, the “intersection point” where both lines met and the PBM from then on showed a better filtration performance in terms of permeability. The specific pressure increase for the PBM was substantially lower than for the pristine PES membrane. Whereas the PBM showed a total 0.3 bar increase within the 119 h the test phase from 0.92 to 1.22 bar, the TMP of the PES increased from 0.53 to 1.31 bar. The specific TMP increase was thus 0.04 compared to 0.11 $\text{mbar}\cdot\text{min}^{-1}$. These parameter progressions showed a faster and higher fouling degree for the PES membrane sample. This was also validated by the clearly visible thicker humic acid fouling layer on top of the membrane surface after replacement (Figure 6-19).

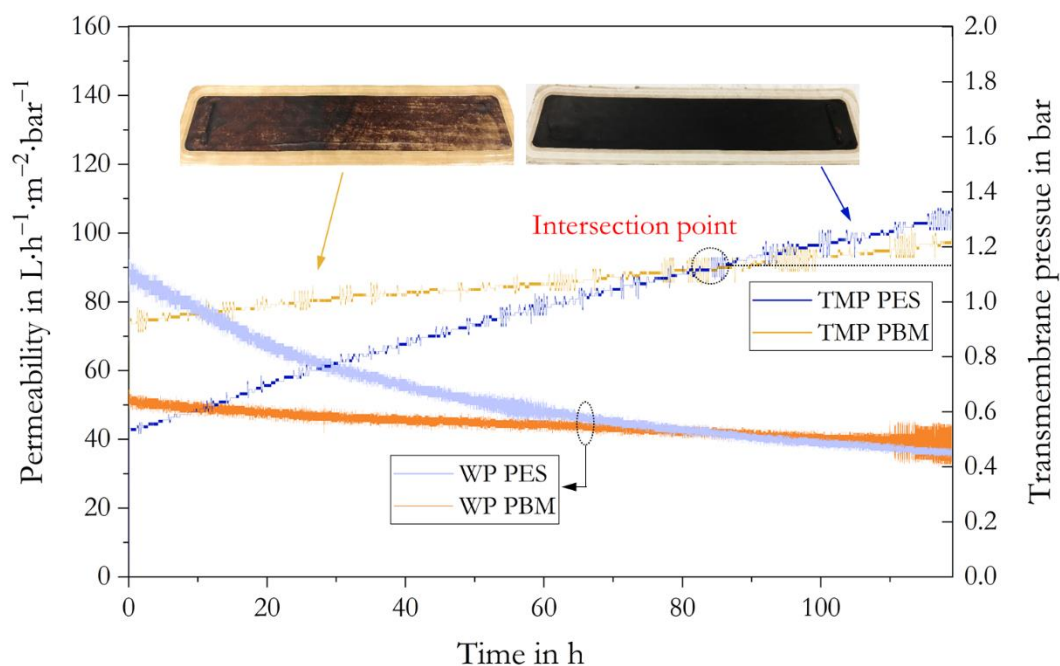


Figure 6-19 Long-term membrane tests at $0.4 \text{ L}\cdot\text{h}^{-1}$ constant volume flow on lab scale

Despite the clear difference in treating domestic wastewater, the commercial PES membrane showed a higher fouling propensity compared to the PBM within lab scale experiments. It was the declared aim of the laboratory tests to represent the reality as best as possible and identify weak links before production upscaling. Therefore, theoretical considerations about the discrepancy between the tests were made.

First of all, the pilot scale and lab scale experiments were based on different filtration principles. The submerged membrane modules did undergo suction pressures of <50mbar (vacuum) as it was the case for the commercial PES membrane (Figure 6-16). The cross-flow test unit in the contrary was a side stream MBR (sMBR) and the filtration a result of positive pressure operation up to 1,300 mbar (Figure 6-19). Thus, a direct comparison was not possible.

However, there are general rules which apply for both membrane filtrations. As discussed within chapter 2.2, the cross-flow velocity (CFV) has a major impact on the cake layer formation as it influences the concentration polarisation (CP). In this sense, lab tests for varying CFV were conducted with a 100 mg·L⁻¹ humic acid solution at 0.5 bar (positive). Calculations were based on the universal law for a volumetric flow through a defined cross-section per unit time. Dimensions for the cross-section are depicted in (Figure 6-20, right). Thereby, the CFV was increased from 0.1 to 0.17 and 0.25 m·s⁻¹ for a 28 (standard), 50 and 72 L·h⁻¹ volume feed flow, respectively. The operation time was 18 h for each test until stable filtration conditions were reached. The relative flux shows the flux decrease over time relative to the initial value from the starting point. In all cases, fouling layer was recoverable and after the tests mechanically wiped off with a fuzz-free cloth. Previous tests confirmed the full recoverability of flux without flux degradation. As it can be seen from the results, fouling propensity reduced with increasing CFV. According to equation 2-3, higher turbulent flow increases the permeate flux rate since particulate back diffusion into the bulk phase is enhanced. As a result, the flux J increased at comparable transmembrane pressure, also shown by the higher obtained relative flux (Figure 6-21, left). Moreover, it is well known that fouling effects are reduced with increasing CFV (Choi et al., 2005).

In contrast, submerged or immersed MBR (iMBR) generally have higher CFV comparative to the lab scale cross-flow unit. For instance, Yoon (2016) stated superficial liquid velocities of 0.3-0.4 m·s⁻¹ for flat-sheet (FS) module configuration, which was synonymous with the CFV. Prieske et al. (2008) studied the hydrodynamics in a pilot scale iMBR and predicted the superficial liquid velocity for membrane modules with varying plate distance. Values were calculated within the range of 0.23-0.32 m·s⁻¹. Complex calculations for the pilot MBR used within this work were not included but a rough estimate was made. The specific aeration demand (SAD) for the pilot iMBR was calculated with a 12 m³·h⁻¹ aeration rate and a total installed 12.5 m² membrane surface area (see chapter 4.3.4). The obtained SAD value of 0.96 m³·m⁻²·h⁻¹ is much higher in respect to pertinent literature of around 0.3 m³·m⁻²·h⁻¹ for submerged FS modules (Judd, 2006). This showed that in tendency higher CFV prevailed in the pilot MBR and substantially improved fouling mitigation.

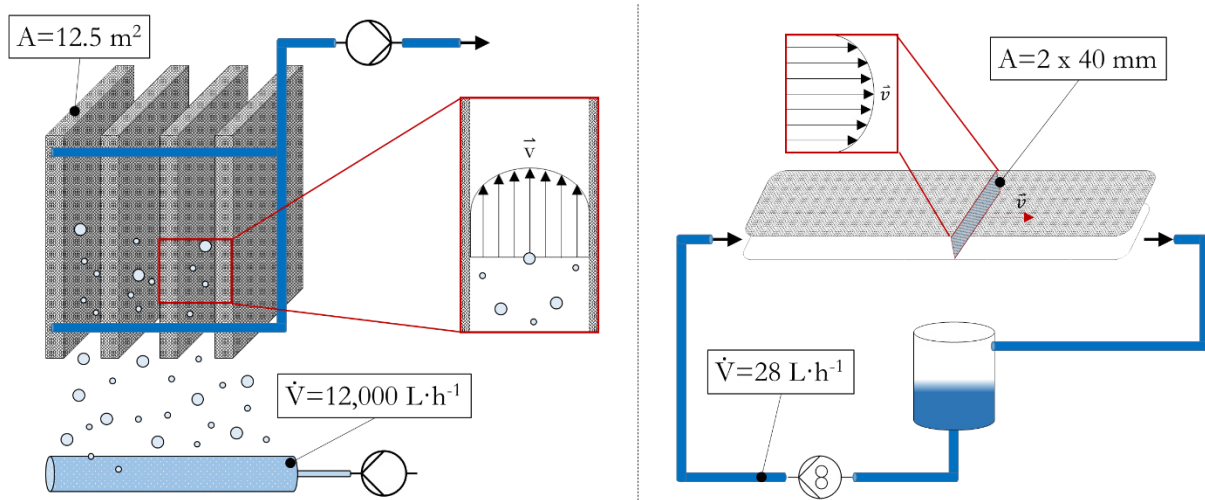


Figure 6-20 Cross flow conditions, submerged pilot MBR (left), cross-flow test unit (right)

Higher prevailing CVF in the pilot MBR stronger reduce fouling propensity compared to lab scale tests inside the membrane cross flow unit.

In addition, the constant flux rate of 25 LMH in the pilot tests were much lower than for the laboratory tests with 47 LMH. Higher permeate flux accelerates the fouling process (see chapter 2.4). At these severe filtration conditions, it was expected that the PBM low-fouling coating could compensate the increased membrane resistance.

Figure 6-21, on the right side, highlights three conducted lab scale experiments at 0.5 bar TMP with a different humic acid bulk solution of 100, 50 and 25 mg·L⁻¹, respectively. The results showed that the flux rate and fouling effect for HA solutions are only marginally dependent of the bulk concentration c_B . The difference at hour 18 is $\pm 5\%$ and the deviation to the mean value are negligible. In the diagrams of Figure 6-21, the relative flux of the PBM (orange line) remains constant since tests were carried out at constant TMP. PBM has a denser structure and thus a reduced flux relative to the more porous PES membrane (blue curve). Fouling was independent of the applied TMP and only provoked by the pertaining flux (equation 2-3). In case of PBM due to the comparatively low flux, less fouling occurred and the flux rate was stable throughout the testing phase. It was expected that major fouling effects for lab scale tests are surface particle adsorption and cake layer formation as a result of the CP.

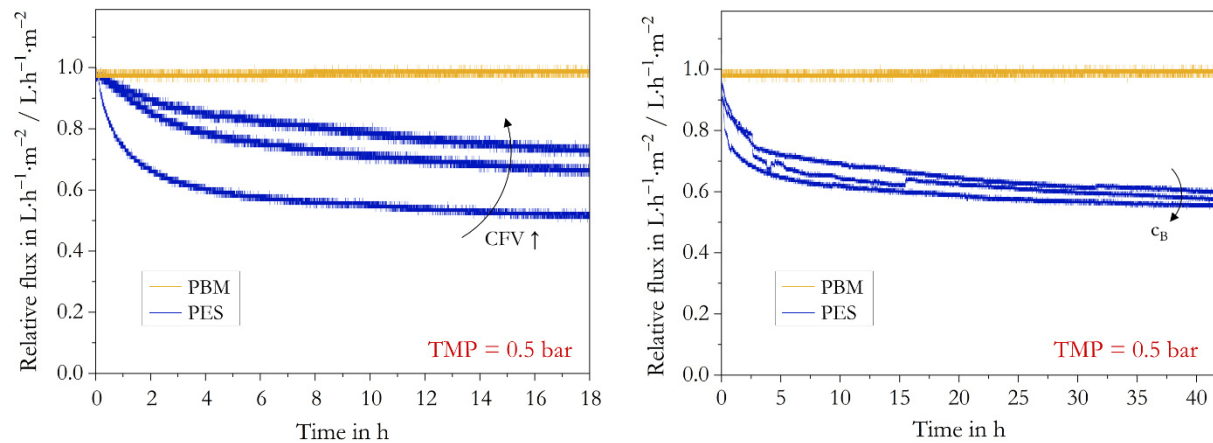


Figure 6-21 Lab scale tests for different CFV and bulk concentrations at constant TMP

The listed points better clarify the difference of laboratorial and pilot trial conditions. Hydrodynamic conditions such as cross-flow velocity, TMP and flux appear to have major impact on the membrane fouling propensity which was also discussed within the fundamental chapter 2.2. A change in bulk phase concentration c_B for humic acid solution however, did not affect the membrane performance. These findings were an explanation for the significantly better efficiency of PES membrane comparatively to the PBM coated membrane during pilot-trials. Nonetheless, comparing the model foulant humic acid with the organic matter present in domestic wastewater was not possible. Different fouling phenomena prevailed and biofouling (see chapter 2.4.2) did not occur for lab tests filtering humic acid solutions. Lab trials using a model foulant, however, are a substantial part of membrane research prior to upscaling processes since a relative comparison can be drawn.

The data and experience from the previously discussed experiments showed the limitations of PBM coatings applied with a spiral casting coating knife, subsequently polymerised by UV-LED light. Low-strength domestic wastewater was not a suitable application.

Besides, the pore intrusion of liquid PBM persisted. In light of these findings, research focused further on the advanced development of the coating process. As described, casting coating holds disadvantages of aggravating the pore intrusion due to occurring shear and mechanical stress. It was expected that atomising the liquid PBM through spray coating application reduced pore intrusion and thus reduced the total membrane resistance with improving permeability. Specifically, small droplets separate from a liquid bulk phase in result of pressure or kinetic energy added. The fan-assisted spray mist was of low energetic energy and only smoothly settled down on the membrane surface. In theory, once settled, the droplets fuse in seeking a preferred low energetic level (lower surface-to-volume ratio). Two spray nozzle types were tested on their feasibility for PBM coating application and their homogeneous spray pattern as well as spray coverage was evaluated. Detailed results can be taken from the following chapters.

6.4 Spray coating application

UV-LED induced PBM polymerisation applied by casting coating has shown its limitations in permeability. Moreover, membrane damage occurred during the coating process when solid particles, originated from the membrane production, were present on the membrane surface. Through casting coating, these particles scratched the membrane layer which resulted in irrecoverable layer damage. Although better filtration capacity is expected for high strength wastewater, a different coating strategy was sought to overcome the given constraints. Spray coating is known to achieve high homogeneous coating layer results with high flexibility in terms of spray mist variations which leads to the desired spray pattern.

6.4.1 Comparing spray nozzle principles

Initial spray tests were carried out with DI-water for both, the pressurised jet nozzle and the duel-fuel or assisted nozzle, described in detail in chapter 4.3.5. Different spray principles did not allow for direct comparison using similar spray coating parameters. For instance, for the jet nozzle only inhomogeneous spray mists below 2 bar (relative) were obtained. Duel-fuel nozzles with an external mixing of pressurised assisted gas (nitrogen, N₂) and the liquid PBM could work at much lower pressure values. Pressures >1.8 bar (relative) caused especially fine droplet distributions due to the high kinetic energy (fogging). As a consequence, the liquid spray mist could no longer be accurately sprayed onto the membrane. Figure 6-22 compares both nozzle results on a glass plate. Trials were done in a 21.5 cm distance from the glass plate with the nozzles in a centred position. The jet nozzle showed very large droplets with an inhomogeneous surface wetting. By increasing the operation pressure up to 4 bar (relative), smaller droplets were achieved which yielded a higher homogeneous coating layer. Duel-fuel nozzles on the other hand showed significant benefits in wetting homogeneity for low pressures along the entire glass surface Figure 6-22, on the bottom.

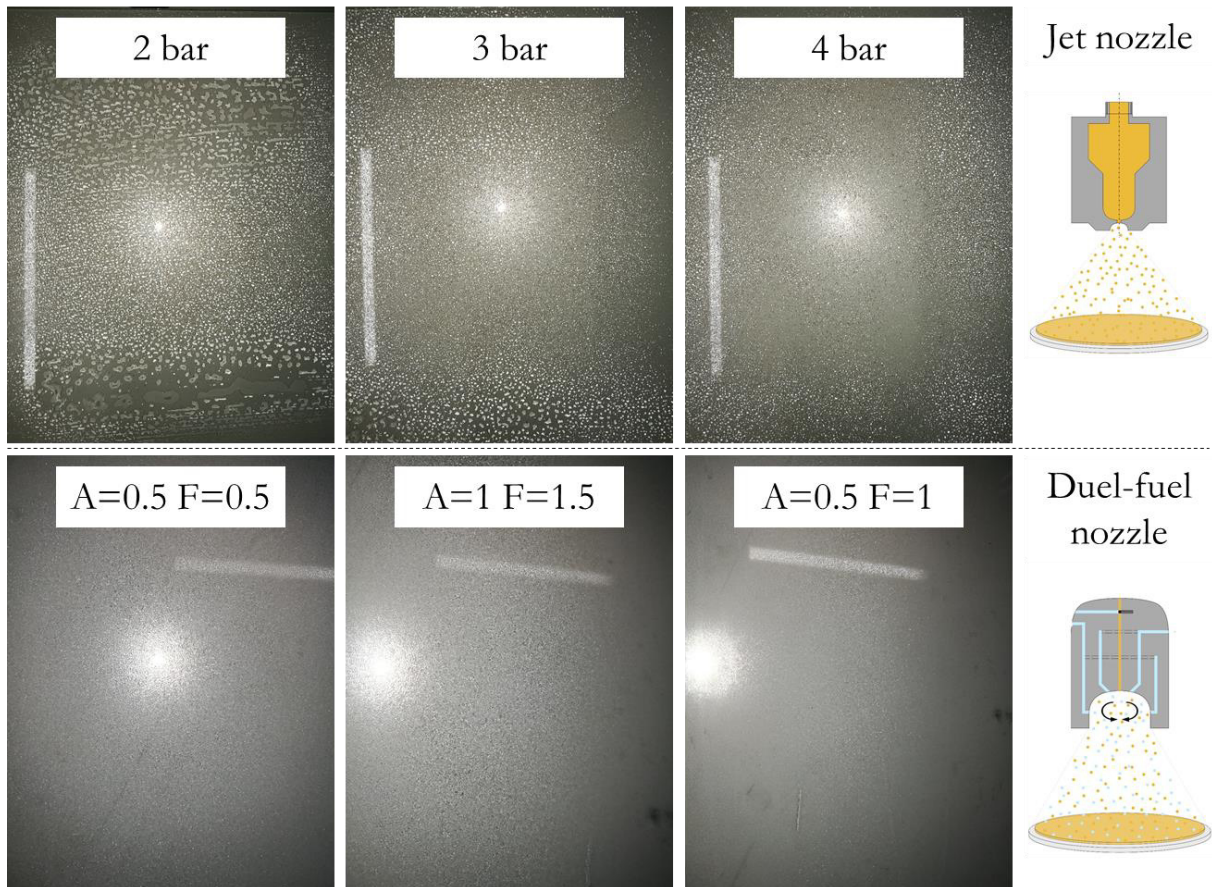


Figure 6-22 Spray test on glass plate using DI-water for different operative parameters

Next, spray parameters were adjusted for additional PBM glass plate tests with the duel-fuel nozzle only. A much higher homogeneous spray layer was achieved at comparatively low-pressure levels (0.5 to 1.8 bar, relative pressure). It was not clear how elevated pressures affected the PBM formulation and precaution was taken to prevent phase separation. According to equation 2-14 and 2-15, the atomisation tendency increases with reduced surface tension. Validated by previous measurements (chapter 5.7), the PBM solution had a much lower surface tension with 30.1 to 72.7 $\text{mN}\cdot\text{m}^{-1}$ for water (21°C). A lower surface tension improved the atomisation degree and, in theory, atomisation and fan pressure should be reduced for a similar spray pattern. Figure 6-23 confirmed this opinion with a more even coating layer along the entire glass plate area, visualised by the magnified areas at the bottom. Comparing the spray coverage parameters, higher pressures achieved smaller droplets and thus improved the homogeneity ($A=1$ and $F=1.8$). How the pressure values affected the spray coverage in shape and volumetric distribution will be discussed further in chapter 6.4.2.

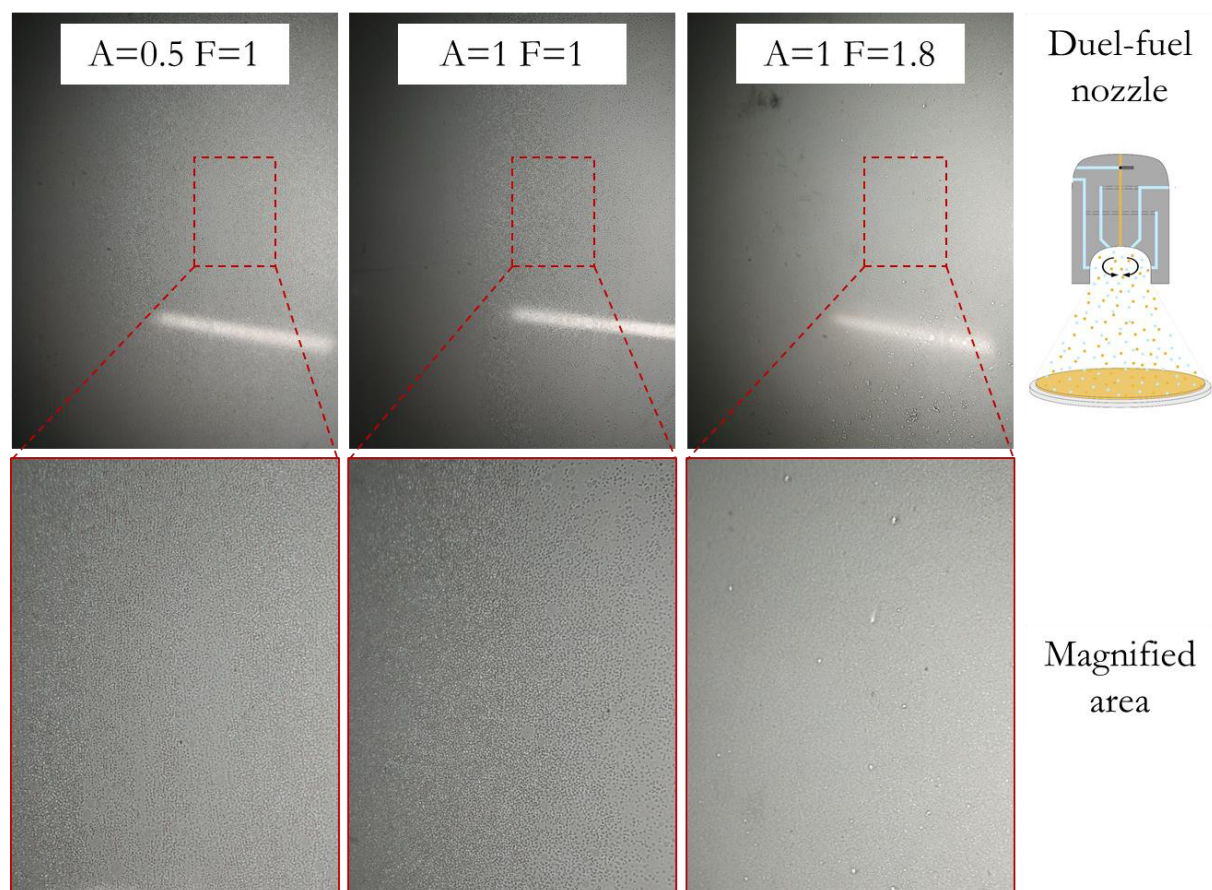


Figure 6-23 PBM spray coating tests on a glass plate using a duel-fuel nozzle

The influence of pressure energy on the thermodynamic stable PBM formulation remained unclear at this point of research. First indications about the real behaviour was the change of transparent to opalescent appearance. For both spray principles, the transparent optic changed to a more opalescent presence. For the pressurised jet nozzle, a highly milky liquid occurred as shown in Figure 6-24, on the bottom left- side. The picture was taken at a 1 bar spray trial but the milky appearance was dominant for all test series over the entire pressure range (1 to 4 bar, relative pressure). Duel-fuel nozzle tests also showed a change in transparency which indicated a phase separation. However, the PBM transparency restored in time which indicated the regain to the initial thermodynamic formulation.

Conductivity measurements were a basic way to distinguish between existing microemulsion formulations. The microemulsion solution significantly changed its electric resistance depending on the micellar structure. Galiano also did some electric conductivity measurements for identifying bicontinuous regions for two different surfactants (Galiano, 2013). Similarly, the conductivity was examined for the PBM solution right before and after the spray tests (duel-fuel nozzle only) as well as 1 h later to check the PBM formulation recovery. Compared with the values given by Galiano, the prepared PBM had a slightly different conductivity with 11.31 to 10.8 $\text{mS}\cdot\text{cm}^{-1}$ (Figure 6-24, right). The reasons could be the greater amount of impurities in the synthesised modified AUTEAB (see chapter 6.1.1) which increased the level of dissolved ions in the solution. In addition, systematic and random measuring errors through pipetting could not be avoided. Immediately after spraying, the conductivity jumped to 12.5 $\mu\text{S}\cdot\text{cm}^{-1}$ indicating a change of PBM formulation. As the transparency recovered after one hour, lower values were observed with 12.03 $\mu\text{S}\cdot\text{cm}^{-1}$.

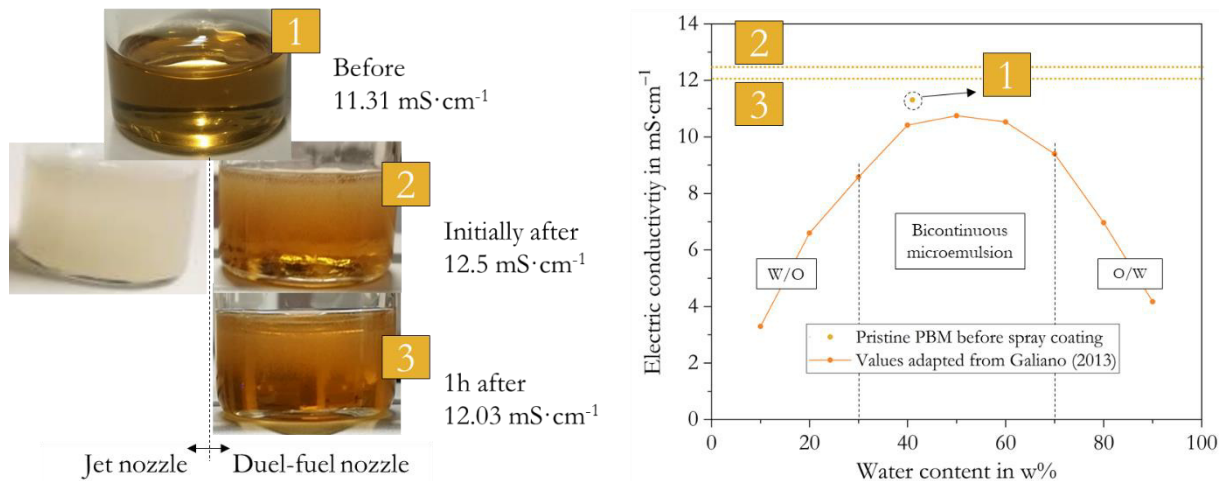


Figure 6-24 Conductivity measurements and opacity change due to spray coating application

Although the conductivity was known, the exact composition compared to the initial state could not be examined. If phase separation occurred, the composition shifts inside the Gibbs triangle (Figure 3-2) and thus, the micellar structure changed (Figure 6-24, point 2 and 3). Though, the question about the actual formulation change remained.

FTIR measurements were taken before (transparent) and after (opalescent) the spraying process in order to bring more clarity (Figure 6-25). The magnification showed a reduction in the characteristic C=O peak intensity and a slight shift in the total spectra. This was a clear evidence that the PBM formulation changed and thus the mass ratio between the components. Opalescence effects caused by pressurised nitrogen infiltration was recoverable in time and a clear transparent microemulsion was again formed. Prior to the pre-trials, the nozzle and collecting pan were sealed to avoid evaporation and material loss changing the liquid PBM composition. Thus, a constant system mass was assumed. As a consequence, opaque appearance was an intermediate state only and did not affect the final PBM formulation on thermodynamic time scale. How this effect affected the coating structure in short time was further investigated with NMR and SEM measurements to verify the feasibility for membrane coating applications. Despite the possible change in composition and micellar structure, spray coated membranes could show a sophisticated permeability and fouling mitigation. In this case, the effect of change formulation would be secondary.

In conclusion, low operating/atomising pressures also affect the PBM transparency. This also occurred for a non-pressurised operation, for instance by flowing through a small opening such as needle valve seats driven only by gravitational force. It appeared that any kind of PBM expansion resulted in shorter or longer loss of initial bicontinuous PBM formulation.

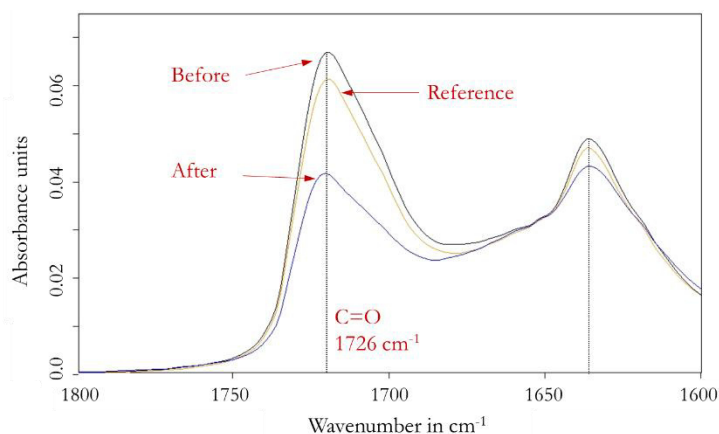


Figure 6-25 FTIR measurements of liquid PBM (without Irgacure 184) before and after spray test

Both nozzles showed broad differences in spray characteristics. The pressurised jet nozzle had a very high volume flow at the minimum operation pressure of 2 bar. Below this pressure the spray pattern was highly inhomogeneous. The corresponding flow rate of $50 \text{ mL}\cdot\text{min}^{-1}$ was roughly 16 times greater than required for the given $6 \text{ cm}\cdot\text{s}^{-1}$ coating speed (see chapter 4.3.5). The wet layer thickness would account for more than $60 \mu\text{m}$, which would substantially increase the filtration resistance. Higher coating speeds for a very thin PBM layer could not be obtained with the given motor gear box. The elevated pressure values in comparison to the moderate dual-fuel nozzle also led to high evaporation of volatile components of the PBM. Accordingly, the risk of phase separation was high. The pressurised nozzle also showed restrictions in handling and a high susceptibility to clogging. The jet nozzle had a small elliptical aperture of 0.2 mm (length) to 0.12 mm (width) and impurities in the coating material easily accumulated at the constriction which significantly changed the spray pattern.

Therefore, the PBM membrane coatings were continued with the dual-fuel nozzle only. Further tests determined the spray coverage as a function of the given spray parameters. Optimum settings were used for the PBM coating with subsequent permeability tests inside the membrane cross-flow unit.

6.4.2 Spray coverage of the dual-fuel nozzle

Generally, the spray coverage followed a Gaussian distribution with highest spray volumes at the centre below the nozzle head. Width and height changed with the two spray parameters and the liquid flow rate. Figure 6-26 shows the spray volume results for a variable liquid feed supply of 17.5 and $37.5 \text{ mL}\cdot\text{min}^{-1}$ for DI-water and ethanol. The spray parameters A and F were set to 0.5 bar prior to the tests. Although the volume flow rate was approximately 2 times higher, the spray volume for water tripled in the centre position. With a lower water flow rate, the spray pressure produced finer droplets with a higher surface-to-volume ratio. Smallest droplets evaporated and proportionally lower water droplets reached the test tube which corresponds to a lower weight and thus lower spray volumes. In contrary, the ethanol shows significantly lower spray volumes. Ethanol has a third of the water's surface tension (21.6 to $72.1 \text{ mN}\cdot\text{m}^{-1}$) and the atomising tendency, as indicated by the Weber and Ohnesorge number We and Oh , were higher (see equation 2-14 and 2-15 in chapter 2.5.3). As a result, the ethanol spray mist contained much smaller droplets.

In conjunction with the high volatility, ethanol evaporated before reaching the test tubes. Moreover, once collected, there was enough time to enter the gas-phase state during the long 5 min spray test which resulted in further material loss.

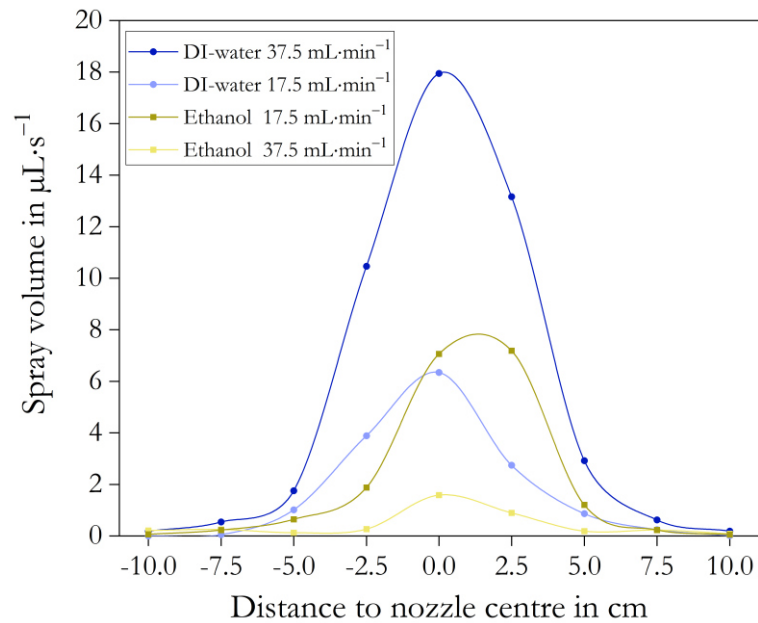


Figure 6-26 Spray coverage for water and ethanol with a different feed supply, A=0.5 and F=0.5

Differences in the spray pattern were more distinct when the spray pressure atomisation A and fan F were adjusted. At this point, the liquid volume flow was constantly at 37.5 mL·min⁻¹ to yield a more distinct spray picture. For a change in the atomisation degree A from 0.5 to 1 bar at constant F=0.5 bar, the Gaussian bell was narrower with slightly higher peak values from 18 to around 20 μL·s⁻¹. Higher atomising pressures increased the kinetic energy of droplets in the z-axis direction (vertical) towards the membrane. This higher acceleration shortened the time between nozzle opening to the impact which reduced the relative velocity in transversal direction. The impact of fan pressure was reduced and the spray coverage was narrower. The variation in fan pressure F had a high impact on the spray coverage homogeneity as it can be seen in Figure 6-27. For the tests, A was kept constant at 0.5 bar and the fan pressure F changed from 0.5 to 1 bar. A higher fan pressure increased the lateral acceleration and dragged the atomised droplets further to the membrane margin. The Gaussian distribution was very wide-ranging with low maximum peak heights.

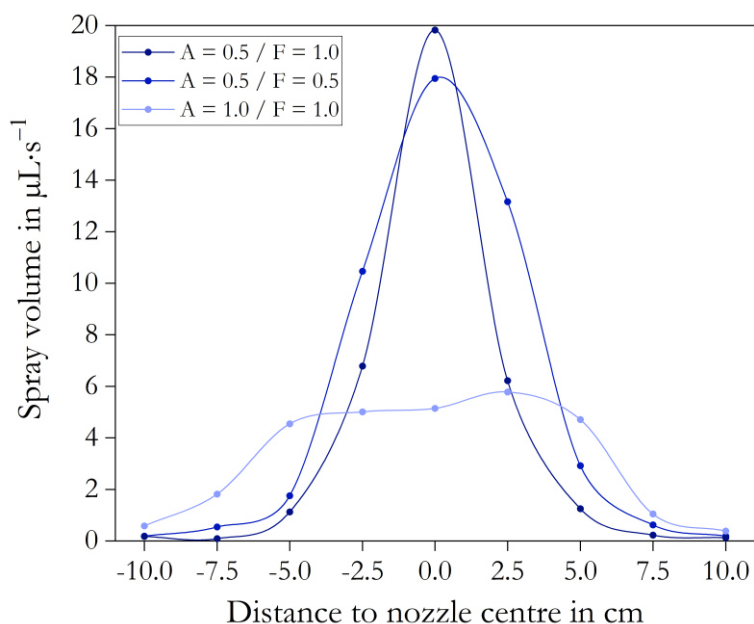


Figure 6-27 Spray parameter variation (A and F) at 37.5 mL·min⁻¹ constant liquid flow rates

In summary, the fan pressure F had the highest impact on the coating homogeneity in the transversal direction. Ethanol already showed much lower spray volumes reaching the test tubes compared with DI-water due to the low surface tension.

1-Octanol has similar fluid properties than the prepared PBM solution (see chapter 4.3.5). Pre-trials were conducted with spray parameters and volume flows analogues to water and ethanol. However, atomisation resulted in a strong fog production and evaporation of very small atomised droplets. Despite the sealed spray box, a detailed study of the spray coverage was not feasible due to missing suction device and safety concerns. Similar results were expected for the liquid PBM of comparable viscosity and surface tension, and thus spray pressure was slightly reduced. In this context, optimum spray parameters should be investigated for specific fluids and application prior to final membrane curing

Spray pattern in longitudinal direction along the membrane length (0.5 m) were controlled with the automated linear guiding system. The PWM equipped gear box enabled a gradual variation of the coating speed and directly affected the wet coating layer thickness. For final membrane coating experiments, the forward speed was orientated towards casting coating application with an average feed speed of 6 cm·s⁻¹ per membrane. Membrane coating via duel-fuel spray application were performed with optimum spray parameters A=0.5 and F=1.0 bar, respectively. The liquid PBM polymerisation was initiated, as customary, with the UVLED inside the glovebox to achieve inert conditions.

FTIR measuring points along the membrane width after polymerisation determined the homogeneity in the spray mist. Ten sampling points were taken after UV-LED polymerisation and the results are given in Figure 6-28. The characteristic C=O at 1726 cm⁻¹ was clearly visible for all measurements confirming the PBM existence.

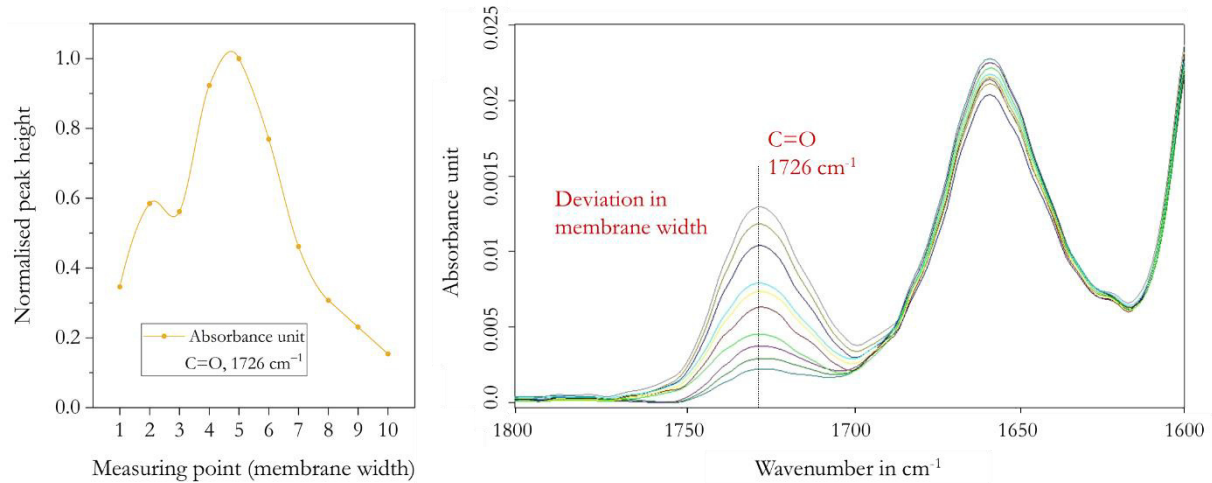


Figure 6-28 FTIR measurements at various spots along the PBM coated membrane width with the duel-fuel nozzle

Peak heights for the duel-fuel nozzle varied greatly and reduced the peak intensity with distance to the centred nozzle. This was in accordance with the expectations. The increasing atomisation pressures elevated the atomising tendency due to the smaller droplet generation. The kinetic energy of the droplets reduced and were less spread in transversal direction by the fan air. Droplets did not reach the outer membrane surface area.

Initial concerns about the PBM coating feasibility due to the encountered problems of the 1-Octanol with similar fluidic characteristic were not confirmed. Different spray properties were presumably caused by the phase interactions of the multi-phase PBM formulation.

6.4.3 Membrane performance tests

After production finished, three membrane samples (#1, #2, #3) were cut out of the 0.11 m² membrane sheet for further testing. FTIR measurements along the width validated the spray coverage also for the PBM solution. Lowest C=O peak values decreased towards the edges and had maximum peak intensity in the centre of membrane cut #2. Higher peak intensities equalled to thicker coating layers. All three membrane cuts were tested inside the membrane cross-flow unit and the permeability values are included in Figure 6-29. Thicker coating layers, respectively higher C=O peak intensities, resulted in a lower permeability as the membrane resistance increased. An improved low-fouling characteristic could be achieved at the cost of lower filtration capacities or, weaker low-fouling properties with a better permeability or lower TMP at constant flux conditions. The end user and ultimately the wastewater composition define the requirements of the membrane applied. For instance, high -strength wastewater requires better low-fouling features obtained by thicker PBM layers. The tests shown in Figure 6-29 followed the common protocol of chapter 4.3.1.

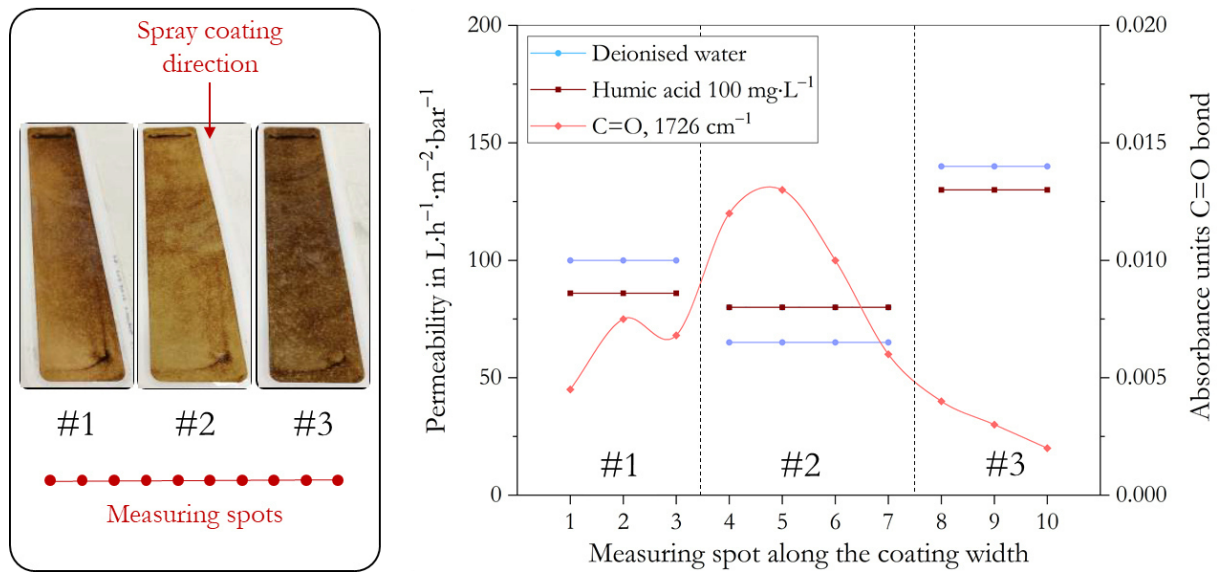


Figure 6-29 Membrane performance test and characterisation of a sprayed PBM coating layer

During the spray tests with PBM as liquid supply, a high fogging effect was observed when compared to water. This resulted from the lower surface tension of the ethanol and PBM which led to very small droplets and a finely distributed spray pattern. Depending on volatility of the substances, material loss varied significantly. For large production quantities, extraction systems must be considered for safety aspects as well as material recovery. FTIR and spray volume tests showed that one nozzle could not coat the membrane along the entire width due to the given limitations of the spray pattern. Two principle options exist to overcome this limitation. As an example, a separate pivoted nozzle suspension with a three-dimensional movement pattern could be implemented. Secondly, the distance between the spray nozzle and membrane can be varied along with the spray angle by means of the freely movable nozzle head. At this stage of research, however, this system was too complex. Moreover, such systems are susceptible and highly expensive. Much more cost-effective and robust solutions are the extension and modification with a linear guidance in transversal direction for a two-axis movement or simply a second spray nozzle which requires only a second supply line. The installed peristaltic pump was equipped with an eight channel pump head which makes the implementation of a second nozzle head simple.

6.5 Casting versus spray coating

There are fundamental differences between the applied coating technologies. Spiral casting knives apply a high shear stress to the coating material to achieve a uniform distribution of the liquid PBM along the membrane surface. The mechanical stress and occurring friction between the casting equipment pushed the PBM inside the membrane pores (enhanced pore intrusion). Additionally, the high mechanical stress led to membrane damages during the upscaling procedure caused by splitter material on the surface resulting from a production failure. Many coated membrane sheets had to be replaced since irrecoverable deep scratches occurred. Spray coating uses pressure energy of an assisting gas, which is converted into kinetic energy required for atomising the liquid PBM. Depending on the operative spray parameters, a defined spray cone shape developed and covered at best the entire membrane width. The process showed a great flexibility in cone shape through spray pressure adjustments and fluids of varying surface tension. Moreover, the atomised spray mist only settled down on the membrane surface and finally formed the PBM layer. No mechanical stress was applied and thus reduced production scraping as is the case for casting coatings. The forward speed of the substrate has a major influence on the spray coating result since it directly correlates with the coating layer thickness.

6.5.1 Contact angle measurements

Spray coating showed a lower contact angle (CA) along the entire membrane width, measured at 9 different spots (Table 6-4). Although the coating thickness varied greatly, a reduction in CA was present for the entire coated surface. This validates that the CA was independent of the coating thickness since only the coating layer surface contributed to the hydrophilic behaviour. Comparing both coating applications, spray coating indicated a higher hydrophilicity of 47° compared to the 64° of the casting coating. The reason could be the difference in PBM texture, visualised by SEM measurements (see next section).

Measurements with a wet surface better represent reality as the membrane are in direct contact with water during the filtration. For more details of the preparation steps see chapter 4.2.6. A higher CA might have resulted from the high surface tension of the water itself which was present in the membrane pores. Impurities on the dry membrane surface could have been present after drying in the dry oven and could have destroyed the surface tension of the 5 µL DI -water drops. Residues of glycerine inside the membrane pores also affect the surface tension between solid polymer and the liquid water drop substantially. For all measurements, including the PES commercial membrane, the results were in line with the previously highlighted values of chapter 6.1.1.1.

Table 6-4 Contact angle measurements comparing casting and spray coating technique

Membrane type	Contact angle CA (dry)	Measuring tolerance	Contact angle CA (wet)	Measuring tolerance
PES commercial	80°	±11°		
Casting coating 4 µm	64°	±2.5°		
Spray coating A=0.5, F=1.0	47°	±6°	59°	±4°

6.5.2 Scanning electron microscopy

Influencing parameters for scanning electron microscopy (SEM) are numerous, for instance, a higher acceleration voltage increases the resolution in subsurface areas (Zhou et al., 2007). Constant measurement parameters and environmental conditions were required to compare the surface pictures obtained by SEM, further outlined in chapter 4.2.8. Views of membrane surfaces for differently applied PBM coatings are highlighted in Figure 6-30 below. The surface structure changed for each measurement of the individual membrane sample. Taken from literature, the REDOX section view (top-right) shows the reference PBM structure (Galiano et al., 2015). As a general observation, the structures changed considerably with a very dense structure for pristine casting coatings using UV-LED initiation with a spiral casting knife of a 20 μm wet layer thickness. As indicated before, viscosity modification by controlled radical polymerisation changed the polymer architecture which could be seen for the modified PBM coatings at the bottom (left: time of inhibition $\Delta t_i=5.5$ min, right: $\Delta t_i=9$ min). Higher viscosity led to lower pore intrusion depth but concurrently, the structural change relative to the pristine PBM resulted in a permeability reduction (Figure 6-13).

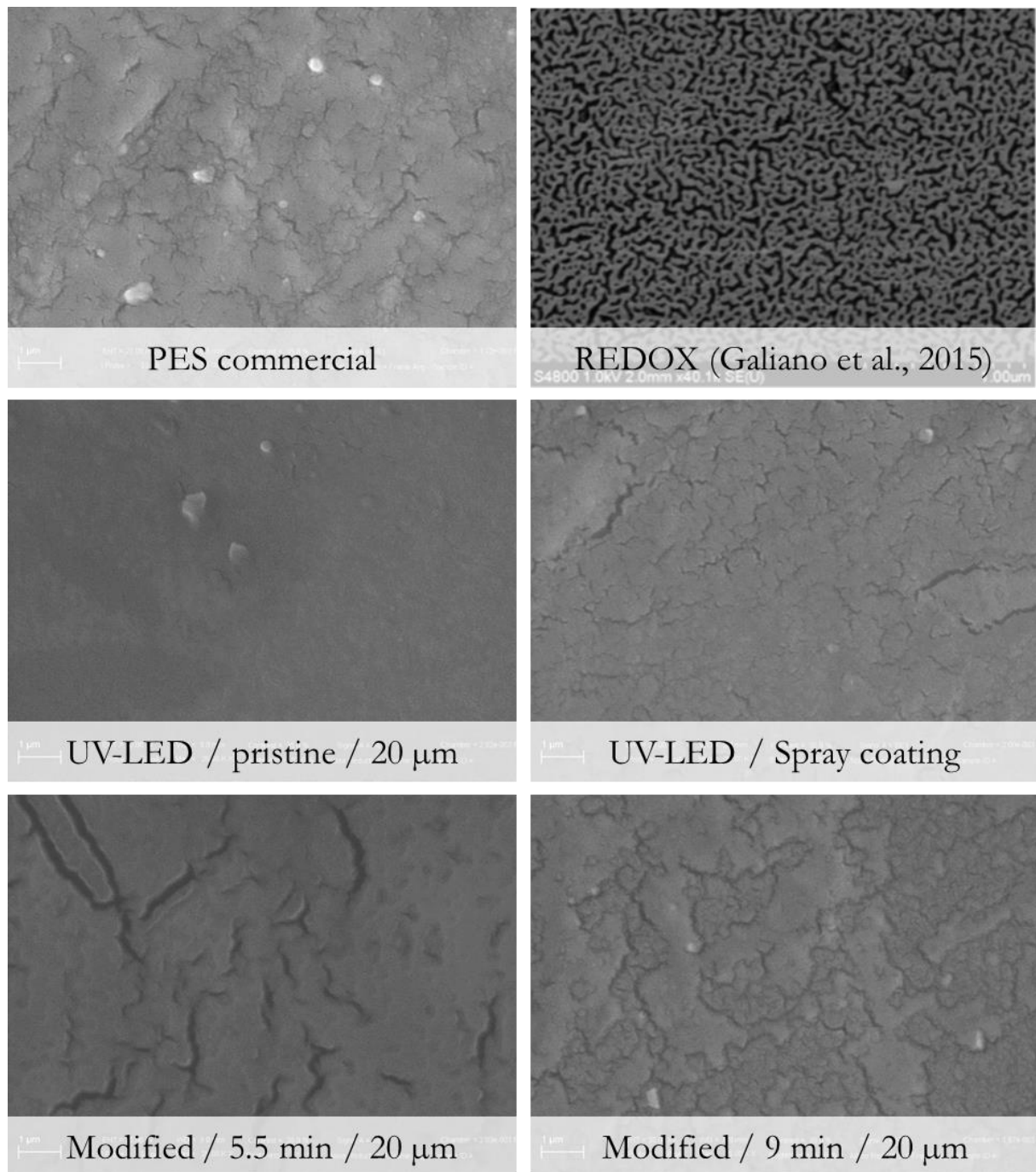


Figure 6-30 SEM analysis of the membrane surface for different polymerisation attempts

The concluded research was not able to determine the exact mechanisms behind the structural differences and the effects on the coated membrane characteristics and their performance. Questions remained unclear at this point and require more detailed, fundamental research which should be addressed within the next period.

6.5.3 Chemical characterisation by solid state NMR

Due to superposition, it was possible to analyse the spectra and only recognise unique resonances characterising a specific molecular entity (see Table 6-5). The two resonances 8 ppm and between 22-29 ppm were produced by AUTEAB only. Signals around 18.1 ppm could be associated to the polymerised MMA (PMMA), HEMA (PHEMA) and the polymerised EGDMA. CPMAS spectra could be interpreted qualitatively since the intensity was a function of the dipolar coupling between neighbouring protons and carbons. Thus, the incorporated carbonyl groups (C=O) of the components were underrepresented due to missing proton bonds. Despite different cross-polarisation dynamics, the analysis could provide qualitative results due to similar analysing parameters and vibration intensities for methylene and methyl groups. For the evaluation, the intensity ratio between the 8.5 and 22-29 ppm signal was compared for all samples (see Table 6-5, CP spectra).

The AUTEAB surfactant was similar for all prepared samples (25 w%, see Table 4-1). However, the integral intensity of the signal between 22-29 ppm relative to the 8.5 ppm reference, and peak ratio were different for the analysed samples although both peaks resulted from the AUTEAB. This was explained by the changing distribution of stereo sequences of PMMA for the different polymerisation approaches. As a consequence, overlapping between two signals occurred. Samples were characterised by their marginally different dynamics of the undecyl chain. For the spray coated sample, the signals were very intense. This was a possible indication of very strong dipolar couplings typically of ordered (almost crystalline) system. It was stated that the UV-LED polymerised samples with varying photo initiator amount showed similar results (also see Figure 6-31). The modified/pre-polymerised ($\Delta t_i=9$ min) PBM had a slightly higher ratio, whereas the REDOX initiated and moreover the spray coated sample varied greatly. An explanation was that the spray sample contained much less PMMA and PHEMA and carbonyl groups with respect to the other analyses. Surprisingly, the modified and UV-LED (5 w%) samples showed clearly detectable signals in the range between 120 and 140 ppm. A possible explanation was the presence of Irgacure residues inside the polymers or some non-reacted double bonds.

Table 6-5 Integrals of significant peaks in ^{13}C MAS NMR spectra

	Reference	Integrals of CP spectra		Integrals HPDEC spectra		
	8.5 ppm	18.1 ppm	22-29 ppm	18.1 ppm	22-29 ppm	177 ppm
REDOX	1	6.2	12.5	0.95	3.05	1.42
UV-LED (1.8%)	1	2.7	9.4	-	-	-
UV-LED (5%)	1	3.3	9.2	0.55	2.89	0.82
Modified (9 min)	1	3.7	7.9	0.86	3.25	1.19
Spray coating	1	18.1	31.4	0.43	2.98	0.75

The HPDEC spectra was recorded with 20 seconds of recycle delay. Amorphous polymers with a low glass transition temperature, in general, can be analysed more quantitatively using HPDEC. This was also confirmed with the nearly constant 1:3 ratio between the methyl groups and the non-directly bonded N or O of the AUTEAB molecules (8.5 and 22-29 ppm, respectively) for all samples. The same trend could be found for the acrylate signals of 18.1 and 177 ppm.

From stoichiometric consideration the peak intensity at 177 ppm should be equal to the sum of the 8.5 and 18.1 ppm integral. This was not a valid assumption since the carbonyl signal was not fully relaxed. Thus the ratio between acrylates (MMA, HEMA and EGDMA) and the AUTEAB was the direct ratio between the methyl signals at 8.5 and 18.1 ppm. The highest amounts accounted for the spray samples whereas the REDOX initiated PBM showed least values. Figure 6-31 depicts the NMR spectra for the UV-LED (1.8 w%) and spray coated sample. The differences in peak intensity were most evident for these two.

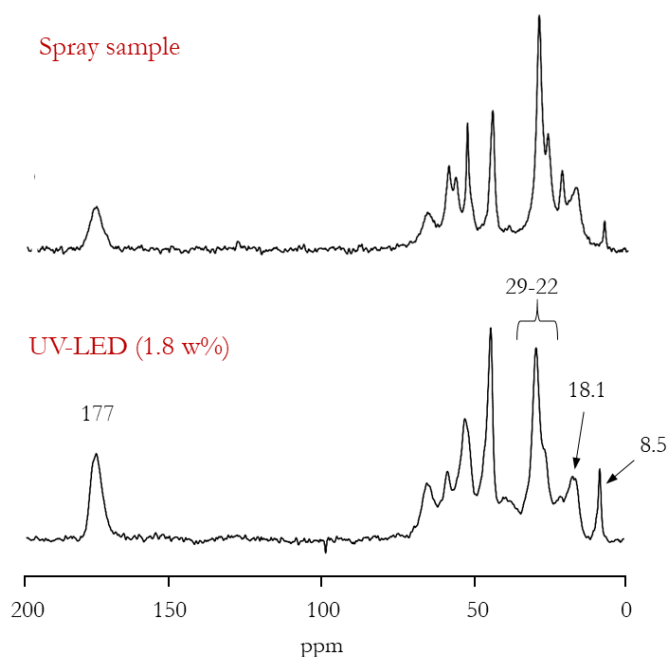


Figure 6-31 Exemplary ^{13}C CPMAS NMR analysis for two different PBM samples

In conclusion, data evaluation of complex multi-phase polymers such as the PBM was challenging due to several molecular interactions. A purely quantitative analysis was not possible, however, the data clearly showed that the polymer architecture changed with varying the polymerisation approach. Contrary to pertinent literature, a roughly three times higher photo initiator (5 to 1.8 w%) for UV-LED polymerisation did not or just insignificantly change the molecule structure. Looking back at previous discussions about the AUTEAB surfactant modifications in chapter 6.1.1, a slightly higher photo initiator of 2.3 to 1.8 w% had minor or no effect on the polymerised product. A change in the achieved spectra was also observed for the modified ($\Delta t_i=9$ min) PBM. It was not possible, however, to quantify the difference which would support the assumption of a denser membrane layer compared to the pristine PBM. After all, the spray sample showed the highest ratio relative to other obtained data. High ratios between corresponding methyl signals at 8.5 and 18.1 ppm indicated the highest polymerisation degree.

6.5.4 Membrane performance test

Figure 6-32 depicts gathered data for the permeability at constant TMP (0.5 bar) for clean DI-water and humic acid solution ($100 \text{ mg}\cdot\text{L}^{-1}$). Casting coating values included all coatings carried out with the $4 \mu\text{m}$ spiral casting knife for 1.8 w% and 2.3 w% photo initiator amount (Irgacure 184).

Spray coating included membrane samples along the entire membrane width with a varying coating layer thickness, also indicated by spray coverage and FTIR test (Figure 6-29). Data evaluation followed the developed protocol in chapter 4.3.1) and the highlighted bars are the mean value of 20 measurement at steady state. The commercial PES permanently was within the manufacturer's recommendation of $>250 \text{ L}\cdot\text{h}^{-1}\cdot\text{m}^{-2}\cdot\text{bar}^{-1}$ for clean water permeability. Clean water permeability for the PBM coated membranes were as expected significantly lower due to increased total membrane resistance. Not just the thickness but also the dense polymer network reduced filtration capacity. Comparing both coating technologies, spray coating on average showed higher permeability for clean water ($123 \text{ L}\cdot\text{h}^{-1}\cdot\text{m}^{-2}\cdot\text{bar}^{-1}$) and the humic acid ($114 \text{ L}\cdot\text{h}^{-1}\cdot\text{m}^{-2}\cdot\text{bar}^{-1}$) solution. PBM casting coatings were significantly lower for clean water tests ($60 \text{ L}\cdot\text{h}^{-1}\cdot\text{m}^{-2}\cdot\text{bar}^{-1}$) and ($96 \text{ L}\cdot\text{h}^{-1}\cdot\text{m}^{-2}\cdot\text{bar}^{-1}$) for the humic acid solution. Deviations of the spray coating approach were slightly higher compared to the casting coating application.

However, if a uniform spray coverage along the width (e.g. through constructive changes) is considered, production tolerances could be further reduced from currently ± 20 (DI-water) and ± 19 (HA).

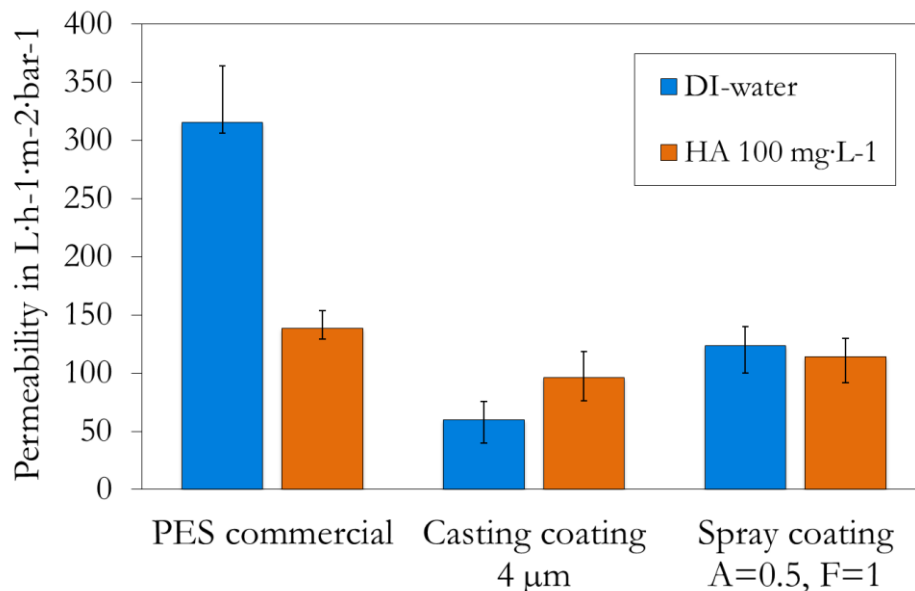


Figure 6-32 Membrane performance for $\text{TMP} = \text{const.} = 0.5\text{bar}$, comparing spray and casting coating technique with commercial PES membranes (all experiments included)

Surprisingly, the permeability of humic acid solution filtration increased for casting coating with 61% relative to the clean water permeability. This effect could also be observed for all coatings carried out with casting knives without having a clear explanation. This effect did not apply for PBM coatings achieved through spray coating application. Quantification and explanation of this effect should be of interest within further research activities.

In conclusion, the results validated the full capability of the synthesised, modified low cost AUTEAB surfactant for forming microemulsion systems. Surface characteristics such as hydrophilicity, surface roughness and the permeability for treating a humic acid solution were comparable to the high purity AUTEAB surfactant. Deviations lied within the production tolerance which arose from preparation errors (chemical purity, pipetting, weighing) and polymerisation conditions (temperature, oxygen level). Consequently, AUTEAB synthesis was adapted and larger quantities could be produced which were required for the PBM coating upscaling.

Controlled radical polymerisation using the inhibitor TEMPO prior to the casting coating process led to a successful increase in PBM modification. However, the permeability within a lab scale cross-flow unit decreased measurably. The results showed that the permeability reduced with a later polymerisation interruption and higher viscosity. Despite this drawback, pre-polymerised PBM coatings could be beneficial for different membrane applications which require more dense membrane structures for a higher selectivity such as in nanofiltration (NF) systems. Ideally homogenised pre-polymerised products, especially for large PBM volumes, require a precisely controlled reactor tank such as for reaction calorimetry. A simple process monitoring via thermocouples simplified the operating expenses for the conducted feasibility study herein. In the future, the developed modification protocol could be considered as innovative way for tailoring membrane surface properties such as permeability and low-fouling characteristic.

Although low-strength domestic wastewater was not suitable for PBM coatings applied with casting knives in comparison with commercial UF PES membranes, important knowledge was gained about the long-term stability. PBM membranes showed a relatively constant permeability over a 137-day trial period including a weak chemical cleaning which indicated the layer stability. Subsequent FTIR measurements of sample cut-outs confirmed previous assumptions. Lab scale tests in a cross-flow test unit validated the permeability and proved the higher critical flux of PBM membranes under laboratory conditions.

Spray coating application using dual-fuel or assisted nozzles offer several advantages over casting coating techniques such as higher flexibility in coating layer thickness by a regulated nozzle or substrate movement speed. Moreover, the spray cone shape and the level of atomisation varied with spray parameter adjustments for the air and fan pressure. The high influence of the surface tension on the atomisation level was demonstrated. Cover layer homogeneity and integrity were specific to the selected liquid. Spray volume tests validated the spray coverage for water, ethanol and the pristine PBM solution. Spray volume tests and FTIR measurements confirmed a Gaussian distribution for the optimum spray parameters. A second spray nozzle or a double-axis guiding system could be implemented to achieve highest possible coating layer homogeneity for larger membrane coating areas. Nevertheless, the results clearly showed that the achieved permeability could be improved with the spray coating technology using a dual fuel nozzle compared with casting coating applications. In contrary to the high mechanical shearing forcing applying for spiral casting technology, spray coating produces a low energetic spray mist which potentially reduced pore intrusion and membrane surface stress.

NMR and SEM analysis clearly showed a distinction between different polymerisation approaches. Although differences in the polymer structure and surface texture were examined, a quantitative conclusion about the mechanisms and dependence on the permeability could not be drawn. This requires further fundamental research

Spray coating using dual-fuel nozzles is considered as most promising to further advance the PBM coating technology.

7 Conclusion and Future Work

The thesis described fundamental relations between material properties and prevailing filtration conditions. Focus was given on the coating process optimisation to compensate for the limitations of UV-LED based polymerisation compared to previously conducted REDOX initiation. Basically, the work provided an improved understanding of the complexity behind membrane coating using polymerisable bicontinuous microemulsion. The ultimate goal was the upscaling of PBM coatings to bridge the gap between fundamental and applied research to industrial application.

7.1 Conclusion

To achieve the given objectives, the following activities were carried out and are concluded below. From the investigations and results within Chapter 6, the following points can be postulated:

- (1) The modified AUTEAB surfactant is suitable for PBM membrane coating application as it shows comparable results relative to the classic AUTEAB of highest purity.

The novel self-synthesised AUTEAB surfactant bears the major production costs of the PBM because it is synthesised in manual batch production. Taking this into consideration, efforts were made to reduce personnel costs along with operational expenditures. AUTEAB synthesis costs were substantially reduced by about 70%. As an important part of this research, laboratory tests verified the full surfactant function for forming transparent, thermodynamically stable PBM systems. Comparable low contact angles indicated a higher hydrophilicity than for commercial PES membranes. A reduction in surface roughness was validated by atomic force microscopy (AFM) and a comparable permeability relative to the PBM prepared with the classic surfactant was examined. This substantial finding helped further PBM upscaling to pilot scale as synthesis costs were reduced considerably with consistent quality.

- (2) Controlled radical polymerisation can be used to modify the PBM **viscosity** to higher values and subsequently re-polymerised with UV-LED light. Compared to the pristine PBM, coating layers by pre-polymerised PBM showed a deteriorated performance for higher dynamic viscosity.

It has been deduced that the dynamic viscosity has a major impact on capillary forces. Deep pores intrusion for the low viscous, pristine PBM was quantified with confocal light microscopy using fluorescent nanoparticles. The viscosity modification approach using controlled radical polymerisation was duplicated from industrial polymer production processes. Temperature measurements monitored the exothermal polymerisation propagation which was specifically stopped by radical inhibition and re-activated with UV-LED light. Inhibitor and initiator are mutually influential and thus, optimising the material input for both was paramount. The study examined the relation of dynamic viscosity to the permeability and the time of reaction inhibition compared to the reference value of pristine PBM. Structural differences in polymer architecture were examined by scanning electron microscopy and NMR analysis which could explained deviations in permeability.

- (3) The developed automated membrane coating machine made it possible to produce high quantities of PBM coated membranes of up to 0.25 x 0.55 m surface area. Upscaling can be done for any flat substrates matching these dimensions and coating material polymerisable by UV-LED light.

The automated membrane coating unit was built in order to meet high reproducibility quality for PBM coating upscaling from 84 cm² to 0.11 m² surface areas. Two batches of 34 x 0.11 m² PBM membranes were successfully coated and laminated for pilot scale trials. During the developing process, major challenges were the large coating areas and the limited space availability given by the existing glovebox. Automation was realised by simple actuation using end-switches in the start and end position of coating and lifting. Casting speed, contact pressure and exposure time could be adjusted. Pushbuttons enabled manual process interruption. Process monitoring included temperature, oxygen level and humidity inside the glovebox. Loading and unloading of the pristine and PBM coated membrane subsequent to the polymerisation was done manually to keep process complexity in a manageable range.

- (4) Treating low-strength domestic wastewater is not the suitable application for PBM coatings as postulated based on pilot scale trials. The benefits of low-fouling properties could not compensate the increased membrane resistance resulting from the additional coating layer. Nevertheless, the stability of PBM on PES membranes was shown within a 4.5 months operation period.

For the first time, UV-LED light induced PBM coating has been applied on a pilot scale of 3.125 m² membrane surface area. Within a pilot project, located in Kisumu, Kenya, a pilot MBR provided purified water to a recirculation aquaculture system (RAS). A virgin commercial PES and a PBM coated module were submerged in parallel which enabled a direct and simultaneous comparison of both membranes. Harsh flux step tests were carried out first. A clear increase in permeability and drop in transmembrane pressure were observed. This indicated a widening of the membrane pores due to the strong permeate flux as this effect was apparent in both modules. A second trial period included the long-term operation at constant flux conditions with a second PBM batch and an additional virgin PES module. As expected, the commercial membrane clearly showed a better performance characterised by a higher permeability and a lower specific pressure increase over time at a constant 25 LMH flux.

Nevertheless, a roughly constant permeability over a 4.5 months period and subsequent FITR measurements validated the stability of PBM at ordinary flux rates used for industrial MBR. Contrary to the results from the pilot scale tests, previous conducted lab scale experiments showed better performance of the PBM relative to the PES membrane. Due to lower cross-flow velocities and high applied pressures inside the test unit, fouling propagation was exacerbated and the benefits of PBM layers become a more important factor.

- (5) PBM spray atomisation for membrane coating showed promising results within laboratory examinations. Overall, spray coated membranes had higher permeability than casted coating layers. With the developed automated setup, spray coating is ready for upscaling.

High mechanical stress owing to frictional forces between casting tool, liquid PBM and solid membrane surface occur for casting coatings. The liquid PBM is thereby pushed inside the membrane pores which lead to a high pore intrusion depth. On the contrary, atomised PBM droplets smoothly settle down on the membrane surface only driven by kinetic and potential droplet energy. Since no frictional forces occur, surface scratches are prevented completely. PBM atomisation yields several benefits over casting coating technologies. The results displayed solutions to achieve highly homogeneous coating layers independent of the coating layer thickness. Spray coating thickness is only limited by the emerging spray cone shape. This varies significantly based on the surface tension and viscosity of the liquid coating material. A twin or dual-fuel nozzle used an “assisted” pressurised gas to achieve a high relative flow velocity to enable fine droplet separation from the liquid bulk phase. The PBM was supplied without pressure and as a result, low phase separation of the PBM was observed. Moreover, spray parameters of the dual-fuel atomiser must be adjusted within a limited range constraint. Independent parameter setting created individual spray cone shapes with a spray coverage changing in width and height. With this in mind, reproducibility can be increased even further upon implementation into the existing automated polymerisation process.

7.2 Future Work

The thesis clearly outlines the limitations of PBM coating using spiral casting techniques. Spray coating technology was discussed and found to be a promising approach for applying PBM membrane coatings on UF PES membranes. Moreover, treating domestic wastewater did not show the benefits of casting coated PBM obtained by UV-LED polymerisation. Serious efforts should be made in order to find appropriate wastewater treatment applications. This would achieve high filtration efficiencies relative to commercial membranes and thus meet economic viability. More specifically, future works should address the following points:

- **Spray coating** for PBM upscaling using a twin-fuel nozzle. Lab scaled tests within a small-scaled MBR with two 0.45 m² membrane modules should be completed using high load model wastewater with high fouling propensity. The implementation of a double-axis system into existing glovebox or a second nozzle head lead to a complete and homogeneous membrane coverage. Another option is to operate a second twin-fuel nozzle head in parallel with the first one.

The forward speed thereby defines the coating layer thickness. Coating layer thickness is an important factor as it increases the total membrane resistance and thus should be kept thin.

- **Multi-layer assessment** of the coating layer thickness using laser light microscopy. This enables simultaneous measurements of the PES substrate, the PBM layer surface roughness and thickness which eliminates conventional sampling for AMF and SEM measurements. Especially for SEM analysis, sample preparation is elaborate and the quality of the results highly depend on the resolution and parameter settings. In regards to multi-layer assessment using laser light microscopy, the samples can be measured non-destructively for layer thickness mode. Light is reflected at the surface depending on the material's deflection factor. A change in deflection is indicated by the measured peak height resulting in the layer's width (Figure 7-1). An issue might arise due to the transparency of the PBM giving high light scattering which could be reduced by exposure limitation.

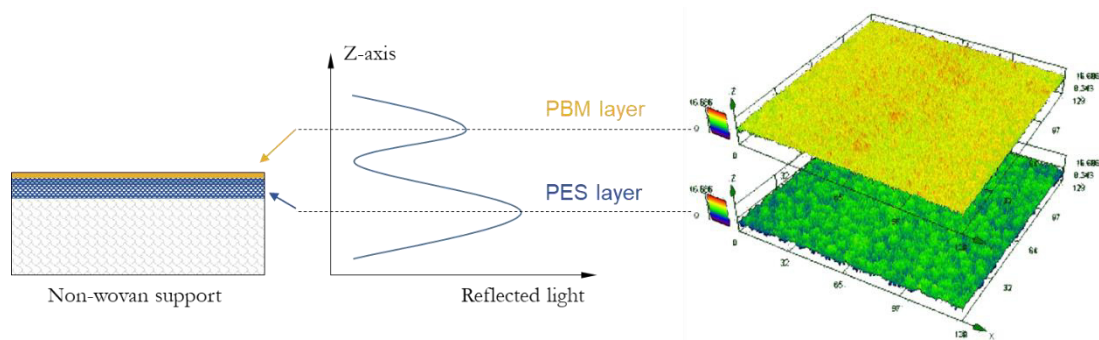


Figure 7-1 Assessment of multi-layer systems by laser light microscopy

- **Evaluating applicative strategies** using a side-stream MBR with activated sludge. Different model wastewater test of varying composition should be carried out to identify the threshold for critical flux values. Pertinent literature describes the highly complex fouling phenomena but the real mechanisms behind them have not yet been completely clarified. Different contaminants stress the membrane individually and PBM coating could be beneficial for specific water composition. Therefore, model foulant performance tests should go hand in hand with antimicrobial activity tests for various bacteria colonies present in the wastewater. As the PBM coating could not yield its full potential treating low-strength domestic wastewater, the following work should focus more on industrial effluents with highly polluted discharge streams such as the coffee and textile and fish processing industries.

References

- Abrar I. and Bhaskarwa A.N. (2019) Microemulsion fuels for compression ignition engines: A review on engine performance and emission characteristics, *Fuel*, Vol. 257, pp. 115-944, Elsevier
- Al-Gharabli S., Kujawa J., Mavukkandy M.O., Arafat H.A. (2017) Functional groups docking on PVDF membranes: Novel Piranha approach, *European Polymer Journal*, Vol. 96, pp. 414-428, Elsevier
- Alvarino T., Torregrosa N., Omil F., Lema J.M., Suarez S. (2015) Assessing the feasibility of two hybrid MBR systems using PAC for removing macro and micropollutants, *Journal of Environmental Management*, Vol. 203, pp. 831–837, Elsevier
- Andrzejewska E. (2015) Chapter 2: Free Radical Photopolymerisation of Multifunctional Monomers; In: Baldacchini T., *Three-Dimensional Microfabrication Using Two-photon Polymerisation – Fundamentals, Technology, and Application*, Micro and Nano Technologies, 1st Edition, pp. 62-81, Elsevier, ISBN: 9780323353212
- Asatekin A., Menniti A., Kang S., Elimelech M., Morgenroth E., Mayes A.M. (2006) Antifouling nanofiltration membranes for membrane bioreactors from self-assembling graft copolymers, *Journal of Membrane Science*, Vol. 285, pp. 81-89, Elsevier
- Ashgriz N. and Yarin A.L. (2011) Chapter 1: Capillary Instability of Free Liquid Jets; In: Ashgriz N., *Handbook of Atomisation and Sprays: Theory and Applications*, p. 6, Springer Science + Business Media LLC, ISBN: 978-1-4419-7263-7
- Atanasova N., Dalmau M., Comas J., Poch M., Rodriguez-Roda I., Buttiglieri G. (2017) Optimized MBR for greywater reuse systems in hotel facilities, *Journal of Environmental Management*, Vol. 193, pp. 503-511, Elsevier
- Bae T.H. and Tak T.M. (2005) Effect of TiO₂ nanoparticles on fouling mitigation of ultrafiltration membranes for activated sludge filtration, *Journal of Membrane Science*, Vol. 249, pp. 1–8, Elsevier

- Bae T.H. and Tak T.M. (2005) Preparation of TiO₂ self-assembled polymeric nanocomposite membranes and examination of their fouling mitigation effects in a membrane bioreactor system, *Journal of Membrane Science*, Vol. 266, pp. 1-5, Elsevier
- Bagastyo A.Y., Anggrainy A.D., Nindita C.S., Warmadewanthi (2017) Electrodialytic removal of fluoride and calcium ions to recover phosphate from fertilizer industry wastewater, *Sustainable Environment Research*, Vol. 27, pp. 230-237, Elsevier
- Baker R.W. (2004) *Membrane Technology and Applications*, pp. 139-145, John Wiley & Sons Ltd., ISBN: 0-470-85445-6
- Balasubrahmanyam A., Patil M.N., Gogate P.R., Aniruddha B.Pandit (2006) Ultrasonic atomisation: Effect of liquid phase properties, *Ultrasonics*, Vol. 44, pp. 146-158, Elsevier
- Battilani A., Schweitzer A., Forslund A., Andersen M., Plauborg F., Steiner M., Lorenzen J., Gola S., Dalsgaard A. (2010) Decentralised water and wastewater treatment technologies to produce functional water for irrigation, *Agricultural Water Management*, Vol. 98, pp. 385-402, Elsevier B.V.
- Bellmann C. (2008) Surface Modification by Adsorption of Polymers and Surfactants, Chapter 12; In: Stamm M., *Polymer Surfaces and Interfaces: Characterization, Modification and Application*, pp. 236-259; Springer-Verlag Berlin Heidelberg, ISBN 978-3-540-73864-0
- Benavente L. Coetsier C., Venault A., Chang Y., Causserand C., Bacchin P., Aimar P. (2016) FTIR mapping as a simple and powerful approach to study membrane coating and fouling, *Journal of Membrane Science*, Vol. 520, pp. 477-489, Elsevier
- BioNexGen (2014) Sustainable water treatment technology – Clean Water. Clean solutions, available at: <http://www.bionexgen.eu>, accessed on: 24th September 2017
- Böhm L., Drews A., Prieske H., Bérubé P.R., Kraume M. (2012) The importance of fluid dynamics for MBR fouling mitigation, *Bioresource Technology*, Vol. 122, pp. 50–61, Elsevier
- Bosch Rexroth AG (2017) *Handbuch Lineartechnik, R310DE (2006.7)*, Bosch Rexroth AG, Schweinfurt, Germany
- Boyle-Gotla A., Jensen P.D., Yap S.D., Pidou M., Wang Y., Batstone D.J. (2014) Dynamic multidimensional modelling of submerged membrane bioreactor fouling, *Journal of Membrane Science*, Vol. 467, pp. 153-161, Elsevier
- Bregnballe J. (2015) *A Guide to Recirculation Aquaculture – An introduction to the new environmentally friendly and highly productive closed fish farming systems*, pp. 21f, the Food and Agriculture Organization of the United Nations and EUROFISH International Organisation

Briceño-Gutiérrez D., Salinas-Barrera V., Vargas-Hernández Y., Gaete-Garretóna L., Zanelli-Iglesias C. (2015) On the ultrasonic atomisation of liquids, *Physics Procedia*, Vol. 63, pp. 37-41, Elsevier

Brinker C.J. (2013) Dip Coating, Chapter 3; In: Schneller T., Waser R., Kosec M., Payne D., *Chemical Solution Deposition (CSD) of Functional Oxide Thin Films*, pp. 231-261, Springer-Verlag Wien, ISBN: 978-3-211-99311-8

Callender S.P., Mathews J.A., Kobernyk K., Wettig S.D. (2017) Microemulsion utility in pharmaceuticals: Implications for multi-drug delivery, *International Journal of Pharmaceutics*, Vol. 526, pp. 425-442, Elsevier

Ceresana Research Technologiezentrum (2018) Ceresana-Report zum Weltmarkt für Tenside – Saubere Zahlen, CHEManager, Wiley-VCH Verlag GmbH & Co. KGaA

Che Mat S., Idroas M.Y., Teoh Y.H., Hamid M.F. (2019) Optimisation of viscosity and density of refined palm Oil-Melaleuca Cajuputi oil binary blends using mixture design method, *Renewable Energy*, Vol. 133, pp. 393-400, Elsevier

Chew C.H., Li T.D., Gang L.H., Quek C.H., Gan L.M. (1998) Bicontinuous-Nanostructured Polymeric Materials from Microemulsion Polymerisation, *Langmuir*, Vol. 14, pp. 6068-6076, American Chemical Society Publications

Chiemchaisri C. and Yamamoto K. (1994) Performance of membrane separation bioreactor at various temperatures for domestic wastewater treatment, *Journal of Membrane Science*, Vol. 87, pp. 119-129, Elsevier

Choi H., Zhang K., Dionysiou D.D., Oerther D.B., Sorial G.A. (2005) Influence of cross-flow velocity on membrane performance during filtration of biological suspension, *Journal of Membrane Science*, Vol. 248, pp. 189-199, Elsevier

Cisneros-Zevallos L. and Krochta J.M. (2003) Dependence of Coating Thickness on Viscosity of Coating Solution Applied to Fruits and Vegetables by Dipping Method, *JFS: Food Engineering and Physical Properties*, Vol. 68, pp. 503-510, Institute of Food Technologists

Codianne B. (2015) Energy Efficiency in MBR Systems, presentation, Columbus, OH, United States, Ohio Water Environment Association (OWEA), Available at: https://www.ohiowea.org/docs/02_EnergyOptimization_MBR.ppsx

CROW (2019) Polymer Properties Database, CROW Copyright © 2015 polymerdatabase.com, available at: <http://polymerdatabase.com/polymer%20physics/sigma.html>, accessed 18-Nov-2019

Deowan S.A., Galiano F., Hoinkis J., Johnson D., Altinkaya S.A., Gabriele B., Hilal N., Drioli E., Figoli A. (2016) Novel low-fouling membrane bioreactor (MBR) for industrial wastewater treatment, *Journal of Membrane Science*, Vol. 510, pp. 524-532, Elsevier

Destarac M. (2010) Polymerisation of Macromolecular Monomers Comprising Diallyamine Structural Units, United States Patent Application US20100093929A1, Rhodia Operations SAS

Drioli E. and Giorno L. (2016) Encyclopedia of Membranes, First Edition, Springer-Verlag Berlin-Heidelberg, ISBN 978-3-662-44325-5

Eastoe J. (2003) Surfactant Chemistry, University of Bristol, School of Chemistry, Bristol, United Kingdom, <http://www.bris.ac.uk/chemistry/people/julian-g-eastoe>

Effendi, H., Widyatmoko, Utomo, B.A., Pratiwi, T.M. (2018) Ammonia and orthophosphate removal of tilapia cultivation wastewater with *Vetiveria zizanioides*, Journal of King Saud University – Science, <https://doi.org/10.1016/j.jksus.2018.04.018>

Ehrhard P. (2016) Kapitel: Mikroströmungen; In: Oertel jr. H., Prandtl – Führer durch die Strömungslehre – Grundlagen und Phänomene, pp. 1-52, Springer Vieweg, ISBN: 978-3-658-08933-7

Eliseus A., Bilad M.R., Nordin N.A.H.M., Putra Z.A., Wirzal M.D.H. (2017) Tilted membrane panel: A new module concept to maximize the impact of air bubbles for membrane fouling control in microalgae harvesting, *Bioresource Technology*, Vol. 241, pp. 661-668, Elsevier

Farahani H., Wagiran R., Hamidon M.N. (2014) Humidity Sensors Principle, Mechanism, and Fabrication Technologies: A Comprehensive Review, *Sensors* Vol. 14, pp. 7881-7939, Multidisciplinary Digital Publishing Institute

Faure B. Salazar-Alvarez G., Ahniyaz A., Villaluenga I., Berriozabal G., Yolanda R De Miguel Y.R., Bergström L. (2013) Dispersion and surface functionalization of oxide nanoparticles for transparent photocatalytic and UV-protecting coatings and sunscreens, *Science and Technology of Advanced Materials* Vol. 14, pp. 1-23, Taylor and Francis Group

Ferrero G., Monclús H., Buttiglieri G., Comas J., Rodriguez-Roda I. (2011) Automatic control system for energy optimization in membrane bioreactors, *Desalination*, Vol. 268, pp. 276-280, Elsevier

Figoli A., Hoinkis J., Gabriele B., De Luca G., Galiano F., Deowan S.A. (2013) Bicontinuous microemulsion polymerised coating for water treatment, Worldwide Patent Application WO2015044335A2, World Intellectual Property Organization

Flory J.P. (1941) Kinetics of Polyesterification: A Study of the Effects of Molecular Weight and Viscosity on Reaction Rate, *Journal of the American Chemical Society*, Vol 61., pp. 3334-3340, American Chemical Society Publication

Gabarrón S., Ferrero G., Dalmau M., Comas J., Rodriguez-Roda I. (2014) Assessment of energy-saving strategies and operational costs in full-scale membrane bioreactors, *Journal of Environmental Management*, Vol. 134, pp. 8-14, Elsevier

- Galiano F., Figoli A., Deowan S.A., Johnson D., Altinkaya S.A., Veltri L., De Luca G., Mancuso R., Hilal N., Gabriele B., Hoinkis J. (2015) A step forward to a more efficient wastewater treatment by membrane surface modification via polymerizable bicontinuous microemulsion, *Journal of Membrane Science*, Vol. 482, pp. 103-114, Elsevier
- Galiano F., Schmidt S.A., Ye X., Kumar R., Mancuso R., Curcio E., Gabriele B., Hoinkis J., Figoli A. (2018) UV-LED induced bicontinuous microemulsions polymerisation for surface modification of commercial membranes – Enhancing the antifouling properties, *Separation and Purification Technology*, Vol. 194, pp. 149-160, Elsevier
- Gallert C., Winter J., Svardal K. (2015) Kapitel 2: Grundlagen anaerober Prozesse, In: Rosenwinkel K.-H., Kroiss H., Dichtl N., Seyfried C.-F., Weiland P. *Anaerobtechnik – Abwasser-, Schlamm- und Reststoffbehandlung, Biogasgewinnung*, pp. 53ff, Springer-Verlag Berlin Heidelberg, ISBN: 978-3-642-24894-8
- Gan L.M., Chieng T.H., Chew C.H., Ng S.C. (1994) T.H. Microporous Polymeric Materials from Microemulsion Polymerisation, *Langmuir*, Vol. 10, pp. 4022-4026, American Chemical Society Publications
- Gan L.M., Liu J., Poon L.P., Chew C.H., Gan L.H. (1997) Microporous polymeric composites from bicontinuous microemulsion polymerisation using a polymerizable nonionic surfactant, *Polymer*, Vol. 38, pp. 5339-5345, Elsevier
- Gao Y., Qin J., Wang Z., Østerhus S.W. (2019) Backpulsing technology applied in MF and UF processes for membrane fouling mitigation: A review, *Journal of Membrane Science*, Vol. 587, pp. 117-136, Elsevier
- Gu Y., Li Y., Li X., Luo P., Wang H., Robinson Z.P., Wang X., Wu J., Li F. (2017) The feasibility and challenges of energy self-sufficient wastewater treatment plants, *Applied Energy*, Vol. 204, pp. 1463-1475, Elsevier
- Gu Y., Li Y., Li X., Luo P., Wang H., Wang X., Wu J., Li F. (2017) Energy self-sufficient wastewater treatment plants: feasibilities and challenges, *Energy Procedia*, Vol. 105, pp 3741-3751, Elsevier
- Gude V.G. (2015) Energy and water autarky of wastewater treatment and power generation systems, Elsevier, *Renewable and Sustainable Energy Reviews*, Vol. 45, pp. 52-68, Elsevier
- Guth U. and Wiemhöfer H.-D. (2019) Chapter 2: Gas sensors based on oxygen ion conducting metal oxides; Barsan N. and Schierbaum K., *Gas Sensors Based on Conducting Metal Oxides: Basic Understanding, Technology and Applications – A volume in Metal Oxides*, pp. 13-60, Elsevier
- Hai F.I., Yamamoto K., Lee C.-H. (2019) *Membrane Biological Reactors – Theory, Modeling, Design, Management and Applications to Wastewater Reuse*, Second edition, p. 503, International Water Association Publishing
- Hartley G. H. and Guillet J. E. (1968). *Photochemistry of Ketone Polymers.II. Studies of Model Compounds*, *Macromolecules* Vol. 1, pp. 413–417, American Chemical Society Publications

- Hatakeyama E.S., Ju H., Gabriel C.J., Lohr J.L., Bara J.E., Noble R.D., Freeman B.D., Gin D.L. (2009) New protein-resistant coatings for water filtration membranes based on quaternary ammonium and phosphonium polymers, *Journal of Membrane Science*, Vol. 330, pp. 104-116, Elsevier
- Hathiwala R., Mehta P.R., Nataraj G., Hathiwala S. (2017) LED fluorescence microscopy: Novel method for malaria diagnosis compared with routine methods, *Journal of Infection and Public Health*, Vol. 10, pp. 824-828, Elsevier
- Hede P.D., Bach P, Jensen A.D. (2008) Two-fluid spray atomisation and pneumatic nozzles for fluid bed coating/agglomeration purposes: A review, *Chemical Engineering Science*, Vol. 63, pp. 3821-3842, Elsevier
- Heimburg T. (2007) Chapter 1: Thermal Biophysics of Membrane; In: *Membranes: An Introduction*, pp. 1-12, Wiley-VCH Verlag GmbH & Co. KGaA, ISBN: 978-3-527-40471-1
- Helfferrich F.G. (2004) Chapter 11 Polymerization; In: *Comprehensive Chemical Kinetics*, Vol. 40, pp. 347-402, Elsevier
- Höflinger G. (2013) Brief Introduction to Coating Technology for Electron Microscopy, Leica Microsystems GmbH, www.leica-microsystems.com, accessed on: 28th October 2019
- Hoinkis J. and Lindner E. (2007) Kapitel 13: Umweltschutztechnik; In: *Chemie für Ingenieure*, 13. Auflage, pp. 575ff/p. 589, Wiley-VCH Verlag GmbH & Co. KGaA, ISBN: 978-3-527-31798-1
- Holman S.R. and Ohlinger K.N. (2007) An Evaluation of Fouling Potential and Methods to Control Fouling in Microfiltration Membranes for Secondary Wastewater Effluent, pp. 6417-6444, Water Environment Federation
- Hubergroup Deutschland GmbH (2012) UV-härtende Farben und Lacke für den Offsetdruck, Ink Academy, INKFORMATION 1. Auflage, 1D17/1D5, Kirchheim, Germany
- Huyskens C., Brauns E., van Hoof E., Diels L., de Wever H. (2011) Validation of a supervisory control system for energy savings in membrane bioreactors, *Water Research*, Vol. 45, pp. 1443-1453, Elsevier
- ifm electronic (2003) Effektor600: Temperatursensoren, ifm electronic GmbH, Essen, Germany
- Inoue N., Takai E., Arakawa T., Shiraki K. (2014) Arginine and lysine reduce the high viscosity of serum albumin solutions for pharmaceutical injection, *Journal of Bioscience and Bioengineering*, Vol. 117, pp. 539-543, Elsevier
- Irzaman, Syafutra H., Siskandar R., Aminullah, Alatas H. (2017) Modified Spin Coating Method for Coating and Fabricating Ferroelectric Thin Films as Sensors and Solar Cells, Chapter 3, pp. 33-53, InTech open science
- Jiang H., Du C., Dong J. (2017) Investigation of rock cutting dust formation and suppression using waterjets during mining, *Powder Technology*, Vol. 307, pp. 99-108, Elsevier

- Johnson D.J. and Hilal N. (2014) Atomic Force Microscopy (AFM); In: Drioli E. and Giorno L., Encyclopedia of Membrane, Springer, Berlin, Heidelberg, ISBN: 978-3-642-40872-4
- Johnson D. and Hilal N. (2017) Chapter 10: Atomic-force microscopy investigations of filtration membranes; In: Figoli A., Hoinkis J., Altinkaya S.A., Bundschuh J., Application of Nanotechnology in Membranes for Water Treatment, Series: Sustainable Water Developments, Vol 5., pp. 189ff, CRC Press Taylor & Francis Group, ISBN: 978-1-138-89658-1
- Judd S. (2006) Chapter 2: Fundamentals; In: The MBR Book: Principles and Applications of Membrane Bioreactors in Water and Wastewater Treatment, pp. 22-29, Elsevier Ltd., ISBN: 978-1-85-617481-7
- Katz S. and Grundestam J. (2016) The Largest MBR in the World... Upgrading The Hendriksdal WWTP, Singapore International Water Week 2016, Conference Paper
- Kaur G. Mehta S.K. (2017) Developments of Polysorbate (Tween) based microemulsions: Preclinical drug delivery, toxicity and antimicrobial applications, International Journal of Pharmaceutics Vol. 529, pp. 134-160, Elsevier
- Kertész S., de Freitas T.B., Cecília Hodúr C. (2014) Characterization of polymer membranes by contact angle goniometer, Analecta Technica Szegedinsia, Vol. 8, pp. 18-22, Open Journal Systems
- Khanjani J., Zohuriaan-Mehr M., Pazokifard S. (2017) Microemulsion and macroemulsion polymerisation of octamethylcyclotetrasiloxane: A comparative study, Phosphorus, Sulfur, and Silicon and the Related Elements, Vol. 192, pp. 967-976, Taylor & Francis Group
- Kim S.-R., Lee K.-B., Kim J.-E., Won Y.-J., Yeon K.-M., Lee C.-H., Lim D.-J. (2015) Macroencapsulation of quorum quenching bacteria by polymeric membrane layer and its application to MBR for biofouling control, Journal of Membrane Science, Vol. 473, pp. 109-117, Elsevier
- Klinge M., Britton B., Breitwieser M., Vierrath S., Zengerle R., Holdcroft S., Thiele S. (2016) A completely spray-coated membrane electrode assembly, Electrochemistry Communications, Vol. 70, pp. 65-68, Elsevier
- Kopczynska, A., Ehrenstein G.W. (2019) Oberflächenspannung von Kunststoffen Messmethoden am LKT, Sonderdrucke, Lehrstuhl für Kunststofftechnik, p. 15, Friedrich-Alexander-Universität, Erlangen, Germany
- Krause S.A. (2001) Entwicklung und Charakterisierung von Mikroemulsionen zur dermalen Applikation von Arzneistoffen, Dissertation, pp. 14ff, Martin-Luther-Universität, Halle-Wittenberg, Germany
- KRÜSS (2010) Technical Note – Determining the surface tension of liquids by measurements on pendant drops, Technical Note, KRÜSS GmbH, Hamburg, Germany
- Krzeminski P., van der Graaf J.H.J.M., van Lier, J.B. (2012) Specific energy consumption of membrane bioreactor (MBR) for sewage treatment, Water Science and Technology, Vol. 65, pp. 380-392, International Water Association Publishing

Kumar Rakshit A., Bappaditya N., Satya Priya Moulik A.P. (2019) Commemorating 75 years of microemulsion, *Current Science*, Vol. 116, pp. 898-912, Current Science Association

Lamine M., Sendy N., Ghrabi A. (2017) A decentralized greywater treatment in Tunisia : Economic Analysis and Water Saving Potential, Conference paper, International Conference in Integrated Management of Environment, At Sousse, Tunisia

Lares M., Ncibi M.C., Sillanpää M., Sillanpää M. (2018) Occurrence, identification and removal of microplastic particles and fibers in conventional activated sludge process and advanced MBR technology, *Water Research*, Vol. 133, pp. 236-246, Elsevier

Laws D.D., Bitter H.M.L., Jerschow A. (2002) Solid-state NMR Spectroscopic Methods in Chemistry, *Angewandte Chemie-International*, Edition 41, pp. 3096-3129, WILEY-VCH Verlag GmbH & Co. KGaA, Weinheim

Le Clech P., Jefferson B., Soung Chang I, Judd S.J. (2003) Critical flux determination by the flux-step method in submerged membrane bioreactor, *Journal of Membrane Science*, Vol. 227, pp. 81-93, Elsevier

Le-Clech P., Jefferson B., Judd S.J. (2005) A comparison of submerged and side stream tubular membrane bioreactor configurations, *Desalination*, Vol. 173, pp. 113-122, Elsevier

Le-Clech P., Chen V., Fane T.A.G. (2006) Fouling in membrane bioreactors used in wastewater treatment, *Journal of Membrane Science* Vol. 284, pp. 17-53, Elsevier

Le-Clech P. (2015) Protein Fouling; In: Drioli E., Giorno L., *Encyclopedia of Membranes*, Springer-Verlag GmbH, Online ISBN: 978-3-642-40872-4

Lechler (2019) Präzisionsdüsen und Zubehör Industrie. Hrsg. von Lechler GmbH, Metzingen, Germany, <https://www.lechler.com/de/produkte>, accessed on: 07. July 2019

Lee J., Ahn W.-Y., Lee C.-H. (2001) Comparison of the filtration characteristics between attached and suspended growth microorganisms in submerged membrane bioreactor, *Water Research*, Vol. 35, pp. 2435-2445, Elsevier

Lefebvre A.H. and McDonell V.G. (2017) Chapter 1 – General Considerations; In: *Atomization and Sprays*, Second edition, pp. 2ff, CRC Press Taylor & Francis Group, ISBN: 9781498736251

Levitsky I., Duek A., Arkhangel'sky E., Pinchev D., Kadoshian T., Shetrit H., Naim R., Gitis V. (2011) Understanding the oxidative cleaning of UF membranes, *Journal of Membrane Science*, Vol. 377, pp. 206-213, Elsevier

Li B., Zhang J., Wu L., Wang A. (2013) Durable Superhydrophobic Surfaces Prepared by Spray Coating of Polymerised Organosilane/Attapulgite Nanocomposites, *CHEMPLUSCHEM*, Vol. 78, pp. 1503-1509, ChemPubSoc Europe

- Li N.N., Fane A.G., Ho W.S.W., Matsuura T. (2008) *Advanced Membrane Technology and Applications*, pp. 131ff/pp. 271ff/pp.297ff, John Wiley & Sons Inc., ISBN: 978-0-471-73167-2
- Li T.D. et al. (1997) Hollow-fiber membranes coated with polymerizable bicontinuous microemulsion, *Journal of Membrane Science*, Vol. 133, pp. 177-187
- Liao B.-Q., Xie K., Lin H.J., Bertoldo D. (2010) Treatment of Kraft Evaporator Condensate Using a Thermophilic Submerged Anaerobic Membrane Bioreactor, *Water Science & technology*, Vol. 61, pp. 2177-2188, International Water Association Publications
- Liu L.-F., Yu S.-C., Wu L.-G., Gao C.-J. (2006) Study on a novel polyamide-urea reverse osmosis composite membrane (ICIC-MPD). II. Analysis of membrane antifouling performance, *Journal of Membrane Science*, Vol. 283, pp. 133-146, Elsevier
- Liu S., Zhang X., Zhang L., Xie W. (2016) Ultrasonic spray coating polymer and small molecular organic film for organic light-emitting devices, *Nature Research, Scientific Reports*, Vol. 6, Article number 37042, Springer Nature Ltd.
- Liu, L.-F., Yu S.-C., Wu L.-G., Gao C.-J.. (2006) Study on a novel polyamide-urea reverse osmosis composite membrane (ICIC-MPD). II. Analysis of membrane antifouling performance, *Journal of Membrane Science*, Vol. 283, pp. 133-146, Elsevier
- Louie J.S., Ingo P., Ciobanu I., Ishida K.P., Ng A., Reinhard M. (2006) Effects of polyether–polyamide block copolymer coating on performance and fouling of reverse osmosis membranes, *Journal of Membrane Science*, Vol. 280, pp. 762-770, Elsevier
- Luo Y., Jiang Q., Ngo H.H., Nghiem L.D., Hai F.I., Price W.E., Wang J., Guo W. (2015) Evaluation of micropollutant removal and fouling reduction in a hybrid moving bed biofilm reactor-membrane bioreactor system, *Bioresource Technology*, Vol. 191, pp. 355–359, Elsevier
- LVEMP (2003) *Lake Victoria Environmental Management Project, Phase 1, Revised Draft Scientific Stocking Report – Progress During LVEMP1 and Challenges for the Future*, World Bank; Washington D.C.
- Madaeni S.S., Falsafi M., Ghaemi N. (2011) A novel method for preparation of low-fouling membranes: Surface coating by extracted wax from leafy cabbage, *Desalination*, Vol. 283, pp. 148-155, Elsevier
- Malvern (2015) *Optimizing Rheology for Paint and Coating Applications*, Whitepaper, Malvern Instruments Limited, Worcestershire, United Kingdom
- Mancuso R., Amuso R., Armentano B., Grasso G., Rago V., Capello A.R., Galiano F., Figoli A., De Luca G., Hoinkis J., Gabriele B. (2017) Synthesis and antimicrobial activity of polymerisable acryloyloxyalkyltriethyl ammonium salts, *ChemPlusChem*; Vol. 82, pp. 1235-1244, ChemPubSoc Europe
- Mannina, G. and Cosenza, A. (2013) The fouling phenomenon in membrane bioreactors: Assessment of different strategies for energy saving, *Journal of Membrane Science*, Vol. 444, pp. 332-344, Elsevier

- Marino T., Blasi E., Tornaghi S., Di Nicolò E., Figoli A. (2018) Polyethersulfone membranes prepared with Rhodiasolv®Polarclean as water soluble green solvent, *Journal of Membrane Science*, Vol. 549, pp. 192-204, Elsevier
- Martínez-Balbuena L., Arteaga-Jiménez A., Hernández-Zapata E., Márquez-Beltrán C. (2017) Applicability of the Gibbs Adsorption Isotherm to the analysis of experimental surface-tension data for ionic and nonionic surfactants, *Advances on Colloid and Interface Science*; Vol. 247, pp. 178-184, Elsevier
- Mauri M., Ponting M., Causin V., Simonutti R., Pesciotti F. (2018) Morphological reorganization and mechanical enhancement in multilayered polyethylene/polypropylene films by layer multiplication or mild annealing. *Journal of Polymer Science*, Vol. 56, pp. 520-531, *Polymer Physics*
- MBR site (2019) www.thembrsite.com/largest-membrane-bioreactor-plants-africa, accessed on: 22 June 2019
- Mburu J.N., Hoinkis J., Njogu P.M., Kinyua R., Gukelberger E., Atiye T. (2019) Pilot trials on testing and Optimization of Polyethersulfone Membranes for Treatment of Fish Processing Wastewater through Membrane Bioreactor Technology, *International Journal of Water and Wastewater Treatment*, Vol. 5, pp. 1-10, Sciforschen
- Meng F., Zhang S., Oh Y., Zhou Z., Shin H.-S., Chae S.-R. (2017) Fouling in membrane bioreactors: An updated review, *Water research*, Vol. 114, pp. 151-180, National Center of Biotechnology Information
- Mehta S.K. and Kaur G. (2011) Microemulsions: Thermodynamic and Dynamic Properties, In: Tadashi M., *Thermodynamics*, pp. 381-406, InTech, ISBN: 978-953-307-544-0
- Menter P. (2000) Acrylamide Polymerisation – A Practical Approach, *Electrophoresis*, tech note 1156, Bio-Rad Laboratories Inc.
- Metz G., Wu X.L., Smith S.O. (1994) Ramped-Amplitude Cross-Polarization In Magic-Angle Spinning NMR, *Journal of Magnetic Resonance, Series A*, Vol. 110, pp. 219-227, Elsevier
- Meuler S., Paris S., Hackner T. (2008) Membrane bio-reactors for decentralized wastewater treatment and reuse, *Water Science and Technology*, Vol. 58, pp. 285 -294, National Center for Biotechnology Information
- Mishra S. and Chatterjee A. (2011) Novel synthesis of polymer and copolymer nanoparticles by atomized microemulsion technique and its characterization, *Polymers Advanced Technologies*, Vol. 22, pp. 1593-1601, John Wiley & Sons Ltd.
- Monclús H., Ferrero G., Buttiglieri G., Comas J., Rodríguez-Roda I. (2011) Online monitoring of membrane fouling in submerged MBRs, *Desalination*, Vol. 277, pp. 414-419, Elsevier
- Monclús H., Dalmau M., Gabarrón S., Ferrero G., Rodríguez-Roda I., Comas J. (2015) Full-scale validation of an air scour control system for energy savings in membrane bioreactors, *Water Research*, Vol. 79, pp. 1-9, Elsevier

- Monsees H., Klatt L., Kloas W., Wuertz S. (2017) Chronic exposure to nitrate significantly reduces growth and affects health status of juvenile Nile tilapia (*Oreochromis niloticus* L.) in recirculating aquaculture system, *Aquaculture Research*, Vol. 48, pp. 3482-3492, John Wiley & Sons Ltd.
- Mulder M. (1996) *Basic Principles of Membrane Technology*, second edition, p. 12/p. 52/pp. 416ff, Kluwer Academic Publishers, ISBN: 0-7923-4247-X
- Muramoto Y., Kimura M., Kondo A. (2019) Internal Quantum Efficiency of UV-LED Chips, *Applied Sciences*, Vol. 9, pp. 1-12, Multidisciplinary Digital Publishing Institute
- Najjar R. (2012) Chapter 1: Microemulsions – A Brief Introduction, In: *Microemulsions – An Introduction to Properties and Applications*, InTechOpen, ISBN: 978-953-51-0247-2
- Nakajima H. (2001) *Microemulsions in Cosmetics*, In: *IFSCC Monograph, Number 7*, International Federation of Societies of Cosmetic Chemists, Micelle Press
- Narvaez A.A., Bolszo C.D., McDonnell V.G., Dunn-Rankin D., Sirignano W.A. (2011) Comparison of Water-in-Oil Emulsion Atomisation Characteristics for Low and High-Capacity Pressure-Swirl Nozzles, *Atomisation and Sprays*, Vol. 21, pp. 391-410, Begell House Inc.
- Nasr G.G (2002) Chapter 3: Sprays in Industrial Production Processes, In: Yule A.J., Bending L., *Industrial Sprays and Atomisation: Design, Analysis and Applications*, pp. 35-118, Springer Verlag London, ISBN 978-1-4471-3816-7
- Nilsson A. and Pettersson L.G.M. (2008) Chapter 2 – Adsorbate Electronic Structure and Bonding on Metal Surfaces; In: *Chemical Bonding at Surfaces and Interfaces*, pp. 57-142, Elsevier
- O'Donnell J. and Kaler E.W. (2007) Microstructure, kinetics, and transport in oil-in-water microemulsion polymerizations, *Macromolecular Rapid Communications*, Vol. 28, pp. 1445-1454, Elsevier B.V.
- Owusu-Agyeman I., Jeyhanipour A., Luxbacher T., Schäfer A.I. (2017) Implications of humic acid, inorganic carbon and speciation on fluoride retention mechanisms in nanofiltration and reverse osmosis, *Journal of Membrane Science*, Vol. 528, pp. 82-94, Elsevier
- Ozaki T., Koto T., Nguyen T.V., Nakanishi H., Norisuye T., Tran-Cong-Miyata Q. (2015) The roles of the Trommsdorff Norrish effect in phase separation of binary polymer mixtures induced by photopolymerisation, *Polymer*, Vol. 55, pp. 1809-1816, Elsevier
- Pardeshi P. and Mungray A.A. (2014) Synthesis, characterization and application of novel high flux FO membrane by layer-by-layer self-assembled polyelectrolyte, *Journal of Membrane Science*, Vol. 453, pp. 202-211, Elsevier
- Paul B.K. and Moulik S.P. (2001) Uses and applications of microemulsions, *Current Science*, Vol. 80, pp. 990-1001, Current Science Association

- Kurzweil P. (2015) Doppelschichtkondensatoren; In: Kurzweil P., Dietlmeier P., Otto K., Elektrochemische Speicher – Superkondensatoren, Batterien, Elektrolyse-Wasserstoff, Rechtliche Grundlagen, Springer Fachmedien Wiesbaden, ISBN: 978-3-658-10900-4
- Peticolas W.L. and Watkins J.M. (1957) The Molecular Structure of Polyethylene. VII. Melt Viscosity and the Effect of Molecular Weight and Branching, *Journal of the American Chemical Society*, Vol. 16, pp. 5083-5085, American Chemical Society Publication
- Platkowski K. and Reichert K.-H. (1999) Untersuchungen zum Stoppen der radikalischen Polymerisation von Methylmethacrylat mit dem Inhibitor 4-Hydroxy-Tempo; In: *Chemie Ingenieur Technik*, Vol. 71, pp. 493-496, Wiley Online Library
- Pollice A., Brookes A., Jefferson B., Judd S. (2005) Sub-critical flux fouling in membrane bioreactors – a review of recent literature, *Desalination*, Vol. 174, pp. 221-230, Elsevier
- Poorasgari W., Bugge T.V., Christensen M.L., Jørgensen M.K. (2015) Compressibility of fouling layers in membrane bioreactors, *Journal of Membrane Science*, Vol. 475, pp. 65-70, Elsevier
- Porter M.C. (1972) Concentration Polarisation with Membrane Ultrafiltration, American Chemical Society, *Industrial & Engineering Chemistry Research*, Vol. 11, pp. 234-248, Elsevier
- Prieske H., Drews A., Kraume M. (2008) Prediction of the circulation velocity in a membrane bioreactor, *Desalination*, Vol. 231, pp. 219-226, Elsevier
- Prince L. (1977) Chapter: Commercial History, In: *Microemulsions – Theory and Practice*, Academic Press Inc., ISBN: 0-12-565750-1
- Pritchard D., Wilson S.K., McArdle C.R. (2016) Flow of a thixotropic or antithixotropic fluid in a slowly varying channel: The weakly advective regime, *Journal of Non-Newtonian Fluid Mechanics*, Vol. 238, pp. 140-157, Elsevier
- Rahimpour A. and Madaeni S.S. (2010). Improvement of performance and surface properties of nanoporous polyethersulfone (PES) membrane using hydrophilic monomers as additives in the casting solution, *Journal of Membrane Science*, Vol. 360, pp. 371-379, Elsevier
- Randall D.J. and Tsui T.K.N. (2002) Ammonia toxicity in fish, *Marine Pollution Bulletin*, Vol. 45, pp. 17-23, National Center for Biotechnology Information
- Rashidi H., GhaffarianHoseini A., GhaffarianHoseini A., Sulaiman N.M.N.S., Tookey J., Hashim N.A. (2015) Application of wastewater treatment in sustainable design of green built environments: A review, *Renewable and Sustainable Energy Reviews*, Vol. 49, pp. 845-856, Elsevier
- Reinertsen H., Halland H., Balkema H. (1995) Book review: Sustainable Fish Farming, *Aquaculture International*, Vol. 4, pp. 386-388, Elsevier

- Stieglitz R. and Heinzl V. (2012) Passive Mechanismen in der Solarenergie, In: Thermische Solarenergie – Grundlagen, Technologie, Anwendungen, pp. 230-237, Springer-Verlag Berlin Heidelberg, ISBN: 978-3-642-29475-4
- Rosenberger S., Evenblij H., te Poele S., Wintgens T., Laabs C. (2005) The importance of liquid phase analyses to understand fouling in membrane assisted activated sludge processes – six case studies of different European research groups, *Journal of Membrane Science*, Vol. 263, pp. 113-126, Elsevier
- Saad S.M.I., Policova Z., Neumann A.W. (2011) Design and accuracy of pendant drop methods for surface tension measurements, *Colloids and Surface A: Physicochemical and Engineering Aspects*, Vol 384, pp. 442-452, Elsevier
- Saeki D., Minami R., Matsuyama H. (2017) Effect of operating conditions on biofouling in crossflow ultrafiltration membrane processes, *Separation and Purification Technology*, Vol. 189, pp. 138-144, Elsevier
- Sagle A.C., Ju H., Freeman B.D., Sharma M.M. (2009) PEG-based hydrogel membrane coatings, *Polymer*, Vol. 50, pp. 756–766, Elsevier
- Samiullah M.H., Pulst M., Golitsyn Y., Busse K., Poppe S., Hussain H., Reichert D., Kressler J. (2018) Solid State Phase Transitions in Poly(ethylene oxide) Crystals Induced by Designed Chain Defects, *Macromolecules*, Vol. 51, pp. 4407-4414, American Chemical Society
- Sanderson M.J., Smith I., Parker I., Bootman M.D. (2014) Fluorescence Microscopy, *Cold Spring Harbour Protocols*, Vol. 10, National Center for Biotechnology Information
- Santamasas C., Rovira M., Clarens F., Valderrama C. (2013) Grey water reclamation by decentralized MBR prototype, *Resources, Conservation and Recycling*, Vol. 72, pp. 102–107, Elsevier
- Schlüpen J. (2000) Entwicklung und Charakterisierung von Mikroemulsionen mit aromatischen Heterozyklen für die Elektropolymerisation, Dissertation, p. 4, Heinrich-Heine-Universität Düsseldorf, Düsseldorf, Germany
- Schmidt J., Schönhart M., Biberacher M., Guggenberger T., Hausl S., Kalt G., Leduc S., Schardinger I., Schmid E. (2012) Regional energy autarky: Potentials, costs and consequences for an Austrian region, *Energy Policy*, Vol. 47, pp. 211-221, Elsevier
- Schmidt S. (2016) Innovative UV-LED Polymerised Bicontinuous Microemulsion Coating for Membrane with Special Emphasis on MBRs, PhD thesis, University of Calabria, Rende (CS), Italy
- Schneider G.A. (2001) Fracture of Piezoceramics, In: Buschow K.H.J., Cahn R.W., Flemings M.C., Ilshner B., Kramer E.J., Mahajan S., Veyssi re P., *Encyclopedia of Materials: Science and Technology*, Second Edition, pp. 3319-3321, Elsevier Ltd., ISBN: 978-0-08-043152-9

- Shao L., Wang Z.X., Zhang Y.L., Jiang Z.X., Liu Y.Y. (2014) A facile strategy to enhance PVDF ultrafiltration membrane performance via self-polymerized polydopamine followed by hydrolysis of ammonium fluotitanate, *Journal of Membrane Science*, Vol. 461, pp. 10-21, Elsevier
- Sharma M.K. and Shah D.O. (1985) *Introduction to Macro- and Microemulsions*, ACS Symposium Series, Vol. 272, pp. 1-18, American Chemical Society Publications
- Shi F., Zhan P., Mao Y., Wang C., Zheng M., Zhao Z. (2017) The nitroxide Tempo inhibits hydroxyl radical production from the Fenton-like reaction of iron(II)-citrate with hydrogen peroxide, *Biochemical and Biophysical Research Communications*, Vol. 483, pp. 159-164, Elsevier
- Shimizu Y., Okuno Y.-I., Uryu K., Ohtsubo S., Watanabe A. (1996) Filtration characteristics of hollow fiber microfiltration membranes used in membrane bioreactor for domestic wastewater treatment, *Water Research*, Vol. 30, pp. 2385-2392, Elsevier
- Shukla T., Upmanyu N., Agrawal M., Saraf Sw., Saraf Sh., Alexander A. (2018) Biomedical applications of microemulsion through dermal and transdermal route, *Biomedicine & Pharmacotherapy*, Vol. 108, pp. 1477-1494, Elsevier
- Skouteris G.S., Arnot T., Jraou M., Sayadi S. (2014) Modelling energy consumption in membrane bioreactors for wastewater treatment in North Africa, *Water Environment Research*, Vol. 86, pp. 232-244, National Center for Biotechnology Information
- Smith A.L., Stadler L.B., Cao L., Love N.G., Raskin L., Skerlos S.J. (2014) Navigating Wastewater Energy Recovery Strategies: A Life Cycle Comparison of Wastewater Energy Recovery Strategies: Anaerobic Membrane Bioreactor and High Rate Activated Sludge with Anaerobic Digestion, *Environmental Science & Technology*, Vol. 48, pp. 5972–5981, International Water Association Publishing
- So M.T., Eirich F.R., Strathmann H., Baker R.W. (1973) Preparation of Asymmetric Loeb-Sourirajan Membranes, *Journal of Polymer Science*, Vol. 11, pp. 201-205, John Wiley & Sons, Inc.
- Song I.H., Bae B.-S., Ha J.-H., Lee J. (2017) Effect of hydraulic pressure on alumina coating on pore characteristics of flat-sheet ceramic membrane, *Ceramics International*, Vol. 43, pp. 10502-10507, Elsevier
- Sindayihebura D. and Dumouchel C. (2003) Ultrasonic Atomisation Technology, European Patent Office Patent Application EP1508382B1, Polyspray sprl.
- Sparks B.J., Hoff E.F.T., Xiong L., Goetz J.T., Patton D.L. (2013) Superhydrophobic Hybrid Inorganic–Organic Thiol-ene Surfaces Fabricated via Spray-Deposition and Photopolymerisation, *Applied Materials & Interfaces*, Vol 5, pp. 1811-1817, American Chemical Society Publication
- Stoffer J.O. and Bone T. (1980) Polymerisation in Water in Oil Microemulsion Systems Containing Methyl Methacrylate, *Journal of Dispersion Science and Technology*, Vol. 1, pp. 37-54, Taylor & Francis Group

Stowe R.W. (1999) Practical aspects of irradiance and energy in UV curing, In: RadTech Asia Organization. Conference Proceedings of RadTech ASIA'99; RADTECH; pp. 436-444, Kuala Lumpur, Malaysia

Susanto H. and Ulbricht M. (2009) Membrane Contactors in Industrial Application, In: E. Drioli and L. Giorno, Membrane Operations: Innovative Separations and Transformations, pp. 499-512, Wiley-VCH Verlag GmbH & Co. KGaA, ISBN: 978-3-527-32038-7

Tian Y., Chen L., Jiang, T. (2007) Characterization and Modelling of Soluble Microbial Products in Membrane Bioreactors, In: van der Bruggen B., Separation and Purification Technology, pp. 326-324, Elsevier

Tng K.H., Antony A., Qang Y., Leslie G.L. (2015) Chapter 11: Membrane ageing during water treatment: mechanisms, monitoring, and control, In: Basile M., Cassano A., Rastogi N., Advances in Membrane Technologies for Water Treatment – Materials, Processes and Applications, pp. 362-372, Elsevier Science, ISBN: 978-1-78242-121-4

Va Dijk L. and Roncken G.C.G. (1997) Membrane bioreactors for wastewater treatment: the state of the art and new developments, Water Science Technology, Vol. 35, pp 35-41, International Water Association Publishing

Verrecht B., Maere T., Benedetti L., Nopens I., Judd S. (2010) Model-based energy optimisation of a small-scale decentralised membrane bioreactor for urban reuse, Water Research, Vol. 44, pp. 4047-4056, Elsevier

VicInAqua (2016) Sustainable, innovative solution for water sanitation, clean water, Lake Victoria, available at: <http://www.vicinaqua.eu>, accessed on: 24 September 2017

Waanders J.W. (1991) Piezoelectric Ceramics – Properties and Applications, N.V. Philips' Gloeilampenfabrieken, Eindhoven, the Netherlands

Wang W., Zhang H., Zhang Z., Luo M., Wang Y., Liu Q., Chen Y., Li M., Wang D. (2017) Amine-functionalized PVA-co-PE nanofibrous membrane as affinity membrane with high adsorption capacity for bilirubin, Colloids and Surfaces B: Biointerfaces, Vol. 150, pp. 271-278, Elsevier

Wang Z., Wu Z., Tang S. (2009) Extracellular polymeric substances (EPS) properties and their effects on membrane fouling in a submerged membrane bioreactor, Water Research, Vol. 43, pp. 2504-2512, Elsevier

Wang Z., Ma X., Tang C.Y., Kimura K., Wang Q., Hn X. (2014) Membrane cleaning in membrane bioreactors: A review, Journal of Membrane Science, Vol. 468, pp. 276-307, Elsevier

Wang H., Wang T., Zhang B., Li F., Toure, B., Omosa, I.B., Chiramba T., Abdel-Monem, M., Pradhan M. (2014) Water and wastewater treatment in Africa – Current practices and challenges, Clean – Soil, Air Water, Vol. 42, pp. 1029-1035, John Wiley & Sons, Inc.

Wärtsilä (2013) Waste & Fresh Water Management, Wärtsilä Water Systems Ltd.

Waterleau HQ (2019) Sidestream MBR, <https://www.waterleau.com/en/contact/offices/head-office>, accessed on: 12. September 2019

Wei D., Weimin D, Xiongkui H. (2009) Droplet size and spray pattern characteristics of PWM-based continuously variable spray, *International Journal of Agricultural and Biological Engineering*, Vol. 2, pp. 8-18, ABE Publishing

Weiss P. (1967) Photo induced Polymerisation, *Pure and Applied Chemistry*, Vol. 15, pp. 587-600, The Scientific Journal of IUPAC

Wicks Jr. Z.W., Jones F.N., Pappas S.P., Douglas A. Wicks D.A. (2007) Chapter 2: Polymerization and Film Formation, In: *Organic Coatings: Science and Technology*, 3rd Edition Applications, Properties, and Performance 2nd edition, John Wiley & Sons, ISBN: 978-0-471-69806-7

Woo S.H., Park J., Min B.R. (2015) Relationship between permeate flux and surface roughness of membranes with similar water contact angle values, *Separation and Purification Technology*, Vol. 146, pp. 187-191, Elsevier

Wozniak G. (2003) Tropfenbildungsmechanismen, In: *Zerstäubungstechnik: Prinzipien, Verfahren, Geräte*, pp. 31-50, Springer-Verlag Berlin Heidelberg, ISBN: 978-3-540-41170-3

Xiao K., Liang S., Wang X., Chen C., Huang X. (2019) Current state and challenges of full-scale membrane bioreactor applications: A critical review, *Bioresource Technology*, Vol. 271, pp. 473-481, National Center for Biotechnology Information

Yan F. and Texter J. (2006) Capturing nanoscopic length scales and structures by polymerization in microemulsions, *Soft matter*, Vol. 2, pp. 109-118, The Royal Society of Chemistry

Yi H., Huang J., Gu X.Z., Ni Z.H. (2011) Study on ultrasonic spray technology for the coating of vascular stent, *SCIENCE CHINA, Technological Sciences*, Vol.54, pp. 3358-3370, Science China Press and Springer Verlag

Yoon S.-H., (2016) *Membrane Bioreactor Processes – Principles and Applications*, CRC Press, Taylor & Francis Group, ISBN: 978-1-4822-5583-6

Yu H.-Y., Xie Y.-J., Hu M.-X., Wang J.-L., Wang S.-Y., Xu Z.-K. (2005) Surface modification of polypropylene microporous membrane to improve its antifouling property in MBR: CO₂ plasma treatment, *Journal of Membrane Science*, Vol. 254, pp. 219-227, Elsevier

Yuan W. and Zydney A.L. (2000) Humic Acid Fouling during Ultrafiltration, *Environmental Science Technology*, Vol. 34, pp. 5043-5050, American Chemical Society

Zhang L., Cheng Z., Han L., Wang X., Liu F., Li X., Zeng M. (2017) A Systematic Study of Shear-Tolerant Micro-Emulsion Fracturing Fluid, *International Journal of Petrochemistry and Research*, Vol. 1, pp. 26-30, Madridge Publishers

Zhang Y., Gao J., Meng G., Liu X. (2004) Production of dense yttria-stabilized zirconia thin films by dip-coating for IT-SOFC application, *Journal of Applied Electrochemistry*, Vol. 34, pp. 637-641, Kluwer Academic Publisher

Zhou W., Apkarian R.P., Wang Z.L., Joy D. (2007) Chapter 1: Fundamentals of Scanning Electron Microscopy, In: Zhou W. and Wang Z.L., *Scanning Microscopy for Nanotechnology*, pp. 1-40, Springer-Verlag New York, ISBN 978-0-387-39620-0

Annex

A.1 Properties of humic acid in solution

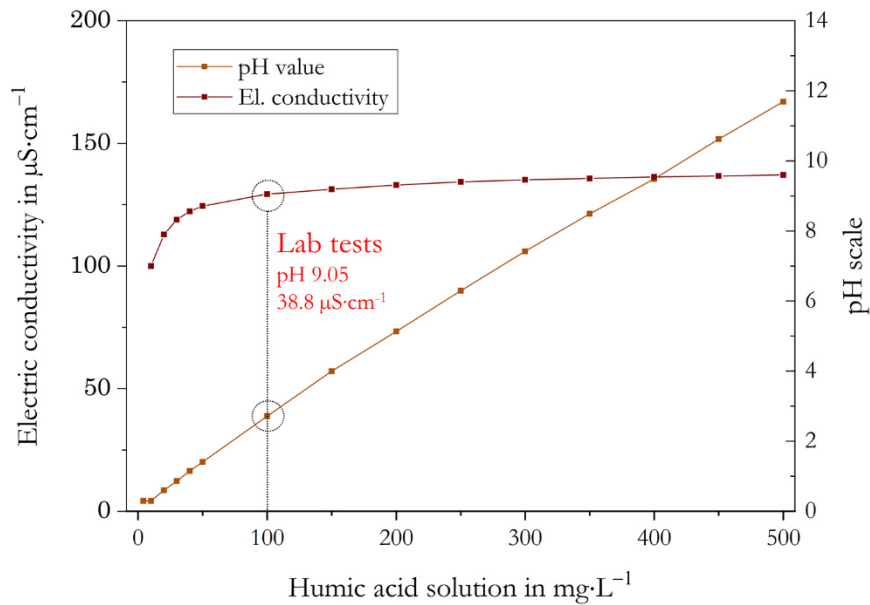


Figure A-1 Properties of humic acid in solution used for laboratory permeability tests

The pH of prepared solution can have a high impact on the level of dissolved matter in terms of the humic acid powder (Owusu-Agyeman et al., 2017). Dissolved and suspended particulates cause different fouling phenomena. Thus identification of both was carried out through the identification of the total organic carbon (TOC) and the dissolved organic carbon (DOC) using the a Total Organic Carbon analyzer (Model: TOC-L CPH/CPN, Shimadzu). Standard deviation of the method was $\pm 0.5 \text{ mg}\cdot\text{L}^{-1}$. Figure X depicts the measuring results for 25, 50 and 100 $\text{mg}\cdot\text{L}^{-1}$ humic acid solution prepared.

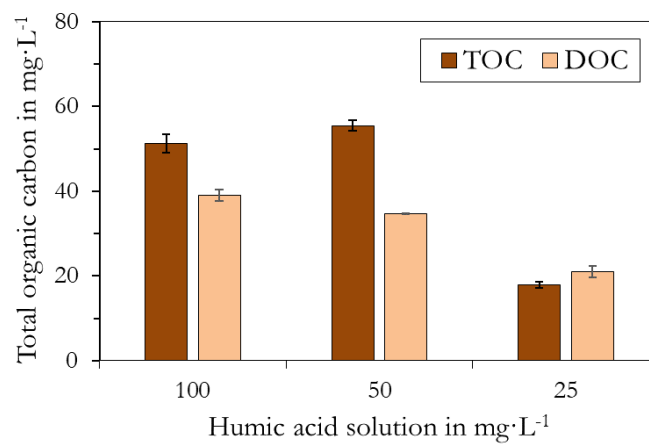


Figure A-2: TOC and DOC depending on prepared humic acid in solution used in this thesis

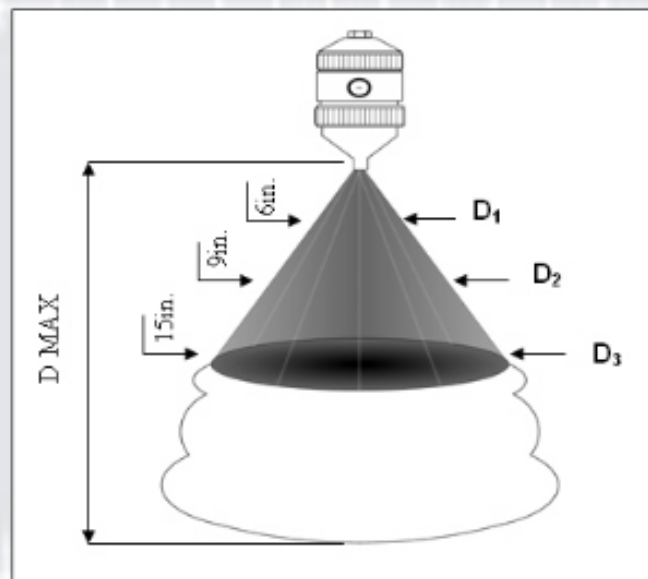
A.4 Approximate spray coverage (Lechler, 2019)



ViscoMist™ Spray Data

Section 3.0

This section presents the Spray Capacity's for possible spray nozzle assemblies. Because the liquid and air pressures are independently controlled, any combinations of these pressures can be referenced to create similar spray results.



P/N: 176.X01.XX.01.00.X			Approximate Spray Coverage (Inches) at specified Distance from Nozzle												
Liquid Capacity		Atom Air (psi)	Fan Air Pressure (psi)	5			10			15			20		
Pressure (psi)	Liquid (gph)			Liquid (psi)	D ₁	D ₂	D ₃	D ₁	D ₂	D ₃	D ₁	D ₂	D ₃	D ₁	D ₂
5	0.8	5	5	4.5	5.0	7.5	4.5	7.0	9.0	6.5	8.0	10.5	7.0	8.0	9.0
			10	4.0	7.0	9.0	7.0	9.0	13.0	9.0	11.0	13.0	10.0	12.0	14.0
			15	5.0	8.0	10.0	6.0	10.0	13.0	9.0	11.0	15.0	9.0	12.0	14.0
			20	6.0	8.0	12.0	9.0	13.0	15.0	10.0	13.0	15.0	11.0	13.0	16.0
10	1.16	10	5	4.5	5.5	7.0	5.5	7.0	10.0	7.0	9.0	12.0	8.0	10.0	13.0
			10	4.0	5.0	7.0	6.0	8.0	10.0	7.0	10.0	13.0	9.0	11.0	14.0
			15	4.5	6.5	8.0	10.0	11.0	13.0	9.0	11.5	14.0	10.0	13.0	15.0
			20	5.0	6.5	8.0	7.0	10.0	14.0	8.0	10.0	15.0	10.0	13.0	17.0
15	1.45	15	5	4.0	5.0	6.5	5.0	7.0	9.0	6.0	9.0	11.0	6.5	8.5	12.0
			10	3.0	4.5	7.0	5.0	7.0	9.0	6.0	8.0	9.0	7.0	9.0	11.0
			15	3.0	5.0	7.0	5.0	7.0	10.0	6.0	9.0	11.0	7.0	9.0	13.0
			20	4.0	6.0	8.0	6.0	7.5	10.0	7.0	10.0	14.0	7.5	10.5	14.0
20	1.69	20	5	2.5	3.5	6.0	3.5	5.0	7.0	5.0	6.0	8.0	6.0	8.0	10.0
			10	2.3	3.5	5.0	4.0	5.0	7.0	5.0	7.0	9.0	5.5	7.5	10.0
			15	2.5	3.5	5.0	5.0	6.0	9.0	4.0	7.0	9.0	6.0	8.0	10.0
			20	3.0	4.0	5.5	5.0	6.5	8.0	5.5	8.0	12.0	7.0	9.5	13.0

* The shaded areas represent the spray data for the #2 Body ViscoMist™ Nozzle Assembly.